Technische Universität München

TUM School of Natural Sciences

Non-perturbative Effects in Production and Detection Processes of Dark Matter

---

Stefan S. Lederer

Vollständiger Abdruck der von der TUM School of Natural Sciences der Technischen Universität München zur Erlangung eines

Doktors der Naturwissenschaften

genehmigten Dissertation.

Vorsitz:		Prof. Dr. Sherry Suyu
Prüfer der Dissertation:	1.	Prof. Dr. Martin Beneke
	2.	Prof. Dr. Alejandro Ibarra

Diese Dissertation wurde am 22.10.2024 bei der Technischen Universtät München eingereicht und durch die TUM School of Natural Sciences am 20.11.2024 angenommen.

Non-perturbative Effects in Production and Detection Processes of Dark Matter

Nicht-perturbative Effekte in Produktions- und Detektionsprozessen von Dunkelmaterie

Stefan Lederer

Abstract

This dissertation examines different non-perturbative effects in production and detection processes of heavy Dark Matter. Annihilation via scattering into resonant unstable particles is shown to factorize from long-range potential effects between initial state particles on an amplitude level, allowing to treat both simultaneously. Neutralino Dark Matter subject to long-range electroweak forces is revisited, improving on the treatment of running couplings and input values and completing the calculation of semi-inclusive annihilation cross sections into high-energetic photons including resummation of electroweak Sudakov logarithms to NLL accuracy. A general study of radiative formation of excited bound states in Coulomb potentials finds a parametric enhancement for repulsive initial states over processes with identically-attractive potentials. This results in eternal depletion during thermal production for non-Abelian gauge symmetries, contrary to the usual freeze-out paradigm, and furthermore violates unitarity systematically at the perturbative leading order for highly excited bound states.

Zusammenfassung

Diese Dissertation behandelt verschiedene störungstheoretisch nicht beschreibbare Effekte in Annihilations- und Detektionsprozessen schwerer Dunkelmaterie. Ein Beweis, dass Annihilation vermittels Streuung in resonante instabile Teilchen von langreichweitigen Kräften im Anfangszustand faktorisiert, erlaubt eine gleichzeitige Beschreibung beider Prozesse. Die bekannte Behandlung von Neutralinodunkelmaterie unter langreichweitigen elektroschwachen Kräften wird im Hinblick auf verwendete Eingangswerte sowie laufende Kopplungen verbessert und die Beschreibung semi-inklusiver Neutralinoannihilation zu hochenergetischen Photonen mit Resummation von Sudakovlogarithmen zur NLL Ordnung wird vervollständigt. Eine allgemeine Betrachtung der radiativen Bildung angeregter Bindungszustände in Coulombpotentialen zeigt eine parametrische Verstärkung von repulsiven Anfangszuständen im Vergleich zu Prozessen mit identischen Potentialen. Dies bewirkt für nichtabelsche Eichtheorien während der thermischen Produktion einen anhaltenden Abbau anstelle des gängigen paradigmatischen Ausfrierens. Des Weiteren wird für hochangeregte Bindungszustände in der führenden störungstheoretischen Ordnung systematisch die Unitaritätsschranke verletzt.

Contents

1 Introduction

Theoretical physics describes processes of nature in the language of mathematics. From a strict system of rules developed on basis of set of experimental results one aims to predict or explain further phenomena, rendering the theory scientifically falsifiable. Due to practical limitations of experimental measurements, also theoretical predictions are only required with finite accuracy and approximate results suffice as no further discrimination is possible on basis of experimentally accessible information. Difficulties arise typically from a conflict between simplicity and accuracy. For useful approximate calculations, it is mandatory to not lose control over all significant contributions whilst correctly identifying negligible ones. A simple enough premise which becomes complicated to fulfill when different simultaneous approximations affect which terms are to be counted as negligible.

In a modern perspective of quantum field theory, the process of approximation is usually performed already on the level of the Lagrangian describing the complete microphysics of the model by construction of an effective field theory. An approximation can generally be stated in terms of some parameter $\epsilon \ll 1$ parametrizing a comparatively small contribution which is identified as negligible. One then expects the physics to remain well described in terms of a perturbative series in powers ϵ^n where higher n are successively suppressed. ϵ could be a small coupling or a ratio of hierarchically separated scales of energies or momenta. The effective theory ansatz ensures all aspects of the theory can be consistently approximated at the same time and additionally defines the procedure for computing arbitrary higher order corrections in the expansion.

This thesis investigates various effects present in annihilation processes of heavy dark matter or, more generally, beyond-Standard Model particles which cause such series expansions to break down and instead demand a resummation of all perturbative orders to produce reliable results. In particular, processes where ϵ is defined by scale ratios and perturbative expansions are broken by the dynamical interplay of different scales are of interest. Large terms at least of order $\mathcal{O}(1/\epsilon^n)$ necessitate such a non-perturbative treatment if they arise systematically at every given order n. It is important to stress that the terminology “non-perturbative”, therefore, does *not* simply refer to a large-coupling regime, in contrast to its common interpretation in physics of the strong interaction. Even in non-perturbative scenarios, effective theories proof to be a useful tool and, provided that they are carefully constructed to respect the power enhanced contributions, can appropriately include them to all orders. A breakdown of perturbativity is therefore not indicative of the breakdown of the effective field theory ansatz but, usually, of shortcomings in the specific employed theory framework. Commonly, this occurs when multiple perturbative expansions are employed simultaneously and the theory framework assumes hierarchies among the different expansion parameters, which may become violated. The later chapters 3 - 6 each study a different source of non-perturbative physics, which is stated at the beginning of the respective chapter in equations (3.1), (4.1), (5.1) & (6.1).

Overall, the topics studied in this thesis may be summarized as precision computations for neutralino Dark Matter, where various simultaneous effects need to be computed reliably, and the impact of excited bound states on Dark Matter production. The remainder of this introduction gives an overview of dark matter and its known or commonly hypothesized properties and behaviors and chapter 2 briefly introduces core concepts of the different effective field theories used throughout this thesis. A brief summary and outlook is provided in chapter 7.

After the introductory chapters, s-channel resonance effects are investigated more closely in chapter 3. The main result is that the Sommerfeld factorization employed in later parts of this work remains justified even in presence of such resonances and no additional soft corrections arise. This chapter may serve as an easy entry point and already introduces Sommerfeld enhancement, which remains ubiquitous throughout this thesis, in a simple model without delving into more detail. Going beyond simplistic toy models, chapter 4 proceeds to analyze Sommerfeld enhancement in electroweakino annihilation, improving on numerical inputs and the treatment of running couplings, including also automated heavy-Higgs decoupling. Building on top of that chapter is the closely related chapter 5 which expands on mixed neutralino Dark Matter by completing the framework to include non-perturbative effects of large Sudakov logarithms in indirect detection photon spectra. Lastly, the core project of this thesis investigated general radiative bound state formation in Coulombic potentials. Results are presented in chapter 6. After a novel derivation of the reaction cross section for general potentials and multipole interactions, theoretical inconsistencies with unitarity for highly excited bound states are proven even when couplings are arbitrarily small. The chapter ends with a study of the phenomenological impact of bound state formation which, surprising to the naive intuition, turns out to be significantly enhanced for repulsive initial states going as far as to invalidate the simple freeze-out paradigm in certain non-Abelian gauged dark sectors. An index of the most important definitions and notations may be found in appendix A. Appendix B lists numerical inputs used for MSSM benchmark studies in chapters 4 and 5. Appendices C and D provide helpful supplementary material to chapter 6.

The present thesis repeats and, in various parts, elaborates in more detail on results which were already or are planned to be published in the following works:

[1] Beneke, Lederer & Urban:
"Sommerfeld enhancement of resonant dark matter annihilation",

[2] Beneke, Lederer & Peset:
"Electroweak resummation of neutralino dark-matter annihilation into high-energy photons",

[3] Binder, Garny, Heisig, Lederer & Urban:
"Excited bound states and their role in dark matter production",

[4] Beneke, De Ros, Garny, Lederer:
"Perturbative unitarity violation in radiative capture transitions to dark matter bound states" [*preliminary, to be published*],

[5] Beneke, Bharucha, Hryczuk, Lederer, Recksiegel, Ruiz-Fermenia:
to be published.

1.1 Evidence of Dark Matter

The riddle of the microscopic nature of Dark Matter (DM) is one of the longest standing unresolved questions in modern physics. Its original conception dates back almost 100 years [6] where an additional "dark", meaning electromagnetically non-luminous and non-reflecting, source of gravitational force was found to be necessary to explain observed rotation curves of galaxy nebulae. The modern Standard Model of particle physics (SM) does not provide a valid candidate for such a dark, massive particle, with neutrinos being ruled out for being too light in mass [7, 8]. Instead, beyond-Standard Model (BSM) physics, usually a novel DM quantum field, need to be considered in order to explain observations. The last century saw tremendous efforts in search of a BSM particle by a variety of means, yet no conclusive evidence was found. A short overview of the most conventional search strategies is given in section 1.4. On the other hand, extragalactic and astrophysical experiments have put forward strong support for the gravitational presence of Dark Matter at length scales ranging from the size of galaxies [6, 9–11] to cosmological large-scale structures [12, 13]. This has firmly rooted DM as a missing piece in modern particle physics and is commonly viewed as one of the few clear indicators that the Standard Model is in fact incomplete.

Under the assumption of DM being some kind of cosmological point-like particle, simulations of structure formation strongly prefer cold, that is massive and low-energetic, DM [14] which is reflected in the fact that to this day the simplistic ΛCDM model of cosmology, provides an excellent fit to most observations despite extending SM physics by only a cold Dark Matter (CDM) component and a cosmological constant (Λ), the latter capturing the even more elusive Dark Energy. Due to its success and minimalism, ΛCDM has become the standard paradigm of cosmology. It allows to derive the energy density of DM from measurements of the cosmic microwave background anisotropies [12], with modern measurements and analyses claiming impressive sub-percent precision on cosmological density parameters,

$$\Omega_{\mathrm{DM}} h^2 = 0.120 \pm 0.001. \tag{1.1}$$

For any generic BSM model which introduces additional non-luminous, stable particles, the quoted value is to be understood as an upper bound which must not be overcome for the theory to remain compatible with cosmological observations. A successful DM candidate, however, should fully saturate this condition solely by itself to reasonable accuracy.

Another implicitly known property of DM derived from experimental null results is a lack of interactions with the SM at "low" energies accessible by current collider experiments. Both above constraints in combination with the required presence of DM on vastly different length scales demand DM to be stable on cosmological time scales [15]. Possible solutions are either a stabilization of DM against decay into lighter SM particles by some additional symmetry under which DM and SM fields have different charges or to simply have essentially no interaction between the two. The latter assumption places DM in a theoretical sector fully secluded from the SM, a scenario in which most experimental searches become obsolete as only gravity remains to infer information about the dark sector. Although possibly reality, such scenarios are theoretically nightmarish due to an inherent lack of falsifiability as well as due to further known problems of the SM. For example, the origin of neutrino oscillations [16] or the catastrophic hierarchy dependence of the Higgs mass term induced by radiative corrections [17] call for extensions of the SM. In light of the vastly unconstrained parameter space of viable DM models spanning dozens of orders of magnitude [18], one may take guidance from the SM by elegantly embedding a viable, stable DM candidate into a solution to known SM shortcomings. This ansatz inherently necessitates an interaction between SM particles and DM.

This thesis exclusively considers cold particle DM candidates with a clear cut connection to the SM, either directly as a charge neutral component of a SM gauge group multiplet or by means of a so-called "portal", an additional, heavier and thus unstable particle which couples to the SM and the DM. To date, uncertainties in the measured properties of the Higgs boson [19] are still large enough to allow for many Higgs portal models. For completeness, it should be noted that also theories explaining the observed DM properties without introducing BSM particles far below the Planck scale exist, for example modeling CDM by primordial black holes or even hypothesizing modifications of gravity on large lengths scales.

1.2 Dark Matter production mechanisms

A successful DM model not only provides a stable, neutral particle which can be sufficiently abundant to saturate Eq. (1.1), but must explain how this abundance results from the cosmological evolution. Even for models of vastly different particle content or phenomenology, particle production can occur by conceptually analogous mechanism. The identification of a viable production mechanism for a given model and its capability to yield the observed DM density is therefore crucial.

The basis to any calculation of particle numbers in the early universe in absence of long range forces is a Boltzmann transport equation for collisions of point-like particles. The physical state of the early universe is a hot plasma of SM particles and possibly further BSM particles such as DM. For simplicity of terminology, the following discussion shall neglect any additional BSM particles. SM particles are continuously rapidly interacting which keeps them in kinetic, chemical and thermal equilibrium. As long as elastic scatterings between DM and SM remain efficient also DM remains in kinetic equilibrium and the equations in terms of phase space abundance densities may be simplified to the Boltzmann equation of number density n, the "Lee-Weinberg equation" [8, 20],

$$\dot{n} + 3Hn = -\left\langle \sigma_{\text{ann}} \text{v} \right\rangle \left(n^2 - n^{eq\,2} \right) . \tag{1.2}$$

Here, H denotes the Hubble rate and $\langle \sigma_{\text{ann}} \text{v} \rangle$ is the thermally averaged annihilation cross-section [20] for the process $\text{DM} + \text{DM} \to X_{\text{SM}}$ where X_{SM} indicates any SM final state of arbitrary multiplicity. When $\langle \sigma_{\text{ann}} \text{v} \rangle$ is large, n^{eq} is the equilibrium attractor solution.

The Boltzmann equation describes the evolution of the number density throughout the history of the Universe. As long as the Hubble rate dominates over the annihilation rate, $n \times \langle \sigma_{\text{ann}} \text{v} \rangle$, as well as the production rate, $n^{eq} \times \langle \sigma_{\text{ann}} \text{v} \rangle$, the dominant effect is a simple dilution caused by the expansion of the Universe. Typically, this state is reached at late times as the number density decreases more rapidly than the Hubble rate. From this point of chemical decoupling onwards, the so-called relic abundance of Dark Matter remains constant until today and thus define the relic energy density $\Omega_{\mathrm{DM}}h^2$. Although in every chapter of this thesis, relic densities are computed, it is only in section 6.5.1 that Boltzmann equations are discussed in more detail in the context of multiple coupled channels since other chapters follow well-known standard procedures.

1.2.1 Thermal relics — freeze-out

One speaks of a thermal relic when DM was in thermal equilibrium, $n = n^{eq}$, in the early Universe when the temperature was still of the order of the DM mass or higher. Inelastic scatterings between SM and DM, typically DM production and annihilation, are taking place efficiently. As temperature falls below the DM mass, annihilation is statistically favored and the DM number follows the exponentially suppressed attractor solution n^{eq} until the annihilation rate becomes inefficient compared to the Hubble rate. Chemical decoupling takes place as described above.

This mechanism of depletion from an initial thermal equilibrium distribution down to the found relic density as temperature decreases is known as freeze-out mechanism, where “freeze-out” denotes the point of complete chemical decoupling itself after which no number-changing reactions notably affect the DM density. Since the *depletion* is driven by the interaction with the remaining bath particles, a key feature of the freeze-out mechanism is that the relic density *decreases* with stronger couplings. Furthermore, thermal and kinetic equilibrium is maintained until the temperature drops significantly below the DM mass, so typically the particle freezing-out is non-relativistic for all relevant processes. Additionally, if all SM masses are negligible, the annihilation cross-section must be proportional to the inverse squared DM mass and smaller DM masses give rise to stronger depletion.

Freeze-out as a production mechanism is attractive since it renders the obtained relic abundance insensitive to the literal production physics which give rise to the large DM abundance in the early universe. Once the abundance is present, all left-over features are erased during thermal equilibration. If either thermal or kinetic equilibrium are violated in the early universe, dynamics become more complicated respectively demanding either separate tracking of DM and SM bath temperatures or even treating Boltzmann equations on full phase space distributions [21].

The terminology of freeze-out being the complete chemical decoupling rather than the point of first significant deviation from equilibrium becomes important in section 6.5. Therein, similarly to the behavior of Sommerfeld-enhanced thermally produced DM, the number density deviates from equilibrium but sees an (eternally) prolonged phase of depletion via intermediately formed unstable bound states.

1.2.2 Non-thermal relics — freeze-in and decay production

Non-thermal relics summarize remnants of a production mechanism where DM never reaches thermal equilibrium in the early universe, typically because coupling strengths are too small or the reheating of the Universe is too low to efficiently produce DM. Since DM is therefore at all times dilute, the annihilation term $\propto n^2$ in Eq. (1.2) is negligible. Instead of seeing a depletion over the course of the Universe, the DM abundance is *built up* over time, a process here (in a minor generalization of nomenclature) referred to as "freeze-in" [22]. The gradual production itself can occur via different processes, including inefficient inelastic scattering (formally the true freeze-in mechanism) or by decay of a heavier particle into the DM. Production by decay is not described by the annihilation term included in Eq. (1.2). This specific case is also known as the "superWIMP" production mechanism [3, 23]. It will see application in section 6.6 where a frozen-out BSM partner decays at late times to DM.

Opposite to the previous section, the initial DM abundance is negligible for any practical application. Since all interaction terms of the DM need to be small anyways (feeble, dilute or otherwise suppressed) in order to avoid thermal equilibrium in the first place, no notable error is made by disregarding it. Since DM abundance ramps up over time, it is possible in certain models to *increase* the relic abundance of DM with stronger couplings. However, this is not necessarily so. For instance, in superWIMP production the number density of DM is approximately in a one-to-one correlation to the decay of the superWIMP mediator. A stronger DM coupling gives rise to shorter lifetimes of the partner, leading to earlier decay, but yields no change in the final DM relic density. Yet, the mediator itself is assumed to be thermally produced and will thus decrease in its abundance at the time of deviation from chemical equilibrium for larger couplings.

This highlights how different production mechanisms can be used simultaneously within non-minimal BSM models of DM to understand successive, well separated dynamics. For too short lifetimes, decay occurs already during the decoupling of the superWIMP mediator and the decoupling of the dynamics of DM and mediator is lost. Such coupled models are rarely well categorized by generic production mechanism and demand dedicated investigations. Accordingly, there is a plethora of thermal and non-thermal production mechanism, nearly as abundant as the range of viable DM models, including "coannihilation" [24], "conversion-driven freeze-out" [25, 26], "superWIMP production" [23], "cannibalistic Dark Matter" [27, 28], "semi-production" [29] (informally known as "pandemic Dark Matter" [30] due to its exponential growth and time of discovery) or "bouncing Dark Matter" [31], to name a few.

1.3 Weakly interacting massive particles as Dark Matter

Typically, a viable DM candidate is charged under neither the electromagnetic nor the strong SM gauge interaction to avoid detection in ordinary baryonic SM matter. This, however, does not exclude the existence of unstable heavy colored or charged particles which efficiently decay on cosmological time scales. Hence, one popular and widely adopted framework for DM or BSM particles is that of a Weakly Interacting Massive Particle (WIMP) which are charged under the SM $\mathrm{SU}(2)_\mathrm{L}\times\mathrm{U}(1)_\mathrm{Y}$ group. Imposing or modeling a $\mathbb{Z}_2$ symmetry to prevent decay of the BSM field into lighter SM states, the lightest member of the electroweak multiplet after electroweak symmetry breaking is rendered stable and, if it is furthermore the charge-neutral component of the multiplet, a DM candidate is obtained. Minimal WIMP models are attractive because of their limited number of degrees of freedom, being classified by only their spin, isospin and hypercharge representations. The hypercharge Y is constrained to half-integer values by the requirement for a charge-neutral component after electroweak symmetry breaking. Beyond this choice of model, the sole remaining free parameter is the mass of the multiplet in the symmetric phase which is constraint by the condition to thermally produce the experimentally observed relic density. Hence, minimal WIMPs can be systematically classified, studied and successively ruled out [32]. More complicated WIMP models can be constructed by introducing additional interactions with SM fields, further unstable BSM fields or by considering multiple WIMPs at the same time out of which only the overall lightest state remains stable.

Yet, the core motivation which lead to the rise of the WIMP as the predominant DM candidate over the last decades is due to a "miraculous" [33] coincidence between the electroweak scales, mass and coupling strength, and the ballpark estimate to produce the correct relic density via thermal freeze-out [20],

$$\Omega_{\mathrm{DM}}h^2 \sim 0.1 \times \frac{2 \times 10^{-26}\mathrm{cm}^3\mathrm{s}^{-1}}{\langle\sigma \mathrm{v}\rangle}. \tag{1.3}$$

Cross sections of the order of $2 \times 10^{-26}\mathrm{cm}^3\mathrm{s}^{-1}$ are roughly found for SM weak couplings and masses in the range around hundreds of GeV - TeV. Although details depend on the specific model, this generic mass range places WIMPs in the range of currently operational or proposed particle colliders [34]. Minimal WIMP DM models of low isospin multiplets yield the correct thermal relic density for masses of 1 - 10 TeV [35].

Apart from their appealing minimalism, WIMPs are often found in theoretically motivated ultraviolet extension of the SM, most prominently in Supersymmetry (SUSY). In the Minimal Supersymmetric Standard Model (MSSM) [36], the superpartners of gauge bosons are then one isospin-doublet Dirac fermion (Higgsino) and one isospin-triplet (wino) and -singlet (bino) Majorana fermion each. Although this model introduces a lot of additional complexity due to couplings between these "electroweakinos" and the Higgs boson sector, it still follows the core concept of demanding R-parity to stabilize the lightest super-symmetric partner [37] which must also be electromagnetically neutral. Chapters 4 and 5 investigate specifically such MSSM neutralino DM candidates. In the case that two of the electroweakino masses are significantly heavier than the third, the DM model is once more well described by a minimal WIMP model. Hence, the isospin doublet and triplet WIMP models are known as Higgsino and wino model, respectively.

Ever repeating updates of experimental null results with increasingly stronger exclusion bounds from all sides over the course of multiple decades made WIMPs begin to fall out of favor with the community and focus has dispersed onto a much broader range of DM models. One prominent candidate at vastly lower mass ranges, μeV - eV, is the axion (or its relatives, axion-like particles), while ultralight DM allows for even much lower masses, reaching Compton wavelengths of astrophysical size. On the other end, primordial black holes or black hole remnant DM theories conjecture DM "objects" (as the term "particle" is hardly applicable here) of astrophysical masses. Although scientifically well motivated, the wealth of investigated DM candidates in modern times is partially in spite of the fact that well-motivated DM models such as the Higgsino remain alive and sound even in face of projected sensitivities of upcoming experiments [38]. In some part, the decline of the WIMP paradigm is also tied to the downfall of low-scale SUSY which was required for it to provide a good answer to the hierarchy problem.

1.4 Experimental constraints on Dark Matter

A large number of experiments have been undertaken, and many more are currently ongoing or planned for the future, in hopes of finding experimental evidence or signatures of DM. Without clear hints towards new physics from shortcomings of the SM at a distinct energies, theoretical considerations are relied upon as guidance in order to identify the most promising phenomenological parameter ranges. To cover the wide variety of theoretically possible models, an almost equally wide range of experimental setups has been conceived, each useful in their own right. Of relevance for this thesis are WIMP DM searches, primarily indirect detection, and also cosmological constraints from structure formation.

1.4.1 Detection avenues for Weakly Interacting Massive Particles

The key features of WIMP DM, a mass in the GeV - TeV scale and a direct connection to the SM via the electroweak interaction, allow for detection from a variety of different physical effects. There are three main conceptually different ways of exploiting the interaction with the SM: i) DM may be directly produced in SM particle collisions in high-energy colliders, ii) DM may scatter off SM particles, making it detectable by energy and momentum deposition in the SM target material, thus leaving a direct evidence of an unknown particle [18, 39], iii) DM may annihilate into lighter SM particles, giving rise to indirect evidence in form of high energetic particles. Such cosmic rays are naturally expected from regions of space with enhanced DM densities such as galactic halos. Indirect detection is further elaborated on below.

Experiments with substantial funding usually also have wide ranging research programs. Nevertheless, much of the combined efforts in modern experimental physics may be viewed as part of a global strategy to probe the WIMP parameter space. The three approaches are complementary and help cover each others blind spots. For example, coannihilation models with a slightly heavier partner to the DM are notoriously difficult to detect in direct or indirect detection if the DM is a singlet under the SM gauge group. Colliders, however, are not limited to the cosmologically abundant DM particle and instead could also produce the coannihilation partner. Note that this example is more precisely a coannihilation model with a BSM WIMP, while the DM candidate is actually not weakly interacting but a SM gauge singlet, yet, such granular nominal differences are often disregarded.

Constraints from high-energy collider experiments are highly model dependent and crucially limited by the accessible energy ranges of the experiment. Current limits on production of neutralinos or charginos remain well below 1 TeV [40–42], where the Higgsino thermal mass resides. Exclusion bounds on the lightest supersymmetric Higgs boson in the MSSM, A^0, strongly depend on the ratio of vacuum expectation values in the MSSM but rule out masses $\lesssim 500\,\mathrm{GeV}$ [43]. Direct detection experiments use recoil effects from DM-nucleon interactions to set constraints on DM interactions with baryonic matter. Existing experiments are most sensitive for WIMP masses of around 10-100 GeV, presently excluding spin-independent cross sections above $10^{-46}\,\mathrm{cm}^2$, but retain some lessened sensitivity also in the TeV range. Such experiments are eventually limited by the atmospheric and diffuse super-nova neutrino background which is predicted to cause an unavoidable background at very low interactions. Neither direct detection nor collider constraints play an important role in the investigations of this thesis and were only briefly touched upon here for completeness.

1.4.2 Indirect detection

At large DM masses in the multi-TeV range, indirect detection becomes the primary source of experimental constraints for many WIMP models. Assuming thermally produced DM to have long decoupled from chemical equilibrium, regions of space with enhanced DM density such as the galactic center or extragalactic DM halos can yield observable fluxes from DM annihilation despite cosmological mean annihilation rates being far below the Hubble rate. Indirect detection relies on the possibility of DM (co-) annihilation and does not constrain asymmetric DM models where the DM field is neither a real field (thus permitting self-annihilation) nor symmetrically abundant between particle and anti-particles (thus differing qualitatively from the baryonic sector). A symmetric abundance is actually a feature of generic thermal production and, additionally, the charge neutral DM candidate in WIMP models is typically a Majorana fermion. Hence, there remains strong motivation to investigate indirect signals for DM.

In 2-to-2 pair annihilation processes of $\chi\chi$ into two photons, kinematics are entirely fixed by the initial state relative velocity and energy-momentum conservation and leading order tree-level calculations predict a line-shaped peak in the gamma-ray spectrum at half the center-of-mass energy smeared by momentum distributions. A detection of such a gamma-ray line at TeV energies originating from regions of high DM densities is considered a smoking gun detection [44] of WIMP DM since no SM processes are expected to produce such features. Alternatively, lower energetic gamma rays may be part of the diffuse, unresolved background radiation which would therefore become anomalously enhanced in regions of high DM density.

Prime targets for indirect detection are thus cosmologically close-by regions of high DM density and low SM background radiation. While the closest target is naturally the Milky Way galactic center [45], it is not particularly clean but contaminated by baryonic sources as it is only observable through the foreground of the galactic plane. Dwarf spheroidal satellite galaxies of the Milky Way, on the other hand, optimize the ratio of expected DM signal to baryonic noise [46] while not being excessively distant. Since annihilation requires two DM particles to be close to each other, indirect detection is sensitive to the precise shape of the DM density profile of any given target, particularly so to the innermost region. However, with only gravitational probes available, DM profiles are difficult to constrain to such detail and, conventionally, simple template models are used instead. The most common analytic templates are known as “Einasto” [47] and “NFW” [48] (for the authors Navarro, Frenk and White) profiles. A “cored” version of the former exists where the density is set constant inside of a critical radius [49] which tends to be in better agreement with observations but deviates from non-interacting CDM models. For the purposes of indirect detection, the main difference is that NFW, being a broken power law, grows to a sharp cups towards the coordinate origin whereas cored profiles predict a much smaller DM density. The DM density integrated along a line of sight of an observation enters in the macroscopic statistical factor for the expected annihilation rate of DM (known as J-factor) and hence the expected particle flux. Thus, J translates observed cosmic ray fluxes to the microphysical annihilation cross-section in a particular DM model. Different choices of DM profiles can weaken indirect detection constraints by multiple orders of magnitude and even upcoming next-generation experiments such as the Cherenkov Telescope Array may still fall short of reaching the generic WIMP thermal relic cross-section $2\times10^{-26}\mathrm{cm}^3/\mathrm{s}$, *cf.* Eq. (1.3), under conservative assumptions [45].

1.4.3 Cosmological constraints

The best-known cosmological constraint on DM is its energy density which is limited according to Eq. (1.1) in the ΛCDM paradigm and understood as an upper bound in theories allowing for multiple DM sub-species. Any model exceeding the experimental measurement overcloses the Universe in its cosmological history and is not compatible with observations. Analogously, cosmological constraints are typically searches for imprints of new physics through otherwise inexplicable physical effects. Despite their highly indirect nature, they can place strong bounds on particle physics models. This section only briefly touches upon some of the more prominent members of this group to place later used bounds into context.

One central result of modern cosmology for DM model building is the exclusion of relativistic (hot) DM in the early Universe on basis of structure formation simulations [14]. A too high number of relativistic degrees of freedom suppresses structure on smaller scales (relative to the simulated large scale structures) and finely grained details become too “washed out” to be in agreement with with cosmological surveys [13, 50]. By direct observations of the so-called Lyman-α forest lines in the spectrum of distant quasars, small scale structure can be measured on redshift scales $z = 2\,\text{-}\,6$ [50, 51], to a large part providing the leading experimental constraints from structure formation. For instance, Lyman-α bounds constrain models where a BSM particle decays into a lighter DM candidate, which is prohibited from being too energetic unless the decay happens sufficiently late [52]. Another cosmological constraint on BSM physics is to maintain successful Big Bang nucleosynthesis for which purely-SM calculations agree to a remarkable degree with the observed ratio of elements heavier than hydrogen [53]. Nucleosynthesis occurs around temperatures of a few MeV, when kinetic energies are insufficient to break nuclear forces, and, roughly speaking, nucleosynthesis bounds imply that any color-charged BSM particles must be absent latest by that time. However, since the strong phase transition occurs beforehand, resulting in color-confinement and making analytic results essentially incalculable, practical limitations of theoretical models are often already found at temperatures $T \sim \Lambda_{\mathrm{QCD}} \sim 1\,\mathrm{GeV}$.

To end with, a remark on gravitational waves is in order. The onset of the era of gravitational wave astronomy has been ushered in by the recent detection of gravitational waves in binary black hole mergers [54] and first stochastic gravitational wave signals [55]. This has led to a surge in interest as one of the few definite properties of DM is its gravitational presence. Rapid advances are expected within the coming decades and the next generation of experiments, yet on its own the impact of gravitational wave measurements on WIMPs is likely to remain limited. Today's primary applications relate to strong phase transitions in the early Universe [56, 57]. Main advantages of gravitational wave astronomy may nevertheless come from improvements to multi-messenger astronomy [58] and the cosmological history, thereby more precisely defining required properties of DM.

1.5 Effective quantum field theory

At last, this introduction closes with a conceptual view on effective field theory (EFT) in quantum physics prior to the introductions of later used frameworks in chapter 2. Especially earlier parts may also be of interest to non-experts while later parts argue for the particular usefulness of EFTs to DM phenomenology.

The modern view on the quantum field theory of the Standard Model is already that of an Wilsonian effective field theory. The SM is known to be incomplete due to various conceptual problems and the exclusion of gravity. While fatal for transcendental interpretations, this poses no direct challenge to the SM as a scientific theory. It solely informs us that the SM is only expected to remain a good description of reality within some window of (comparatively small) energies. Any effects of, for example, quantum gravity may happen at very short scales or high energies, yet by defining the free parameters of the SM to agree with experimental results, short distance effects are included even if a proper description of the dynamics of gravitons is impossible within the SM.

This is the basic principle of EFTs, that for a sufficiently large separation of scales (be they energies, distances or couplings) the description of physical processes becomes approximately independent of the details of much smaller or larger scales, provided that appropriate degrees of freedom are used to describe the system. This scientific philosophy is evidently in agreement with everyday experiences. To ride a bicycle, it suffices to possess an intuitive impression of Newton's laws [59] that pushing the pedals will make them move. There is no need to grasp the full quantum movement of electrons at the interface between pedal and foot, nor a necessity to understand the details of Higgs condensation or color confinement giving rise to the masses of electrons and atoms to keep them stuck by the gravitational field of the Earth. The separation holds in both directions. Certainly the majority of cyclists has only little insight in the dynamics of quantum gravity, yet also the SM of particle physics has little knowledge of the existence of cyclists. Attempts to calculate the wealth of low energy physics directly from the SM as first-principle are unpromising since there are numerous emergent phenomena which arise as unforeseen when only looking at the quantum fields of quarks, leptons and gauge bosons.

To construct a successful EFT, the relevant dynamical degrees of freedom which appropriately describe the given problem of interest must be identified as well as the relevant energy scales which contribute in processes to be described by the theory. The two ingredients are often related. In fact, it is possible to implement the method of regions for integration [60] directly at operator level in an EFT. To do so, one defines multiple instances of the same physical quantum field each carrying only one of the momentum scales of the theory, accordingly expanding all mathematical objects in calculations, despite integrating still over the complete phase space volume.

It should be noted that beyond the top down approach of model building pursued in this thesis, EFTs also flourish in bottom up approaches by parametrizing our ignorance of the nature of DM in a set of BSM Wilson coefficients. In this approach, basically, not only some but all of the BSM momentum modes are integrated out of the theory, rendering it entirely independent of the need to specify an ultraviolet SM extension. The model ansatz is motivated by the exceptional success of the SM in a wide range of energies, even far beyond the its heaviest particle masses. Hence, a split description of SM and BSM physics, which is inherently suggestive of an EFT treatment, appears to yield a good approximation of processes nature.

For one example, WIMP DM has been excluded at masses close to the electroweak scale and pushed into the TeV range, as was introduced above. As a consequence, there is a growing ratio of scale between the SM and BSM physics which causes a series of non-perturbative effects in DM theories as the simultaneous description of free DM and free SM particles becomes inadequate. Among other effects, this development challenges the long-standing WIMP paradigm where annihilation rates for thermal production or indirect detection may simply be taken from perturbative calculations directly in the full theory. Since calculations in quantum field theory are notoriously difficult and usually only possible within perturbation theory [61], EFTs become a particularly powerful tool when non-perturbative effects give rise to a change in the relevant degrees of freedom, for example in the description of bound states. In addition to the usual perturbative expansion in interaction strengths in QFT, there are two main approximations which stand to reason when treating thermally produced WIMPs. Firstly, as mentioned, masses of all SM particles become negligible compared to the DM mass in the TeV range. Secondly WIMP velocities are typically already non-relativistic at the onset of chemical decoupling and decrease as time goes on. The interplay of these expansions and non-perturbative effects sourced thereby constitute the core of this thesis.

2 Overview of effective theories

A variety of non-perturbative effects are investigated in this thesis, each requiring a uniquely different effective field theoretical description. An EFT framework allows to implement useful physical approximations already on a Lagrangian level and thus, if constructed appropriately to a given problem, to focus on the physically relevant degrees of freedom. The present chapter briefly introduces the core ideas of the EFTs used in the later parts, collecting schematic Lagrangian terms as well as the most important definitions in a general notation. Detailed derivations are skipped and may be found in pertinent textbooks or the provided citations. Especially, soft-collinear effective theory in section 2.4 is a complicated theory but broken down to the relevant qualitative description of Sudakov enhancement. This is in part to avoid to reiterate too much on [62] wherein all required soft-collinear EFT results are already presented.

All throughout this thesis, Dark Matter is denoted by χ, with required specifications introduced as needed via additional notation. This implies that considered non-relativistic two-constituent states usually consist of χ or, possibly, its anti-particle and hence the DM mass M_χ sets the hard energy scale. The only exception is found in section 6.6 where a heavy t-channel mediator $\tilde{q}$ decays to much lighter χ, thus $M_{\tilde{q}} \gg m_\chi$. In context of the MSSM, χ^0 refers to neutralinos, hence χ is its own anti-particle, but also charginos $\chi^\pm$ occur. To ease a bit the notation, $M_\chi = M_{\text{LSP}}$ will be used there. Notably, it is thus not ubiquitously defined whether χ refers to Majorana or Dirac fermions or even charged scalars. In light of this, also the present introductory chapter is kept in a rather general formalism, using simply M to denote large mass scales.

Although the analyses of chapters 3 - 6 are for the most part discussed separately, the different physical phenomena are by no means exclusive to each other. Quite in contrast, all ingredients can act in concert in certain processes of neutralino annihilation.

2.1 Shared concepts

The investigated physical processes in all chapters start from a two-particle state $|p_a, p_b\rangle$ of a non-relativistic relative velocity

$$\text{v} = |\vec{\text{v}}| = |\vec{\text{v}}_a - \vec{\text{v}}_b| \approx \left| \frac{\vec{p}_a}{M_a} - \frac{\vec{p}_b}{M_b} \right| . \tag{2.1}$$

The approximation in the second step holds for slowly moving, that is “heavy”, particles v $\ll 1$. The center-of-mass momentum is arbitrary as one may always use translational invariance to boost to the center-of-mass frame of the 2-particle system, $\vec{p}_a = -\vec{p}_b$, where it vanishes. Calculations are always performed in the center-of-mass frame.

All subsequent chapters investigate heavy particles transforming under some gauged unitary symmetry, with varying additional Yukawa interactions. The relevant UV-complete BSM Lagrangian terms can therefore be conceptualized by generic scalars (Φ) and fermions (Ψ) as

$$\begin{aligned}\mathcal{L}_{\mathrm{UV}} = {} & (D\Phi)^\dagger_\mu (D\Phi)^\mu - M_\Phi^2|\Phi|^2 + \overline{\Psi}\left(i\not{D} - M_\Psi\right)\Psi \\ & - \frac{1}{4}F^{\mathfrak{a}}_{\mu\nu}F^{\mu\nu,\mathfrak{a}} + \overline{\Psi}\mathbf{y}_{\Phi\Psi}\Phi\Psi + \text{“h.c.”} \ , \end{aligned} \tag{2.2}$$

using

$$D_\mu \equiv \partial_\mu + i\hat{g}\,\hat{T}^{\mathfrak{a}}A^{\mathfrak{a}}_\mu . \tag{2.3}$$

$\mathfrak{a}$ sums over adjoint indices of all gauge symmetries present in the theory, including SM gauge groups, and $\hat{T}^{\mathfrak{a}}$ is the gauge generator operator with $\hat{g}$ the gauge coupling constant (which, technically, is a simple diagonal matrix $g^{\mathfrak{ab}}$). The contact interaction between Ψ and Φ involves matrix valued Yukawa couplings $\mathbf{y}_{\Phi\Psi}$ which may be non-trivial gauge structures, namely Clebsch-Gordan coefficients, with entries given by $(y_{\Phi\Psi})^{\mathfrak{abc}}$ to maintain gauge symmetry. Different mass scalings of $M_{\Phi,\Psi}$ will be considered as well as cases where multiple scalars or fermions are present. Equation (2.2) implicitly uses complex scalars (Dirac fermions) whereas for real scalar fields (Majorana fermions) the usual factor $\frac{1}{2}$ must be added to all terms quadratic in the respective field.

Typical expansion parameters used to define the particular expansions of a given EFT are small coupling strengths α, which are dimensionless by convention, or ratios of dimensionful quantities such as energy, momentum or mass. The EFT picture shows its full power when all scales present in a theory can be factorized from each other, turning otherwise complicated multi-scale problems into a set of simpler single scale problems. If multiple unrelated expansion parameters are present in a theory, a power counting relating them is required and, once set, must be strictly maintained in order to consistently perform expansions.

To set terminology, the following momentum modes will be considered, here counted by an expansion parameter $\lambda \ll 1$ and a single large scale M:

mode		*scaling*	*description*
hard	h	$p_h \sim M$	all components highly energetic
collinear	c	$n_+p_c \sim M$, $n_\perp p_c \sim M\lambda$, $n_-p_c \sim M\lambda^2$	high-energetic light-like along n_-
soft	s	$p_s \sim M\lambda$	all components low energetic
potential	p	$p_p^0 \sim M\lambda^2$, $\vec{p}_p \sim M\lambda$	instantaneous off-shell modes
ultrasoft	us	$p_{us} \sim M\lambda^2$	all components very low-energetic

Anti-collinear modes $\bar{c}$ are identical to collinear ones under exchange $n_+ \leftrightarrow n_-$ with $n_\pm$ introduced in section 2.4. Each of the following sections serves the purpose of providing an overview of the respective EFT sufficient to build an understanding of where non-perturbative effects arise from and how they are treated by the EFT with no claims to completeness.

2.2 Non-relativistic effective theory — NREFT

Non-relativistic effective theory (NREFT) [63] describes particles moving at velocities much smaller than the speed of light

$$\mathrm{v}_\psi \ll 1.$$

In the following ψ denotes a general non-relativistic field of velocity v_ψ, left unspecified in its spin-statistics as bosonic or fermionic but always of mass-dimensions $[\psi] = 3/2$. For on-shell particles, the (single particle) 4-velocity is approximated to first order as

$$v_\psi \equiv \begin{pmatrix} 1 \\ \vec{0} \end{pmatrix} + \begin{pmatrix} 0 \\ \vec{\mathrm{v}}_\psi \end{pmatrix} + \mathcal{O}(\mathrm{v}_\psi^2) \tag{2.4}$$

and the virtuality of slow moving particles is of order $p^2 - M^2 = \mathcal{O}(M\mathrm{v}_\psi^2)$. In the leading (static) approximation, its momentum is simply given by the rest mass, $p_\psi \approx M v_\psi + \mathcal{O}(M\mathrm{v}_\chi)$. The residual momentum can be at most of the potential scale in order for ψ to remain on-shell. Having integrated out hard momentum modes, the result for the gauge kinetic Lagrangian term is [63, 64]

$$\mathcal{L}_{\text{NREFT}}[\psi] = \psi^\dagger \left(iD^0 - \delta M_\psi + \frac{\vec{D}^2}{2M} \right) \psi + \mathcal{O}\left(M^4 \mathrm{v}^6\right). \tag{2.5}$$

Technically, δM_ψ is a generic Wilson coefficient which is found by matching to be $\delta M_\psi \equiv M_\psi - M$. The NREFT Lagrangian still describes soft, potential and ultrasoft momentum modes. This also affects light annihilation- or decay-products of heavy particles and annihilation operators of heavy fields arise in NREFT as imaginary-valued local 4-point vertices between non-relativistic states. Inelastic cross sections are then computed by use of the optical theorem [65]. For the non-relativistic description of heavy external states to be sensible, one requires $M_\psi = M + \mathcal{O}(M\mathrm{v}^2)$ or else the residual mass term dominates the propagator, $M_\psi - M \gg iD^0$. If only a single heavy mass exists in the theory, $M \equiv M_\psi$ is the most sensible choice and the residual mass term vanishes. Yet, some $\delta M_\psi \neq 0$ are in general unavoidable in theories of multiple nearly degenerate non-relativistic fields. A simultaneous description of multiple hard scales with large scale separations between them is possible [64]. Several discussions in chapters 4 and 5 concern the applicability of (P)NREFT in case of $\delta M \sim M\mathrm{v}$. For now, δM is a (diagonal) residual mass term of the formally correct power counting $\delta M_\psi \leq \mathcal{O}(M\mathrm{v}^2)$.

When integrating out hard modes, all propagators are approximated according to their momentum power counting, following the method of regions prescription. As a consequence, the matching becomes blind to resonant effects if some internal particle is counted as a hard mode while the propagator denominator is actually anomalously small due to cancellations, $M_R - (M_1 + M_2) \sim \mathcal{O}(M\mathrm{v})$ in the example of s-channel resonance scattering. Instead, the non-relativistic initial two-particle state and the resonance field are now (almost) mass degenerate and may be described by a single non-relativistic EFT description. The presence of two small parameters, v and $\delta M_R/M$ breaks the usual perturbative expansion in v.

Non-relativistic particles of finite lifetime formally warrant their own unique unstable particle EFT [66, 67] which is in most practical aspects similar to heavy quark effective theory [68] or NREFT. There are some conceptual differences, nonetheless. The pole mass of unstable particles, and thus the residual mass, develops an imaginary part which is explicitly written in terms of the decay width, $\delta M_\psi - \mathrm{i}\Gamma_\psi/2$, *cf.* Eq. (3.1). Notably, external states in scattering theory are evaluated at infinite past or future times and cannot involve any particles of a finite lifetime, hence one must not apply cutting rules to unstable particle propagators. In the example of s-channel scattering via an unstable particle, one must instead once more use the optical theorem to gain access to the annihilation cross-section via the resonance funnel and the EFT would be formally insensitive to specific final states. This is directly analogous to the above statement on annihilation operators, however now applied to two-point "interactions", that is propagators, which translates to prompt decay of one heavy particle into hard modes.

2.3 Potential non-relativistic effective theory — PNREFT

Soft modes and potential modes can be additionally integrated out from the NREFT Lagrangian, giving rise to instantaneous, spatially non-local interactions known as potentials from classical physics. They arise as non-perturbative effects when the relative momentum between two particles,

$$p = p_{\mathrm{rel}} = \frac{M\mathrm{v}}{2}, \tag{2.6}$$

anomalously enhances t-channel diagrams of interactions via a light mediator. The obtained EFT is known as potential non-relativistic effective theory (PNREFT) [69].

As long as the mass of the virtual mediator propagating in the t-channel is comparatively small, $m_{med} \lesssim M\mathrm{v}$, and its coupling strength to ψ satisfies $\alpha \gtrsim \mathrm{v}$, *cf.* Eq. (4.1), successive t-channel exchanges in NREFT are not systematically suppressed in powers of α. Perturbation theory in powers of the mediator coupling strength α breaks down due to the interplay of the multiple expansion parameters in the theory. Even infinitely many successive t-channel exchanges remain of the same power counting order as the kinetic term in the Lagrangian and the potential-mode t-channel exchange diagram must be treated as a non-perturbative term in the Lagrangian. Such diagrams reproduce in position space well-known non-local Yukawa potentials [70–72],

$$\mathcal{L} \supset -\int d^3\vec{r}\,(\psi_1\psi_2)\,(t,\vec{X})V_{(12),(34)}(r)\,(\psi_3\psi_4)\,(t,\vec{X}+\vec{r}) \tag{2.7}$$

where

$$V(r) = \frac{-\alpha^{\mathrm{eff}}}{r}\mathrm{e}^{-m_{med}\,r}. \tag{2.8}$$

Here, α^{eff} indicates that it is typically not directly the coupling strength of a theory but an effective potential strength involving additional factors assumed to be $\mathcal{O}(1)$. Naturally, massless mediators source Coulomb potentials. Implying the summation over possibly different particle species 1-4, the Lagrangian term may be given compactly in terms of constituent field notation, that is still without projecting onto the 2-constituent space, as

$$\begin{aligned}\mathcal{L}_{\mathrm{PNR}}\left[\psi\right] = \psi^\dagger \left(\mathrm{i}\partial^0 - \delta M_\psi + \frac{\vec{\partial}^2}{2M_\psi}\right)\psi \\ - \int \mathrm{d}^3\vec{r}\ \left[\psi^\dagger\psi\right](t,\vec{X}+\vec{r})\ V(r)\ \left[\psi^\dagger\psi\right](t,\vec{X}).\end{aligned} \tag{2.9}$$

ψ may be read as a vector including all non-relativistic species present in the theory which for complex fields means at least the particle and its anti-particle. Correspondingly, δM_ψ and $V(r)$ are then understood as matrices where the former is only diagonal in the mass eigenbasis of a given model. The covariant derivative temporal component is dropped in favor of ∂^0 to ensure a uniform power counting. Since $\alpha \sim \mathrm{v}$ and $p \sim 1/r$, the kinetic and potential terms all are of order $M_\psi^4 \mathrm{v}^5$. Beyond the leading order Lagrangian (2.9), also ultrasoft modes of light fields remain in the theory and interact with ψ. They give rise to multipole interactions and thus to radiative transitions between energy levels of multi-particle states [73, 74]. Multipole interactions of two-constituent states will be introduced in general in chapter 6 without relating them to any particular UV completion. The Lagrangian after projection onto the two-constituent space [75] is also given there assuming a decomposition of $[\psi_1\psi_2]$ into eigenstates of the potential, $\mathcal{S}$ and $\mathcal{B}$, see Eq. (6.11). The two-constituent field operators are then bilinear functionals of the constituent field operators folded by the two-particle wave function Ψ [61].

After the projection onto two-constituent states, the equations of motion in PNREFT are given by the quantum mechanical Schrödinger equation as in NREFT, however now with the addition of the potential term, making solutions more interesting than simple, non-interacting Fourier modes. Since soft modes decouple to leading order from non-relativistic fields already in NREFT and potential mode exchanges are resummed to all orders, interaction terms such as for example imaginary four point interactions describing annihilation are essentially unchanged from NREFT on the Lagrangian level. Yet, upon calculating correlation functions, differences arise from the modification of the wave functions by including the potential in the equations of motion. For the generic short-distance annihilation forward-scattering operator, the impact of potential interactions is encoded in the wave function at the origin absolute square,

$$\int \mathrm{d}^3\vec{r}\ \langle p|\ \left[\psi^\dagger\psi\right]^\dagger(\vec{r})\,\mathrm{i}f\delta^3(\vec{r})\ \left[\psi^\dagger\psi^\dagger\right](\vec{0})\ |p\rangle = \mathrm{i}f\ |\Psi_p(0)|^2. \tag{2.10}$$

f is an agnostic Wilson coefficient and $\Psi_p(r)$ the two-particle state wave function obtained by projecting the single constituent field operators onto the external state of relative momentum p. Translation invariance allows to set one coordinate to $\vec{0}$ and the optical theorem now relates the forward scattering amplitude to an (inclusive) inelastic cross section. Sommerfeld enhancement [76] is now defined as the multiplicative modification of the cross section with respect to using free, non-interacting wave functions of NREFT, $|\Psi_p^0(0)| = 1$. The definition is analogous for other observables or in more complicated processes [77]. Concretely, the Sommerfeld factor in the example of a cross section in a simplistic single field model is thus

$$S \equiv \frac{\sigma}{\sigma_0} = \frac{|\Psi_p(0)|^2}{|\Psi_p^0(0)|^2} = |\Psi_p(0)|^2, \tag{2.11}$$

where σ_0 denotes the perturbative cross section. For Coulomb potentials, S depends only on the ratio $\alpha^{\text{eff}}/\text{v}$, hence the Sommerfeld factor is typically thought of as a function of velocity $S = S(\text{v})$ while M and α^{eff} are fixed. Performing a partial wave decomposition on the two-particle states, the s-wave Sommerfeld factor in a Coulombic potential, Eq. (2.8) with $m_{med} = 0$, is

$$S_0(\text{v}) = \frac{2\pi \frac{\alpha^{\text{eff}}}{\text{v}}}{1 - \mathrm{e}^{-2\pi \frac{\alpha^{\text{eff}}}{\text{v}}}}. \tag{2.12}$$

This holds for any Coulombic potential, including repulsive scenarios $\alpha^{\text{eff}} < 0$, without violating that $S_0(\text{v}) > 0$. In a more modern language, the Sommerfeld factor is seen as a multiplicative contribution obtained from the modified spectral probability density compared to the free, non-interacting case. Such is the formulation in the language of retarded 4-point (or 2-particle) Green functions evaluated at the origin which is theoretically convenient due to its extensibility to descriptions at finite temperature [78]. In vacuum, there are no differences to the wave function formulation given above.

2.4 Soft-collinear effective theory — SCET

When heavy particles annihilate or decay into significantly lighter fields, final states are highly energetic and an effective theory to describe nearly massless particles must be employed to disentangle the different scales of the process. This is achieved in soft-collinear effective theory (SCET) [79, 80] wherein fields are expanded around a dominant hard mode, $n_+p \sim M$, in the direction a light-like vector n_-. At leading order, hard annihilation or decay processes emit two light fields fixed into a back-to-back configuration in the center-of-mass frame by momentum conservation. These primary fields emitted from the hard vertex may undergo additional soft or collinear splittings and the physical final state is a two jet event collimated along the jet axes

$$n_- \equiv \begin{pmatrix} 1 \\ 0 \\ 0 \\ +1 \end{pmatrix} \quad \text{and} \quad n_+ \equiv \begin{pmatrix} 1 \\ 0 \\ 0 \\ -1 \end{pmatrix}. \tag{2.13}$$

The spatial momentum direction is arbitrarily chosen. Being light-like, $n_\pm^2 = 0$ while $n_+n_- = 2$. It thus becomes clear why above the large mode along the direction n_- is projected out by acting with n_+. On a technical level, SCET performs an expansion of the orthogonal mode $\lambda = p_\perp/n_+p$ where $n_\pm p_\perp \equiv 0$. For a collinear particle of momentum p_c, the different modes then scale as

$$n_+p_c \sim M\,, \quad p_{c\perp}^\mu \sim M\lambda\,, \quad n_-p_c \sim M\lambda^2\,,$$

where the latter is a consequence of demanding $p_c^2 \sim M\lambda^2$, since masses are negligible at energies of $\mathcal{O}(M)$. For anti-collinear particles, the roles of $n_\pm$ are simply interchanged. The operator fields are again split according to the method of regions into hard, (anti-) collinear and soft modes.

In computing loop diagrams, divergences arise in SCET in the kinematic limit where emitted radiation momenta become soft, $p_{c,s,us} \to 0$, or collinear with one of the jet axes, $\vec{p}_{c,s,us} \| \vec{p}_{\text{primary}}$. The simultaneous soft and collinear limit yields quadratic divergences which, after renormalization, give rise to Sudakov double logarithms [79, 81] of ratios between the widely separated scales of the theory, $L = \log(1/\lambda)$. A combined expansion in the perturbative coupling α and L can be written as

$$\sum_n \alpha^n \left(c_{\text{LL}}\, L^2 + c_{\text{NLL}}\, L + \mathcal{O}(1) \right)^n . \tag{2.14}$$

Such scale logarithms are troublesome as EFT is founded on the very assumption that $\lambda \ll 1$. Once $L \gtrsim 1/\alpha$, perturbation theory by expanding in α (that is in loop orders) breaks down. To obtain reliable results to $\mathcal{O}(1)$, all leading and next-to-leading logarithmic (NLL) contributions need to be resummed to all orders. Furthermore, to maintain a single power counting parameter, it is convention to count each logarithm as $L \sim 1/\lambda \sim 1/\alpha$. For practical applications in DM phenomenology, the hard and soft scales are usually identified with twice the DM mass and the SM gauge boson mass scale, respectively. The inherent construction of the EFT on basis of a separation of scales can be recovered as a factorization theorem between multiplicatively separated hard, collinear, anti-collinear and soft functions of the cross section. It allows to evaluate each function at its natural scale, where logarithms are small, and subsequently evolve all of them to a single common scale in a non-perturbative fashion, see [82] for an example. In performing the resummation of LL and NLL terms to all orders, one includes repeated dominant emission of soft and collinear modes off of the primary collinear modes.

As an aside, it should be noted that even stronger "super-leading" logarithmic enhancements are known to arise in certain processes of QCD [83], making the above identification "leading" and "next-to-leading" logarithmic powers a processes and, possibly, loop-order dependent one. Nevertheless, the multi-loop accuracy striven for in QCD are far beyond any useful accuracy for the purposes in DM phenomenology.

2.5 Effective theory of heavy Dark Matter — PNRDM

The potential non-relativistic effective theory of Dark Matter, including effects from PNREFT and SCET, is designed to describe annihilation processes of heavy, non-relativistic electroweak multiplets which host a DM candidate annihilating into highly-energetic, light standard model particles, here specifically photons. In the following, it is abbreviated as PNRDM, adopting an existing name [82, 84] for simplicity, with an implicit presence of SCET. With typical WIMP DM masses, the large scale ratio between M_χ and SM scales is automatic and SCET is included in matching computations of short distance annihilation operators of PNREFT opposed to the usual inclusive hard Wilson coefficients. PNRDM thus captures non-local potential interactions between initial states as well as large logarithmic enhancements in the soft and collinear limits. Its non-inclusive annihilation cross-sections are needed to accurately predict cosmic ray spectra searched for in indirect detection experiments. The initial state to the processes consists of a pair of DM Majorana fermions. The theory keeps only a single power-counting parameter to uniformly describe all expansions,

$$\lambda \equiv \frac{m_W}{2M_\chi} \sim \mathrm{v} \sim \alpha. \tag{2.15}$$

All scales of the standard model (the electroweak scale, boson masses or the onset of importance of fermion masses) are uniformly approximated by m_W while the DM mass scale $2M_\chi$ remains open to the specific BSM model. Since DM is only the lightest state of a gauge multiplet, with mass splittings sourced by loop corrections and electroweak symmetry breaking, there are additional almost degenerate states nearby $2M_\chi$ which contribute to the annihilation. On the Lagrangian level, PNRDM introduces no essential new difficulties beyond the successive implementation of SCET and PNREFT. The simultaneous presence of many scales, masses and couplings does, however, lead to sizable complexity during computations.

Factorization theorems splitting not only the Sommerfeld enhancement but all contributing scales into separate factors were found for annihilation near the endpoint where most of the energy is carried away by a single gauge boson and the final state is again a back-to-back two-jet event described in SCET [82, 85]. In a first step, the annihilation cross-section of DM is split into the annihilation matrix Γ_{IJ} and the long distance Sommerfeld effect S_{IJ} analogous to Eq. (2.10) [77, 86],

$$\sigma \mathrm{v} = \sum_{IJ} S_{IJ}\, \Gamma_{IJ}, \tag{2.16}$$

The summation runs over all charge neutral two-particle state indices I, J, *e.g.* $I = (I_1 I_2)$, from the BSM gauge multiplet (mass-) eigenstates. Rather than encoding the total annihilation cross-section into a single anonymous Wilson coefficient f, now Γ resolves additional final state physics allowing to treat (semi-) exclusive annihilation processes near the spectral endpoint. Being matrices in the NR field space themselves, potential exchanges can scatter different multiplet states into each other and I (J) need no longer coincide with the physical initial (final) state of the scattering process. Moreover, $I \neq J$ still defines a forward scattering process. Hence, the above S_{IJ} includes the Sommerfeld enhancement for $\chi\chi$ scattering into I by infinitely many ladder exchanges *and* the corresponding final state process of J scattering into $\chi\chi$. In practice, this means that the annihilation of any states sufficiently degenerate to the DM candidate can contribute to the DM annihilation process. To describe the Sommerfeld effect in arbitrary initial states, an even more general form than S_{IJ} is needed, *cf.* section 4.2.1.

As an inheritance from SCET, Γ_{IJ} further factorizes into separate hard, collinear, anti-collinear and soft functions,

$$\Gamma_{IJ} = H_{kl} \cdot [Z_\gamma \times J \times \mathbf{w}]_{IJ,kl}\,. \tag{2.17}$$

The notation abbreviates some mathematical technicalities such as Mellin space transformations and an integration in the final state photon energy E_γ. Full details may be found in [2, 82, 87]. As a technical aside, the unobserved jet function J demands the introduction of hard-(anti-)collinear light-like modes where $n_- p_{hc} \sim M\lambda$, due to the parametric counting of the resolution window of the observed photon energy $E^{\gamma}_{res} \sim m_W$ [82]. In practice, this detail is irrelevant to here presented investigations and henceforth omitted. H_{kl} is the hard function describing the local annihilations into primary emitted SCET fields where k and l label the inserted annihilation operators. To leading order, H is simply given by the product of two hard annihilation coefficients C_k,

$$H_{kl} = C_k C_l^* . \tag{2.18}$$

In order to perform Sudakov resummation up to the NLL order written in (2.14) the full one loop anomalous dimension of the hard Wilson coefficients is required [2, 62]. This includes also soft exchanges between initial state legs of the annihilation vertices. Note that the topology of such initial state interactions is diagrammatically identical to the final ladder wrung already resummed into the Sommerfeld factor S_{IJ}, yet there is no double counting, as the Sommerfeld enhancement treats potential mode exchanges whereas the anomalous dimension one loop computation includes exchanges of soft modes.

The full framework of PNRDM, and for that matter SCET, only becomes necessary when one is interested in the details of the annihilation spectra of DM, which will be investigated in chapter 5 for mixed neutralino DM candidates. All other chapters are primarily concerned with the full annihilation rate in order to compute freeze-out relic abundances.

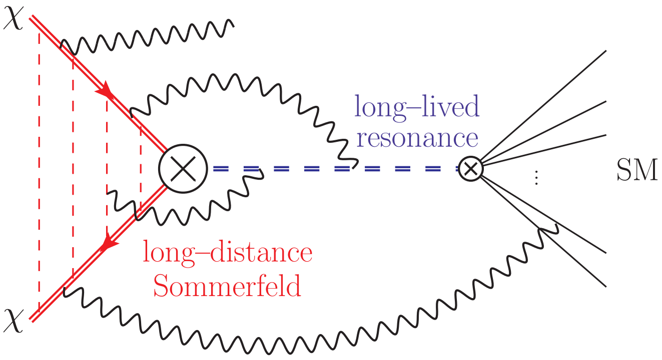

Figure 3.1: Schematic depiction of the resonant s-channel annihilation process. In blue the long-lived intermediate resonance and in red, the exchange of a light mediator that produces the long-distance Sommerfeld effect. Light Standard Model final states are shown as straight black lines. Long-distance (soft) gauge boson modes (black wavy lines), including real emissions, vanish at leading order according to Eq. (3.16). The figure was taken from [1].

3 Resonant particle decay

This chapter regards inelastic scattering of a non-relativistic two-particle initial state via an intermediate s-channel mediator which is produced close to on-shell in the annihilation process. That is, for initial state particles of masses $M_{a,b}$ the s-channel mediator of mass M_R has to fulfill the resonance condition

$$\boxed{\left|\frac{M_R^2}{(M_a+M_b)^2-M_R^2}\right| \gg 1.} \tag{3.1}$$

Taking $\chi_{a,b}$ and R to be heavy, non-relativistic particles, the physical process of interest is thus

$$\chi_a\chi_b \to R \to F \tag{3.2}$$

where $F \neq \chi_a\chi_b$ denotes inelastic final states to be specified later. The process breaks perturbative power counting by virtue of the internal propagator being anomalously enhanced near the resonance condition. The propagator is only regulated by finite mass splittings or by a non-vanishing decay width of R, which is obtained from all-order resummation of higher loop processes in the two-point function. In DM annihilation, $\chi_a\chi_b$ form a particle anti-particle pair annihilating into light degrees of freedom. Going beyond minimalistic models, χ is assumed to be charged under some gauge symmetry giving rise to initial state potentials according to PNREFT. A diagrammatic depiction of the process under consideration is shown in Fig. 3.1. The total process sees an initial two-particle initial state $\bar{\chi}\chi$ experience a long-distance Sommerfeld effect (red) and scatter into a number SM final state particles (black straight lines) via an intermediate s-channel resonance (blue). Black wavy lines depict crucial soft gauge fields which can a priori connect any two parts of the process or be emitted as an on-shell final state particle from the initial state. Such soft interactions spoil a simple factorization between Sommerfeld enhancement and the s-channel resonance or the final state. They will be shown to cancel out at leading order.

By use of effective theories, the physics of different scales can be systematically disentangled with the goal of turning the multi-scale calculation into several purely multiplicative factors, each involving only one single scale. Although not guaranteed to exist, finding such a factorization theorem can dramatically reduce the complexity of a problem, as was outlined already in section 2.5.

To place the rather technical factorization theorem on a solid foundation, section 3.1 discusses the details of the used (P)NREFT Lagrangian in a schematic toy model. Next, sections 3.2 and 3.3 derive the decoupling of soft gauge boson modes and the factorization theorem of the annihilation cross-section, respectively. Finally, some exemplary phenomenology will be discussed relating to an MSSM inspired toy model realization in section 3.4.

The work presented in this chapter has been published under the title "Sommerfeld enhancement of resonant dark matter annihilation" [1].

3.1 Model setup

Starting from a rather general ansatz, this study of intermediate s-channel resonances in DM annihilation processes considers a particle anti-particle initial state $\chi_a = \bar{\chi}_b$ of mass $M_a = M_b \approx M_R/2$ together with a heavy, resonant field R. Both fields, χ and R, are assumed to transform under some representation of a gauge symmetry G such that their trilinear combination $\chi^* \otimes \chi \otimes R$ can form a gauge singlet and, thus may appear in a gauge invariant Lagrangian. The written tensor products combine vector representations of G. For simplicity, the possibility of R carrying spin is neglected, however the factorization theorem later on is unaffected by this restriction and solely relies on gauge invariance of the EFT Lagrangian and identical velocities of $\bar{\chi}\chi$ and R. The complete Lagrangian used for this chapter is decomposed into the gauge-kinetic and potential (P)NREFT terms of χ and R, the trilinear interaction coupling to the resonance as well as local χ 4-point operators,

$$\mathcal{L}_{\text{res}} = \mathcal{L}_\chi + \mathcal{L}_R + \mathcal{L}_{\bar{\chi}\chi R} + \mathcal{L}_{(\bar{\chi}\chi)(\bar{\chi}\chi)}. \tag{3.3}$$

The direct annihilation of χ into light fields, such as the gauge bosons of G, is captured in the EFT by imaginary short-distance Wilson coefficients of 4-point operators, $\sim (\bar{\chi}\chi)^\dagger(\bar{\chi}\chi)$. They are not relevant for the decoupling theorem but become of significance in later phenomenological studies. Annihilation cross-sections are computed from the imaginary part of the forward scattering amplitude of the process $\bar{\chi}\chi \to R \to \bar{\chi}\chi$ by employing the optical theorem in the UV-complete theory, even though PNREFT now involved non-hermitian operators. To provide an annihilation channel, R must be unstable and boast a non-zero decay width $\Gamma_R > 0$ as a consequence of Dyson-resumming the decay depicted in Fig. 3.1 as part of the 1-loop irreducible bubble chain of the R two-point function. As a simplification, only inclusive processes (summing over all $F \neq \bar{\chi}\chi$) are regarded for now, which allows to remain agnostic about the final state. Branching fractions to specific F are introduced later on. While the leading terms of the χ Lagrangian are identical to PNREFT, R is described by unstable particle effective theory and has a kinetic Lagrangian

$$\mathcal{L}_R = R_w^\dagger \left(\mathrm{i}D^0 - \delta M_R + \frac{\mathrm{i}\Gamma_R}{2} \right) R_w. \tag{3.4}$$

The index w gives the velocity of R, $w^\mu = (1, \vec{0}) + \mathcal{O}(\mathrm{v})$ in the center-of-mass frame of the initial state. R appears exclusively in the single-particle s-channel process, therefore there is no need to describe also its potential interactions, which are non-local only in space but occur instantaneously. Since $M_a + M_b \approx M_R$ holds merely as an approximation, there is a small residual mass term,

$$\delta M_R \equiv M_R - M_s - M_b = M_R - 2M_\chi \ll M_R, \tag{3.5}$$

when measuring energy in the rest frame of the initial state. This choice leaves the kinetic Lagrangian of χ without a residual mass term $\delta M_\chi = 0$ in Eq. (2.9),

$$\mathcal{L}_\chi \equiv \mathcal{L}_{\mathrm{PNR}}[\chi_w]. \tag{3.6}$$

The essential interaction term for the s-channel resonance is written in terms of a Wilson coefficient C and a general Clebsch-Gordan tensor y_{abc} as

$$\mathcal{L}_{\bar{\chi}\chi R}(X) = J(X) + \text{“h.c.”} = \frac{C}{\sqrt{2M_R}} y_{abc} \left(\chi_w^{a\dagger} \chi_w^b R_w^c \right)(X) + \text{“h.c.”}, \tag{3.7}$$

with gauge indices on the field operators made explicit only here and the hermitian conjugate implied by “h.c.”. By explicitly extracting the mass factor, C is kept dimensionless. Lastly, there are the local 4-point annihilation vertices of χ to describe the pair annihilation by hard processes captured in

$$\mathcal{L}_{(\bar{\chi}\chi)(\bar{\chi}\chi)} = \sum_k \left(\chi^\dagger \chi \right)^\dagger f_k \left(\chi^\dagger \chi \right) \tag{3.8}$$

where any possible gauge or spin structures of $(\bar{\chi}\chi)$ may be contracted in the generic short-distances coefficients f_k, hence the unspecified summation. This well-known term will help emphasize the parametric s-channel resonance dominance and provide a second, direct annihilation channel later on which follows simply Born-level calculations in the UV-complete theory. Hence, further details may be disregarded in this general formalism.

The forward scattering matrix element of $\bar{\chi}\chi$ is

$$\mathrm{i}\mathcal{T} = \int \mathrm{d}^4X \, \langle \bar{\chi}\chi | \, T\{\mathrm{i}J^\dagger(X) \, \mathrm{i}J(0)\} \, | \bar{\chi}\chi \rangle + \delta^4(X) \, \langle \bar{\chi}\chi | \, \mathrm{i}\mathcal{L}_{(\bar{\chi}\chi)(\bar{\chi}\chi)}(0) \, | \bar{\chi}\chi \rangle \tag{3.9}$$

where one can clearly observe the s-channel resonance as a long-distance effect being evaluated at different space-time points with only one coordinate shifted to 0 by translational invariance, in contrast to the local annihilation vertex. By dimensional analysis one finds that the second local annihilation vertex is suppressed as $\mathcal{O}(\Gamma_R/M_R, \delta M_R/M_R)$ relative to the s-channel term, provided there is no further scale hierarchy between the coupling constants in $\mathcal{L}_{(\bar{\chi}\chi)(\bar{\chi}\chi)}$ and $\mathcal{L}_{\bar{\chi}\chi R}$. As the dominant process is now a long-distance effect which, unlike short distance processes, are resolved by soft modes, the question arises whether there are additional contributions from soft gauge boson interactions which do not decouple at leading order.

3.2 Soft gauge boson decoupling theorem

The decoupling of soft gauge boson modes at leading order NREFT and leading order in Γ_R/M_R from the resonant annihilation processes is derived formally in the following. This proves that the long-range Sommerfeld effect remains fully factorized from the long-lived s-channel resonance meaning there can be no soft gauge boson exchanges between the DM initial and SM final state decay products of the resonance nor the resonance itself, for that matter. To this end, it is most convenient to make all soft interactions explicit on the Lagrangian level by use of soft Wilson lines

$$W_w(x) = \mathcal{P}\left\{ \mathrm{e}^{\mathrm{i}g \int_{-\infty}^{0} \mathrm{d}t\, w_\mu A_s^\mu(x+tw)} \right\}, \tag{3.10}$$

g being a respective gauge coupling of $A = A^a \hat{T}^a$. The soft gauge boson field is explicitly labelled as A_s. Due to $W_w(x)$ being a linear matrix multiplication and phase rotation, the field redefinition is straightforward,

$$R_w(x) \,\to\, W_w(x_w) R_w(x)\,, \quad \chi_w \,\to\, W_w(x_w)\chi_w(x), \tag{3.11}$$

involving $x_w = (w_\mu x^\mu)w$ which follows from multipole expanding the Wilson line to leading order to maintain a consistent power counting everywhere. Wilson lines obey the key property that they eliminate the soft gauge field dependence when acted upon by a longitudinal soft-gauge covariant derivative term,

$$w_\mu D_s^\mu\, W_w(x) = W_w(x)\, w_\mu \partial^\mu. \tag{3.12}$$

The redefinition renders the fields manifestly gauge invariant, so they act as a singlet in the covariant derivative, *i.e.* $D = \partial$ acting on them. In turn, all complications due to soft interactions are placed as explicit Wilson lines into the interaction operators. The kinetic terms are known to be invariant under the soft decoupling transformation. It is now possible to find simplifications of soft interactions on the Lagrangian level, which would otherwise occur only as cancellations between explicitly computed Feynman diagrams.

The essential aspect to proving the decoupling is quite simple and follows from gauge invariance of the Lagrangian. Therefor, it is important to note that all distinct Lagrangian pieces in Eq. (3.3) are separately gauge invariant, specifically also $J(X)$ and its hermitian conjugate. Under the above field redefinitions, the trilinear interaction becomes

$$J(X) \to \frac{C}{\sqrt{2M_R}} \left[W_w^{\tilde{a}a}(X_w)^\dagger\, W_w^{\tilde{b}b}(X_w)\, W_w^{\tilde{c}c}(X_w)\; y_{\tilde{a}\tilde{b}\tilde{c}} \right] \left(\chi_w^{\dagger,a} \chi_w^b R_w^c \right)(X). \tag{3.13}$$

The Wilson lines are actually identical to a gauge transformation with the phases

$$\varphi^a = \mathrm{i}g \int_{-\infty}^{0} \mathrm{d}t\, w^\mu A_\mu^a(x+tw) \tag{3.14}$$

giving a gauge transformation under some representation $\mathbf{R}$ as

$$U_{[\mathbf{R}]} \equiv \mathrm{e}^{\mathrm{i}\varphi^a T^a_{[\mathbf{R}]}} = W_w(x). \tag{3.15}$$

The generators of a specified representation $T_{[\mathbf{R}]}$ are implicitly included as operators $\hat{T}$ in the definition (3.10). Now, gauge invariance demands $\mathcal{L}_{\bar{\chi}\chi R}$ to be a singlet and unaffected by any gauge rotation, hence simply by rewriting (3.13) shows its invariance,

$$\begin{aligned} J(X) &\to \frac{C}{\sqrt{2M_R}} \left[U^{\tilde{a}a}_{[\mathbf{R}_\chi]}\, U^{\tilde{b}b}_{[\mathbf{R}_\chi]}\, U^{\tilde{c}c}_{[\mathbf{R}_R]}\; y_{\tilde{a}\tilde{b}\tilde{c}} \right] \left(\chi_w^{\dagger,a} \chi_w^b R_w^c \right)(X) \\ &= J(X). \end{aligned} \tag{3.16}$$

Having performed the decoupling field redefinition by use of soft Wilson lines, gauge invariance of the Lagrangian term under concern implies that an operator involving exclusively fields with identical velocities does not yield any soft gauge boson interactions to leading order.

At higher orders, the path ordering in W_w gives essential differences between the Wilson line and a gauge rotation. Only a single production operator $J(x) \propto \chi^\dagger \chi$ was implicitly assumed, whereas in general many operators $J_m(x)$ could exist, giving rise to a summation $\sum_{m,n} J_m^\dagger J_n^\dagger$ in (3.9). As long as gauge invariance is ensured for each term separately, the proof remains unchanged since it applies already on Lagrangian level.

3.3 Factorization in presence of an s-channel resonance

The proven decoupling of soft modes to leading order allows to insert a complete set of states between the different contributions to $\mathrm{i}\mathcal{T}$ and confidently approximate it at leading order simply by the vacuum state $|\Omega\rangle\langle\Omega|$, resulting in

$$\mathrm{i}\mathcal{T} = \int \mathrm{d}^4X \; \langle \bar{\chi}\chi |\, T\{ \mathrm{i}J^\dagger(X)\, \mathrm{i}J(0) \}\, | \bar{\chi}\chi \rangle \tag{3.17}$$

$$\begin{aligned} &= \frac{-|C|^2}{2M_R} \int \mathrm{d}^4X\, \mathrm{e}^{\mathrm{i}Et}\, \langle \bar{\chi}\chi |\, \left[\chi_w^{\dagger a} \chi_w^b \right](0)\, |\Omega\rangle \times \langle \Omega |\, \left[\chi_w^{\dagger a'} \chi_w^{b'} \right]^\dagger(0)\, | \bar{\chi}\chi \rangle \\ &\qquad \times \langle \Omega |\, \left[y_{a'b'c'} R_w^{c'}(X) \right]^\dagger \left[y_{abc} R_w^c(0) \right] |\Omega\rangle \end{aligned} \tag{3.18}$$

$$= \frac{-|C|^2}{2M_R} \Psi^{ab}_{\bar{\chi}\chi,E}(0) \left[\Psi^{a'b'}_{\bar{\chi}\chi,E}(0) \right]^* \frac{\mathrm{i}\delta^{cc'} y^*_{a'b'c'} y_{abc}}{E - \delta M_R + \frac{\mathrm{i}}{2}\Gamma_R} \tag{3.19}$$

where, alike the usual Sommerfeld treatment [77], translation invariance was used to shift both $\bar{\chi}\chi$ wave functions to the origin, which yields the same Sommerfeld factor as for short distance annihilation. The optical theorem now gives the cross section to leading order as

$$\sigma \mathrm{v} = \mathrm{Im}\{\mathcal{T}\} = \frac{|C|^2\, Y \cdot S(\mathrm{v})}{2M_R} \times \frac{\mathrm{Im}\left\{ \frac{\mathrm{i}}{2}\Gamma_R \right\}}{\left(E - \delta M_R\right)^2 + \frac{1}{4}\Gamma_R^2} \tag{3.20}$$

$$\equiv \frac{|C|^2 Y}{4M_\chi^2}\, S(\mathrm{v})\, R(\mathrm{v}) \tag{3.21}$$

introducing

$$R(\mathrm{v}) = \frac{\frac{1}{2} M_\chi \hat{\Gamma}_R}{(\frac{1}{4}M_\chi \mathrm{v}^2 - \delta M_R)^2 + \frac{1}{4}\Gamma_R^2}. \tag{3.22}$$

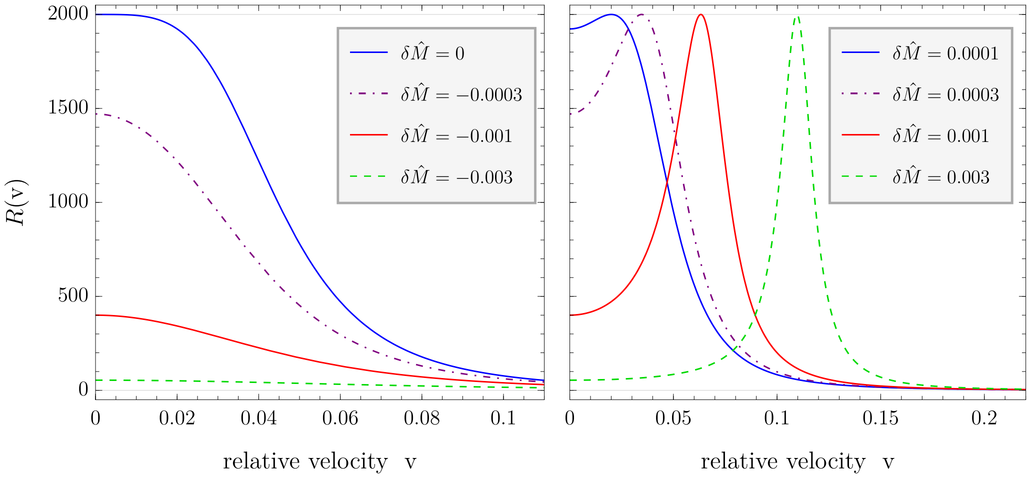

Figure 3.2: Resonance enhancement factors $R(\mathrm{v})$, Eq. (3.22), for $\delta M_R < 0$ (*left*) and $\delta M_R > 0$ (*right*) plotted over relative velocity v for exemplary parameters in units of M_χ, $\Gamma_R = 0.001 M_\chi$ and $\delta\hat{M} \equiv \delta M_R / M_\chi$.

$Y \cdot S(\mathrm{v})$ is a schematic notation for the respective irreducible gauge representation channel Sommerfeld enhancement factor. It is included as part of the fraction in (3.21) which is defined to make contact to the gauge factors in usual Born approximated calculations. The numerator of $R(\mathrm{v})$ involves $\hat{\Gamma}_R$ which refers to a *partial* width of R into some specific final states. In order to describe inelastic processes to which the optical theorem is applicable, $\hat{\Gamma}_R$ must exclude the decay channel back into $\bar{\chi}\chi$, which is open if $\delta M_R > 0$.

It should be noted that one does not actually cut the R propagator but, essentially, only one single bubble insertion of lighter states in the Dyson-resummed propagator of R. Correspondingly, when regarding exclusive final states only the numerator of $R(\mathrm{v})$ picks up the appropriate branching fraction $\hat{\Gamma}_R/\Gamma_R$. The remainder of the infinite bubble chain remains intact and still results in the total decay width in the denominator, as naively expected. A simpler way of reading Eq. (3.22), to simply state that the cross section is proportional to Γ_R and thus may be rescaled by simple multiplication of a branching fraction, assumes that (3.20) remains valid even in elastic forward scattering scenarios. This is, however, not guaranteed by the optical theorem.

$R(\mathrm{v})$ deserves a brief analysis to understand its expected physical implications. The function itself is the well-known Breit-Wigner peak shape [88] commonly found for unstable particle production. There are two qualitatively different regimes set by $\delta M_R < 0$ and $\delta M_R > 0$ shown separately in the left and right panel of Fig. 3.2 for different values. For positive δM_R, some non-zero initial kinetic energy is required to produce R exactly on its mass shell, $E - \delta M_R = 0$, and the resonance enhancement reaches its maximum at this finite velocity, $\mathrm{v}_{\max} = 2\sqrt{\delta M_R / M_\chi}$. For negative mass splittings, this obviously does not yield a solution for real velocities and the strongest possible enhancement is instead always found at rest $\mathrm{v} = 0$. In this low-velocity limit, both cases agree. The maximum enhancement for negative mass splittings is set by $\frac{1}{2} M_\chi \Gamma_R / (\delta M_R^2 + \Gamma_R^2/4)$ and approaches the peak value $R_{\text{max}} = R(\text{v}_{\text{max}}) = 2M_\chi/\Gamma_R$ for $\delta M_R = 0$. Physically, this corresponds to the fact that even at zero velocity, a lighter single particle state can only be produced with some virtuality and never exactly on-shell. For $R = R_{\text{max}}$, the cross section must saturate the s-wave unitary bound [89] up to a possible suppression by spin-statistical multiplicity factors. For example, in case of fermionic χ only the spin-singlet combination can couple to a scalar R, and the initial state spin average introduces a factor 1/4. The saturation is expected, since a leading order calculation treating the decay of R perturbatively diverges for on-shell production and upon regularization by Dyson resummation any other non-divergent process is hence suppressed by "$1/\infty = 0$".

From the above statement, unitarity becomes apparently worrisome when incorporating Sommerfeld and resonance enhancement simultaneously in the factorized form of Eq. (3.21). Introducing the Resonance and Sommerfeld factors separately leads to inconsistencies whenever $S(\text{v}_{\text{max}}) > 1$ and $\delta M_R > 0$. This is caused by neglecting a dominant scattering contribution in the non-perturbative 4-point function of χ which involves only potential ladder exchanges but disregards R. A proper, simultaneous treatment of both effects requires to include the s-channel in the non-perturbative Lagrangian which fully resums it in the two-particle propagator by a Dyson type resummation of the s-channel process. This means the s-channel resonance scattering, which itself already includes the 1-loop self-energy bubble-chain giving rise to Γ_R, is to be included in the equations of motion of χ. Similarly, unitarity violation in Sommerfeld resonances is known to be cured by inclusion of the local annihilation operators in the Schrödinger equation [90]. However, in the present case of resonance scattering, the effective 4-point interaction becomes non-local in time and equations of motion can no longer be molded into the a Schrödinger equation, and a solution for the wave function becomes more complicated to obtain. A closer investigation of such a resummation of s-channel scatterings is beyond the scope of this thesis.

3.4 Resonance & Sommerfeld enhanced annihilation

The novelty here compared to already established resonant DM annihilation mechanisms [20, 24, 33] is the simultaneous treatment of a strongly Sommerfeld enhanced initial state whilst having confidence in the stability of the result under soft interactions. This section discusses an exemplary toy model to illustrate the possible effects for DM phenomenology.

3.4.1 Expected phenomenology

To illuminate the chosen exemplary benchmark model a brief discussion of expected effects is in order.

Mainly two properties of dark matter are of interest to this thesis, the annihilation cross-section in the early universe setting the particle abundance via the freeze-out process at velocities around $\text{v} \sim 0.1$ and the late-time annihilation cross-section in gravitationally bound dark matter halos, where $\text{v} \sim 10^{-3}$, which is subject to constraints from indirect detection experiments. The importance of DM self-scattering for structure formation is disregarded here, although resonant s-channel enhancement could constitute a sizable effect. The two respectively relevant velocities differ by multiple orders of magnitude demanding a choice to be made in model building for where the predominant resonance enhancement is to be found and $\delta M_R > 0$ is to be chosen accordingly. For δM_R negative or so small as to affect only late time annihilation, the space of viable dark matter models remains virtually unchanged, yet in some resonantly tuned models, indirect detection constraints are now enhanced.

Since the Sommerfeld enhancement near a resonance grows monotonically towards small velocity similar to the case of $\delta M_R < 0$, the case of resonance enhancement during freeze-out is conceptually more interesting and opens new mass ranges for viable DM candidates. In case of χ being a WIMP, the Sommerfeld coupling strength α^{eff} is fixed by SM parameters $\alpha_{1,2}$ and the sole remaining question is whether a given model choice of hypercharge, isospin, M_χ, Γ_R and δM_R and violates existing experimental bounds. Furthermore, the Sommerfeld enhancement in WIMP models is dictated by Yukawa potentials which themselves yield resonant enhancements at specific, discrete points of M_χ corresponding to the presence of a near-threshold bound state in the spectrum. One may attempt to determine M_χ to be near such a resonance, resulting in strongly enhanced late time annihilation cross-sections, and tune δM_R to still obtain the correct relic density. Γ_R may be used to further hone the tuning, however it is constrained from two aspects. Firstly, in order to see an appreciably resonant enhancement, $\Gamma_R \lesssim \delta M_R$ should remain fulfilled. Secondly, the abundance is set by the thermally averaged cross section in which the smeared area of the resonance peak enters. This becomes largely independent of $\Gamma_R \approx 0$ as the peak approaches a delta distribution. Furthermore, for $\delta M_R > 0$, the coupling parameter to the s-channel, C, also sets a lower bound on the resonance width $\Gamma_R \geq \Gamma_{R\to\bar{\chi}\chi} \sim |C|^2$.

To give a meaning to the toy model aside from a qualitative study of doubly enhanced phenomenology effects, the parameters for the toy model are inspired by valid MSSM scenarios in hopes of coarsely predicting viable regions in parameter space once the impact of s-channel resonances are taken into account.

3.4.2 MSSM inspired toy model

The Lagrangian for the chosen toy model schematically corresponds to the one given at the start of this chapter in (3.3), although now treating an explicitly fermionic χ charged under a dark Abelian gauge symmetry $U(1)_D$ mediated by a massive gauge boson X of field strength $X^{\mu\nu}$. The full-theory Lagrangian in terms of relativistic fields is

$$\begin{aligned}\mathcal{L} =& \overline{\chi}\left(\mathrm{i}\not{D} - M_\chi\right)\chi - \frac{1}{4}X^{\mu\nu}X_{\mu\nu} + yA\overline{\chi}\chi \\ &+ \frac{1}{2}\left(\partial A\right)^2 - \frac{1}{2}M_A^2 A^2 + \mathcal{L}_{\mathrm{SM}+int},\end{aligned} \tag{3.23}$$

where A is a real scalar field taking the role of the s-channel resonance R. The naming is chosen to be suggestive to the Higgs pseudoscalar appearing in the MSSM after electroweak symmetry breaking. The analogy here, with no claim to predictiveness, is to understand χ as simultaneously filling the role of the neutralino DM candidate and the degenerate chargino state which experiences strong

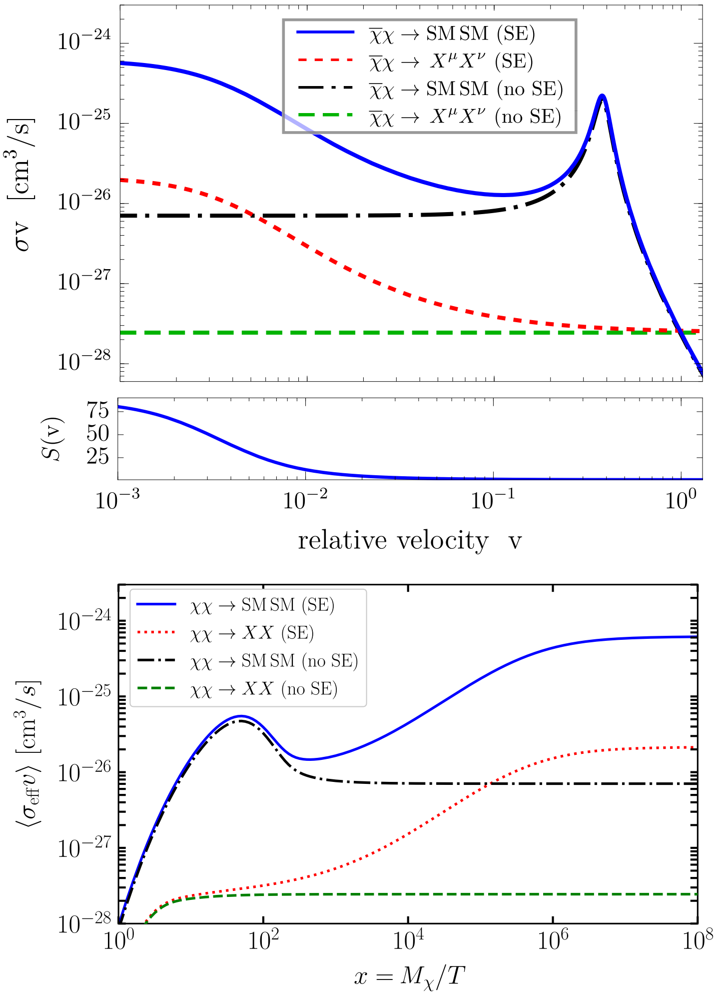

Figure 3.3: *Upper panel*: DM annihilation cross-section plotted over velocity with subtended panel for Sommerfeld enhancement S(v) sharing the same axis. Cross sections for SM finals states (black dot-dashed, blue) and dark gauge bosons $X\,X$ (green dashed, red dotted) are shown each when neglecting or including of Sommerfeld enhancement. *Lower panel*: The same annihilation cross-sections thermally averaged and plotted over inverse temperature.

Sommerfeld enhancement. A rigorous treatment of Sommerfeld enhancement in the MSSM for neutralino DM is discussed in further detail in chapter 4. From a model building perspective, the gauge boson mass m_X is simply introduced to avoid constraints from warm dark matter as it allows to introduce a small kinetic mixing to the Standard Model photon. It is neglected in Eq. (3.23), assuming it to arise from some spontaneous symmetry breaking of $U(1)_D$, instead emphasizing the gauge invariance of the Lagrangian, which is central to the soft decoupling theorem. The scalar A decays into standard model fields where the corresponding interaction and all standard model terms are hidden in $\mathcal{L}_{\mathrm{SM}+int}$. The resonance condition (3.1) implies $|\delta M_A| \ll M_\chi$. As Γ_A is the parameter to be defined by the desired phenomenology, its detailed origin is irrelevant here. Instead the relevant quantities are the s-channel annihilation cross-section at Born level,

$$(\sigma v)^{\text{Born}}_{\bar{\chi}\chi\to A\to \text{SM}\,\text{SM}} = \frac{y^2}{2M_\chi}\frac{\frac{1}{2}\Gamma_{A\to\text{SM}}}{(\frac{1}{4}M_\chi v^2 - \delta M_A)^2 + \frac{1}{4}\Gamma_A^2}, \tag{3.24}$$

and the direct annihilation cross-section of χ,

$$(\sigma v)^{\text{Born}}_{\bar{\chi}\chi\to X\,X} = \frac{\pi\alpha_X^2}{M_\chi^2}. \tag{3.25}$$

The choice of Γ_A must only respect the mentioned lower bound from the decay into $\overline{\chi}\chi$,

$$\Gamma_{A\to\bar{\chi}\chi} = \frac{y^2 M_\chi^2}{2\pi M_A}\sqrt{1-\frac{4M_\chi^2}{M_A^2}}\,\theta(M_A - 2M_\chi). \tag{3.26}$$

Obeying (3.1), this rate is negligible as it is highly phase space suppressed by

$$\sqrt{1-\frac{4M_\chi^2}{M_A^2}} \sim \left|\frac{M_A^2}{(M_\chi+M_\chi)^2 - M_A^2}\right|^{-1/2} \ll 1. \tag{3.27}$$

With all these conditions in place, a MSSM-inspired benchmark model was constructed on basis of the electroweak interactions of typical Higgsino models,

$$\begin{aligned}
\alpha_X &= \frac{1}{2}\alpha_2(m_Z) = 0.0168,\\
y &= \sqrt{2\pi\alpha_2(m_Z)}\times 0.152 = 0.0987,\\
m_X &= m_W = 80.385\,\text{GeV},\\
\Gamma_{A\to\text{SM}} &= \frac{M_A}{150} = 88.2\,\text{GeV}
\end{aligned}$$

and

$$M_\chi = 6.5\,\text{TeV},\quad M_A = 13.23\,\text{TeV},\quad \text{thus}\ \ \delta M_A = 230\,\text{GeV}.$$

The small numerical factor in y models the fact that pure Higgsino states in the MSSM do not couple by themselves to A but require some admixture of the bino (or wino). Keeping in mind a Higgsino-dominated model, such a bino admixture is thus approximated as just a numerical suppression due to small mass mixing contributions entering linearly in y. Hence, the factor 0.152 implies a 2% bino admixture. The mass splitting $\delta M_A > \Gamma_{A\to\text{SM}}$ gives rise to a distinct peak feature in the annihilation cross-section, which can be seen in the upper panel of Fig. 3.3. Blue and black (dot-dashed) curves show the s-channel resonance annihilation cross-section into SM, respectively with and without including the Sommerfeld effect. The red (dotted) and green (dashed) curves show analogously the annihilation cross-section into dark gauge boson $X^\mu X^\nu$. The center panel, sharing the same horizontal axis, shows only the Sommerfeld factor $S(\text{v})$ computed using a code developed in scope of [87]. $S(\text{v})$ remains small near $\text{v} = \text{v}_{\max}$ but becomes strongly enhanced by about two orders of magnitude in the low-velocity limit. Sommerfeld enhancement sets in once $\text{v} \lesssim \alpha_X$ and saturates towards a constant plateau below $\text{v} < 10^{-3}$ due to the non-negligible potential mediator mass setting a finite range to the potential. The bottom panel shows the thermally averaged cross sections plotted over $x = M_\chi/T$. The mass splitting is chosen such that the resonance is located just in the crucial velocity range where departure from chemical equilibrium takes place during thermal production, $x \sim 25$, prolonging the phase of efficient annihilation. The chosen value of $M_\chi = 6.5\,\text{TeV}$ exactly saturates the relic density constraint, $\Omega_{\text{DM}}h^2 = 0.120$, and thus predicts a possible region of MSSM parameter space of Higgsino dominated models in the multi-TeV range for resonant Higgs sectors.

Obviously, the constructed toy model is rather crude and many additional aspects must be considered when translating this prediction to actual MSSM models, predominantly the increased complexity from coannihilation in true Higgsino models and the presence of several additional Higgs bosons in the MSSM scalar spectrum which are expected nearby M_A. The strong Sommerfeld enhancement at late times boosts particle flux predictions, rendering this parameter range possibly detectable in cosmic-ray indirect detection experiments. Overall, this Higgsino inspired model yields a stark contrast in its phenomenology compared to the thermal pure Higgsino. The latter is located at a mass of $M_\chi = 1.1\,\text{TeV}$ with Sommerfeld enhancement being almost negligible at the percent-level and evades even optimistic projections of the future Cherenkov Telescope Array experiment [49], see also Fig. 5.4 below.

As a concluding remark, note that it is possible to construct truly doubly resonantly enhanced models where $S(\text{v})$ and $R(\text{v})$ are simultaneously large. For instance, a wino-inspired model similar to the above at $M_\chi = 3.85\,\text{TeV}$ and tiny negative $\delta M_A = -5\,\text{GeV}$ sees almost two orders of magnitude s-channel resonance enhancement and another 3 orders of magnitude of Sommerfeld enhancement. However, realistic implementations of such parameter ranges are almost certainly excluded by existing null results from experiments and, moreover, raise concerns about the validity of disregarding the s-channel resonant self-scattering in the DM potential. In a different setup of resonant Higgs-portal DM ($M_\chi \approx 62.5\,\text{GeV}$), constructing a similarly doubly enhanced model was found to be impossible due to a combination of stringent experimental bounds and theoretical constraints. With the s-channel resonance mass value fixed to the Higgs boson mass and upper and lower bounds to its decay width, the model loses too much freedom which is not to be compensated by the increased freedom of choosing $\alpha_X \leq \text{v}$ or m_X.

The simple toy models studied in this chapter introduced Sommerfeld enhancement, its origin in PNREFT calculations and its rough general velocity dependence without going into any further detail. The following chapter delves deeper into Sommerfeld enhancement in the MSSM before its eventual application in mixed neutralino indirect detection spectrum calculations including Sudakov resummation, which is presented in chapter 5. In both chapters, s-channel resonant regions are carefully avoided due to technical limitations of available tools, albeit with the results presented here, the theoretical path to treating Sommerfeld enhanced resonant annihilation has been cleared.

4 Sommerfeld-effect for neutralino Dark Matter

For this chapter, Sommerfeld enhanced neutralino DM annihilation in the Minimal supersymmetric Standard Model is reiterated upon [77, 91]. Novel ingredients to the discussion are a more thorough investigation of the Higgs sector and electroweak symmetry breaking, also in preparation of the subsequent chapter 5, and the inclusion of complete one-loop and electroweak two-loop running couplings as well as state-of-the-art accurate SM inputs to the computation.

The Sommerfeld effect (SE), interchangeably referred to as Sommerfeld enhancement in the attractive case, dates back more than one hundred years [92] when it was derived for electrons in atomic systems in humble quantum mechanics. Its significance for applications in dark matter was brought to the attention of the community more recently [76, 93] and has been widely studied since. It has strong implications for thermal freeze-out and indirect detection searches as in both cases the participating particles are non-relativistic. The physical picture is that long range forces, encoded in non-local potentials in the EFT, give rise to a qualitative modification of the behavior of particles at low relative velocity v. More technically, the relativistic calculation of light, *i.e.* approximately massless, t-channel exchanges diverges at low momentum exchange which breaks the perturbative expansion in α. Sommerfeld enhancement thus becomes a relevant non-perturbative effect once velocities are at most of the order of the t-channel coupling strength,

$$\boxed{\frac{1}{\mathrm{v}} \sim \frac{1}{\alpha} \gg 1.} \tag{4.1}$$

Following [77], the traditional wave function formalism is adopted here, as introduced in Eq. (2.11). The Sommerfeld factor S will be defined more concretely in section 4.2. The infinite ladder exchanges resummed by solving the two-particle Schrödinger equation are indicated in Fig. 4.1 by three dots. Instantaneous potential modes are drawn as dashed lines, hence all loop momenta are of the potential scale, while non-relativistic particles are represented as solid lines. A single insertion of the short-distance annihilation vertex $\hat{f}$ is shown in blue, explicitly denoting the field labels e_{1-4} which make up the two-particle external states to the annihilation operator. No internal particle species of the ladder is denoted since, naturally, all possibilities need to be respected in the resummation. This includes also up-scattering from the neutral DM to almost degenerate states and even kinematically closed virtual states. Although the total electric charge is conserved in ladder exchanges, individual internal two-particle states may consist of chargino anti-chargino pairs. Corresponding charge arrows are neglected in the diagram. To describe forward scattering and thus allow for an application of the optical theorem to obtain the total annihilation cross-section, the initial and final states $(\chi_i\chi_j)$ are the same (ignoring here possible permutations). As an aside to this more exhaustive definition of SE one should note that SE commonly refers only to effects on scattering states and no analogous term is coined for bound states which do not permit for a free-theory counterpart description.

Some novel results of this chapter were published in [2], mainly regarding the Higgs decoupling in sections 4.3 and 4.4. Some minor repetition of contents of

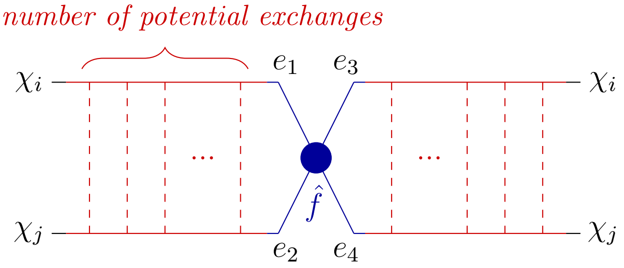

Figure 4.1: Exemplary forward scattering diagram with repeated, possibly charged, ladder exchanges of potential modes (red dashed lines) between non-relativistic fields (solid). $\hat{f}$ denotes the short distance operator (blue) and i, j and e_i are generic field labels for neutralinos or charginos as occurring in Eq. (4.4). Charge and fermion flows are suppressed.

[62] is, for the sake of completeness, unavoidable in this and the following chapter. Further improvements and modifications of the numerical code base from [77] have been developed in collaboration with M. Beneke, A. Bharucha, P. Ruiz Femenía, A. Hryczuk and S. Recksiegel with a publication planned in combination with a feature-complete code release in the near future [5].

4.1 Overview of neutralino dark matter

Supersymmetry [36] originally gained much attention for providing a solution to the hierarchy problem of the SM [17, 94, 95] and has been widely studied since. The hierarchy problem is resolved in SUSY once all super-multiplet components are dynamical, protecting SM scalar masses from quadratic ultraviolet divergences by cancellation between fermionic and bosonic field contributions in each complete superfield. However, SUSY must therefor introduce (at least) one superpartner to each degree of freedom in the SM, different only in its spin representation, and thus predicts a plethora of new particles, even in its minimal realization. Many superpartners are charged under electromagnetic and/or strong interactions providing attractive targets for collider searches, however none have yet been observed in experiments. Tensions with experimental null-results drive the need for ever larger scale separations between the known SM and hypothesized supersymmetric scales eventually threatening the possibility to solve the hierarchy problem as the SUSY scale itself is large already. Current collider searches begin to reach into the low TeV region [96] which is also of phenomenological interest for the purposes of neutralino DM.

The minimal supersymmetric extension of the Standard Model includes several WIMPs where the lightest one is stabilized by R-parity and can therefore take the role of DM. For this work, the lightest supersymmetric particle (LSP) is taken to be a neutralino, where any admixture of Higgsinos or gauginos is permitted, while other SUSY partners are assumed to be sufficiently heavier to not affect freeze-out computations. As departure from equilibrium occurs around temperatures $T \sim 25 M_{\text{LSP}}$, thermal upscattering to heavier states at times most crucial to thermal production becomes inefficient as long as the mass splitting is larger than $\sim 10\%$, *i.e.* $\mathcal{O}(10\text{-}100\,\mathrm{GeV})$ for TeV DM masses. In a maximally reduced form, pure Higgsino or wino WIMP DM models become attractive due to their minimality and theoretical simplicity and many results have been found for general electroweak multiplets [32, 35, 82, 87, 97–104]. The mass range of thermally produced DM was found to be broadly around 1 - 15 TeV, disregarding also sterile bino-dominated models, with 1.1 and 2.8 TeV for the thermal pure Higgsino and pure wino.

The relevant Lagrangian terms to describing the dynamics of non-relativistic electroweakinos are only the gauge-kinetic terms and Higgs-interactions,

$$\begin{aligned}\mathcal{L}_{\mathrm{MSSM}} = \mathcal{L}_{\mathrm{SM}} + \frac{1}{2}\begin{pmatrix}\tilde{B}\\ \tilde{W}\\ \sqrt{2}\tilde{H}\end{pmatrix}^{\dagger}\gamma_0\left(\mathrm{i}\not{\partial} - \mathrm{diag}\left\{M_1,\, M_2,\, M_{\tilde{H}}\right\}\right)\begin{pmatrix}\tilde{B}\\ \tilde{W}\\ \sqrt{2}\tilde{H}_1\end{pmatrix}\\ + \sqrt{2}\tilde{H}^{\dagger}\gamma_0 P_L\left(g_2\tilde{W}^aT^a + g_1\tilde{B}\right)\mathrm{i}\sigma^2 H_2^*\\ + \sqrt{2}\tilde{H}^{\dagger}\gamma_0 P_R\left(g_2\tilde{W}^aT^a + g_1\tilde{B}\right)\mathrm{sign}(\mu)H_1 + \text{“}h.c.\text{”}.\end{aligned} \tag{4.2}$$

$\tilde{B}$ is the singlet bino, $\tilde{W}$ the wino isospin triplet and $\tilde{H}$ the Higgsino doublet with hypercharge $Y_{\tilde{H}} = -1/2$. Being charged, $\tilde{H}$ is a Dirac fermion encompassing the Weyl-fermion super partners of both Higgs bosons $H_{1,2}$, whereas $\tilde{W}$ and $\tilde{B}$ are Majorana fermions. The kinetic terms of the Higgs bosons are insignificant beyond the fact that they give rise to the mass mixing angle α_H as discussed in section 4.3. The strictly positive mass term $M_{\tilde{H}} \equiv |\mu|$ is obtained after absorbing $\mathrm{sign}(\mu)$ into the upper component of $\tilde{H}$, *c.f.* Eq. (4.7), which puts it into the Yukawa terms instead. It would be possible to analogously redefining the sign of the corresponding boson H_1, *cf.* [62], in which case the freedom to choose $\mu < 0$ in the MSSM Lagrangian affects in the Higgs potentials, not stated here. However, this complicates applications of known results from the literature without much benefits. Gauge indices are suppressed aside from the wino in the Yukawa couplings. For more details on the interactions and mass mixing in the electroweakino sector, see [105, 106].

The mass eigenstates in the electroweak broken phase are a set of four neutralinos, Majorana fermions $\chi^0_{1,2,3,4}$, and two electromagnetically charged charginos, Dirac fermions $\chi^+_{1,2}$. For the theory to provide the desired DM candidate, the LSP must be a neutralino. It is conventional to order the neutralinos and charginos according to their mass, thus

$$M_\chi \;=\; M_{\mathrm{LSP}} = M_{\chi^0_1} \equiv \min\{M_{\chi^0_i}\}. \tag{4.3}$$

Note that bosonic Higgs fields are not considered superpartners such that there may even be BSM particles lighter than the LSP. Since the Higgs vacuum expectation value (VEV) is a soft scale quantity, $v \sim m_Z$, the hard scale remains unaffected by mass shifts under electroweak symmetry breaking, $M_{\mathrm{LSP}} \sim \min\{M_{\tilde{H},1,2}\}$. Superpartners of SM fermions (sfermions) may mediate annihilation processes but are disregarded in calculations of the PNREFT potentials. Hence, sfermion coannihilation models of near-degenerate sfermions to the DM cannot be treated here and their mass must here be chosen at least 25% heavier than M_{LSP} [107]. Conversely, neutralino-sfermion coannihilation models neglecting electroweak SE have also been considered in the literature [108, 109] and are accessible in a publicly available tool [110].

As long as the lightest electroweakino is sufficiently split in mass from the other two, thermal production dynamics are well approximated by a minimal WIMP model. However, to parametrically rule out the possibility of up-scattering by potential interactions demands mass splittings to be beyond the soft and therefore of the hard scale. Furthermore, a decoupled description as a minimal WIMP would also become inaccurate in models where s-channel scattering through Higgs particles is resonant, *cf.* chapter 3. Resonant models are avoided in the following.

4.2 Sommerfeld enhancement in non-minimal models

The rich particle content with a large number of independent parameters in the MSSM, even under the above limitations, causes several subtleties in when computing Sommerfeld enhancement. An appropriate framework to obtain numerical solutions has been developed in [64, 77, 111]. This section repeats the central concepts and required definitions for later use without delving into too much detail of what is already known in the literature for over a decade at the time of writing.

4.2.1 Factorization

For almost degenerate electroweakinos, *i.e.* $M_{\tilde{H},1,2}$ close enough to impact the obtained relic density or annihilation spectra, the phenomenology of the model becomes much richer and calculations correspondingly more complex than a minimal WIMP model. Specifically, for mass splittings of the order or below the potential momentum scale the potential exchanges between two electroweakinos can scatter between the degenerate fields. This means there are simultaneously two complications present compared to the simple picture drawn in Eq. (2.11), due to off-diagonal mass matrices and off-diagonal potential interactions. Once electroweak symmetry is broken the Yukawa interactions of $\mathcal{L}_{\mathrm{MSSM}}$ give rise to the new mass eigenstates $\chi^{\pm}_{1,2}$ and $\chi^0_{1,2,3,4}$ and the couplings to Higgs bosons involve mass mixing matrices. Secondly, even when setting up a mixed initial two-particle scattering state, it can scatter into other two-particle states of the same total electromagnetic charge but not necessarily of identical constituent charges meaning $\chi^0_{e_1}\chi^0_{e_2}$ may scatter into $\chi^+_{e_3}\chi^-_{e_4}$ by exchange of a charged boson.

Analogous to Eq. (2.11), the leading order SE $S(\hat{f})$ is defined as the ratio between the resummed and tree-level approximated result, however now for each specific short-distance annihilation process individually [77]. The hard 4-fermion Wilson coefficients $\hat{f}$ take the form of a matrix in the space of two-particle states as seen in Fig. 4.1. The Sommerfeld factor becomes a rank-3 tensor, accounting now for the possibility of scattering the initial state into any other state. For annihilation of a specific initial state $\chi_i\chi_j$, it reads

$$S^{ij\to ij}(\hat{f}) \equiv \sum_{\{e_k\}} \frac{[\psi_{e_4e_3,ij}(0)]^* \, \hat{f}_{(e_1e_2)(e_4e_3)} \, \psi_{e_1e_2,ij}(0)}{\hat{f}_{(ij)(ij)}} \tag{4.4}$$

where all indices e_k, $k = 1, 2, 3, 4$, are summed over chargino and neutralino labels. The total annihilation cross-section is

$$(\sigma \mathrm{v})^{ij \to \mathrm{light}} = S^{ij \to ij}(\hat{f})\ \hat{f}_{(ij),(ij)}. \tag{4.5}$$

As this thesis attempts to balance many different notations as best as possible, the definition here differs slightly from its [77] where the SE is introduced carrying subscript initials state indices (S_{ij}). Considering angular momentum L and spin S, which remain conserved in non-relativistic scattering processes to leading order, the two-particle states can be decomposed accordingly and the corresponding wave functions carry the quantum numbers $\psi^{(L,S)}_{ij,e_1e_2}$. Since $\hat{f}$ was kept general, Eq. (4.4) adapts correspondingly and $\hat{f}$ becomes the annihilation matrix of a specific partial wave barring potential interactions [64].

For the present chapter, single particle labels (i, j, e_k) are used while the later chapter 5 investigates neutralino annihilation at late times where only DM initial states are present ($i = j = \chi^0_1 = \chi$) and uses more compact two-particle labels I, J. This distinction serves to emphasize the different physical surroundings between freeze-out and annihilation processes as well as to stay close to the respective literature. The s-wave annihilation matrix relevant to chapter 5 is identified as $\hat{f}(^1S_0) = \Gamma^{\mathrm{Tree}}$ and the respective s-wave DM-DM annihilation Sommerfeld factor relates to the above definition as

$$S_{IJ} \equiv S^{\chi\chi \to \chi\chi}_{(I_1I_2)(J_1J_2)}\left(\hat{f}(^1S_0)\right) = \left[\psi^{(1,0)}_{J_1J_2,ij}(0)\right]^* \psi^{(1,0)}_{I_1I_2,ij}(0). \tag{4.6}$$

4.2.2 Qualitative properties

The strength of SE is crucially governed by the precise mass splittings between different states rather than the overall mass scale, set aside Sommerfeld resonances where the interplay of both is important, and one-loop corrections to electroweakino mass eigenvalues are mandatory to obtain reliable results [107, 112]. Potential modes after the electroweak phase transition involve massive gauge bosons and, moreover, in the MSSM also Higgs boson exchanges between electroweakinos are possible. As a consequence, long-range forces always involve non-Coulombic Yukawa interactions and wave functions at the origin $\psi_{e_1e_2,ij}(0)$ as they appear in Eq. (4.4) need to be computed as numerically solutions to the Schrödinger equation. SEs sourced by Yukawa potentials differ qualitatively compared to the simpler case of Coulomb potentials, primarily due to the presence of Sommerfeld resonances, regions in parameter space near a point where a zero-energy bound state solution occurs in the spectrum [93]. Sommerfeld factors near such resonances grows more rapidly with the inverse velocity, exceeding the usual $1/\mathrm{v}$ low-velocity limit scaling of Coulombic SE, and allows for multiple orders of magnitude correction to perturbative results at phenomenologically relevant velocities. As the non-relativistic particle mass increases and the scale ratio between the long range force mediator and the high scale grows, the potential is gradually better approximated by a Coulomb potential and also the number of bound state solutions grows. Hence, the “first” Sommerfeld resonance is named after the lowest constituent mass M below which no negative energy solutions exist in the physical spectrum. The first resonances for pure Higgsino and wino models are

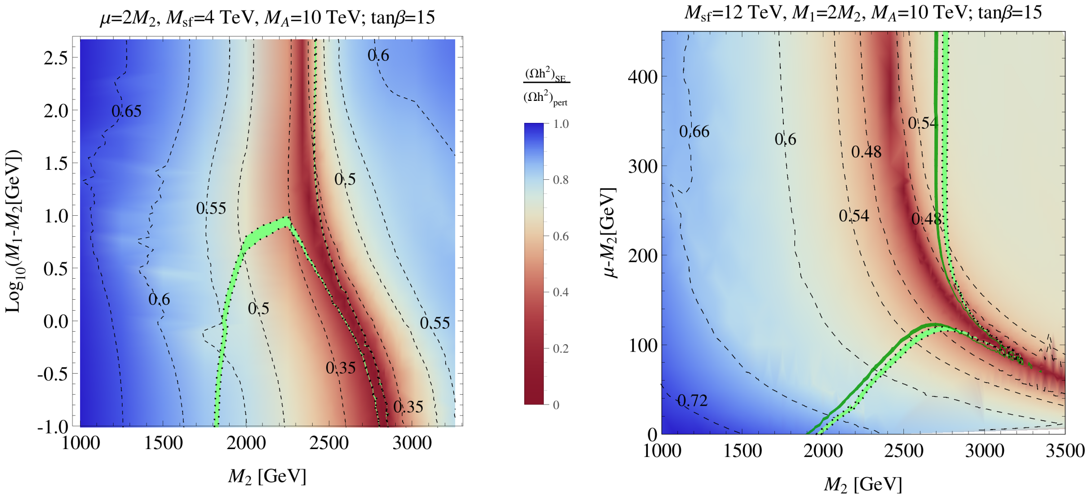

Figure 4.2: Sommerfeld enhancement measured by its impact on relic density shown as an intensity map as well as by discrete contours. The light green band indicates the region of 2σ deviation around of the dark matter density (0.1188). Other MSSM parameters are as indicated, with $A_i = 8\,\text{TeV}$ and X_t is fixed by the measured Higgs mass. Figures were adapted from [107]. *Left*: Parameter space $\log_{10}(M_1 - M_2)$ over M_2 is depicted with $\mu = 2M_2$. *Right*: Parameter space $\mu - M_2$ over M_2 is depicted with $M_1 = 2M_2$. A dark green band was added from the updated analysis, see section 4.6 for discussions.

located near 7 and 2.28 TeV while the second wino resonance is found at 8.77 TeV [87, 98].

In the full MSSM, the resonances are hypersurfaces through the parameter space, slices of which are depicted in Fig. 4.2 [107] for varying wino masses (horizontal) and bino or Higgsino splittings (vertical, left or right panel). Note the logarithmic vertical scale for the bino mass splitting. The coloring indicates the obtained relic density relative to the respective perturbative result and thereby parametrically the strength of SE during freeze-out. Green bands indicate agreement with the experimental ΛCDM energy density, light green being the original analysis [107] and dark green the updated numerical analysis discussed in section 4.6. A reduced relic abundance (red coloring) implies a more strongly enhanced annihilation cross-section. The first Sommerfeld resonance is clearly visible around $M_2 = 2.5\,\text{TeV}$ when the LSP is wino dominated and shifting to larger masses as bino or Higgsino admixtures increase. Note that sfermion masses have sizable impact on the location of the correct relic density contour even when they are seemingly decoupled from the electroweakino masses [107]. The parameter space of Higgsino-admixed DM is under severe constraints from direct and indirect detection experiments [91], which is not included in Fig. 4.2.

The expected parameter space of thermal wino-admixed DM can be read off as approximately $M_\chi = 2{-}3\,\text{TeV}$ and largely close to, yet above, the first Sommerfeld resonance. Technically, this means that bound state formation should be included in the early universe dynamics, see section 6.5 for a detailed description, it is never included in MSSM analyses included in this work. One may justify this by firstly the fact that BSF, while significant, usually reduces the obtained relic density only on order of 10%. Secondly, as shall be derived in chapter 6, shallow bound states typically become of relevance only at low velocities, that is when chemical decoupling is almost complete and effects from enhanced annihilation via bound state formation are less impactful.

It remains to understand how this framework handles mass splittings beyond the typical (P)NREFT power counting $\delta M = \mathcal{O}(M\mathrm{v}^2)$. First off, hydrogen-like systems where two non-relativistic particle species exist with a large mass separation, $\delta M \gg M_{\mathrm{LSP}}$, are straightforward in their treatment. It suffices to keep track of mass splittings to two NREFT reference scales [77]. In order to obtain a uniform theory, this is always done in the calculation of potential t-channel diagrams as well as for short distance annihilation processes, see also the later section 5.2.2. To do so, however, one must justify the use of NREFT propagators $\mathrm{i}/(p^0 - \vec{p}^{\,2}/2M - \delta M)$ for large mass splittings $\delta M \gg M\mathrm{v}^2$. This is possible under the additional weak assumption that any interaction vertex other than the bilinear NR kinetic terms (*i.e.* any three-point vertices or higher) are proportional to a small coupling constant $g \lesssim \sqrt{\mathrm{v}}$. It is very much natural to do so, as any unsuppressed interaction would be indicative of an overall non-perturbative theory, meaning that soft interactions to non-relativistic fields would be power suppressed in the EFT yet arbitrarily high order of purely-soft loops would contribute identically at that order. From simple power counting, one can now show that the one-particle irreducible two-point function is, at next-to-leading power in the EFT counting, simply given by the insertion of the kinetic bilinear term. Hence, the resummed propagator becomes the usual one while any insertion of further interactions may still be treated in perturbation theory. Lastly, the question arises whether also the PNREFT leading-order two-particle Green function, that is the Sommerfeld factor, respects the fact that some mass splittings may be large and set the ladder off-shell thus breaking the non-perturbative power counting. In the example of neutralinos, ladder diagrams depend on δM only through W- and Z-boson exchanges, via terms [77]

$$\frac{\delta M_{e_4 e_1} \delta M_{e_3 e_2}}{m_Z^2} \times v^V_{e_4 e_1} v^V_{e_3 e_2},$$

where v^V denote the respective vector boson couplings between the subscripted mass eigenstates. This means v^V is systematically suppressed by mass mixing matrix elements once $\delta M_{e_a e_b} \gg m_Z$. The combination of both terms remains under control and, therefore, every perturbative ladder diagram is found to always be of order $g^2(\vec{q}^{\,2} + m_Z^2)^{-1} \times \mathcal{O}(1)$. In summary, the combined power counting $\mathrm{v} \sim \alpha_2 \sim m_W/M_\chi$ ensures that the mass mixing appropriately decouples heavy channels in the potential terms.

Apart from theoretical concerns, there are practical problems caused by non-degenerate masses when numerical methods are invoked without sufficient care being taken to include such kinematically closed channels. Instabilities occur once mass splittings become too large yet can be circumvented using an appropriate mathematical formulation of the Schrödinger problem [77, 113].

Treating the power counting in short distance annihilation operators while resumming large Sudakov logarithms involves yet some additional care and will be discussed in the next chapter. For now, it shall suffice to have confidence in the computed Sommerfeld enhancement for tree-level short distance annihilation processes.

4.3 Higgs sector in the MSSM

The present section 4.3 and the following section 4.4 include details on the treatment of the Higgs sector and electroweak symmetry breaking in the MSSM. For completeness and homogeneity of the structure, this section collects all required bases and angles even though the unbroken mass eigenbasis is only relevant to chapter 5.

There are three different field bases for the Higgs sector, all useful in their own right: the "SUSY basis" ($H_{1,2}$), the mass eigenbasis in the electroweak symmetric theory (h, H) and the mass eigenbasis after electroweak symmetry breaking (h^0, A^0, $H^\pm$, H^0). Additionally, in the NREFT of electroweakinos there arises a convenient rotation of the Higgs bosons titled the "parity decomposition" ($H_\pm$). All calculations for neutralino annihilation concern energies of at most the hard scale, $2M_{\mathrm{LSP}}$, where all heavier R-parity odd superpartners are already integrated out. Hence, usefulness and convenience of the notation refers solely to the relation between Higgs bosons and electroweakinos. The SM and Higgs sectors may at this point also be thought of as a special case of the 2 Higgs-doublet model [114] with interactions fixed by SM gauge couplings.

4.3.1 SUSY field basis

Invariance under supersymmetry requires interaction terms to be given by a holomorphic superpotential [36] which forbids the presence of the usual SM Yukawa interactions where a single Higgs isospin doublet couples to the right-handed up-type and down-type quarks simultaneously. Instead a second scalar Higgs doublet, alongside a corresponding fermionic Higgsino super-partner, is introduced which takes the place of the SM charge-conjugated Higgs boson. The two Weyl-spinor super partners demanded by SUSY supply the required degrees of freedom to construct the Higgsino Dirac 4-spinor, which is still an isospin doublet in every component,

$$\tilde{H} = \begin{pmatrix} \mathrm{sign}(\mu)\, \psi_1 \\ -\mathrm{i}\sigma^2\, \psi_2^c \end{pmatrix} \tag{4.7}$$

where charge conjugation is denoted by c and σ^2 is the isospin Pauli matrix. The explicit $\mathrm{sign}(\mu)$ ensures the positive mass term $M_{\tilde{H}}$ in Eq. (4.2).

This fundamental requirement of holomorphy in SUSY makes the "SUSY basis" $H_{1,2}$ most natural basis of the MSSM for the scalar components of the supermultiplets. By construction, this basis disentangles the coupling to up-type and down-type right-handed fermion flavors and $H_{1,2}$ must therefore carry opposite hypercharges $Y = \mp 1/2$, writing $\hat{g} = Yg$ for the corresponding coupling in Eq. (2.3). Exploiting the pseudoreal fundamental representation of SU(2), $\widetilde{H}$ still has a well-defined hypercharge but in turn involves the anti-symmetric tensor $\mathrm{i}\sigma^2$. Analogous combinations follow for field rotations of the Higgs bosons. Throughout this thesis, the term "super-partner" is applied to Higgs and Higgsino degrees of freedom irrespective of assumed bases, even though $H_{1,2}$ are the literal super-partners of the Higgsino $\tilde{H}$.

4.3.2 High energy mass eigenbasis

The notational convention to differentiate large from small masses by capital letters enters muddy waters with the MSSM Higgs sectors which may be of the electroweak scale or much heavier than M_{LSP} for the BSM particle content. To ease comparison to existing notations and allow to write the SM Higgs boson consistently, all Higgs boson mass parameters are denoted by small letters, m instead of M. Regardless, also scenarios of (partially) heavy Higgs masses will be considered within this notation. The mass matrix of the scalar Higgs sector involves off-diagonal entries m_{12}^2 in the SUSY basis [105] already in the electroweak-symmetric phase, giving rise to a mixing angle α_H. The symmetric mass eigenbasis is defined by an orthogonal rotation

$$\begin{pmatrix} h \\ H \end{pmatrix} \equiv \begin{pmatrix} -c_{\alpha_H} & s_{\alpha_H} \\ s_{\alpha_H} & c_{\alpha_H} \end{pmatrix} \cdot \begin{pmatrix} \mathrm{i}\sigma^2 H_1^* \\ H_2 \end{pmatrix} \tag{4.8}$$

where s_x, c_x, t_x abbreviate the sine, cosine and tangent of x and α_H is defined by

$$t_{\alpha_H} = \frac{-2m_{12}^2}{m_{H_2}^2 - m_{H_1}^2 + \sqrt{4m_{12}^4 + (m_{H_2}^2 - m_{H_1}^2)^2}} \tag{4.9}$$

to diagonalize the mass Higgs boson mass matrix. Note that [2] has a mistyped exponent (m_{12}^2) in the root of its equation (A.2). $m_{H_{1,2}}$ and m_{12} are the soft SUSY breaking parameters and the obtained mass eigenvalues in the unbroken Higgs sectors are

$$m_{h,H}^2 = M_{\tilde{H}} + \frac{m_{H_1}^2 + m_{H_2}^2}{2} \pm \frac{m_{12}^2}{s_{2\alpha_H}}. \tag{4.10}$$

4.3.3 Low energy mass eigenbasis

After electroweak symmetry breaking, which will be discussed in more detail in section 4.4, the Higgs potential is expanded around a different minimum. Hence, one finds new masses and also a new mixing angles, α and β, relative to the SUSY basis. In many applications, α is more common than α_H as it sets the relation between the charge-neutral super-partners $H_{1,2}^0$ and the lightest charge neutral real scalar h^0 [36],

$$\frac{1}{\sqrt{2}} \begin{pmatrix} -s_\alpha & c_\alpha \\ c_\alpha & s_\alpha \end{pmatrix} \cdot \begin{pmatrix} h^0 \\ H^0 \end{pmatrix} + \frac{\mathrm{i}}{\sqrt{2}} \begin{pmatrix} -c_\beta & s_\beta \\ s_\beta & c_\beta \end{pmatrix} \cdot \begin{pmatrix} G^0 \\ A^0 \end{pmatrix} \equiv \begin{pmatrix} H_1^0 \\ H_2^0 \end{pmatrix} + \text{const.} \tag{4.11}$$

The right hand side dropped constant terms from vacuum expectation values. G^0 is the Nambu-Goldstone boson, turning into the longitudinal Z-boson mode. To agree with experimental measurements, m_{h^0} must coincide with the 125 GeV resonance measured at the Large Hadron Collider [19, 115]. Loop corrections to m_{h^0} are sizable, however, here only leading order effects are regarded. The Higgs boson spectrum in the electroweak-broken phase is well known [36] and includes 5 real degrees of freedom in the light and heavy neutral scalars h^0 and H^0, the neutral pseudoscalar A^0 and the charged scalars $H^\pm$.

4.3.4 Parity decomposition

The degrees of freedom of $\tilde{H}$ are in NREFT separate particle annihilator and anti-particle creator fields which, to leading order, are eigenstates of the parity even projection operator P_+. In a 4-component notation, $P_+ = (\mathbf{1} + \gamma^0)/2$. From the Weyl fermion representation of the Higgsino, Eq. (4.7), it becomes clear that the non-relativistic fields ψ_1 and $\mathrm{i}\sigma^2\psi_2^c$ both rotate symmetrically by a $\pi/4$ rotation [2, 62]. Since all hard modes are integrated out in NREFT, only the respective annihilation operators are of relevance and, by virtue of the underlying supersymmetry in the MSSM Lagrangian, also only the parity even scalar Higgs combination appears,

$$\mathcal{L}_{\mathrm{UV}}[H_{1,2}] \longrightarrow \mathcal{L}_{\mathrm{NR}}[H_\pm] = \mathcal{L}_{\mathrm{NR,LO}}[H_+^{(\mathrm{UV})}] + \text{higher orders.}$$

Only $H_+^{(\mathrm{UV})}$ remains in leading-order NREFT. Disregarding masses of the Higgs bosons for the moment, $H_\pm^{(\mathrm{UV})}$ are the unbroken-phase parity eigenbasis of the Higgs fields,

$$H_\pm^{(\mathrm{UV})} \equiv \frac{\pm\mathrm{sign}(\mu)\, H_1 + \mathrm{i}\sigma^2\, H_2^*}{\sqrt{2}}, \tag{4.12}$$

mirroring the $\pi/4$ rotated definition of the NREFT Higgsino annihilation operator fields (which do have equal masses). The absence of $H_-^{(\mathrm{UV})}$ in the NR MSSM was already observed in [62] together with the analogous analytic decoupling of one of the four neutralino eigenstates from the mass-mixing, yet not all subtleties regarding sign(μ) and $H_\pm^{(\mathrm{UV})}$ were understood in detail at the time.

In full one-loop computations with propagating Higgs fields, the interactions must now be projected into the mass eigenbasis in order to have diagonal propagators. However, for the computation of the anomalous dimension used in chapter 5 the finite masses are irrelevant to the required UV divergences [2, 62], which makes $H_\pm^{(\mathrm{UV})}$ a useful decomposition. Still, m_H can become large in which case H is to be considered as static and does not propagate such that the projection onto H yields 0 as the loop is suppressed by the approximately infinite mass m_H. This decoupling can be incorporated in a straightforward fashion as a discrete step in the interactions by changing the number of active Higgs bosons $n_H = 2 \to 1$. The interaction Lagrangian in NREFT becomes

$$\mathcal{L}_{\mathrm{NR,LO}}[H_+^{(\mathrm{UV})}] \longrightarrow \mathcal{L}_{\mathrm{NR,LO}}[h, H, n_H] = \mathcal{L}_{\mathrm{NR,LO}}[H_+]$$

where H_+ is now the linear combination of the unbroken mass eigenstate fields

$$H_\pm \equiv \frac{s_{\alpha_H} \pm \mathrm{sign}(\mu) c_{\alpha_H}}{\sqrt{2}}\, h + \delta_{2\,n_H} \frac{c_{\alpha_H} \mp \mathrm{sign}(\mu) s_{\alpha_H}}{\sqrt{2}}\, H\,, \tag{4.13}$$

with the Kronecker-delta $\delta_{2\,n_H}$ removing the second term once $n_H = 1$. Again, only H_+ appears in the LO NREFT Lagrangian. Due to this definition, $H_\pm$ are not canonically quantized fields and should be thought of as mere linear combinations abbreviating interactions with the mass eigenstate present at the considered energy scale. The surviving term for $n_H = 1$ gives an effective coupling upon integrating out the heavy Higgs doublet and since only internally propagating Higgs fields are considered in chapter 5, the entire decoupling can be easily incorporated into calculations via

$$a_+ \equiv \begin{cases} \frac{1}{\sqrt{2}}\left(s_{\alpha_H} + \mathrm{sign}(\mu) c_{\alpha_H}\right) & \text{if } n_H = 1 \\ 1 & \text{if } n_H = 2 \end{cases}. \tag{4.14}$$

The definition differs slightly from the corresponding expressions in [62] by incorporating $\mathrm{sign}(\mu)$ explicitly in Eq. (4.12) and therefore a_+ whereas α_H now remains independent of it. The main advantage of this updated construction is that α_H is now unambiguously defined by t_{α_H} in (4.9) and does not flip sign alongside μ.

4.4 Treatment of electroweak symmetry breaking

This section clarifies some aspects of the treatment of electroweak symmetry breaking (EWSB) in the model and the practical implementation for the purpose of calculating SE. To achieve a homogeneous power counting, the various scales for the gauge boson masses, the top quark decoupling and EWSB are assumed to all coincide at the soft scale,

$$\hat{\mu}_{\mathrm{EWSB}} \sim m_W \sim m_Z \sim m_t \sim M\mathrm{v}, \tag{4.15}$$

which is the lowest scale relevant to chapters 4 and 5. In thermal production, the kinetic energy is set by the bath temperature and thus the Sommerfeld enhanced region is to be considered to take place in the electroweak broken phase, demanding the PNREFT potentials to respect electroweak gauge boson masses. The natural choice is now to match to (P)NREFT already in the EWSB basis. Furthermore, at or below $\hat{\mu}_{\mathrm{EWSB}}$ any ultraviolet extension must match onto the SM such that parameters are defined by experimental measurements and all BSM particles are latest integrated out at m_W. As a consequence, $m_{h^0} = 125\,\mathrm{GeV}$ must be fulfilled.

The electroweak phase transition is triggered from the Higgs potential developing a new minimum at non-zero field values. These VEVs are commonly defined in the SUSY basis as $\left\langle H^0_{1,2} \right\rangle = v_{1,2}/\sqrt{2}$ [105]. Their geometric sum defines the total VEV measured in the SM, $v_{\mathrm{sm}} = \sqrt{v_1^2 + v_2^2} = 246.22\,\mathrm{GeV}$ [116]. Remaining degrees of freedom of the Higgs sector are typically parametrized by m_{A^0} and

$$t_\beta = \tan(\beta) \equiv \frac{v_2}{v_1}. \tag{4.16}$$

The VEV angle β coincides with the pseudoscalar rotation angle in the EW broken phase already introduced in section 4.3.3 [36]. The fact that the mass eigenbasis after EWSB does not coincide with the SUSY basis has interesting consequences for the interpretation of the Yukawa couplings in the MSSM. In the SM, the Yukawa couplings are simply derived from measurements of fermion masses. However in the MSSM, both SUSY basis Higgs states gain a VEV, meaning that the SM Yukawa coupling must actually be smaller than what is found in the MSSM, by factors

$$y_f^{\mathrm{sm}} = \frac{\sqrt{2}\, m_f}{v_{\mathrm{sm}}} = \frac{\sqrt{2}\, m_f}{v_{2,1}} \frac{v_{2,1}}{\sqrt{v_1^2 + v_2^2}} = y_f^{\mathrm{MSSM}} \times \begin{cases} \sin(\beta) & \text{if } f \in U \\ \cos(\beta) & \text{if } f \in D \end{cases} \tag{4.17}$$

where $U = \{u,\, c,\, t\}$ indicates any up-type quark and $D = \{d,\, s,\, b,\, e,\, \mu,\, \tau\}$ any down-type fermion which couple to H_1 and H_2, respectively. This becomes of relevance when one allows for $m_W \ll m_{A^0} \ll M_{\rm LSP}$ in which case a decoupling step of the heavier Higgs bosons must be included when evolving the couplings from the hard to the low scale. A subtlety to this renormalization scale independent statement is that the factors s_β (or c_β) were found under the assumption that $m_{A^0} \sim \hat{\mu}_{\rm EWSB} \sim m_W$. A detailed analysis shows that in a heavy Higgs scenario, one would instead find an effective coupling $y_{f,\rm eff} = y_f^{\rm sm}\, s_{\alpha_H}/s_\beta$ at the scale m_W and an analogous matching factor to the one derived in Eq. (4.17) but in terms of the EW symmetry rotation angle s_{α_H} (or c_{α_H}) at the decoupling scale m_{A^0}. These differences can safely be neglected, instead always relying directly on Eq. (4.17) at the renormalization scale $\hat{\mu} = m_{A^0}$, since a scenario where $m_{A^0} \gg m_W$ also implies $\alpha_H = \beta + \mathcal{O}(m_W^2/m_{A^0}^2)$ [36].

EWSB causes mass mixing terms of order of the soft scale, $\sim g_{1,2}\, v_{\rm sm}$, which change the electroweakino mass eigenstates and shift the eigenvalues by $\mathcal{O}(m_W)$. As a consequence, only a subset of neutralinos and charginos can be degenerate within ultrasoft mass splittings, see section 5.2.1. Concerns arising from soft or hard mass splittings regarding the computation of the SE were already alleviated by the earlier discussions regarding the applicability of PNREFT in section 4.2.2.

With the setup of the MSSM and EWSB clarified, this chapter will now introduce the renormalization group running to get precise input values for the numeric results of section 4.6 and also chapter 5.

4.5 Renormalization group evolution in the SM and MSSM

"Running couplings", that is the renormalization group equation (RGE) solution of coupling strengths, is by far the best known resummation procedure in quantum field theory and conceptually analogous to the Sudakov resummation investigated in chapter 5. Instead of using a single experimentally determined value for the coupling strength, one derives an all-order solution to the fixed order differential equation obtained from the condition that physical observables must be independent of any renormalization scale choice at every perturbative order. Since the SE and hard annihilation process are evaluated at widely separated scales, one expects notable effects from inclusion of running couplings. This section discusses the implementation of one-loop Yukawa and two-loop electroweak couplings, going beyond previously used treatments. Furthermore, state-of-the-art numerical inputs for all SM couplings are derived.

To clearly separate the Higgsino mass parameter μ from the dimensional regularization renormalization scale $\hat{\mu}$, the latter is denoted with a circumflex accent ("hat" symbol). To further preclude possible misinterpretation Yukawa couplings and gauge coupling strengths are also denoted with a hat, $\hat{y}$ and $\hat{\alpha}$, when referring to their values in the minimal subtraction scheme in dimensional regularization ($\overline{\rm MS}$). Their un-hatted values instead refer to the respective on-shell scheme values.

A convenient notation for the RGEs uses the reduced coupling strengths

$$a_1 \equiv \frac{5}{3}\frac{\hat{\alpha}_1(\hat{\mu})}{4\pi}, \qquad a_{2,3} \equiv \frac{\hat{\alpha}_{2,3}(\hat{\mu})}{4\pi}, \qquad a_f \equiv \frac{\hat{y}_f(\hat{\mu})^2}{16\pi^2}, \tag{4.18}$$

where $f \in \{e, \mu, \tau, u, d, c, s, t, b\}$. This definitions efficiently absorb all factors of π from the RGEs, leaving compact expressions in terms of only rational numbers.

The factor 5/3 in the reduced hypercharge coupling strength is adopted from a wide-spread convention which originated from SU(5) grand unified theories [117]. Specifically, the running couplings solve a system of coupled differential equations defined by the beta-functions $\beta(\hat{\mu})$,

$$\frac{\mathrm{d}a_x}{\mathrm{d}\log\hat{\mu}^2} = 2\hat{\mu}\,\frac{\mathrm{d}a_x}{\mathrm{d}\hat{\mu}} \equiv \beta_x \equiv a_x\left(\beta_x^{(0)} + a_x\beta_x^{(1)} + \mathcal{O}(a_x^4)\right), \tag{4.19}$$

where $\beta_x^{(i)}$ are homogeneous functions in all a_x of combined order $i+1$.

The RG running will always be performed in the unbroken phase since $\hat{\mu}_{\mathrm{EWSB}}$ is the lowest scale (soft scale) in all processes, even though the Universe may have already undergone EWSB. On the one hand, this greatly simplifies the analytic expressions by removing many additional mass scales. Furthermore, the running couplings are also required in chapter 5 where the running of hard annihilation Wilson coefficients is computed in the EW symmetric phase. The choice is one between assuming the running to the hard scale to be caused by field fluctuations of such short wavelength that EWSB remains ineffective or assuming the EW broken thermal environment with a Higgs condensate background to define even the dynamics of virtual quantum fluctuations.

4.5.1 Full Yukawa dependence of the RGE

This subsection compiles the complete one loop beta functions for all reduced coupling strengths and also two-loop terms for the electroweak gauge couplings $a_{1,2}$. These results are not conceptually new and were adopted by combining existing results [114, 117–119] but are nonetheless not present in the literature in the here required form. The number of dynamical Higgs fields n_H is kept general which in turn allows to decouple the heavier Higgs doublet H at an arbitrary scale later on. This is needed since m_{A^0} is a free input parameter of the MSSM. Furthermore, the number of active flavors n_q is left unspecified as in known results which technically also allows to decouple the top quark at any scale, however this is not used in later numerical evaluations instead relying on starting inputs already in the $n_q = 6$-flavor scheme.

To one-loop accuracy, the gauge coupling renormalization remains independent of any other couplings whereas Yukawa interactions yield mixing already at this order. The one-loop contributions are

$$\beta_1^{(0)} = a_1\left(\frac{1}{10}n_H + \frac{2}{3}n_q\right), \tag{4.20}$$

$$\beta_2^{(0)} = a_2\left(-\frac{44-n_H}{6} + \frac{2}{3}n_q\right), \tag{4.21}$$

$$\beta_3^{(0)} = a_3\left(-11 + \frac{2}{3}n_q\right), \tag{4.22}$$

$$\begin{aligned}
\beta^{(0)}_{U,g} =& -\frac{17}{20}a_1 - \frac{9}{4}a_2 - 8a_3 \\
&+ 3\|\tilde{a}_U\| + \delta_{1,n_H}\left(3\|\tilde{a}_D\| + \|\tilde{a}_L\|\right) + \frac{3}{2}\tilde{a}_{U,g} - \frac{4\delta_{1,n_H}-1}{2}\tilde{a}_{D,g}, \qquad (4.23)\\
\beta^{(0)}_{D,g} =& -\frac{1}{4}a_1 - \frac{9}{4}a_2 - 8a_3 \\
&+ 3\delta_{1,n_H}\|\tilde{a}_U\| + 3\|\tilde{a}_D\| + \|\tilde{a}_L\| + \frac{3}{2}\tilde{a}_{D,g} - \frac{4\delta_{1,n_H}-1}{2}\tilde{a}_{U,g}, \qquad (4.24)\\
\beta^{(0)}_{L,g} =& -\frac{9}{4}a_1 - \frac{9}{4}a_2 \\
&+ 3\delta_{1,n_H}\|\tilde{a}_U\| + 3\|\tilde{a}_D\| + \|\tilde{a}_L\| + \frac{3}{2}\tilde{a}_{L,g}, \qquad (4.25)
\end{aligned}$$

where $\beta_{U(D/L),g}$ is the Yukawa coupling beta function for the up-type quark (down-type quark / charged Lepton) of generation g. The compact notation uses

$$\|\tilde{a}_U\| \equiv \sum_g \tilde{a}_{U,g} = \sum_{x=u,c,t} \tilde{a}_x, \qquad (4.26)$$

$$\|\tilde{a}_D\| \equiv \sum_g \tilde{a}_{D,g} = \sum_{x=d,s,b} \tilde{a}_x, \qquad (4.27)$$

$$\|\tilde{a}_L\| \equiv \sum_g \tilde{a}_{L,x} = \sum_{x=e,\mu,\tau} \tilde{a}_x, \qquad (4.28)$$

provided all respectively summed fermions are dynamic. Further,

$$\tilde{a}_U = \begin{cases} a_U & \text{for } n_H = 2, \\ a_U \cdot \sin^2(\beta) & \text{for } n_H = 1 \end{cases}, \qquad (4.29)$$

$$\tilde{a}_D = \begin{cases} a_D & \text{for } n_H = 2, \\ a_D \cdot \cos^2(\beta) & \text{for } n_H = 1 \end{cases}, \qquad (4.30)$$

$$\tilde{a}_L = \begin{cases} a_L & \text{for } n_H = 2, \\ a_L \cdot \cos^2(\beta) & \text{for } n_H = 1 \end{cases} \qquad (4.31)$$

takes care of the mixing to the light mass-eigenstate h which still propagates in the loops even when the heavier doublet is integrated out. As mentioned above, $\alpha_H \approx \beta$ is used in the matching the decoupled $n_H = 1$ theory. In the literature, the Yukawa couplings are often encoded in 3-by-3 matrices $\mathbf{Y}_{\mathrm{U,D,L}}$ and traces thereof. In contrast, here a vectorial representation as a_F $(F = U, D, L)$ is preferred, implicitly pointing to the fact that no mass mixing is considered for the light fermions.

For $n_H = 1$, the definitions (4.20)-(4.24) correspond to the result of the SM if the $\tilde{a}_{U,D}$ were treated as traditional Yukawa couplings $a_{U,D}$ [117]. For $n_H = 2$ they agree with the MSSM where only the second Higgs doublet is left dynamic out of the entire BSM particle content, whereas all R-parity odd particles decouple below $2M_{\mathrm{LSP}}$ [114]. The results of [114] only include the third generation fermion couplings $a_{t,b,\tau}$ but can be generalized to respect all generation without additional calculations. For example, for $\beta^{(0)}_b$ the only complication to including all generations is to understand which contribution of a_b arise from $\|a_D\|$, that is from the generation-independent Higgs self-energy diagrams, and which ones from $a_{D,g=3}$ that is from generation-specific triangle diagrams connecting to the external bottom-quarks present in the Yukawa-interaction operator. The former must coincide with the lepton contribution up to a factor $N_c = 3$ counting the number of colors. The terms mixing $a_{U,g}$ and $a_{D,g}$ at one loop originate from from the left-handed quark isospin doublet self-energies and must be specific to the given generation g when neglecting mass mixing effects. The two conditions can be expressed mathematically as

$$\frac{\partial}{\partial \|\tilde{a}_U\|}\beta^{(0)}_{U,g} = \frac{\partial}{\partial \|\tilde{a}_D\|}\beta^{(0)}_{D,g} = N_c\frac{\partial}{\partial \|\tilde{a}_L\|}\beta^{(0)}_{D,g}, \tag{4.32}$$

as well as

$$\frac{\partial}{\partial \|\tilde{a}_U\|}\beta^{(0)}_{D,g} = \frac{\partial}{\partial \|\tilde{a}_D\|}\beta^{(0)}_{U,g} \tag{4.33}$$

because up-type quarks are assumed to not affect the down-type quark RGEs of a different generation or lepton couplings in the MSSM. Similarly, for the generation-specific terms

$$\frac{\partial}{\partial \tilde{a}_{U,g}}\beta^{(0)}_{U,g} = \frac{\partial}{\partial \tilde{a}_{D,g}}\beta^{(0)}_{D,g}. \tag{4.34}$$

The electroweak 2-loop terms required by power-counting for NLL Sudakov resummation in chapter 5 are [2, 62]

$$\begin{aligned}\frac{1}{4}\beta^{(1)}_1 =& \frac{9n_H}{50}a_1 + \frac{9n_H}{10}a_2 + n_q\left(\frac{19}{30}a_1 + \frac{3}{10}a_2 + \frac{22}{15}a_3\right)\\ &- \frac{17}{10}\|\tilde{a}_U\| - \frac{1}{2}\|\tilde{a}_D\|, \end{aligned}\tag{4.35}$$

$$\begin{aligned}\frac{1}{4}\beta^{(1)}_2 =& \frac{3n_H}{10}a_1 - \frac{272-13n_H}{6}a_2 + n_q\left(\frac{1}{10}a_1 + \frac{49}{6}a_2 + 2a_3\right)\\ &- \frac{3}{2}\|\tilde{a}_U\| - \frac{3}{2}\|\tilde{a}_D\|. \end{aligned}\tag{4.36}$$

All other coupling strengths are kept at one-loop accuracy since they only enter at NLO in the running of $\alpha_{1,2}$. Therefore the quartic Higgs self-coupling never enters in the computation of the running couplings. These two-loop results are included in numerical evaluations of this chapter as well.

The results of this subsection define the system of differential renormalization group equations. Due to the complicated coupled differential equations in the Yukawa couplings, where formally all Yukawa couplings are counted equally despite the hierarchy $y_t \gg y_{f\neq t}$ present in realistic systems, analytic solutions are not considered, directly relying on numerical results instead.

4.5.2 Precise numeric Standard Model parameters

To solve the RGEs numerically, experimental data is necessary for realistic boundary conditions to the system of differential equations. However, also theoretically it is important to use a well defined renormalization scheme at all points in the computations by choosing a unique set of independent input parameters and systematically deriving any dependent quantities at a fixed precision. For example, the electroweak sector of the SM is often defined by [120] the (inverse) electromagnetic fine structure constant, the squared Weinberg angle sine, the Z-boson mass and the Fermi constant which makes the W-boson mass a dependent value $m_W = m_W(\alpha^{-1}, s_W, m_Z, G_F)$. The importance of a consistent renormalization scheme can exemplified already at tree-level. If one was to compute the annihilation of a neutralino pair into photons to first order in the gauge couplings, neglecting SE, naive physical understanding correctly predicts this cross section to be zero as all participating particles are neutral under photon interactions. However the (EW symmetric) electroweakinos mixing into the neutralino mass eigenstate do in fact annihilate into pairs of gauge bosons, including photons. This is necessarily so as they also make up the chargino mass eigenstates. The neutralino annihilation cross-section therefore only vanishes due to the relation between the electroweak gauge couplings $\alpha_{1,2}$ and the Weinberg angle, $s_W^2 = \sin^2\theta_W = \alpha_1/(\alpha_1 + \alpha_2)$. A careless approach might now use s_W^2 not related to the exact values of $\alpha_{1,2}$ but taken from some other experimental input hence breaking theoretical consistency, violating the cancellation in electromagnetic processes of neutralinos and leading to non-vanishing annihilation cross-sections. Note that a seemingly similar yet physical non-cancellation occurs when resumming electroweak Sudakov logarithms in neutralino annihilation to leading order, where the resummed inclusion of charged gauge-boson emission allows for a loop-order coupling to the photon which is enhanced by the large Sudakov logarithms [62].

The renormalization scheme employed here makes use of on-shell m_Z and m_W masses in the electroweak sector with the addition of the fine structure constant in the $\overline{\text{MS}}$-scheme at m_Z setting the Higgs VEV. All inputs are listed in Tab. 1. Following [99], $\overline{\text{MS}}$ values are indicated by hatted quantities and the 6-flavor scheme is implied as the top-quark is considered dynamic above m_Z. The fine structure constant and W and Z-bosons are known to high precision in the SM while a dependence on G_F only produces unnecessary complications when aiming to compute processes in the EW symmetric phase.

Due to the rather large interaction strength of the strong interaction (QCD), higher loop orders are not as rapidly suppressed as for electroweak processes and the public tool `RunDec` is employed to precisely compute $\hat{\alpha}_3$ in the 6-flavor scheme as well as the quark masses at m_Z, which provides state-of-the-art values. To do so, quark decouplings are assumed at their respective $\overline{\text{MS}}$-masses and decoupling and RG evolution was done at 5-loop accuracy, with inputs taken from [116]. The top quark mass is given only in the on-shell scheme and was matched to $\overline{\text{MS}}$ at 4-loop accuracy assuming $n_f = 5$. All masses and $\hat{\alpha}_3$ are obtained at $\hat{\mu} = m_Z$ for $n_f = 5$ and only then matched onto the 6-flavor scheme. For the Lepton Yukawa couplings, recent results at the scale $\hat{\mu} = Q_0 = 172.5\text{GeV}$ exist for $\hat{y}_{e,\mu,\tau}$ [122] and can be run to m_Z with $n_H = 1$. This introduces the assumption $m_{A^0} > Q_0$ which is reasonable given current experimental constraints. In practice, this assumption is numerical almost unnoticeable. Yukawa couplings are actually only needed at one-loop accuracy allowing to us simple tree-level matching relations to extract them from the mass values, which themselves are now computed at much higher accuracy than formally required,

$$\hat{y}_q(m_Z) \equiv \frac{\sqrt{2}\,\hat{m}_q(m_Z)}{246.22\,\text{GeV}}\,, \quad q = u, d, s, c, b, t. \tag{4.37}$$

input quantity	**symbol & value**
Z-boson mass	$m_Z = 91.1876\,\text{GeV}$
W-boson mass	$m_W = 80.385\,\text{GeV}$
fine structure constant	$\hat{\alpha}_{em} = 1/128.143$
Weinberg angle sine square	$\hat{s}_W^2 = 0.232444$
strong coupling constant	$\hat{\alpha}_3 = 0.10778$
up-Yukawa	$\hat{y}_u = 7.14413 \times 10^{-6}$
down-Yukawa	$\hat{y}_d = 0.0000154459$
strange-Yukawa	$\hat{y}_s = 0.000308918$
charm-Yukawa	$\hat{y}_c = 0.00359552$
bottom-Yukawa	$\hat{y}_b = 0.0164189$
top-Yukawa	$\hat{y}_t = 0.972632$
electron-Yukawa	$\hat{y}_e = 2.77803 \times 10^{-6}$
muon-Yukawa	$\hat{y}_\mu = 0.000585231$
tauon-Yukawa	$\hat{y}_\tau = 0.00994096$

Table 1: Precise numerical standard model inputs used to define the renormalization scheme for calculations in chapters 4 and 5. Hatted quantities are understood in the $\overline{\text{MS}}$-scheme with 6 active quark flavors evaluated at $\hat{\mu} = m_Z$. $\hat{\alpha}_{em}$ and $\hat{s}_W^2$ are computed by one-loop matching [99] from the on-shell values $m_{W,Z}$, $\alpha_{\text{em}}^{\text{on-shell}} = 1/128.943$, in turn taken from [116]. $\hat{\alpha}_3$ corresponds to $\hat{\alpha}_3^{n_q=5}(m_Z) = 0.1181$ for 5-active flavors and has been matched at 4-loop accuracy using RunDec 3.1 [121]. Yukawa couplings relate to the masses of Tab. 2 according to Eq. (4.37).

The ad-hoc introduction of the measured SM Higgs VEV [116] does not break the renormalization scheme as it is used only prior to setting the inputs of any calculation and is thus fully degenerate with experimental uncertainties. Lastly, electroweak coupling strengths in $\overline{\text{MS}}$ are computed from one-loop matching relation to the on-shell masses $m_{W,Z}$ and $\hat{\alpha}_{em}(m_Z)$ [99], finding $\hat{\alpha}_1(m_Z) = 0.0101671$ and $\hat{\alpha}_2(m_Z) = 0.0335727$, and define the starting values to solve the RGEs together with $\hat{\alpha}_3$ and the Yukawa.

4.5.3 Numerical evaluation of the running couplings

Using the SM inputs derived in the previous section, there are two remaining degrees of freedom in the numerical solution which need to be fixed by BSM parameters. Firstly, the VEV mixing angle t_β is a conventional input to MSSM models. Secondly, the decoupling step for the heavy Higgs doublet is chosen as m_{A^0}, the lightest mass eigenstate of the BSM Higgs sector after EWSB. Other choices such as m_{H^+} or m_H are possible but almost identical as the mass splittings between the two is relatively small whenever there is a notably large scale separation to m_Z. The derivation of the RGEs in section 4.5.1 and the found numerical values of section 4.5.2 for the SM inputs were confirmed in a blind double-check.

Fig. 4.3 shows the numerical result,s taking $\tan(\beta) = 3$ and $m_{A^0} = 1\,\text{TeV}$, for the running of the gauge coupling strengths (upper panel) and the Yukawa cou-

fermion	$\overline{\text{MS}}$ mass at m_Z
up	$\hat{m}_u = 1.24382\,\text{MeV}$
down	$\hat{m}_d = 2.68919\,\text{MeV}$
strange	$\hat{m}_s = 53.7838\,\text{MeV}$
charm	$\hat{m}_c = 625.994\,\text{MeV}$
bottom	$\hat{m}_b = 2.85859\,\text{GeV}$
top	$\hat{m}_t = 169.339\,\text{GeV}$
electron	$\hat{m}_e = 483.666\,\text{keV}$
muon	$\hat{m}_\mu = 101.891\,\text{MeV}$
tauon	$\hat{m}_\tau = 1.73076\,\text{GeV}$

Table 2: Precise SM fermion masses $\hat{m}_f$ in the $\overline{\text{MS}}$-scheme with 6 active quark flavors evaluated at $\hat{\mu} = m_Z$. Quark masses were matched and evolved to m_Z at 4 and 5-loop accuracy, respectively. Starting values for both are taken from [116]. Lepton Yukawa couplings are taken from [122] at $Q_0 = 172.5\,\text{GeV}$ and evolved to m_Z using the coupled system of RGEs given in section 4.5.1.

plings (lower panel) with each value normalized to its respective boundary conditions from Tab. 1. m_Z and m_{A^0} are indicated by vertical lines. Note that all depicted curves are continuous since the Yukawa couplings $\hat{y}$ are being shown rather than the discontinuous objects $\tilde{a}_f$ from Eqn. (4.29)-(4.31). At scales $\hat{\mu} > m_{A^0}$, the decoupling firstly enhances the depicted up- and down-type Yukawa couplings by powers of $1/\sin(\beta)$ and $1/\cos(\beta)$. Secondly, several diagrams vanish once the complete 2 Higgs-doublet field content is dynamical. Crucially, lepton RGEs then become independent of the two largest SM couplings, $y_t^2/4\pi \sim \alpha_3 \sim 0.1$. This is not the case for quarks, where still the left-handed doublet self-energy loop gives rise to a contribution from $\hat{y}_t$ and also the strong coupling $\hat{\alpha}_3$ contributes sizably making the dependence on n_H less noticeable. Hence, the Higgs decoupling step is especially significant for lepton couplings (black curves in the lower panel) where even the sign of the beta-functions changes. Similar, albeit weaker, effects are seen in the light up- and down-type quarks of the first two generations (dashed red and blue curves) above $\hat{\mu}_H$. This leads to the interesting feature that around typical neutralino DM masses, $\hat{\mu} = 1 - 5\,\text{TeV}$, the evolved Lepton couplings are almost identical to their starting values, $y(2M_\chi) \approx y(m_Z)$. For the light quarks u, c and d, s as well as all three leptons, the RGE is always dominated by $\hat{y}_{b,t}$ or gauge couplings and they are indistinguishable in the depicted resolution.

4.6 Numerical impact of improved coupling values

The impact of the improved running couplings is discussed in this section an illustrative MSSM benchmark points to exemplify the importance of running Yukawa couplings and confirm the found results with expectations. Finally, also updates to the relic density contour of wino-Higgsino DM is studied in a single slice of parameter space.

According to Fig. 4.3, inclusion of renormalization group evolution is expected to result in $\mathcal{O}(30\%)$ effects in $t\bar{t}$ or $b\bar{b}$ channels, since $\hat{y}_f$ enters at least squared in the

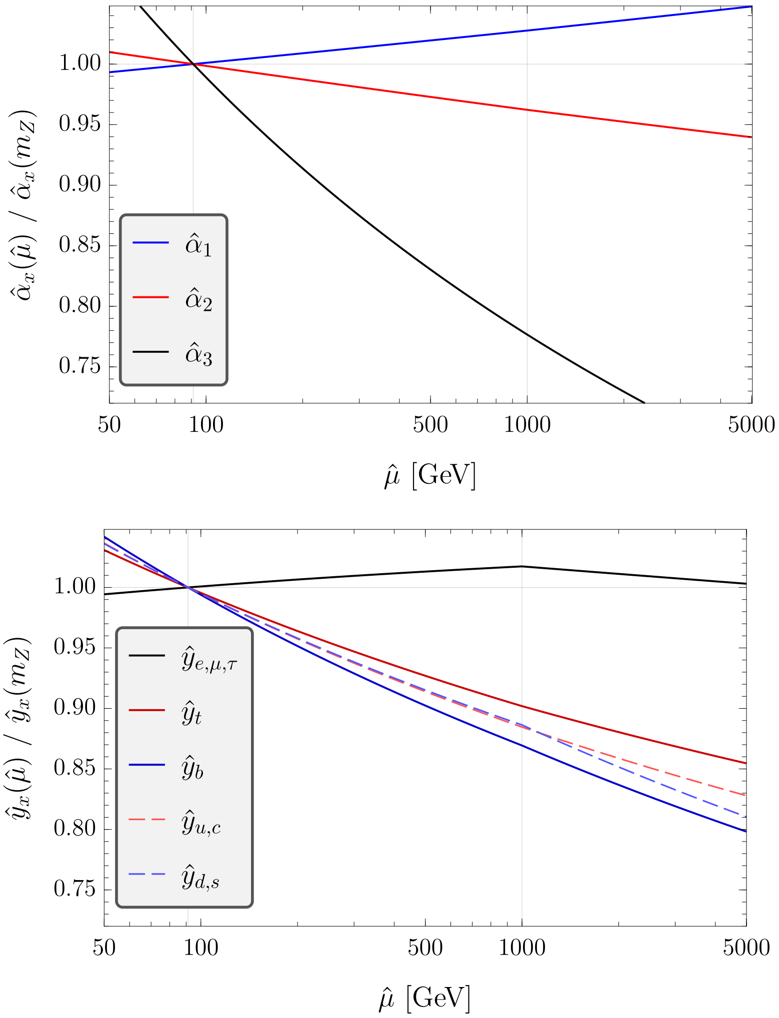

Figure 4.3: Numerical solutions for the $\overline{\text{MS}}$ running couplings (4.20)-(4.25), including the two-loop terms (4.35) and (4.36), normalized to the respective boundary values at m_Z as given in section 4.5.2. $\tan(\beta) = 3$ and the heavy Higgs is decoupled below $m_{A^0} = 1\,\text{TeV}$. *Upper panel*: The gauge coupling strengths $\hat{\alpha}_{1,2,3}$ (blue, red, black). *Lower panel*: The Yukawa couplings y_f where for $f = e, \mu, \tau$ (black), $f = u, c$ (dashed red) and $f = d, s$ (dashed blue) the normalized couplings are respectively almost identical. $\hat{y}_{b(t)}$ are shown by the solid blue (red) curves. The discontinuous factor $\delta_{1,n_H} + \delta_{2,n_H} \cos^2\beta$ of $\tilde{a}_{L,D}$ or $\sin\beta$ for a_U, is not part of $\hat{y}_f$.

cross section. Both, the running of the weak and hypercharge coupling strength are notably less significant, of $\mathcal{O}(5\%)$, while the QCD coupling $\hat{\alpha}_3$ only enters in WIMP annihilation through loop processes. The importance of including RG evolutions is thus expected to be strongest in models with a large primary branching fraction $BR_{t\bar{t}} \sim 1$. One such illustrative model is given by `BHW-mass`, as defined in Tab. 4 in App. B. All electroweakinos are close in mass and the LSP has more than 5% admixture from bino, wino and Higgsinos while $t_\beta = 2.2$ is relatively small enhancing the MSSM top-quark coupling. The total Sommerfeld-enhanced DM annihilation cross-section with complete one-loop running couplings is $2.4 \times 10^{-27}\mathrm{cm}^3/\mathrm{s}$ at a typical late-time DM velocity $\mathrm{v} = 0.002$. It is almost evenly split between four primary final state channels: W^+W^- (29%), H^0Z (23%), $t\bar{t}$ (21%) and A^0H^0 (20%). Excluding RG evolution of any couplings, the total annihilation cross-section would be larger by 12%, which is driven by a reduction of the W^+W^--channel by about -10% from RG evolution to the hard scale, itself entirely dominated by running of the gauge couplings, and a reduction of the $t\bar{t}$-channel by -29%. As predicted, the latter is primarily affected by inclusion of running Yukawa couplings (-23%) and less so by only the running of the gauge couplings. These values are nicely in agreement with, for example, the estimated dependence of a s-channel Z-boson interaction $\chi_1^0\chi_1^0 \to Z \to t\bar{t}$. Both $\hat{\alpha}_{1,2}$ and $\hat{y}_t^2$ enter the cross section linearly and the strength of the running can be approximately read from Fig. 4.3 around $\hat{\mu} = 2\,\mathrm{TeV}$.

In order to reach percent-level precision on annihilation cross-sections and thereby relic abundances, RG evolution must be respected. Branching ratios into primary $b\bar{b}$ can be even more strongly affected, $\geq 30\%$. However, for a large set of experimentally viable models, annihilation into primary W^+W^- pairs dominates the cross section [107] and the impact of running couplings, specifically Yukawa couplings, on the total cross section is correspondingly smaller. Moreover, from analyzing all benchmarks listed in App. B, this is found to be predominantly the case for experimentally viable models near the Sommerfeld resonance such that when the SE leads to dramatic enhancements, often times one-loop running of the electroweak gauge couplings might suffice for achieving a reliable relic abundance. In total, previous results in the literature for viable MSSM DM regions in parameter space are not expected to be strongly affected. Nevertheless, indirect detection bounds from on high-energetic cosmic-ray observations of a particular particle species, *e.g.* bottom quarks, depend on the respective branching ratio and are thus directly affected.

Coupling strengths evolved to the high scale $\hat{\alpha}(2M_{\mathrm{LSP}})$ only enter the hard annihilation vertex while the potential ladder exchanges remain unaffected. Importantly, this means that the contours shown in Fig. 4.2, and crucially the location and strength of the Sommerfeld resonance, are not expected to change as an effect of RG evolutions. An analogous scan of the depicted parameter space of Higgsino-wino mixed models using improved numerical SM input values from Tab. 1 confirmed this expectation. The combination of Yukawa running and updated inputs give rise to a minor change in the exact location of the experimentally observed relic density contour. The result is included in Fig. 4.2. Both panels are taken from [107], however the right panel is modified to include a second, darker green band for the region where the thermal relic abundance matches to the experimentally observed DM energy density, $\Omega_{\mathrm{DM}}h^2 = 0.120 \pm 0.003$. The targeted relic density value differs from 0.1188 used in [107], however, this choice is unnoticeable for the depicted band widths. Overall, the thermal mass contour shifts to smaller M_2 by roughly 60 GeV. In the wino-like region, $M_2 \gg M_{\tilde{H}}$, this translates to a relative mass shift of about -2% and in the mixed Higgsino-wino region, $M_2 \approx M_{\tilde{H}}$, of about -4%. The relative mass shifts are similar when comparing perturbative relic density contours where no SE is included in the calculation. The dominant annihilation branching fractions, regarding the primary final states, at late times are in both cases W^+W^- (65% and 68%) and ZZ (12%), hence predominantly the weak gauge coupling $\hat{\alpha}_2$ is important. From the simple estimate $\Omega_{\text{DM}}h^2 \sim M_{\text{LSP}}/(\sigma \text{v})^{\text{tot}} \sim M^3_{\text{LSP}}/\alpha_2^2$, one finds that a constant relic density requires an agreement between the relative changes in DM mass and the weak gauge coupling strength according to $\Delta_M \sim 2/3 \times \Delta_{\alpha_2}$. From Fig. 4.3, Δ_{α_2} is found to be about -5% (slightly less negative in the degenerate case but slightly more for s-channel processes where the coupling would be evaluated at $2M_{\text{LSP}}$ rather than M_{LSP}). This agrees nicely with the above found changes in the DM mass, especially when taking into account that, firstly, also the SE sees a minor decrease ($\sim -1\%$) in the degenerate case by virtue of changing M_2 by the mentioned -4% and, secondly, the ZZ channel gains also enhancing contributions from $\hat{\alpha}_1$ while the $t\bar{t}$, channel, which is only notably present in the degenerate case, is fourfold more strongly decreased by the running of its Yukawa coupling than the estimated Δ_{α_2}. Thus, one already expects the reduction by $2/3 \times |\Delta_{\alpha_2}| = 3.3\%$ to be an underestimate for the mixed and an overestimate for the wino-like scenario. In practice, the relic abundance is affected in much more complicated ways from varying branching fractions throughout the thermal evolution and also minor influences from changed LSP admixtures. Such effects are not captured by the above estimate.

The one-loop RGEs for all SM couplings with an automated heavy Higgs decoupling step constitutes one technical improvement to the existing code base used for numerical evaluation in previous analyses. As part of the work performed in the scope of this thesis, the derived one- and two-loop RGE solutions are fully integrated into this code. Furthermore, in preparation of an eventual publication, several practical improvements in regards to ease-of-use and large-scale scanning applications were implemented. Apart from this, the developed RGE solver can be used as a complete, stand-alone module in MATHEMATICA. The implementation of an appropriate treatment of s-channel resonances according to chapter 3 remains one open point with work ongoing at the time of writing of this thesis. The inclusion of resonances will facilitate a major improvement step towards a complete treatment of the neutralino DM parameter space in a unified framework, giving reliable relic density and annihilation cross-section predictions to a percent level of theoretical uncertainty.

5 Sudakov-resummation in neutralino annihilation

This chapter concerns precision computations of indirect detection spectra for mixed neutralino dark matter including resummation of large Sudakov logarithms in PNRDM. In SCET, the large separation of the hard energy scale ($\hat{\mu}_h$) of the order of the annihilating particles mass from the soft scale ($\hat{\mu}_s$) of small transverse momenta gives rise to Sudakov double logarithms which change the naive power counting in the electroweak coupling strengths $\alpha_{1,2}$, as introduced in section 2.4. The power-counting of these large logarithms is taken to be

$$\boxed{L \equiv \log\left(\frac{\hat{\mu}_h}{\hat{\mu}_s}\right) \sim \frac{1}{\lambda} \gg 1.} \tag{5.1}$$

λ is the simultaneous power counting parameter, see Eq. (2.15),

$$\lambda \sim \frac{m_W}{2M_{\mathrm{LSP}}} \sim \alpha_{1,2} \sim \mathrm{v}. \tag{5.2}$$

Since an expansion according to Eq. (2.14) is now non-perturbative, leading and next-to-leading logarithmic terms need to be resummed to all orders to systematically neglect only terms suppressed in λ. The appropriate framework for the combined treatment of Sommerfeld and Sudakov resummation effects is PNRDM, outlined in section 2.5 [82]. Sommerfeld enhancement in the MSSM was discussed in chapter 4 and is accordingly included in the numeric results of section 5.3. The resummation of Sudakov logarithms to NLL accuracy in degenerate models was achieved already in [62]. This chapter completes the framework to arbitrarily mixed models by ensuring all power expansions remain under control throughout the entire MSSM parameter plane.

After laying some groundwork in section 5.1, the necessary modifications to the annihilation matrix allowing to extend it to non-degenerate MSSM models are discussed in section 5.2. Finally, section 5.3 constructs and analyzes a set of benchmark models which probe interesting parts of parameter space for mixed neutralino DM. Familiarity with either [2] or [62] will be assumed in some more technical discussions of section 5.2 to avoid excessive repetitions.

Theoretical foundations may be found in [62, 82] and the derived framework for arbitrarily mixed neutralino DM annihilation has been published under the title “Electroweak resummation of neutralino dark-matter annihilation into high-energy photons” [2].

5.1 Preliminaries

In contrast to the analysis of thermal relic densities, which were in the focus of discussions of chapter 4, now late-time annihilation of DM into observable final states are considered. This changes the physical picture as indiscriminate total annihilation cross-sections are no longer of interest but only concrete final states involving high-energy gamma-rays and, moreover, their spectral distribution near the endpoint.

Concretely, this chapter discusses necessary modifications to the semi-inclusive CP-even s-wave annihilation matrix Γ_{IJ} into high energetic photons $(\gamma + X)$ in fully degenerate models [62] in order to cover arbitrarily mixed neutralino annihilation. The Sommerfeld enhanced annihilation cross-section $(\sigma \mathrm{v})^{\chi\chi\to\gamma X}$ is obtained following Eqn. (4.5) and (4.6), albeit including Sudakov resummation in the hard annihilation coefficients as

$$(\sigma \mathrm{v})^{\chi\chi\to\gamma X} = \sum_{I,J} S_{IJ}\,\Gamma_{IJ}, \tag{5.3}$$

carrying over the explicit summation of two-particle indices I and J from Eq. (4.4), there in form of four single particle indices, which was already written schematically in the (2.16). The respective accuracy to which Sudakov logarithms are being resummed will be denoted as a superscript, $\Gamma^{\text{Tree}} = \Gamma^{\text{Tree,EFT}}$ being the perturbative result in the framework of PNRDM, which is not identical to the exact relativistic result $\Gamma^{\text{Tree,exact}}$. Γ^{NLL} denotes the next-to-leading logarithmic order resummed result generalized to arbitrarily mixed neutralinos which will be derived in section 5.2, while $\Gamma^{\text{NLL,EFT}}$ is adopted from [62] as the result for strictly ultrasoft-degenerate initial states.

The semi-inclusive cross section is integrated over a certain “intermediate” resolution window to describe the endpoint energy bin which is assumed to be of the soft scale, ranging from $2M_{\text{LSP}} - E^{\gamma}_{\text{res}}$ to $2M_{\text{LSP}}$. The EFT is specifically constructed to treat $E^{\gamma}_{\text{res}} \sim m_W$ and is not identical to a narrow (ultrasoft) resolution window [82, 98]. Technically, E^{γ}_{res} is not of further concern for this thesis since its integral is easily resolved at NLL accuracy for intermediate resolutions. Presented numerical analyses set $E^{\gamma}_{\text{res}} = m_W$.

5.1.1 Effective theory framework

The UV-complete Lagrangian remains unchanged from Eq. (4.2), treating a MSSM model hosting a neutralino LSP as a DM candidate with sufficiently split sfermions to not impact SE. The second Higgs doublet is allowed at any scale using the results of chapter 4 and CP-conservation is assumed in the construction of the SCET annihilation operator basis. As a concequence of the latter, the hard annihilation processes of electroweakinos into at least one photon are inelastic 2-to-2 scattering processes of two fermions into bosonic final state and cannot be mediated by sfermions [2, 62]. Hence, sfermions play no role in the hard annihilation processes under investigation in this section and the BSM model reduces to only the electroweakino fields (bino, wino and Higgsinos) and the two-Higgs doublet sector.

From this, the PNRDM Lagrangian can be constructed for neutralino DM in straightforward analogy to the pure wino and pure Higgsino cases [82, 87]. The explicit construction of the PNRDM Lagrangian and the hard annihilation operator basis was demonstrated in [62]. The hard annihilation process is most conveniently written in the electroweak unbroken basis whereas the physical DM abundance consists of the lightest neutralino, a EWSB mass eigenstate. Therefore, the soft function $\mathbf{w}$ in Eq. (2.17) translates between the broken and unbroken bases, a step which, in pure Higgsino or wino models, is almost irritatingly simple due to their limited field content allowing for additional freedom. In mixed models,

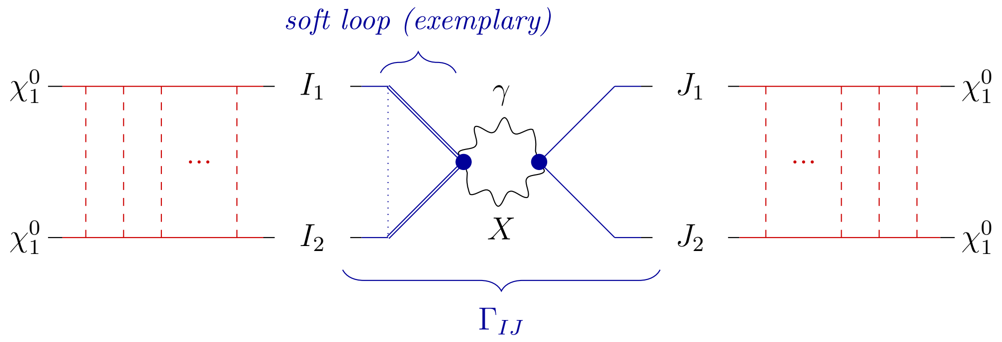

Figure 5.1: Sketch for the annihilation process Eq. (5.4) forward scattering, resolving the short distance 4-fermion vertex Γ_{IJ} for exemplary primary final states γ, X (black). Hard final state radiation connects to soft modes, *cf.* Fig. 3.1, and undergoes soft and collinear splittings (not shown). A single soft loop is depicted (dotted: soft exchange, double-struck lines: internal state which may be heavy). All soft one-loop and certain two-loop exchanges are resummed in Γ^{NLL} [62].

the soft function is to leading order defined simply by neutralino and chargino mixing matrices. The most natural order of EFTs is therefore to compute the annihilation operator basis in the unbroken theory, match onto PNRDM and only then introduce EWSB. This is opposite to the EFT tower used in chapter 4 and the compatibility of both descriptions is discussed in more detail in subsection 5.2.1.

5.1.2 Process overview

Realistic cosmic-ray indirect detection experiments of DM annihilation can only ever observe a single final state of any one annihilation process which renders the correct theoretical observable to be a semi-inclusive process,

$$\chi + \chi \; \to \; \gamma + X. \tag{5.4}$$

Obeying CP, charge and angular momentum conservation, the primary unobserved field in X is constraint to be some unobserved SM gauge boson. These are much lighter than χ, hence the annihilation results in a collimated (back-to-back 2-jet) event morphology, justifying the use of PNRDM. This also means the detected energetic photon γ is itself part of a jet involving multiple secondary soft or collinear particles. An illustration of the complete DM annihilation process is drawn in Fig. 5.1. Unlike the similar Fig. 4.1, the hard 4-fermion annihilation vertex $\hat{f}(^1S_0) = \Gamma_{IJ}$ is now resolved in greater detail. The primary final states γ and X are denoted as wavy lines and one exemplary soft mode exchange between the external legs I is depicted as a dotted line. The notion of "external" is understood in the context of the annihilation matrix Γ_{IJ} and does not refer to the microphysical "initial" state χ_1^0 prior to potential interactions. The "internal" fermions in the soft loop are instead given by double-struck lines indicating that they are not necessarily identical to $I_{1,2}$. Species changes between gauginos and Higgsinos occur only for soft Higgs boson exchanges.

The drawn primary final states source jet events described by resummation of soft and collinear splittings which give rise to Sudakov logarithms. Since this resummation in Γ_{IJ} in Eq. (5.3) combines multiplicatively with the SE, neither can be neglected for accurate predictions of gamma-ray spectra in neutralino DM annihilation. Unlike for freeze-out in the early universe, where all states whose mass splitting is below the current temperature are abundant, in the late-time Universe only DM, $\chi = \chi_1^0$, remains as an initial state to the microphysical process. An important distinction here is that SE remains a microphysical process in terms of the statistical physics of gamma-ray detection where the abundance of χ is treated as a dilute particle gas of only a single species. Nonetheless, scattering into any mass eigenstate by repeated ladder exchanges still gives rise to the need for the full annihilation matrix Γ_{IJ}, thus also $I \neq J$ contribute in the DM annihilation. The annihilation itself is then once again a point-like process relative to long-range potential interactions.

On a technical level, the Sudakov logarithms are resummed by running the hard and jet functions from their natural scales to the soft scale using appropriate RGEs. For simplicity, the hard and soft renormalization scales are chosen explicitly to coincide with their natural scales,

$$\hat{\mu}_h \equiv 2M_{\mathrm{LSP}} \quad \text{and} \quad \hat{\mu}_s = m_W, \tag{5.5}$$

hence their appearance in Eq. (5.2). The freedom of scale choice is attributed to the theoretical uncertainty of the result and was studied already in [62], including also jet and rapidity renormalization scales which are irrelevant to discussions here. As before, the soft scale $\mathcal{O}(m_W)$ simultaneously approximates the gauge boson masses, the electroweak symmetry breaking scale and thereby the onset of relevance of fermion masses, *cf.* Eq. (4.15), and the BSM Higgs doublet is decoupled at m_{A^0}.

5.2 Viability for arbitrarily mixed neutralino models

This section comprises a complete discussion of how the annihilation matrix in arbitrarily mixed neutralino models can be computed, controlling all terms up to corrections of $\mathcal{O}(\lambda)$. All significant issues were known in [62], though not resolved. In particular, the treatment of non-decoupling heavy internal states had been left to future work and will now be dealt with in subsection 5.2.4. Redundancies with [62] are minimized to the extent necessary to provide a solid line of argument.

5.2.1 Ordering of NREFT and EWSB

The present chapter assumes a formally different tower of EFTs than chapter 4 by matching onto PNRDM before introducing EWSB. By taking the non-relativistic limit, certain interactions of the Higgs scalars to the electroweakinos are lost which, however, would give rise to mass terms after EWSB. The concern is that the $\mathcal{O}(M\mathrm{v})$ terms dropped in NREFT, despite being suppressed relative to the *hard* scale, might still give rise to important contributions in EWSB, since they count as the same order, $M\mathrm{v} \sim m_W$. For any self-consistent construction where EFT operators and Wilson coefficients are consistently computed to the same accuracy, the ordering of the NR limit and EWSB may only give rise to higher order corrections which are to be systematically neglected which is to be confirmed. This was proven explicitly for chargino masses in [62] but only by numerical tests for the neutralino sector. A shortcoming which is rectified here.

The two orderings of EFT towers are titled

$$\begin{aligned} \text{“}\textbf{path 1}\text{”:}\quad & \text{full} \;\to\; \text{NR} \;\to\; \text{NR} + \not{\text{EW}}, \\ \text{“}\textbf{path 2}\text{”:}\quad & \text{full} \;\to\; \not{\text{EW}} \;\to\; \text{NR} + \not{\text{EW}}. \end{aligned}$$

For the following, x and X shall respectively denote the neutralino mass eigenvalues in paths 1 and 2 directly after EWSB, meaning the desired identification is $X = x + M_{\text{LSP}}$. Starting from the neutralino mass matrix in path 2 [105], it takes a convenient form under an orthogonal rotation and writing $M_2 - M_1 = \Delta$,

$$\mathbf{M}_N^{(\text{P2})} = \begin{pmatrix} M_2 - c_W^2\Delta & -s_W c_W \Delta & 0 & 0 \\ -s_W c_W \Delta & M_2 - s_W^2 \Delta & \frac{e}{2 s_W c_W} v_+ & \frac{e}{2 s_W c_W} v_- \\ 0 & \frac{e}{2 s_W c_W} v_+ & M_{\tilde{H}} & 0 \\ 0 & \frac{e}{2 s_W c_W} v_- & 0 & -M_{\tilde{H}} \end{pmatrix} \tag{5.6}$$

where $\langle H_\pm^0 \rangle = v_\pm/\sqrt{2}$ and s_W and c_W are the Weinberg angle sine and cosine. This form is useful to compare three of the eigenvalues to path 1 on the level of the characteristic polynomial P_N without evaluating explicit solutions, yet the fourth (negative) eigenvalue must be treated separately. Real fields such as Majorana particles do not permit general unitary rotations but only orthogonal ones and the minus sign cannot simply be absorbed by a complex phase rotation. However, the use of characteristic polynomials comes to rescue where it gives a mere overall sign change insignificant to its roots. Dividing out the negative diagonal entry, the thus reduced characteristic polynomial of $\mathbf{M}_N^{(\text{P2})}$ for eigenvalues X is defined as

$$\bar{P}_N^{(\text{P2})}(X) \equiv \frac{P_N^{(\text{P2})}(X)}{-M_\chi - M_{\tilde{H}} - X} \tag{5.7}$$

$$\begin{aligned} &= (M_{\tilde{H}} - X)\,(M_2 - X)\,(M_2 - \Delta - X) \\ &\quad - \left(M_2 - c_W^2\Delta - X\right) \frac{e^2}{4 s_W^2 c_W^2} \left(v_+^2 - v_-^2 \frac{M_{\tilde{H}} - X}{M_{\tilde{H}} + X} \right) \end{aligned} \tag{5.8}$$

In path 1, the negative eigenvalue found above corresponds to a fully decoupled Higgsino eigenstate [62], which is expected from (5.6) and earlier statements in subsection 4.3.4 that, to leading power, only H_+ appears in NREFT. With

$$\mathbf{M}_N^{(\text{P1})} = \begin{pmatrix} \delta M_2 - c_W^2\Delta & -s_W c_W \Delta & 0 & 0 \\ -s_W c_W \Delta & \delta M_2 - s_W^2 \Delta & \frac{e}{2 s_W c_W} v_+ & 0 \\ 0 & \frac{e}{2 s_W c_W} v_+ & \delta M_{\tilde{H}} & 0 \\ 0 & 0 & 0 & \delta M_{\tilde{H}} \end{pmatrix}, \tag{5.9}$$

where $\delta M_{1,2,\tilde{H}} \equiv M_{1,2,\tilde{H}} - M_{\text{LSP}}$, one finds the reduced characteristic polynomial

$$\begin{aligned}
\bar{P}_N^{(\text{P1})}(x) &\equiv \frac{P_N^{(\text{P1})}(x)}{\delta M_{\tilde{H}} - x} && (5.10)\\
&= \left(\delta M_2 - c_W^2\Delta - x\right)\left[\left(\delta M_2 - s_W^2\Delta - x\right)\left(\delta M_{\tilde{H}} - x\right) - \frac{e^2 v_+^2}{4 s_W^2 c_W^2}\right]\\
&\quad - s_W^2 c_W^2 \Delta^2 (\delta M_{\tilde{H}} - x) && (5.11)\\
&= \bar{P}_N^{(\text{P2})}(x + M_{\text{LSP}}) \;-\; \frac{e^2 v_-^2}{4 s_W^2 c_W^2}\frac{\left(\delta M_{\tilde{H}} - x\right)\left(\delta M_2 - c_W^2\Delta - x\right)}{2M_{\text{LSP}} + \delta M_{\tilde{H}} + x}. && (5.12)
\end{aligned}$$

The last line explicitly extracts the differences to path 2 which are suppressed by one order in m_W/M_{LSP} when counting the mass splittings as $\delta M = \mathcal{O}(m_W/M_{\text{LSP}})$. This proves that for at most near-degenerate masses (*i.e.* soft-scale mass splittings),

$$M_{\chi_i^0}^{(\text{P1})} = M_{\chi_i^0}^{(\text{P2})} + \mathcal{O}\left(\frac{m_W^2}{M_{\text{LSP}}}\right). \tag{5.13}$$

This reasoning does not apply to non-degenerate cases where some $\delta M \gg m_W$, however a straightforward case separation and consistent expansion in $\mathcal{O}(\lambda)$ covers also this shortcoming with unchanged outcome. Moreover, it is manifest in Eq. (5.12) that differences are due to the parity odd combination of the Higgs fields H_-, yet again in agreement with earlier observations that H_- is absent in NREFT to leading order. Since eigenvalues agree up to higher order corrections, also the respective mixing matrices must agree,

$$R_{N,C}^{(\text{P1})} = R_{N,C}^{(\text{P2})} + \mathcal{O}\left(\frac{m_W}{M_{\text{LSP}}}\right) \tag{5.14}$$

where $R_{N,C}$ acts on the vector of neutralinos or charginos. This coincidence of mixing matrices is guaranteed up to some corner cases concerning cancellations, which can be rigorously ruled out by explicit comparison of analytic results, yet expressions are unwieldy and uninsightful and hence omitted. More details on the relations of $R_{N,C}$ in both paths are provided in appendix A of [2]. They are not of further interest here, coinciding with [62] beyond minor improvements to the notation.

The results of this subsection allow to confidently combine S_{IJ} as computed in chapter 4 with Γ_{IJ} computed in its natural tower of EFTs in PNRDM. Any possible mistakes due to using different EFT orderings in different parts of the calculation are power suppressed in λ. Nevertheless, the choice of path is overall not negligible. The SE crucially depends on mass splittings to the point that one-loop mass corrections are to be included [107]. This is due to the kinematic accessibility of coannihilating states as well as the precise position of zero-energy bound state in the spectrum which lead to resonant Sommerfeld enhancement by orders of magnitude. Eq. (5.13) only proves that the hard annihilation matrix agrees to the desired order between both paths, yet it makes no statement about the full Sommerfeld enhanced cross section. It is therefore path 2 which is to be employed to calculate mass splittings in the full relativistic theory without further approximations.

A closer analysis of the characteristic polynomials yields that at most two neutralinos can possibly be degenerate within an ultrasoft splitting at the same time. This is easily understood as one Higgsino decouples completely and the usual see-saw behavior of eigenvalues gives rise to at least one eigenvalue gaining a positive contribution from the VEVs in EWSB. This applies analogously to the two chargino masses and overall at most three degenerate mass eigenstates (two Majorana and one Dirac fermion) exist after EWSB. In pure Higgsino or pure Wino models, these states still encompass the full field content while, generally, they are unspecified mixed states. The lightest state is always a maximally mixed state, that is, the first diagonal "bino-wino" entry $\delta M_2 - c_W^2\Delta$ in Eq. (5.9) which becomes an eigenvalue in the limit $M_1 \to M_2$ is *never* the LSP mass, nor is it the decoupled Higgsino eigenvalue $\delta M_{\tilde{H}}$.

5.2.2 Exact tree-level mass dependence

The leading order mass dependence of Γ_{IJ} as calculated in [64] was included in [62] in its entirety. Definitions and core concepts are repeated here to collect all corrections to Γ_{IJ} in a uniform notation.

The PNRDM annihilation matrix can be improved to include the exact leading order mass dependence of the initial state, valid at any mass splittings, by replacing the sole dimensionful factor $1/(2M_{\text{LSP}})^2$ by a matrix $1/M_{IJ}^2$,

$$M_{IJ}^2 = \frac{1}{2}\left(M_{I_1} + M_{I_2} + M_{J_1} + M_{J_2}\right). \tag{5.15}$$

Note that here the masses are in fact exactly Lagrangian mass terms and no longer non-relativistic approximations of the total energy in the annihilation process. This holds because s-channel annihilation diagrams do not contribute in matching the operator basis for $\gamma + X$ final states. Hence, this description remains correct independently of the physical initial state prior to SE which determines the total center-of-mass energy. The leading order mass dependence can be straightforwardly corrected for by multiplication of Γ_{IJ}^{EFT} with $(2M_{\text{LSP}})^2/M_{IJ}^2$. In addition, the exact relativistic result $\Gamma^{\text{Tree,exact}}$ includes minor corrections from single particle velocities and thereby differs even beyond the leading mass dependence. Although those differences are formally beyond the accuracy of the theory, they tempt numerical evaluations to aim for a better central value within the theoretical uncertainty by including them. On the other hand, $\Gamma_{IJ}^{\text{Tree,exact}} = 0$ in case I or J consist of two neutralinos, rendering this approach inapplicable. Overall, the leading mass dependence may be implemented by an improvement factor

$$\Gamma_{IJ}^{\text{NLL},imp} \equiv \mathcal{G}_{IJ}\,\Gamma_{IJ}^{\text{NLL,EFT}}, \tag{5.16}$$

$$\mathcal{G}_{IJ} \equiv \begin{cases} \frac{(2M_{\text{LSP}})^2}{M_{IJ}^2} & \text{if} \quad \Gamma_{IJ}^{\text{Tree,EFT}} = 0, \\ \frac{\Gamma_{IJ}^{\text{Tree},exact}}{\Gamma_{IJ}^{\text{Tree,EFT}}} & \text{else.} \end{cases} \tag{5.17}$$

The exact annihilation matrix elements are defined by the sum of all exclusive processes into photons [64],

$$\Gamma_{IJ}^{\text{Tree,exact}} \equiv 2\,\Gamma_{IJ}^{I\to\gamma\gamma\to J}({}^1S_0) + \Gamma_{IJ}^{I\to\gamma Z\to J}({}^1S_0), \tag{5.18}$$

accounting for the relative weighing in the $\gamma\gamma$ channel where either photon could be the observed gamma ray. No other $\gamma+X$ final states are accessible at tree level.

5.2.3 Leading order decoupling of non-degenerate states

This section briefly justifies why Eq. (5.3) sums over all neutralino and chargino states irrespective of their mass splitting to the LSP. Clearly, any particles much heavier than χ, $\delta M \gtrsim M_{\mathrm{LSP}}$, should be integrated out of the theory before matching to NREFT in the first place and their impact on physical observables must vanish as the scale separation grows large. The correctness of S_{IJ} when including non-degenerate states in the theory was elaborated on in section 4.2.2. As mentioned, only near-degenerate states are efficiently scattered into under potential interactions, thus, no non-degenerate external states e_i are expected to contribute without already parametrically small suppressions from S_{IJ}. For the annihilation matrix Γ_{IJ}, the observable cross section decouples from heavy states due to mass mixing suppression.

The annihilation operator basis for the hard Wilson coefficients C_k is written in terms of the EW symmetric fields $\tilde{B}$, $\tilde{W}$ and $\tilde{H}$. All annihilation operators are being summed over in the calculation of Γ_{IJ} and the soft function translates between the external mass eigenstates I, J and the annihilation operator basis via the mass mixing matrices, $R_{N,C}$. For strongly non-degenerate states, the mass matrix $\mathbf{M}^{(\mathrm{P1})}$ is dominated by δM and the mixing of such heavy states into states (near-) degenerate to the LSP, $\delta M = \mathcal{O}(m_W)$, is systematically power suppressed. Hence, to leading power in the EFT, short-distance annihilation operators of much heavier external states decouple in tree-level calculations either by suppressed Sommerfeld scattering or suppressed mass mixing in the soft function. For example, a wino-like model with $\delta M_{1,\tilde{H}} \gtrsim M_{\mathrm{LSP}}$ becomes independent of any annihilation operators involving either the Higgsino or bino. Even if paths 1 and 2 are to differ, they differ in systematically sub-leading terms once the Sommerfeld summation picks out only those I and J which are at least near-degenerate to χ. At most, the accuracy of Eq. (5.14) becomes relevant in bino-dominated models where the tree-level result for annihilation into photons naturally vanishes. In this case, any results must be taken with some care as power suppressed corrections may still contribute to the "leading non-vanishing" term. Still, results are never anomalously enhanced by ratios $\delta M/M_{\mathrm{LSP}} \gtrsim 1$.

A caveat of the argumentation in this subsection is its limitation to tree-level processes. Once soft loop diagrams of the hard Wilson coefficients are included in the Sudakov resummation, heavy states contribute unrelated to their mass mixing matrix entries simply by virtue of Higgs-Higgsino-gaugino couplings. This problem is treated in the following subsection.

5.2.4 Treatment of non-decoupling heavy internal states

The decoupling by mass mixing suppression discussed in the previous subsection does not extend to NLL accuracy. Problems arise from soft loop diagrams which are computed in PNRDM, that is under the assumption that propagators are correctly expanded according to the method of regions and δM are systematically neglected in the calculation of UV divergences. To understand the problem in a concrete example, consider the simple case of the bino self-energy, which removes any further complications due to operator mixing. Using x to generally denote the ratio between the internally and external state masses,

$$x \equiv \frac{\textit{internal field mass}}{\textit{external field mass}}\,, \tag{5.19}$$

the UV-pole subtracted full relativistic result of the one-loop bino self-energy in presence of bino-Higgsino-Higgs Yukawa interactions and vanishing Higgs boson masses is

$$\left.\frac{\partial\,\Sigma_{\tilde{B}}}{\partial \not{p}}\right|_{\not{p},\mathrm{IR}} = \frac{\alpha_1 a_+^2}{4\pi}\left(2 + 4x^2 + 4x^4\ln(1-x^{-2})\right), \tag{5.20}$$

where $x = M_{\tilde{H}}/M_1$ and a_+ is defined in Eq. (4.14) to automate the heavy Higgs decoupling step. The self-energy can be approximated in the infinitely heavy, degenerate and massless internal-particle mass limits to

$$\left.\frac{\partial\,\Sigma_{\tilde{B}}}{\partial \not{p}}\right|_{\not{p},\mathrm{IR}} \approx \frac{\alpha_1 a_+^2}{4\pi}\begin{cases} -\frac{4}{3}x^{-2} - x^{-4} & \text{for} \quad x\to\infty, \\ 6 + 4\ln(1-x^{-2}) & \text{for} \quad x\approx 1, \\ 2+4x^2 & \text{for} \quad x\to 0. \end{cases} \tag{5.21}$$

The logarithmic enhanced term evidently vanishes for $x \gg 1$ (here meaning $M_{\tilde{H}} \gg M_1$) which is not reproduced in the strict EFT anomalous dimension matrix calculation where δM are systematically neglected as parametrically small quantities. Note that for near-degenerate mass splittings, $\delta M \sim m_W$, the soft loop is still computed correctly since there is no impact on the ultraviolet behavior yet. Only once $\delta M \gg m_W$, should the soft loop process decouple. The non-decoupling is baked into EFT by assumption and a known danger in dimensional regularization. Little more can be done other than to artificially impose a decoupling condition on loop contributions of heavy internal states once they exit the near-degenerate mass range, using the knowledge of the full result to improve EFT calculation in regions outside the formal regime of validity of near-degenerate states.

Before discussing the specific implementation of the decoupling condition, potentially problematic terms in the hard anomalous dimension matrices [62] need to be identified first. Leading logarithmic terms, the cusp-logarithms, arise exclusively from (anti-)collinear gauge boson interactions which cannot source species changes in the non-relativistic initial state and are therefore unproblematic. At NLL accuracy, all soft one-loop processes need to be included in computing the ultraviolet anomalous dimension for the annihilation operator Wilson coefficients. These involve soft Higgs boson loops in self-energies or triangle diagrams such as the one depicted in Fig. 5.1 which do not dynamically decouple for arbitrarily heavy internal (double struck) lines, as in the considered self-energy example above. One conclusion of [62] was already the identification of non-decoupling in soft Higgs boson loops in self-energy diagrams, however problems in triangle diagrams were overlooked. Gauge boson interactions do not change the species of a given electroweakino state such that external and internal states necessarily coincide and earlier decoupling arguments apply. The only problematic diagrams are soft Higgs boson loops where the internally propagating fermions are much heavier than the external fermions. The problematic terms are thus conveniently traced by a_+. It contributes to the hard anomalous dimension matrices in one of two positions: either on diagonal entries induced by self-energy diagrams of the external state, which do not mix Wilson coefficients of different annihilation operators, or as off-diagonal entries which mix Higgsino-Higgsino annihilation operators with bino-bino, wino-bino and wino-wino annihilation [2, 62] and are sourced by the previously mentioned soft triangle diagrams. Obeying SUSY, the Yukawa interaction between Higgsino and bino or wino fields are respectively given by $g_{1,2}$. Hence, tracking terms proportional to $\alpha_1 a_+^2$ and $\alpha_2 a_+^2$ in the anomalous dimension matrix alongside their position within the matrix unambiguously determines the diagram giving rise to the respective contribution. This will be exploited below to uniquely determine the value of x in every occasion.

With the bookkeeping taken care of, it is time to treat the decoupling implementation itself. Rather than imposing a sharp cutoff, it is desirable to introduce a matching function to smoothly interpolate from 1 to 0, depending on x, without introducing artificial features to parameter space scans. An arc tangent function compactified to a finite interval $]-\infty,\infty[\to]t_1,t_2[$ can obey these conditions and the function

$$f(x) \;=\; \frac{1}{2} - \frac{1}{\pi}\arctan\left[\frac{\pi\, s}{2n}\left(\frac{-1}{|t_1-x|^n} + \frac{1}{|t_2-x|^n}\right)\left|\frac{t_2-t_1}{2}\right|^n\right], \tag{5.22}$$

serves as a convenient tool. It has four free parameters: $t_{1,2}$ to set the interpolation window $[t_1,t_2]$, $s>1$ to set the slope at the mid-point $x=(t_2+t_1)/2$ and $n>1$ to control smoothness of the merging at $x\to t_{1,2}$. Note that not all values of n produce featureless interpolation. Well suited values are found to be $s=1$, $n=2$. For the attempted accuracy a any reasonable choice of f suffices and no attempts at optimization were pursued. The matching window of the interpolation should respect the expected range of validity of the theory, hence $t_1 = 1+2m_W/M_{\mathrm{LSP}}$ is chosen, allowing for a factor 2 variation above the natural soft scale. The upper bound is chosen as $t_2=1.3$ which permits up to 30% non-degeneracy before all effects of heavy states are excluded. Due to the asymptotic behavior of the arctangent, $f(x)<0.1$ is reached already after only three quarters of the matching window, $x(t_2-t_1)-t_1 = 0.76$. Consistency of the ordering $t_1<t_2$ requires $2m_W < 0.3M_{\mathrm{LSP}} \Rightarrow M_{\mathrm{LSP}} > 0.54\,\mathrm{TeV}$, which allows the complete TeV LSP mass range and no additional parameter space restrictions follow from the choice of t_2.

The decoupling is implemented in the annihilation matrix as

$$\Gamma_{IJ}^{\mathrm{NLL}} \;=\; \Gamma_{IJ}^{\mathrm{NLL},imp}\Big|_{a_+^2\to a_+^2\cdot f(x)} \tag{5.23}$$

where x adapts to the respective external and internal masses by the identification procedure outlined above. Note on the aside that [2] implicitly includes the modification (5.23) in $\Gamma_{IJ}^{\mathrm{NLL},imp}$ whereas here the symbol is kept separate from Γ_{IJ}.

This subsection concludes by a brief numerical study to demonstrate the workings of the decoupling in a realistic MSSM model. The dashed curve in Fig. 5.2 shows non-decoupling of a heavy wino, $M_2 - M_{\tilde{H}} \gg m_W$, by comparison to a mixed bino-Higgsino-wino model where $M_2/M_{\tilde{H}}$ is gradually increased (keeping $M_{1,\tilde{H}}$ constant). The benchmark model "BHW-mix" from Tab. 4 in App. B serves as a basis for numerical inputs and the point $M_2 = 4M_1$ estimates the decoupled

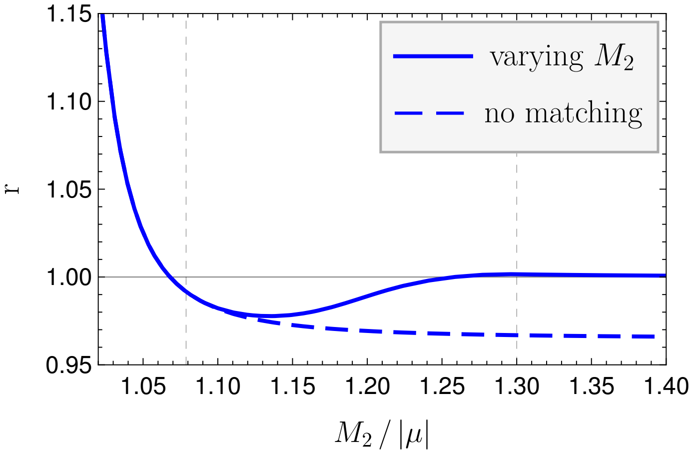

Figure 5.2: Ratios r and $r^{(\text{no-matching})}$ (solid and dashed) of Eqn. (5.24) and (5.25), comparing the diagonal lightest-chargino annihilation matrix element to its heavy-wino limit ($M_2 \approx 4M_1$) by varying M_2. Other parameters coincide with benchmark `BHW-mix` of Tab. 4 in App. B.

scenario. For convenience, the diagonal lightest-chargino pair annihilation entry $\Gamma_{C_1C_1}$ is considered. Concretely, the bold and dashed curves respectively depict the values

$$r(x) = \frac{\Gamma^{\text{NLL}}_{C_1C_1}}{\Gamma^{\text{NLL}}_{C_1C_1}\big|_{M_2=4M_1}} \tag{5.24}$$

and

$$r^{(no\ matching)}(x) = \frac{\Gamma^{\text{NLL},imp}_{C_1C_1}}{\Gamma^{\text{NLL}}_{C_1C_1}\big|_{M_2=4M_1}} = \frac{\Gamma^{\text{NLL}}_{C_1C_1}\big|_{f(x)=1}}{\Gamma^{\text{NLL}}_{C_1C_1}\big|_{M_2=4M_1}}\,. \tag{5.25}$$

The non-decoupling yields around $\sim 5\%$ difference (dashed line) at large $M_2/|\mu|$ and remains stable. $t_{1,2}$ are indicated by vertical lines and the desired smooth behavior of $f(x)$ is apparent. The decoupled value is already reached within 1% for $x = 1.2$ which translates to a mass splitting of 400 GeV. The impact of the decoupling can appear much more dramatic in neutralino channels, however this is artificial as neutralino annihilation lacks a tree-level leading order contribution. Note that due to the adaptive nature of x to each respective diagram contribution, not all channels are affected equally. This becomes especially intricate for stacked non-degeneracies such as $M_{\tilde{H}} - M_2 \sim M_2 - M_1 \sim 3m_W$. The wino may still be efficiently scattered into and the anomalous dimension matrix has not fully decoupled soft Higgsino loop contributions for external wino channels but does already decouple soft Higgsinos loops when the external state is a bino.

5.2.5 Logarithmic mass corrections

Finally, the approximation $M_{1,2,\tilde{H}} \approx M_{\text{LSP}}$ in the cusp-logarithms present in the anomalous dimensions are of concern for the accuracy of the obtained results. The detailed mass dependence in case of non-degenerate and near-degenerate mass splittings was already studied in [62] finding the approximation to remain in both cases to remain unproblematic. Suffice here to say that differences between the full kinematic dependence are always power suppressed, $\mathcal{O}(m_W/M_{\text{LSP}})$, as a consequence of having either only small, soft scale corrections in the logarithm arguments or, otherwise, being suppressed in the mass mixing, see section 5.2.3.

In total, this section derived how the NLL resummed annihilation cross-section computed in PNRDM, $\Gamma^{\text{NLL,EFT}}$ can be extended to arbitrarily mixed neutralino models in a controlled fashion by implementing leading order mass corrections in Eq. (5.16) and a manually imposed decoupling function in Eq. (5.23). Furthermore the analytic proof for the commutation of EWSB and (P)NREFT matching for neutralino mass eigenvalues, and consequently their mixing matrices, allows to confidently follow path 2 in calculations of the Sommerfeld enhancement and Sudakov resummation.

5.3 Phenomenological analysis

The corrections discussed in this chapter complete the framework for computations of neutralino annihilation spectra near the endpoint. This allows to study accurate theoretical predictions in entire neutralino LSP parameter space of interest as long as sfermions are sufficiently heavy to decouple from the theory. SM input values as well as the running couplings required to resum Sudakov logarithms were already discussed in chapter 4. The resummation procedure itself was investigated in [62], see also [82]. This section focuses on the available parameter space, sampling regions of interest [49, 91, 123] by a set of benchmarks, and on phenomenological constraints from indirect detection of cosmic high energy gamma rays.

5.3.1 Reduced MSSM parameter space

The parameter space of interest can be broken down a set of 5 central free parameters defining the electroweakino masses and the BSM Higgs sector.

Γ_{IJ} was calculated in a CP-preserving and flavor-diagonal MSSM model where, additionally, contributions of sfermions are negligible for Sommerfeld enhancement and Sudakov resummation. Sfermions only impact the one-loop mass corrections to neutralinos and charginos and the total annihilation cross-sections required in the computation of the thermal relic density [107]. For simplicity, all sfermion masses are set to a common value $M_{sf} > 2M_{\text{LSP}}$, in most models $M_{sf} > 4M_{\text{LSP}}$. The gluino mass is fixed at $M_{\tilde{G}} = 30\,\text{TeV}$ (correcting on a typo in [2] stating $30\,\text{GeV}$), yet it is irrelevant for computations here. No justifications for the presence of such scale hierarchies within the MSSM are regarded, taking a merely practical standpoint to reduce phenomenological complexity as far as possible. Since the theoretical calculation for the anomalous dimension in PNRDM is not available via automated tools for the full MSSM, such a reduction of the field and operator bases is mandatory to maintain a practical scope of the project. Combined with the required alignment limit in the Higgs sector, $m_h \approx 124 \pm 5\,\text{GeV}$ allowing some variation due to expected theoretical uncertainties in the mass from higher loop corrections, the vast number of over one hundred free parameters of the full

MSSM reduces to only 5 BSM parameter plus the almost irrelevant scale M_{sf}. The remaining free parameters of interest for neutralino DM models are

$$M_1\,,\ M_2\,,\ \mu\,,\ m_{A^0}\,,\ \tan(\beta). \tag{5.26}$$

Of primary importance are the electroweakino masses $M_{1,2}$ and μ, the latter of which is allowed to become negative, for they determine the DM mass scale roughly as

$$M_\chi = M_{\text{LSP}} \approx \min\{M_1, M_2, |\mu|\} + \mathcal{O}(m_W). \tag{5.27}$$

m_{A^0} sets the scale of the extended Higgs sector by virtue of being the lightest BSM Higgs boson mass. Collider searches exclude values close to the electroweak scale $m_{A^0} < 400\,\text{GeV}$ [43], yet $m_{A^0} < M_{\text{LSP}}$ remains permitted. Since the automated decoupling of the heavy Higgs doublet is an interesting feature of the derived Sudakov resummation and the running couplings of section 4.5, models with $m_{A^0} < 2M_{\text{LSP}}$ will be distinctly denoted. Experimental constraints were checked for each model individually. The main phenomenological effects of having an energy range with two dynamical Higgs doublets are additional annihilation channels during freeze-out thus primarily reducing the found relic density when keeping all other parameters fixed. The VEV ratio $\tan(\beta)$ determines the remaining freedom in the Higgs sector. It enters in the neutralino mass mixing matrix and also the RG evolution of the running couplings when $m_{A^0} < 2M_{\text{LSP}}$. However, its primary phenomenological impact comes from changing the interaction strengths of up- or down-type SM fermions to BSM Higgs bosons which has important consequences for direct detection and collider constraints. Values of $\tan(\beta) < 1$ are long excluded already by LEP data up to very large values of m_{A^0} [124]. For the analysis here only $\tan(\beta) \leq 20$ are regarded and the photon resolution is chosen as $E^\gamma_{\text{res}} = m_W = 80.385\,\text{GeV}$.

To best make use of the gained theoretical accuracy in mixed models, at least two of the electroweakino masses should be degenerate within $\mathcal{O}(m_W)$. Additionally, bino and wino do not mix directly but only via their interactions with the Higgsinos, hence, models with $M_{\tilde{H}} \gg M_1 \approx M_2$ are seemingly in a coannihilation scenario but do not possess sizable interaction with each other. On the other hand, direct detection rules out essentially any model of $\mu > 0$ where Higgsino and Wino fields strongly mix into a mass eigenstate in the range $\mathcal{O}(100\text{GeV} - 10\text{TeV})$. For $\mu < 0$, the spin-independent nucleon scattering cross-section decreases and some level of mixing may be present without causing tensions to experimental data [91, 125].

While collider searches are only starting to probe into the TeV range and direct detection loses out on sensitivity at small cross sections such as bino-dominated models or also at large masses [39, 123, 126, 127], indirect detection promises to probe large parts of the wino-bino mixed parameter space. That said the minimalistic pure-Higgsino region around 1 TeV remains out of reach even for upcoming experimental sensitivities of direct and indirect detection [125].

For SM inputs, the values listed in Tab. 1 were used in the numerical analysis. BSM parameters derived from the set of inputs above (masses for Higgs bosons, neutralinos, charginos and sfermions and their respective mixing matrices) were obtained by generating SLHA2 cards [128] for each investigated model by use of the Mathematica release of FEYNHIGGS [120] (version 2.14.4) with the respective numerical input values tabulated in App. B. Even though one loop corrections to the neutralino and chargino masses, which are crucial to obtain accurate SE results, are included, the mixing matrices are directly taken from the SLHA card for all subsequent steps. This latter aspect is a minor source of conceptual conflict, since heavy states are manually decoupled in Γ_{IJ} as described in subsection 5.2.4 while their contributions via (suppressed) mass mixing effects remains ever present. As was shown above, this effect is consistently power suppressed and its impact is correspondingly expected to be less than the claimed accuracy. A designated numerical confirmation was, however, omitted.

5.3.2 Selected benchmark models

Disregarding effects of the chosen M_{sf}, the remaining 5-dimensional parameter space is still not easily scanned without constructing efficient sampling and evaluation methods beyond the scope of this thesis. Instead the expected effects of the logarithmic resummation shall be demonstrated by a set of selected benchmark models which primarily illuminate two aspects. Firstly, they should cover all relevant corners of the parameter space such as generic pure Higgsino or Wino models and secondly they are to probe the relevant cases of mixed neutralino DM which currently evade experimental constraints from collider measurements and direct detection searches. The results of the Higgsino- and wino-like models also served as a check of the implementation and have been confirmed by comparison to existing results [82, 87].

The set of benchmark models studied in this thesis was originally constructed in the scope of [2]. In that work, most MSSM models were tuned to produce DM relic density of $\Omega_{\mathrm{DM}}h^2 = 0.1187$ within sub-percent variations. However, the present analysis uses an updated evaluation based on the SM input parameters and running couplings found in chapter 4, see Tab. 1, and the previously tuned benchmarks now yield thermal relic densities of $\Omega_{\mathrm{DM}}h^2 = 0.128 \pm 0.004$. This corresponds to a 3% interval around a +10% deviation from the experimentally found ΛCDM value. Models marked by an asterisk (`B`, `BW-coan`, `H+`) were not tuned and do not target the experimental relic density value.

Although most considered models now exceed the quoted uncertainty band of the experimental relic density value, the selection of benchmarks merely serves to highlight qualitative features in the parameter space and a minor mismatch is thus acceptable. Furthermore, each selected benchmark was confirmed to evade tensions with experimental collider or direct detection experiments by use of the public tool micrOMEGAs (version 5.2.7.a) [129]. A perturbative analysis of the relic density neglecting SE as well as running couplings done in the scope of [2] found agreement with results from micrOMEGAs. Differences resided within 2% for most models and $\mathcal{O}(10\%)$ in models with significant contributions from the $t\bar{t}$ annihilation channel. The latter is caused by running coupling effects of the top-quark mass in micrOMEGAs.

The complete set BSM input parameters for the chosen benchmarks are given in appendix B and the numerical results of interest are given in Tab. 3 which lists the name, LSP and lightest-chargino mass value in the first three columns. The forth column is the result for the NLL resummed semi-inclusive annihilation cross-section into photons according to (5.3), (4.6) and (5.23) and the fifth col-

model	M_{LSP} [GeV]	$M_{\chi_1^\pm}$ [GeV]	$\langle\sigma \mathrm{v}\rangle_{\gamma X}^{\mathrm{SE+NLL}}$ [$\mathrm{cm}^3\mathrm{s}^{-1}$]	$\frac{\langle\sigma \mathrm{v}\rangle_{\gamma X}^{\mathrm{SE+NLL}}}{\langle\sigma \mathrm{v}\rangle_{\gamma X}^{\mathrm{SE}}}$	$\frac{\langle\sigma \mathrm{v}\rangle_{\mathrm{tot}}^{\mathrm{SE}}}{\langle\sigma \mathrm{v}\rangle_{\mathrm{tot}}^{\mathrm{LO}}}$
pure models					
*B	2144.9	6997.4	$4.00 \cdot 10^{-36}$	$\mathbf{2.05 \cdot 10^5}$	1.03
H	1111.6	1112.4	$1.47 \cdot 10^{-28}$	**0.81**	1.57
W	2849.5	2849.6	$7.38 \cdot 10^{-26}$	**0.61**	78.1
doubly mixed					
BH	1065.3	1069.8	$7.16 \cdot 10^{-29}$	**1.10**	1.29
BW	2141.7	2143.8	$1.46 \cdot 10^{-27}$	**0.65**	5.34
HW	2830.9	2831.1	$2.24 \cdot 10^{-25}$	**0.59**	281
fully mixed					
BHW-mix	1916.1	1922.0	$1.12 \cdot 10^{-28}$	**0.65**	2.11
BHW-mix2	1966.0	1971.3	$1.65 \cdot 10^{-28}$	**0.64**	2.35
BHW-mass	1621.1	1632.4	$1.62 \cdot 10^{-29}$	**0.70**	1.40
BHW-nh2	1797.1	1808.5	$2.97 \cdot 10^{-29}$	**0.66**	1.63
additional					
*BW-coan	2144.9	2147.6	$2.64 \cdot 10^{-31}$	**0.65**	1.16
*H+	1111.4	1112.2	$1.50 \cdot 10^{-28}$	**0.80**	1.58
H2	1236.5	1238.9	$1.02 \cdot 10^{-28}$	**0.77**	1.48
BW-2520	2516.4	2516.9	$1.50 \cdot 10^{-25}$	**0.62**	189
BW-e	1825.7	1830.5	$1.76 \cdot 10^{-28}$	**0.68**	2.26
BW-e-nh2	2054.0	2056.1	$1.81 \cdot 10^{-28}$	**0.65**	3.57
HW-nh2	2912.2	2912.4	$1.28 \cdot 10^{-25}$	**0.57**	174
BH-undet	1296.1	1316.0	$3.13 \cdot 10^{-30}$	**0.83**	1.16
BW-nfw	2073.6	2075.7	$3.72 \cdot 10^{-28}$	**0.65**	4.10
BW-ce	2284.8	2285.7	$7.24 \cdot 10^{-27}$	**0.64**	15.6
BW-2670	2663.0	2664.0	$3.94 \cdot 10^{-26}$	**0.59**	58.5
BW-nh2	2436.0	2436.7	$3.38 \cdot 10^{-26}$	**0.63**	43.6
BW-ce-nh2	2162.9	2164.1	$3.50 \cdot 10^{-27}$	**0.64**	9.60

Table 3: Names of the benchmark MSSM models from Tab. 4 in App. B together with the respective lightest neutral and charged superpartner masses, $M_{\mathrm{LSP}} = M_{\chi_1^0}$ and $M_{\chi_1^\pm}$, the semi-inclusive annihilation cross-section into photons $\langle\sigma \mathrm{v}\rangle_{\gamma X}^{\mathrm{SE+NLL}}$, the correction factor relative to the result neglecting Sudakov resummation (bold-font column) and the Sommerfeld factor to the total annihilation cross-section. Results are computed for a relative velocity $\mathrm{v} = 2 \times 10^{-3}$.

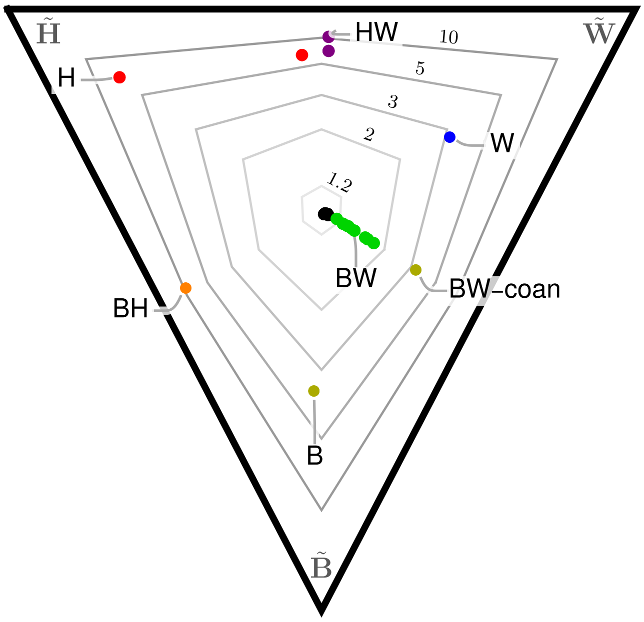

Figure 5.3: Projection of the selected benchmarks of Tab. 4 in App. B onto a two-dimensional plane of normalized inverse mass differences according to Eqn. (5.28) and (5.29). Contours connect points of constant mass ratios $(1.2, 2, 3, 5, 10)$ according to Eq. (5.30). The coloring indicates LSP admixtures larger than 5%, coincident with Fig. 5.4.

umn extracts only the modification factor obtained by including the $\Gamma_{IJ}^{\mathrm{NLL}}$ instead of $\Gamma_{IJ}^{\mathrm{Tree}}$. Hence, it is the primary indicator for phenomenological importance of specifically Sudakov resummation. Lastly, the Sommerfeld enhancement on the total annihilation cross-section is given in the final column, serving as an indicator for the relative strength of the SE.

In all cases, the fist part of the names and the colorings in Figs. 5.3 and 5.4 are chosen to indicate which of the bino (`B`), the Higgsino (`H`) or wino (`W`) contribute more than 5% of the LSP mass eigenstate. All models for which $m_{A^0} < 2M_{\mathrm{LSP}}$ and hence the regime $n_H = 2$ becomes relevant in the running are denoted by a suffix `nh2`. The benchmarks carefully avoid s-channel resonances between Higgs bosons and any pair of neutralinos and/or charginos.

Before turning to the phenomenological analysis in subsection 5.3.3, the intent of the most prominent benchmark models is discussed. For ease of reference and accessibility, Fig. 5.3 projects each benchmark into a 2-dimensional plane according to the electroweakino masses to intuitively show expected LSP admixtures and phenomenologically similar behavior. The horizontal and vertical positions of each point are calculated from $M_{1,2,\tilde{H}}$:

$$\text{horizontal:}\quad \frac{1}{3} \times \frac{M_2^{-1} - \delta M_{\tilde{H}}^{-1}}{\left(M_1^{-1} + M_2^{-1} + \delta M_{\tilde{H}}^{-1}\right)}\,, \tag{5.28}$$

$$\text{vertical:}\quad \frac{-1}{2\sqrt{3}} \times \frac{M_1^{-1} - M_2^{-1} - \delta M_{\tilde{H}}^{-1}}{M_1^{-1} + M_2^{-1} + \delta M_{\tilde{H}}^{-1}}\,. \tag{5.29}$$

These inverse mass ratios have no theoretical motivation but were chosen for representational convenience. Higgsino-, bino- and wino-like models are hereby sorted towards the left, bottom and right corners, respectively, while fully mixed models are sorted towards the center of the plot. Information on the absolute mass scale M_{LSP} gets lost in this representation. To quantify the degeneracy of M_1, M_2 and $\delta M_{\tilde{H}}$, gray contours connect points corresponding to a constant multiplicative difference for between the masses as detailed in the following. Calling the $\mathfrak{m}_{1,2,3}$ the lightest to heaviest mass parameter (which may be degenerate), the six discrete points (kinks) of each gray contour satisfy

$$\text{either} \quad \frac{\mathfrak{m}_2}{\mathfrak{m}_1} = \frac{\mathfrak{m}_3}{\mathfrak{m}_2} = const \quad \text{or} \quad \frac{\mathfrak{m}_3}{\mathfrak{m}_1} = \frac{\mathfrak{m}_3}{\mathfrak{m}_2} = const. \tag{5.30}$$

where the constant values (1.2, 2, 3, 5, 10) are denoted on each line. This means the three points oriented towards the triangle corners satisfy $\mathfrak{m}_2 = \mathfrak{m}_3$ (pure-like model) while their mid-points satisfy $\mathfrak{m}_1 = \mathfrak{m}_2$ (two-degeneracy).

The set of pure models `B`, `H` and `W` is nicely oriented towards the outer corners, indicating that two masses are non-degenerate. Analogously, doubly mixed models `BH`, `HW` lie near the outer edge mid-points indicating that only one mass is non-degenerate. Benchmark `W` may give an impression of being significantly more degenerate than the other pure models, yet it still has M_2 split to both the Higgsino and bino by almost a factor 3 and, in absolute value, is split by more than 5 TeV, almost the same as for `H`.

The model `BW` is degenerate within 40% of the LSP since it was constructed to be of phenomenological interest, which requires the Higgsino to not be fully decoupled or else there is no mixing between wino and bino fields. Instead, `BW-coan` uses all-identical input values except for $\mu = 7\,\mathrm{TeV}$ in place of 2.91 TeV, giving a properly non-degenerate Higgsino in that model. `BW-coan` does not produce the correct relic density, as indicated by the asterisk in Tab. 3, to fully isolate the effect of changing $\mu = 1.36 M_{\mathrm{LSP}} = M_{\mathrm{LSP}} + 9.6 m_W$ to $\mu = 3.26 M_{\mathrm{LSP}}$. Both cases would traditionally be considered decoupled and the mass splitting is far above the soft scale m_W, yet the phenomenology is quite different and for `BW-coan` a decoupled scenario is found where indirect detection signals are near 4 orders of magnitude smaller than for `BW`, see Tab. 3. This behavior is caused by the bino being the LSP, $M_1 = M_2 - 3\,\mathrm{GeV}$. Since it is assumed that exclusively the LSP is present as DM in the late Universe, the annihilation cross-section strongly decreases according to the suppressed mixing into the wino or suppressed by higher powers in the large Higgsino mass. Even slight, per-mille level changes in M_2 can tip the scales to have a wino-dominated LSP with a drastically different phenomenology. In the representation of Fig. 5.3 such models are indeed distinctly separated. `BW` and `BW-coan` are clearly separated already and a wino-like LSP model would be colored blue rather than yellow.

In a similar fashion, `H+` is identical to `H` up to sign(μ) being positive and the model is hence also not tuned to produce the correct relic abundance nor to obey experimental constraints. The last model not obeying the relic density constraint is `B`, a pure bino model in the TeV range which is far away from its thermal mass and only serves qualitative or illustrative purposes. The additional Higgsino-like and Higgsino-wino mixed benchmarks (`H2` and `HW-nh2`) are visible near `HW`. All other models are bino-wino like (green) or fully mixed (black). Most remaining models are not well distinguishable in the scaling of Fig. 5.3, possibly calling for a logarithmic representation of the degeneracy contours. The various mixed-BW models continuously connect to the fully mixed case simply by reducing $\delta M_{\tilde{H}}$.

Since large simultaneous Higgsino-wino admixtures are under strong constraints and bino-dominated models yield undetectably small annihilation cross-sections into photons, the direction of fully mixed models with rather large $\delta M_{\tilde{H}}$ towards the pure wino case, that is starting from the center going to the right hand side, is of primary interest.

5.3.3 Indirect detection constraints from highly-energetic γ-rays

The semi-inclusive annihilation cross-section into photons near the endpoint, listed in the fourth column of Tab. 3 is plotted in Fig. 5.4 against the LSP mass. The coloring is chosen as for Fig. 5.3, indicating LSP admixtures larger than 5% and the benchmarks `B` and `BW-coan` are outside the vertical plot range due to the vanishing coupling between bino and photons. The points at the lower end of the error bars denotes the NLL resummed result, the upper end shows the result barring Sudakov resummation, that is for $\Gamma^{\text{Tree},imp}$. Hence, the bar length indicates how strongly each respective benchmark is shifted by resummation of Sudakov logarithms, *cf.* column five in Tab. 3. Benchmark `BH` is an exception showing an enhancement of +10% gained from resumming Sudakov logarithms, a known behavior in pure Higgsino models at small masses $\delta M_{\tilde{H}} < 1\,\text{TeV}$ [87]. This enhancing feature arises here at slightly larger masses due to the bino admixture.

The red shaded region (bounded by a dashed line) shows exclusion bounds from null-observations by H.E.S.S. on a 95% confidence level [130] for the more optimistic cuspy NFW profile of the DM halo in the galactic center [48]. An analogous analysis assuming a cored Einasto profile [47] yields a weaker bound by approximately a factor of 2 [130]. The dot-dashed and dotted lines (gray shaded area) show forecasts for exclusion bounds obtained by null-results from the Cherenkov Telescope Array (CTA) for both profiles using the sensitivity to the monochromatic gamma ray lines provided in the ancillary files to [49].

Recently, concern were raised in [38] regarding the correctness of the limits obtained in [130], claiming them to be strongly overestimated due to neglecting diffuse gamma ray background in the detected region surviving the masking procedure and additional effects in certain specific channels. Concretely, according to a reconstruction from externally available experimental information and data, upper limits on W^+W^- annihilation channels should be a factor 8 weaker. However, for $\gamma\gamma$, the estimated modifications are about a factor of 2 and easily exceeded by astrophysical uncertainties such as the choice of DM density profile. Being aware of this unresolved conflict, the bounds of [130] are anyways shown without further modification for one, rather optimistic, NFW DM profile. In a conservative approach respecting [38] and more cored profile choices, almost the entire depicted parameter space remains valid. Note that conventionally provided experimental constraints on photon-photon annihilation cross-sections must be scaled up by a factor 2 to apply to the semi-inclusive $\gamma + X$ cross-sections depicted here.

The importance of indirect detection searches is apparent as the shown limits cut right through the set of bino-wino mixed benchmarks. This also demonstrates the importance of including precise NLL resummed results in order to derive reli-

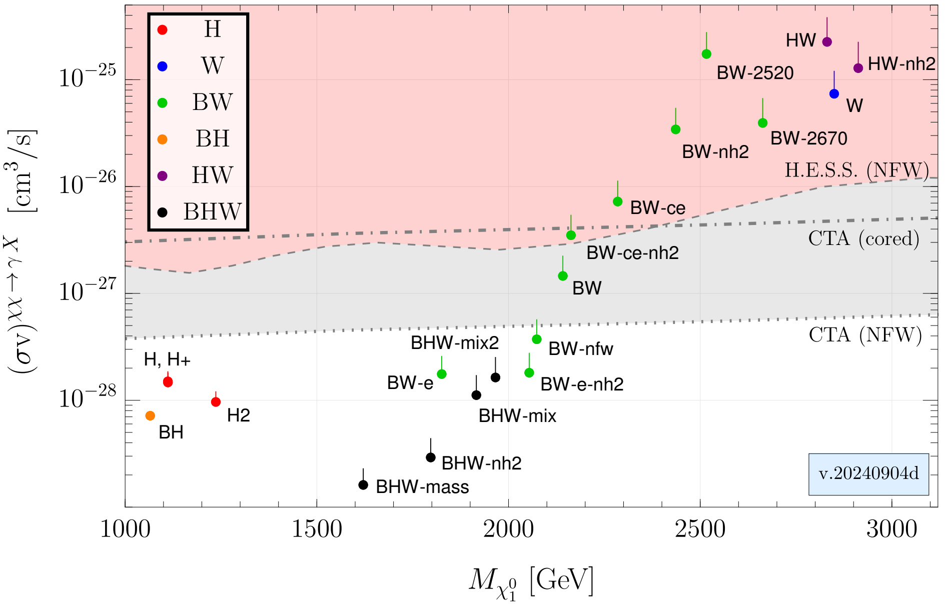

Figure 5.4: $(\sigma v)^{\mathrm{SE+NLL}}_{\gamma X}$ (dots) and Sudakov resummation effect (attached vertical lines) plotted against the LSP mass $M_{\chi_1^0}$ for the benchmarks of Tab. 3. Benchmark names are denoted near each point. The color-coding and naming indicate LSP admixture of at least 5% for any combination of bino "B", Higgsino "H' or wino "W", as listed in the legend. Shaded areas show exclusion limits from H.E.S.S. [130] (red, dashed boundary) and projected exclusions bounds for the CTA experiment [49] (gray, bold boundary), both assuming a NFW profile for the DM density distribution. Bounds weaken by about an order of magnitude for the cored Einasto profile (dot-dashed). Changes from Fig. 2 in [2] are minuscule.

able constraints on the MSSM parameter space. Various models would resign in the experimentally excluded region when neglecting Sudakov resummation whereas the resummed result reduces the tension to experimental data, *cf.* benchmark `BW-nfw`. The relevance of NLL resummation increases towards higher M_{LSP} already simply due to the more pronounced scale ratio $\lambda = m_W/2M_{\mathrm{LSP}}$ and additionally due to the stronger couplings between gauge bosons and the wino caused by $\mathcal{O}(1)$ gauge constants of the adjoint representation [62, 82, 87]. Simultaneously, larger DM masses require a larger annihilation cross-section to produce the correct relic abundance, which can generically be realized by smaller bino and larger wino LSP admixtures. Hence the annihilation cross-section roughly increases with M_{LSP} and so does the wino LSP mixing.

The first pure-wino SE resonance is located near $M_2 = 2.25\,\mathrm{TeV}$ [82, 91], contributing to the enhancement in the cross section for increasing wino admixtures at identical masses. For DM masses beyond 3 TeV, models must sit near a Sommerfeld resonance to have a chance of producing the correct relic abundance by thermal freeze-out. If existent, such models are expected to be in strong tension with current observations. The simplistic s-channel toy model described in section 3.4 indicates that neutralino models around $m_{A^0} \approx 2M_{\mathrm{LSP}} \approx 12\,\mathrm{TeV}$ could also produce the observed DM relic abundance.

As mentioned above, models with suffix `nh2`, primarily differ in their thermal history where the additional annihilation channels help depleting the DM abundance which means they require a slightly larger DM mass to saturate the relic density bound. Hence, those models systematically tend to slightly larger mass values in Fig. 5.4 compared to their rather similar "non-`nh2`" counterparts.

The strength of the corrections from including NLL resummation to the Sommerfeld enhanced tree-level calculation is found to vary between -20% around $M_{\mathrm{LSP}} = 1\,\mathrm{TeV}$ in dominantly Higgsino models up to -43% for $M_{\mathrm{LSP}} \approx 3\,\mathrm{TeV}$ in pure wino or mixed wino-Higgsino models. Overall, as a coarse rule of thumb, it may thus be expected as a reduction by one third across the 1-3 TeV regime of thermal neutralino DM. The effect is roughly in agreement with the findings of [62] of 20 - 60% reduction in the chargino annihilation matrix elements.

By construction, the accuracy of the Sommerfeld-enhanced and NLL-resummed cross section is expected to be of $\mathcal{O}(\lambda) \sim 5\%$, yet no systematic study of theoretical uncertainties has been performed for this analysis. For a discussion relating to results from pure wino and Higgsino models, see [82, 87]. Variation of the resummation scale in the hard function at NLL accuracy were studied in [62]. No large corrections are expected according to these investigations.

Comparing the last two columns in Tab. 3, SE is found to remain the dominant source of corrections to a naive tree-level calculation in most models, nevertheless resummation of Sudakov logarithms can be similarly or even slightly more important in specific parts of the parameter space with strong bino admixture, *cf.* benchmarks `BH`, `BW` or `BHW-mass`, where SE is small.

The presented analysis focused on the gamma-ray line feature near the spectrum endpoint within an intermediate energy resolution of the order of the soft scale m_W and disregarded continuum contributions expecting them to be subleading [131]. Constraints on the MSSM parameter space obtained from analyzing also the continuum spectrum [100, 132] can therefore be less strongly impacted by Sudakov resummation if the diffuse continuum contributes notably to the likelihood statistics.

6 Bound state formation

The main subject of research of this thesis is bound state formation (BSF) by radiative emission of a light mediator where both the non-relativistic initial scattering and final bound state experience separately general Coulomb potentials of strengths α_s and α_b. The scattering state is characterized by its relative velocity v and angular momentum ℓ' and the bound state by the usual major, angular and magnetic quantum numbers, n, ℓ and m. The latter will always be summed over. By physical intuition of effective theories, which is proven to be correct below, one expects interesting physical phenomena to take place when the momenta of initial scattering state is similar to the Bohr momentum of the formed bound state. In this regime, the leading order quantum mechanical matrix elements computed in section 6.2 grows large and partial wave unitarity [89] can become violated on this perturbative level even for small couplings. For a simple parametric estimate, efficient BSF and, in particular, perturbative unitarity violation (UVi) occur when

$$\boxed{\frac{1}{n\mathrm{v}} \sim \frac{1}{\alpha_b} \gg 1.} \tag{6.1}$$

The systematic occurrence of UVi even for perturbative couplings will be proven analytically and shown numerically to arise in any $\alpha_s < \alpha_b$ at low velocities. Other central results are an algorithmic approach to compute BSF radial overlap integrals for arbitrary multipole interactions and general $\alpha_{b,s}$, n, ℓ and ℓ' detailed in App. C.2 and the emergence of eternal depletion in the early universe for non-Abelian gauge theories which conflicts with the simple WIMP paradigm of thermal production.

This chapter constructs the computational framework and treats theoretical problems in the first sections prior to more phenomenological studies in later sections. After some brief introduction, section 6.2 derives the Coulombic BSF cross-section of general multipole interactions, stating explicit solutions up to quadrupole interactions. A semi-classical analogy and approximate quantum mechanical results confirm this full quantum mechanical result in section 6.3. Section 6.4 derives UVi from the computed BSF cross-sections, demonstrating a theoretical problem in BSF processes which remains technically unresolved yet is formally known to be cured by resummation [133]. Relating more directly to DM applications, section 6.5 considers the effect of bound state formation and decay on early Universe dynamics of heavy fundamental SU(N_c) constituents. The simplistic thermal freeze-out paradigm turns out to not be applicable for $N_c > 2$ as no complete chemical decoupling is ever reached. Lastly, for a concrete phenomenological application, section 6.6 numerically investigates a colored and charged t-channel mediator DM model where now also transitions between different bound states are present. Bound state effects source a dependence of the obtained relic densities on the mediator lifetime in contrast to typical superWIMP production. App. C collects many supplementary analytic expressions and App. D includes a detailed functional analysis of the found BSF cross-sections from section 6.2 which is summarized in the main text.

The chapter follows a logical rather than a historical build up, with the earlier sections dominantly consisting of more recent research, core aspects of which are at the time of writing in finalizing stages of a publication under the title “Perturbative unitarity violation in radiative capture transitions to dark matter bound states” [4]. Later phenomenological analyses as well as some of the groundwork of the first sections has been published already as “Excited bound states and their role in dark matter production” [3].

6.1 Overview

Attractive long-range forces between particles can allow for bound state $\mathcal{B}$ in the two-particle spectrum at negative energies relative to the rest mass of two non-interacting particles, $2M_\chi$. Identically heavy particles will be assumed in all later sections, yet a generalization to reduced and total masses is straightforward. Bound states appear in PNREFT as discrete poles on the negative real axis of the complex energy plane $E < 0$, labeled by $n \in \mathbb{N}$, as a consequence of the non-local potential interaction. Poles are only shifted into the negative complex half-plane upon non-perturbative inclusion of a finite decay width in the Hamiltonian. These solutions are absent in NREFT, hence, bound states are an emergent phenomenon in PNREFT from the point of view of perturbation theory.

The exponential term in Yukawa potentials implements a typical range $1/m_\phi$ to the potential and the spectrum of bound states depends on the ratio m_ϕ/M_χ which must be small to yield long range interactions in the first place. The Sommerfeld resonances observed in chapter 4 are indicative of a new bound state solution appearing in the spectrum on-threshold, meaning close to zero binding energy. No such resonances arise in Coulomb potentials,

$$V(r) \;=\; -\frac{\alpha^{\text{eff}}}{r}, \tag{6.2}$$

which are devoid of any inherent dimensionful scale. However, an infinite number of bound state solutions $\mathcal{B}_n$, $n \in \mathbb{N}$, exists independently of M_χ for attractive coupling strengths $\alpha^{\text{eff}} = \alpha_b > 0$. Their Bohr energies are, written only here using the general reduced mass μ for conformity with common expressions,

$$\langle \mathcal{B}_n | \, H \, | \mathcal{B}_n \rangle \;=\; -E_n \;=\; -\,\frac{\mu_{\mathcal{B}} \alpha_b^2}{2n^2} \tag{6.3}$$

with corresponding Bohr momenta and Bohr radii

$$p_n \;=\; \frac{\mu_{\mathcal{B}} \alpha_b}{n} \quad \text{and} \quad r_n \;=\; \frac{n}{p_n}. \tag{6.4}$$

For each eigenenergy, there exist multiple degenerate $\mathcal{B}_{n\ell m}$ of angular momentum $\ell < n$, $\ell \in \mathbb{N}_0$ and magnetic quantum number $m \in \mathbb{Z}$, $-\ell \leq m \leq \ell$.

For this chapter, radiative bound state formation processes

$$\chi_a \,+\, \chi_b = \mathcal{S}_{p\ell'} \;\longrightarrow\; \mathcal{B}_{n\ell m} \,+\, \phi_\omega \tag{6.5}$$

are considered, where the initial state of two non-relativistic constituents $\chi_{a,b}$ is an eigenstate of relative momentum $p = |\vec{p}_a - \vec{p}_b|/2$ and angular momentum ℓ' between the two. Calculating in the center-of-mass frame, the kinetic energy of the initial state is then $K = p^2/2\mu_{\mathcal{S}}$ with the reduced mass $\mu_{\mathcal{S}}$ of $\mathcal{S}$. The final state consists of the bound state $\mathcal{B}_{n\ell m}$ and an emitted mediator of energy ω which is assumed to be a massless scalar ϕ, for simplicity. The generalization to unpolarized processes of gauge boson BSF mediators will be discussed later, see section 6.5. A non-zero BSF mediator mass only gives rise to a simple known factor $\sqrt{1 + m_\phi^2/p_\omega^2}$ in the cross section. A description in PNREFT involves only ultra-soft modes of ϕ which necessitates that the masses of $\mathcal{B}$ and $\mathcal{S}$ are similar, so to leading order $\mu_{\mathcal{S}} \approx \mu_{\mathcal{B}}$. In the following also pairs of (nearly-) degenerate particles are assumed, thus $p = M_\chi \mathrm{v}/2$. Note that $\mathcal{B}$ is constructed as a single-particle state in the Fock-space of two-constituent fields [61], so the process in Eq. (6.5) is indeed a 2-to-2 inelastic scattering process and as such subject to partial wave unitarity conditions which will be considered in section 6.4. The Coulomb potential strengths of $\mathcal{S}$ and $\mathcal{B}$ are not constraint, except for the necessary condition $\alpha_b > 0$, and may differ. For a simple example, one may think of a doubly charged scalar emission via mediator interaction with charged fermions, $\chi^+ + \chi^+ \to \phi^{2+} + \mathcal{B}_{\chi^-\chi^+}$. More commonly, non-Abelian gauge groups give rise to potentials with varying sign, *cf.* section 6.5. Until then, the calculations are performed in the general framework assuming scalar mediators since results translate in a straightforward fashion to gauge bosons as long as the BSF mediator is treated fully inclusively in regards to phase space, polarization and other internal degrees of freedom.

Convenient variables for the process are the ratio of potentials κ and the ratio of two-constituent state momenta ζ_n,

$$\zeta_s \equiv \frac{\alpha_s}{\mathrm{v}}, \tag{6.6}$$

$$\zeta_b \equiv \frac{\alpha_b}{\mathrm{v}}, \tag{6.7}$$

$$\zeta_n \equiv \frac{p_n}{p} = \frac{\alpha_b}{n\mathrm{v}}, \tag{6.8}$$

$$\kappa \equiv \frac{\zeta_s}{n\zeta_n} = \frac{\alpha_s}{\alpha_b}. \tag{6.9}$$

The introduced inverse velocity ζ_s sees widespread usage in the literature. Here, the notation of the corresponding "bound state inverse velocity" $\zeta_b = n\zeta_n = \zeta_1$, which is more clearly identified as the ratio of Bohr and relative momentum, is generalized to include n as a subscript, slightly honing the notation of [3]. Nevertheless, ζ_b becomes useful for inclusive processes where n is being summed over. The second steps of expressing ζ_n and κ employ that the reduced masses must coincide to the considered accuracy. By energy conservation, the radiated energy ω is now

$$\omega = |\vec{p}_\omega| = K + E_n = \frac{M_\chi \mathrm{v}^2}{4}\left(1 + \zeta_n^2\right). \tag{6.10}$$

Neither the angular distribution of the emitted ϕ nor of the initial relative momentum are of interest here, nor would be any possible polarization or other internal degrees of freedom for less minimal mediators. Averaging and summing over these parameters drastically simplifies the calculation of angular overlap integrals later on.

6.2 General radiative Coulombic BSF

This section derives a compact, efficiently evaluated form of the most general LO radiative BSF radial overlap integral in Coulombic potentials. The first subsections define the relevant Lagrangian, the matrix element and re-derive the angular integral. The general radial overlap integral is solved in subsection 6.2.4 and subsequently employed in the BSF cross-section. The result can always be reduced to involve only a single, unique hypergeometric function once specific values for multipole order and angular momentum change are inserted, as outlined in subsection 6.2.5. This reduction to compact closed-form expressions is explicitly performed for maximal angular-momentum changing BSF cross-sections up to quadrupole interactions with results stated and analyzed in the final subsections. Discussions in this section mostly remain technical while a deeper understanding of the physics of BSF will be built in the dedicated section 6.3.

In terms of single field constituent operators, the relevant non-perturbative Lagrangian simply remains in the form of $\mathcal{L}_{\mathrm{PNR}}[\chi]$ in Eq. (2.9) for all constituent fields making up $\mathcal{S}$ and $\mathcal{B}$. However, knowing that only radiative transitions between 2-constituent states, or at most their constituent annihilation captured by local 4-point interactions, are of interest, one may project directly into the two-constituent space. This has the advantages of including only the desired degrees of freedom and directly separating the potentials according to their effective coupling strengths $\alpha_{b,s}$ [134–136]. The Lagrangian describing both two-particle state species, $\mathcal{S}$ and $\mathcal{B}$, in the center-of-mass frame is [75]

$$\begin{aligned}\mathcal{L}_{\mathrm{BSF}} = \quad & \mathcal{S}^\dagger(R,\vec{r})\left(\mathrm{i}\partial^0 + \frac{\vec{\partial}_{\vec{r}}^2}{M_\chi} - \delta M_{\mathcal{S}} + \frac{\alpha_s}{r}\right)\mathcal{S}(R,\vec{r}) \\ & + \mathcal{B}^\dagger(R,\vec{r})\left(\mathrm{i}\partial^0 + \frac{\vec{\partial}_{\vec{r}}^2}{M_\chi} - \delta M_{\mathcal{B}} + \frac{\alpha_b}{r}\right)\mathcal{B}(R,\vec{r}) + \mathcal{L}_{\mathrm{BSF}}^{\mathrm{m.p.}} + \mathcal{L}_{\mathrm{BSF}}^{\mathrm{light}} \end{aligned} \tag{6.11}$$

where integrations in $\mathrm{d}^3\vec{r}$ is dropped, annihilation operators are disregarded and mass splittings are only included for completeness. Spatial derivatives with respect to the center-of-mass (4-vector) coordinate R are suppressed in v in the center-of-mass frame, even compared to a dipole interaction operator. $\mathcal{L}_{\mathrm{BSF}}^{\mathrm{m.p.}}$ includes multipole interactions of $\mathcal{S}$ and $\mathcal{B}$ and all remaining light modes are described in $\mathcal{L}_{\mathrm{BSF}}^{\mathrm{light}}$. The spectrum of two-constituent states $\mathcal{B}$ in (6.11) also includes scattering states $\mathcal{B}_{\vec{p}\ell}$ and, provided $\alpha_s > 0$, that of $\mathcal{S}$ includes bound states $\mathcal{S}_{n\ell m}$, as well. Neither of these are relevant to calculations of this thesis and $\mathcal{S}$ and $\mathcal{B}$ are always considered as scattering and bound states, respectively, in the following. Dropping the scattering and (possible) bound terms in the spectral decomposition of $\mathcal{B}(R,\vec{r})$ and $\mathcal{S}(R,\vec{r})$, respectively, also ensures that all discussions are applicable to the case where only a single species is present, $|\mathcal{S}_n\rangle = |\mathcal{B}_n\rangle$, without any double counting.

6.2.1 Agnostic multipole interaction Lagrangian

This chapter is limited to leading order effects and tree-level processes only and no higher power or loop corrections are considered. The goal is nevertheless to investigate also higher multipole interactions. Limiting the analysis to tree-level strongly reduces the set of relevant interaction operators but also limits the viable processes where tree-level amplitudes of multipole interactions yield the complete leading order scattering matrix element as discussed below.

Even though the heavy, non-relativistic states are conserved in number in (P)NREFT, regarded interactions may induce species changes between $\mathcal{S}$ and $\mathcal{B}$, thus giving rise to BSF. Disregarding multi-field emissions for being additionally suppressed in the multipole coupling strength, interactions contributing at tree-level must be linear in $\mathcal{S}$, $\mathcal{B}$ and ϕ. Furthermore, expanding all occurrences of $\phi(R,r)$ obtained in the PNREFT matching in $r/R \ll 1$, the interactions form a multipole series counted in $a \in \mathbb{N}_0$ with terms

$$\begin{aligned}\mathcal{L}_{\mathrm{BSF}}^{\mathrm{m.p.},\,a} &\equiv g_a^{\mathrm{eff}}\, p_\phi^a\, r^a P_a(\hat{p}_\phi \cdot \hat{r})\; \mathcal{B}^\dagger(R,\vec{r})\, \phi^\dagger(R)\, \mathcal{S}(R,\vec{r}) \\ &= \frac{4\pi}{2a+1} \sum_{\tilde{m}} g_a^{\mathrm{eff}}\, p_\phi^a\, r^a\, Y_{a\tilde{m}}(\hat{p}_\phi)\phi^\dagger(R)\; \mathcal{B}^\dagger(R,\vec{r}) Y_{a\tilde{m}}^*(\hat{r})\, \mathcal{S}(R,\vec{r}).\end{aligned} \tag{6.12}$$

The g_a^{eff} are Wilson coefficients defined by matching and p_ϕ is the momentum operator acting on $\phi(R)$. This expression relates to the more common expansion in Cartesian monomials $(\vec{p}_\phi \cdot \vec{r})^a$ by reverse Legendre polynomials [137]. The given form is general due to the absence of any other 3-vectors in the problem. Note that for spinful mediators this is complicated by mediator polarizations, which are only summed over on cross-section level. The mediator mode is ultrasoft, $p_\phi \sim p\mathrm{v}$, which makes all multipole interactions power suppressed with respect to the kinetic or potential terms by

$$g_a^{\mathrm{eff}}\, \mathrm{v}^a. \tag{6.13}$$

This systematic power suppression in v implies that, when considering a given multipole interaction a, all lower multipoles $a' < a$ and also higher power EFT corrections thereof must be considered carefully in computing the matrix element, see for example [138]. What comes to rescue are familiar angular momentum selection rules, arising in this chapter from Eq. (6.32), according to which each multipole can only induce changes in the angular momentum by

$$\Delta \equiv \ell' - \ell, \tag{6.14}$$

$$-a \leq \Delta \leq a, \tag{6.15}$$

Δ increasing in steps of 2. It follows that in maximal angular momentum transitions, $|\Delta| = a$, any lower multipole insertions $a' < a$ vanish. This holds true since the problem maintains its spherical symmetry even under higher power corrections, hence the quantization in terms spherical harmonic functions remains intact and the angular overlap integral exact. On the basis of this justification, the multipole interactions in Eq. (6.12) for regarded processes are at leading order given by

$$\mathcal{L}_{\mathrm{BSF}}^{\mathrm{m.p.}} \approx \mathcal{L}_{\mathrm{BSF}}^{\mathrm{m.p.},\,|\ell'-\ell|} \tag{6.16}$$

and there can be only one diagram contributing at tree-level. The major quantum number n may still be summed over, which will be studied in section 6.4.3. Furthermore, depending on the process of interest, the initial or final state angular momentum may be summed in both allowed values $\ell' = \ell \pm \Delta$. Summation of both, ℓ and ℓ', is only briefly discussed in App. D.2.

Note that regardless of this argument, $g_a^{\rm eff}$ may vanish in certain configurations at the leading order accuracy in v. Most prominently, a total charge neutral two-constituent state such as $\chi^+\chi^-$ has a vanishing monopole term under U(1) gauge interactions, corresponding to the fact that there is no far field.

6.2.2 Multipole transition matrix element

The cross section for the radiative BSF process in Eq. (6.5), averaged over the incoming momentum direction $\hat{p}$ and summed in the bound state magnetic quantum number m and all internal degrees of freedom of ϕ, denoted as d_ϕ, for distinguishable initial states constituents reads

$$(\sigma \mathrm{v})^a_{p\ell'\to n,\ell} = \frac{(1+\zeta_n^2)\mathrm{v}^2}{2^9\pi^2 M_\chi^2} \times \sum\!\!\!\!\!\!\!\int_{m,\,d_\phi} \frac{\mathrm{d}^2\hat{p}}{4\pi}\mathrm{d}^2\hat{p}_\omega \left|\mathcal{M}^{a,\ell'-\ell}_{p,n\ell m}\right|^2 \tag{6.17}$$

with the leading order scattering matrix element applicable for $|\Delta| = a$

$$\mathrm{i}\,\delta^4(P_{in}-P_{out})\,\mathcal{M}^{a,\Delta}_{p,n\ell m} \equiv \langle \phi_\omega\,, \mathcal{B}_{n\ell m}| \int \mathrm{d}^4 R\,\mathrm{d}^3\vec{r}\;\, \mathrm{i}\mathcal{L}^{\rm m.p.,\,a}_{\rm BSF}\; |\mathcal{S}_{p,\ell+\Delta}\rangle\,. \tag{6.18}$$

The tree-level expression immediately factorizes and ϕ can be contracted with the external state, setting $\vec{p}_\phi = \vec{p}_\omega$. To arrive at the electric multipole operator normalization of $Q_{a\tilde{m}}$ [139] one performs the phase space integral over $\hat{p}_\omega$ but maintains the operator definition such that widespread cross section formulas still apply without further modification except that $\tilde{m}$ is averaged decoherently,

$$\sum_{\tilde{m},\tilde{m}'} \int \mathrm{d}^2\hat{p}_\omega\; \frac{(4\pi)^2}{(2a+1)^2} Y_{a\tilde{m}}(\hat{p}_\omega) Y^*_{a\tilde{m}'}(\hat{p}_\omega) = \int \mathrm{d}^2\hat{p}_\omega\; \frac{\sum_{\tilde{m}}}{2a+1}\bigg|_{\tilde{m}'=\tilde{m}} \sqrt{\frac{4\pi}{2a+1}}^{\,2}\,, \tag{6.19}$$

resulting in

$$(\sigma\mathrm{v})^a_{p\,\ell'\to n\ell} = \frac{g_a^{\rm eff\,2} M_\chi (1+{\zeta_n}^2)\mathrm{v}^2}{8\pi(2a+1)^2} \sum\!\!\!\!\!\!\!\int_{m,\tilde{m}} \frac{\mathrm{d}^2\hat{p}}{4\pi}\mathrm{d}^2\hat{p}_\omega \left| \int \mathrm{d}^3\vec{r}\,\mathcal{B}^*_{n\ell m}(\vec{r}) p^a_\omega r^a Y^*_{a\tilde{m}}(\hat{r}) \mathcal{S}_{\vec{p}\ell'}(\vec{r}) \right|^2. \tag{6.20}$$

Where the two particle state normalizations must be respected when contracting to the external states [61]. The cross section is now given in terms of the well-known and expected matrix element from quantum mechanics $\langle \mathcal{B}_{n\ell m}|\, Q_{a\tilde{m}}\, |\mathcal{S}_{\vec{p},\ell'}\rangle$ using $Q_{a\tilde{m}} = p^a_\omega\, r^a Y_{a\tilde{m}}(\hat{r})$ where $p_\omega = \omega$ is still included to keep mass dimensions constant when considering different multipoles. p_ω can be taken out of the integral and the remaining wave function overlap decomposes in spherical coordinates into separate radial and angular terms. The well-known Coulomb wave functions are

$$\mathcal{B}_{nlm}(\vec{r}), = \mathcal{B}_{nl}(r) Y_{\ell m}(\hat{r}), \tag{6.21}$$

$$\mathcal{S}_{\vec{p},\ell'}(\vec{r}) = \mathcal{S}_{p,\ell'}(r)\, \mathrm{i}^{\ell'} \mathrm{e}^{\mathrm{i}\ell' \arg(\Gamma(1+\ell'-\mathrm{i}\zeta_s))} (2\ell'+1) P_{\ell'}(\hat{r}\cdot\hat{p}) \tag{6.22}$$

with the radial pieces

$$\mathcal{B}_{nl}(r) = \frac{(2p_n)^{\ell+\frac{3}{2}}\, r^{\ell}}{(2\ell+1)!}\sqrt{\frac{(n+\ell)!}{2n(n-l-1)!}}\mathrm{e}^{-p_n r}\,{}_1F_1\left(-n+\ell+1; 2\ell+2; 2p_n r\right), \tag{6.23}$$

$$\mathcal{S}_{p\ell'}(r) = \frac{(2pr)^{\ell'}}{(2\ell'+1)!}\mathrm{e}^{\frac{\pi}{2}\zeta_s}\left|\Gamma(1+\ell'-\mathrm{i}\zeta_s)\right|\mathrm{e}^{\mathrm{i}pr}\,{}_1F_1\left(-\mathrm{i}\zeta_s+\ell'+1; 2\ell'+2; -2\mathrm{i}pr\right). \tag{6.24}$$

$P_{\ell'}$ denotes Legendre polynomials and $Y_{\ell m}$ are the orthonormal spherical harmonic functions evaluated for the polar and azimuth angles of the unit vectors. The usual Sommerfeld factor is encoded in the complex gamma function,

$$\mathrm{e}^{\pi\zeta_s}\left|\Gamma\left(1+\ell'-\mathrm{i}\zeta_s\right)\right|^2 = \frac{2\pi\zeta_s}{1-\mathrm{e}^{-2\pi\zeta_s}}\prod_{j=1}^{\ell'}\left(j^2+\zeta_s^2\right) \equiv (\ell'!)^2\, S_{\ell'}(\zeta_s). \tag{6.25}$$

The separate radial and angular squared overlap integrals are

$$I_R^{a,\Delta} \equiv p_\omega^{2a}\left|\int \mathrm{d}r\, r^{2+a}\, \mathcal{B}^*_{n,\ell}(r)\, \mathcal{S}_{p,\ell+\Delta}(r)\right|^2 \tag{6.26}$$

and

$$I_A^{a,\Delta} \equiv \sum_{m,\tilde{m}} \frac{\int \mathrm{d}^2\hat{p}}{4\pi}\int \mathrm{d}^2\hat{p}_\omega \left|(2\ell+2\Delta+1)\int \mathrm{d}^2\hat{r}\; Y^*_{\ell m}(\hat{r})Y^*_{a\tilde{m}}(\hat{r})\, P_{\ell+\Delta}(\hat{r}\cdot\hat{p})\right|^2. \tag{6.27}$$

The cross section written in terms of these two integrals is simply

$$(\sigma \mathrm{v})^a_{p\,\ell'\to n\ell} = \frac{g_a^{\mathrm{eff}^2} M_\chi (1+{\zeta_n}^2)\mathrm{v}^2}{8\pi(2a+1)^2} \times I_A^{a,\ell'-\ell} \times I_R^{a,\ell'-\ell}. \tag{6.28}$$

The following two subsections repeat the solution to I_A and, as a novelty, discuss in detail how to solve I_R for general processes.

6.2.3 Squared angular overlap integral

The angular integral in Eq. (6.27) is independent of the major quantum number n and the incoming momentum p. Its solution is long-known from the early days of quantum mechanics. The average over the initial momentum direction allows for a particularly simple derivation by multiplying out the absolute square and rewriting the Legendre polynomials as

$$P_{\ell'}(\hat{r}\cdot\hat{p}) \;=\; \sum_{m'}\frac{4\pi}{2\ell'+1}\, Y_{\ell' m'}(\hat{r})\, Y^*_{\ell' m'}(\hat{p}). \tag{6.29}$$

Doing so in both contributions from the absolute square, which are complex conjugates of each other, introduces separate summation indices m' and m''. Similarly, the two integration variables are $\hat{r}$ and $\hat{r}'$. Performing the average over $\hat{p}$,

$$\frac{1}{4\pi}\int \mathrm{d}^2\hat{p}\; Y^*_{\ell' m'}(\hat{p})\, Y_{\ell' m''}(\hat{p}) = \frac{\delta_{m',m''}}{4\pi}, \tag{6.30}$$

cancels one summation. There are now three summations left (m, $\tilde{m}$ and m') and 6 spherical harmonic Y where always two are related by complex conjugation and exchange of the integration variable coordinate $\hat{r} \leftrightarrow \hat{r}'$. Using Eq. (6.29) in reverse to perform each sum yields

$$I_A^{a,\ell'-\ell} = \frac{1}{4\pi}(2a+1)(2\ell+1)(2\ell'+1) \int \mathrm{d}^2\hat{r}\, \mathrm{d}^2\hat{r}'\; P_a(\hat{r}\cdot\hat{r}')\; P_\ell(\hat{r}\cdot\hat{r}')\; P_{\ell'}(\hat{r}\cdot\hat{r}'). \tag{6.31}$$

One of the integrals is now trivial while the remaining integral results in a known solution in terms of a squared three-j symbol,

$$I_A^{a,\ell'-\ell} \;=\; 4\pi(2a+1)(2\ell+1)(2\ell'+1) \begin{pmatrix} a & \ell & \ell' \\ 0 & 0 & 0 \end{pmatrix}^2 . \tag{6.32}$$

The three-j symbol vanishes unless a, ℓ and ℓ' satisfy a triangle inequality $a \leq \ell + \ell'$ and $a \pm \Delta > 0$. The second condition justifies the pursued ansatz to consider tree-level BSF diagrams of only a single multipole interaction as long as $a = |\Delta|$. The former condition poses a bound on the maximal multipole which can contribute, however this is a weak bound in practice as soon as $\ell, \ell' \geq 1$ since interactions beyond quadrupole are rarely ever calculated. The average in $\hat{p}$ is computationally convenient but not necessary to solve the integral [140].

6.2.4 General radial overlap integral

To solve $I_R^{a,\Delta}$, it is convenient to start from a more minimal definition of a mathematical integral problem $J_{p,p_n}^{a,\Delta}$. The technicalities of radial overlap integrals for arbitrary multipole insertions were already solved for electromagnetic interactions, *i.e.* $\kappa = 1$, in [141]. Discussions therein regard BSF, bound-to-bound transitions and bremsstrahlung and take great concerns of mathematical rigor with analyses of convergence conditions, poles and branch cuts in the analytic continuations performed for all different cases. Relying on the thus proven existence of the integrals, most concerns of convergence are ignored for this section. A different route making use of a more general equation, see identity 1. in section 7.622 of [142],

$$\begin{aligned} \int_0^\infty \mathrm{d}t\, \mathrm{e}^{-st}\, t^{(c-1)}\, {}_1F_1(a;c;t)\, {}_1F_1(\alpha;c;\lambda t) \;=\; \\ = \Gamma(c)(s-1)^{-a}(s-\lambda)^{-\alpha} s^{a+\alpha-c}\, {}_2F_1\left(a, \alpha; c; \frac{\lambda}{(s-1)(s-\lambda)}\right), \end{aligned} \tag{6.33}$$

has been employed to solve the quadrupole scenario in the case of $\kappa = 1$ [138], yet no further generalizations in κ or a were considered. With the results of this subsection, arbitrary Coulombic potentials and multipoles can be treated. Furthermore this thesis formulates the problem entirely in spherical coordinates, which are suited to the problem in the absence of any distinguished external axes.

Introducing the abbreviations [141]

$$\bar{n} \equiv n - \ell - 1, \tag{6.34}$$

$$\bar{n}_s^* \equiv -\mathrm{i}\zeta_s - \ell' - 1, \tag{6.35}$$

the starting point of the calculation is the definition

$$J^{a,\Delta}_{p,p_n}(\bar{n}_s,\bar{n},\ell) \equiv \int_0^\infty \mathrm{d}r\, r^{2+a+2\ell+\Delta}\, \mathrm{e}^{-\mathrm{i}pr-p_n r} \\ \times\, {}_1F_1(-\bar{n}_s^*;2\ell+2\Delta+2;2\mathrm{i}pr)\,{}_1F_1(-\bar{n};2l+2;2p_n r). \tag{6.36}$$

This form is more general than the needed case of $\Delta = \pm a$ and the procedure described here is also applicable for radial overlap integrals of arbitrary BSF processes. Before being able to apply the solution (6.33), the integral needs to first be brought into the correct form by two main transformations. From usual hypergeometric relations one finds

$${}_1F_1(a;c+2|\Delta|;x) \;=\; \frac{\Gamma(c+2|\Delta|)}{x^{2|\Delta|}\Gamma(c)}\sum_{j=0}^{2|\Delta|}(-1)^j\binom{2|\Delta|}{j}\,{}_1F_1(a-j;c;x). \tag{6.37}$$

This allows to bring both second parameters of the confluent hypergeometric functions in $J^{a,\Delta}_{p,p_n}$ to the same value. Now, only the polynomial power of r is not in the desired form of Eq. (6.33). This is resolved by introducing an ancillary variable s in the exponential term as $(-\mathrm{i}p-p_n)rs$, thus defining a more general integral $J^{a,\Delta}_{p,p_n}(\bar{n}_s,\bar{n},\ell;s)$ which obeys

$$J^{a,\Delta}_{p}(\bar{n}_s,\bar{n},\ell;1) = J^{a,\Delta}_{p,p_n}(\bar{n}_s,\bar{n},\ell), \tag{6.38}$$

$$\partial_s\, J^{a,\Delta}_{p,p_n}(\bar{n}_s,\bar{n},\ell;s) = -p(\mathrm{i}-\zeta_n)J^{a,\Delta+1}_{p,p_n}(\bar{n}_s,\bar{n},\ell;s). \tag{6.39}$$

The construction allows to trade surplus powers in r for derivatives with respect to s. Note that by having *reduced* the higher of the two hypergeometric functions' second parameters in Eq. (6.37), it is ensured that there will be surplus powers of r rather than a lack of powers of r which could not be absorbed into simple derivatives. As a consequence, the cases $\Delta > 0$ and $\Delta < 0$ work out slightly differently in intermediate results $J^{a,\pm|\Delta|}_{p,p_n}$, yet, ultimately take very similar forms. It is noted in passing that negative powers of r are also one pitfall why this approach may be insufficient for overlap integrals integrals in higher-power EFT insertions, which introduce powers $\sim \vec{\partial}^2 \sim 1/r$ according to leading order equations of motion. Higher order effects were not investigated in any more detail. To arrive at the exact form of Eq. (6.33), one must introduce $1+a-|\Delta| > 0$ differentiations,

$$r^{2+2\ell_m+a-|\Delta|}\mathrm{e}^{-rp(\mathrm{i}+\zeta_n)} \;=\; \frac{(-1)^{1+a-|\Delta|}}{(\mathrm{i}+\zeta_n)^{1+a-|\Delta|}}\;(\partial_s)^{1+a-|\Delta|}\Big|_{s=1}\, r^{2\ell_m+1}\,\mathrm{e}^{-rp(\mathrm{i}+\zeta_n)s} \tag{6.40}$$

where $\ell_m = \min\{\ell,\ell'\} = \ell + (\Delta - |\Delta|)/2$. The simplicity of the case $\Delta = \pm a$ becomes apparent as a minimization of number of differentiations. Before inserting Eq. (6.33), note that it comes with conditions of convergence, $\mathrm{Re}(2\ell+2) > 0$ and $\mathrm{Re}(s(1+\mathrm{i}/\zeta_n)) > 1 + \mathrm{Re}(\mathrm{i}/\zeta_n)$, where s refers to the differentiation variable. The first condition is trivially fulfilled while the latter is consistently violated for any $s < 1$, even when allowing for imaginary momenta. However, for physical values the confluent hypergeometric function in the bound state wave function actually collapses simply to a polynomial, which is assumed to extend the radius of convergence. This is supported by numerical results later on. Hence, bravely disregarding concerns about convergence, the integral solution may be inserted, identifying the integration variable as $t = 2p_n r$. With a convenient redefinition $s \to 1 + s/(\mathrm{i} + \zeta_n)$, the integral yields for $\Delta > 0$

$$\begin{aligned} J^{a,\Delta}_{p,p_n}(\bar{n}_s, \bar{n}, \ell) =& \frac{(-1)^{1+a}}{2^{2\Delta}\, p^{a+2\ell+\Delta+3}} \\ &\times\ (\partial_s)^{1+a-\Delta}\Big|_{s=0} \sum_{j=0}^{2\Delta} (-1)^j \binom{2\Delta}{j} \frac{\Gamma(2\ell+2\Delta+2)}{(s+\zeta_n+i)^{2l+2}} \\ &\times\ \left(\frac{s-\zeta_n+i}{s+\zeta_n+i}\right)^{\bar{n}} \left(\frac{s+\zeta_n-\mathrm{i}}{s+\zeta_n+\mathrm{i}}\right)^{\bar{n}_s^*} \left(\frac{s+\zeta_n-\mathrm{i}}{s+\zeta_n+\mathrm{i}}\right)^{j} \\ &\times\ {}_2F_1\left(-\bar{n}, -\bar{n}_s^* - j; 2\ell+2; \frac{-4i\zeta_n}{(\zeta_n - i)^2 - s^2}\right) \end{aligned} \tag{6.41}$$

and for $\Delta < 0$ (writing the sign explicitly, to prevent any possible confusion)

$$\begin{aligned} J^{a,-|\Delta|}_{p,p_n}(\bar{n}_s, \bar{n}, \ell) =& \frac{\zeta_n^{-2|\Delta|}(-1)^{1-a+|\Delta|}}{2^{2|\Delta|}\, p^{a+3+2\ell-|\Delta|}} \\ &\times\ (\partial_s)^{1+a-|\Delta|}\Big|_{s=0} \sum_{j=0}^{2|\Delta|} (-1)^j \binom{2|\Delta|}{j} \frac{\Gamma(2\ell+2)}{(s+\zeta_n+\mathrm{i})^{2\ell'+2}} \\ &\times\ \left(\frac{s-\zeta_n+\mathrm{i}}{s+\zeta_n+\mathrm{i}}\right)^{\bar{n}} \left(\frac{s+\zeta_n-\mathrm{i}}{s+\zeta_n+\mathrm{i}}\right)^{\bar{n}_s^*} \left(\frac{s-\zeta_n+\mathrm{i}}{s+\zeta_n+\mathrm{i}}\right)^{j} \\ &\times\ {}_2F_1\left(-\bar{n} - j, -\bar{n}_s^*; 2\ell'+2; \frac{-4\mathrm{i}\zeta_n}{(\zeta_n - \mathrm{i})^2 - s^2}\right). \end{aligned} \tag{6.42}$$

Apart from some differences mostly concerning the interchange of $\ell \leftrightarrow \ell'$, the main conceptual difference is that now the *first* argument of the hypergeometric function is being iterated by the summation. Notably, the number of differentiations and also the summation index j are here of order $a = \mathcal{O}(1)$ which is a strong simplification compared to the known results of [140] in terms of at least $n + \ell + 2$ differentiations. The differentiation are easily performed analytically using Eq. (C.9) since all three parameters of the hypergeometric function are independent of s. All other terms are technically straightforward rational polynomials, even though their analytic form becomes cumbersome in practice. An algorithmic prescription to obtain compact analytic results for specified a and Δ is given in App. C.2.

Before moving on to the explicit results of the radial overlap integrals I_R, some especially simple cases are regarded. For later use in analytic treatments, it will be useful to have a better understanding of the most relevant case $\Delta = a$. Evaluating the single remaining derivative, Eq. (6.41) yields

$$\begin{aligned} J^{a,a}_{p,p_n}(\bar{n}_s, \bar{n}, \ell) =& \frac{(-1)^a \mathrm{e}^{-2\zeta_s \mathrm{ArcCot}(\zeta_n)}}{2^{2a-1}\, p^{2a+2\ell+3}} \frac{\Gamma(2\ell+2a+2)}{(\mathrm{i}-\zeta_n)^{2\ell+4}} \\ &\times \sum_{j=0}^{2a} \binom{2a}{j} (-1)^j\, \mathrm{e}^{2\mathrm{i}(a-j-1-n)\mathrm{ArcCot}(\zeta_n)}\, (n\zeta_n - \zeta_s + \mathrm{i}(a-j)) \\ &\times\ {}_2F_1\left(-\bar{n}, -\bar{n}_s^* - j; 2\ell+2; \frac{-4\mathrm{i}\zeta_n}{(\zeta_n - \mathrm{i})^2}\right). \end{aligned} \tag{6.43}$$

Further considering $\ell = n-1 \Leftrightarrow \bar{n} = 0$ trivializes the hypergeometric function, ${}_2F_1(0,b;c;z) = 1$, and leads to the solution

$$J^{a,a}_{p,p_n}(\bar{n}_s, 0, n-1) = \frac{2n\zeta_n}{p^{2n+2a+1}} \frac{\Gamma(2n+2a)}{(1+\zeta_n^2)^{1+a+n}} \left(1 + \frac{a}{n} - \kappa\right) \mathrm{e}^{-2\zeta_s \mathrm{ArcCot}(\zeta_n)}. \tag{6.44}$$

Its simplicity makes the case of maximal $\ell = n-1$, meaning near-circular orbits, theoretically attractive for analytic studies. A curious feature of Eq. (6.44) is that BSF cross-sections will directly proportional to $(1 + a/n - \kappa)^2$. Hence, it predicts cancellations occurring at certain combinations of a, n and rational positive $\kappa > 1$. Specifically, and of most immediate interest, radiative dipole *ground* state formation vanishes at LO in Coulombic systems where the initial state potential is twice as strong as the bound state potential, *i.e.* $\kappa = 2$. This cancellation is not captured by any conventional multipole transition rule. An investigation of possible consequences is beyond the scope of this thesis.

6.2.5 Simplified squared radial overlap integral

The radial overlap (6.26) relates to the integral J by straightforward multiplication of the absolute square,

$$I_R^{a,\ell'-\ell} = \frac{p_\omega^{2a}(2p_n)^{2\ell+3}(2p)^{2\ell'}}{2n} \frac{\Gamma(n+\ell+1)}{\Gamma(2\ell+2)^2\Gamma(2\ell'+2)^2} \frac{\mathrm{e}^{\pi\zeta_s}|\Gamma(\bar{n}_s)|^2}{\Gamma(\bar{n}+1)} \left|J^{a,\Delta}_{p,p_n}(\bar{n}_s,\bar{n},\ell)\right|^2. \tag{6.45}$$

Using Eqn. (6.41) and (6.42), I_R may now be evaluated into a closed form. The consecutive derivatives produce an equal number of different hypergeometric functions according to Eq. (C.9) which can be simplified by repeated use of hypergeometric identities, *cf.* App. C.1.2, following App. C.2. It turns out that (even for general Δ) all hypergeometric functions can be related to only a single one, $F_+(0)$, where

$$F_+(X) \;=\; {}_2F_1\left(-\bar{n},\, X+\ell+\mathrm{i}\zeta_s;\, 2\ell+2;\, \frac{-4\mathrm{i}\zeta_n}{(\mathrm{i}-\zeta_n)^2}\right) \tag{6.46}$$

Introducing the complex phase γ_n,

$$\gamma_n \equiv \arg(\mathrm{i}+\zeta_n) = \mathrm{arccot}(\zeta_n) \;\Leftrightarrow\; \mathrm{e}^{2\mathrm{i}\gamma_n} = \frac{\mathrm{i}+\zeta_n}{\mathrm{i}-\zeta_n} \tag{6.47}$$

one can see the argument of the hypergeometric function is located on a unit circle centered around 1, a critical property in the reduction to $F_+(0)$. Two notable steps in the simplification should be briefly highlighted. First, after arriving at an expression in terms of $F_+(X)$ with $X = 0,1,2$, one makes use of

$$F_+(1) = \frac{1+\zeta_n^2}{2\mathrm{i}\zeta_s} \frac{(1+\ell+\mathrm{i}\zeta_s)\,\mathrm{e}^{2\mathrm{i}\gamma_n}F_+(2) - (1+\ell-\mathrm{i}\zeta_s)\,\mathrm{e}^{-2\mathrm{i}\gamma_n}F_+(0)}{\zeta_n^2 - \left(1-\frac{2}{\kappa}\right)}, \tag{6.48}$$

a simplification which was not implemented in the literature previously [75, 140]. Secondly, $F_+(X)$ obeys

$$F_+(X) = \mathrm{e}^{4\mathrm{i}\gamma_n\bar{n}}F_+^*(2-X). \tag{6.49}$$

At $X = 2$, this mirror property allows to rewrite the radial overlap integral in terms of only $F_+(0)$ and its complex conjugate.

Note that Eq. (6.48) seemingly introduces a nonphysical pole at $\zeta_n^2 = 1 - 2/\kappa$. However, $F_+(X)$ at integer $n, \ell \in \mathbb{N}_0$ are just polynomials of degree $\bar{n}$ in the argument of the hypergeometric function and ζ_s, thus $F_+(1)$ is not divergent and the pole is ensured to be lifted in the numerator. While this is apparent from Eq. (6.48), once the absolute square of the integral $I_R^{a,a}$ is inserted in the BSF cross-section, this mathematically concerted cancellation will become unobvious. Note on the aside, that Eq. (6.48) begins the trend of using redundant notation, including ζ_s and κ simultaneously.

The fully simplified squared radial overlap integral now only depends on

(i) the prefactors inherited from the wave functions according to (6.45), including the Sommerfeld factor,

(ii) the exponential term written in (6.44) which are obtained from the complex fractions in (6.43),

(iii) $F_+(0)$ and its complex conjugate and

(iv) all remaining contributions of ζ_n, n and κ left over after performing the derivatives in the ancillary parameter s and the reduction to $F_+(0)$. These form a well behaved rational polynomial R.

Remarkably, the algorithmic reduction to $F_+(0)$ must hold for any a and Δ and $F_+(0)$ is thus the defining hypergeometric function for any Coulombic radiative multipole BSF at LO. $I_R^{a,\Delta}$ for general a and $\Delta = \pm a$ is therefore given by

$$\begin{aligned} I_R^{a,\pm a} &= \frac{2^{4\ell-2a+5}\mathrm{v}^{2a-3}\zeta_n^{2\ell+3}}{M^3\left(1+\zeta_n^2\right)^{2\ell+4-2a}} \frac{\mathrm{e}^{-4\zeta_s\gamma_n} S_{\ell\pm a}(\zeta_s)\left((\ell\pm a)!\right)^2}{\zeta_s^2} \frac{\Gamma(n+\ell+1)}{n\Gamma(2\ell+2)^2\Gamma(n-\ell)} \\ &\quad\times \frac{\left|1-\mathrm{e}^{2\mathrm{i}(2\gamma_n(n-l)-\gamma_{\pm a}-\gamma_F)}\right|^2}{\left(\zeta_n^2-\left(1-\frac{2}{\kappa}\right)\right)^2} \left|F_+(0)\right|^2 \left|R_{\pm a}\right|^2 \end{aligned} \tag{6.50}$$

where γ_n is defined in Eq. (6.47) and, analogously, γ_F and γ_Δ are the complex phases of $F_+(0)$ and R_Δ. a is not denoted explicitly on R_Δ, but implied by $a = |\Delta|$. The second term in (6.50) involving the Sommerfeld factor $S_{\ell'}$ includes also the usual arc cotangent term $\exp\{-4\zeta_s\gamma_n\}$ which is a known ingredient to BSF cross-sections [141, 143]. The third term arises directly from the wave function normalizations and the second line involves the non-trivial terms obtained from the radial integration and simplification steps. It includes the two absolute squares of the rational polynomials and the defining hypergeometric function as well as a fraction which is, in its entirety, referred to as “phase factor”. The denominator originates from Eq. (6.48) and should not be considered independently. Explicit expressions of R_Δ up to quadrupole interactions are provided in section 6.2.6. The result of Eq. (6.50) is analyzed in more detail in section 6.2.7 and App. D.

The reduction to a single hypergeometric function is a significant simplification and unexpected ab initio. It opens the path to better analytic treatment thanks to more tractable expressions, as well as numerical stability and efficiency. Similar results in terms of a single hypergeometric function are known in the literature for the reduced cases of monopole BSF, $I_R^{0,0}$ [144], or "Abelian" quadrupole BSF, $I_R^{2,\Delta}|_{\kappa=1}$ [138]. The terminology "Abelian" simply refers to identical initial and final state potentials $\kappa = 1$ irrespective of the responsible multipole interaction being a U(1) gauge interaction. Both works found solutions involving only $F_+(1)$ which avoids the issue of the lifted pole but hides the highly oscillatory nature of the final result. Moreover, $F_+(1)$ is insufficient to describe more general BSF as Eqn. (6.48) and (6.49) cannot be inverted to find $F_+(0)$ in terms of $F_+(1)$ without $F_+(2)$. Still two or three hypergeometric functions were used in [75] and none of the known results were applicable to simultaneously general a, Δ and κ. The oscillatory behavior of the BSF cross-section observed already in the literature [3, 140, 144] is for all significant parts entirely manifest in (6.50) from the phase $\gamma_n(n-\ell)$ as long as $\kappa \leq 0$.

6.2.6 Analytic results for Mono-, Di- or Quadrupole interaction

Following the simplification procedure of C.2, the rational polynomials $R_{\pm a}$ in Eq. (6.50) defining the different multipole BSF cross-sections of the monopole, dipole and quadrupole ($a = 0, 1, 2$) operator are obtained as

$$R_0 \equiv n\zeta_n(1-\kappa)(1+\zeta_n^2)(1+\ell-\mathrm{i}\zeta_s), \tag{6.51}$$

$$R_1 \equiv \zeta_s(1+\zeta_n^2) + n\zeta_n(1-\kappa)\left(2+2\mathrm{i}n\zeta_n(1-\kappa)+(1+\zeta_n^2)(\ell+1)\right), \tag{6.52}$$

$$\begin{aligned} R_{-1} \equiv\ & \left[\zeta_s(1+\zeta_n^2) + n\zeta_n(1-\kappa)\left(2+2\mathrm{i}n\zeta_n(1-\kappa)-(1+\zeta_n^2)\,\ell\,\right)\right] \\ & \times (l-\mathrm{i}\zeta_s)\,(1+\ell-\mathrm{i}\zeta_s)\,, \end{aligned} \tag{6.53}$$

$$\begin{aligned} R_2 \equiv\ & \frac{n\zeta_n}{(\zeta_s^2+(\ell+2)^2)(1+\zeta_n^2)}\left[(1+\zeta_n^2)^2(\ell+1)(2\ell+3)(2+\ell(1-\kappa))\right. \\ & + 2(1+\zeta_n^2)(\mathrm{i}\zeta_s+\ell+2)\,(2+2\ell(1-\kappa)+\mathrm{i}n\zeta_n(1-\kappa)(2\ell(1-\kappa)+3)) \\ & \left. +4(1-\kappa)(\mathrm{i}\zeta_s+\ell+2)\,(1+\mathrm{i}n\zeta_n(1-\kappa))\,(2+\mathrm{i}n\zeta_n(1-\kappa))\right], \end{aligned} \tag{6.54}$$

$$\begin{aligned} R_{-2} \equiv\ & \frac{(\ell-\mathrm{i}\zeta_s)(1+\ell-\mathrm{i}\zeta_s)}{1+\zeta_n^2}\left[\left(1+\zeta_n^2\right)^2\ell(2\ell-1)((1-\ell)n\zeta_n(1-\kappa)+2\zeta_s)\right. \\ & - 2\left(1+\zeta_n^2\right)(1-\ell+\mathrm{i}\zeta_s) \\ & \quad \times (2\zeta_s - n\zeta_n(1-\kappa)(\mathrm{i}(2\ell-1)n\zeta_n(1-\kappa)-\mathrm{i}\zeta_s+2(\ell-\mathrm{i}\zeta_s))) \\ & \left. -4n\zeta_n(1-\kappa)(1-\ell+\mathrm{i}\zeta_s)(-2+\mathrm{i}n\zeta_n(1-\kappa)(-3-\mathrm{i}n\zeta_n(1-\kappa)))\right]. \end{aligned} \tag{6.55}$$

The form given here makes all cancellations of the "Abelian" case manifest as terms $(1-\kappa)$, highlighting the strong simplifications of the Abelian case. Anticipating the analysis of section 6.4, the large n and ℓ behavior $n, \ell \gg \bar{n} = \mathcal{O}(1)$ shows a dependence on the non-Abelian nature of the interaction,

$$R_a|_{n,\ell\gg\bar{n}} \propto n^2(1-\kappa) + \mathcal{O}(n). \tag{6.56}$$

Abelian cross sections boast a parametrically weaker dependence on $n \gg 1$ compared to general-potential BSF processes by two powers since $|R_a|^2$ contributes. Note that this estimate holds only for positive $\Delta = a$ while for $\Delta < -a$ already the wave-function normalization Gamma-functions in Eq. (6.50) count differently.

Nevertheless, the leading order in n is still proportional to $(1-\kappa)$ allowing for the same line of argument. This suggests the existence of a different form of the radial overlap integral which has identical power counting in large n for R_a and R_{-a}, yet for all analytical investigations as well as efficient numerical evaluation, the here used form (6.50) suffices. Lastly, the complex phase of R_a in monopole and dipole interactions vanishes in the Abelian case, $\gamma_\Delta|_{\kappa=1} = 0$ at $\Delta = 0, 1$, however this feature does not generalize to $\Delta < 0$ or $\Delta \geq 2$.

The presentation of R_Δ completes the analytic computation of the general-multipole BSF cross-sections (6.28) expressed by the angular integral (6.32) and the radial squared overlap integral (6.50) where the above $R_{\pm a}$ are to be inserted.

The power counting of the cross section is $(\sigma \mathrm{v})_{\mathrm{BSF}} \propto (g_a^{\mathrm{eff}})^2 \mathrm{v}^{2a-1}$, in agreement with the multipole interaction operator in Eq. (6.13). All contributions of $\alpha_{b,s}$ are implicitly encoded in ζ_n, κ or ζ_s which are $\mathcal{O}(1)$ quantities in the EFT power counting. The presented results were confirmed by an independently double check, direct numerical integration of the wave functions at small n and well behaved v and extensive numerical comparisons to a numerical code developed in early stages of [3] (build for $a = 1$ and stable to high $n \leq 1000$). Note that the mathematical algorithm implemented in that code differs fundamentally from Eq. (6.50), relying on a system of recursion relations of 5th order derived from the derivative expression Eq. (52) in [140]. The found complete numerical agreement is therefore also viewed a check of the disregarded concerns about the radius of convergence formally constraining the use of Eq. (6.33) [142]. The above expression also reproduces existing analytic expressions of the radial overlap for monopole [144], dipole [75, 140] as well as for quadrupole [138] for the available low $n \leq 3$.

Compared to the multi-derivative expressions given in [140], the radial integral was solved for arbitrary a and Δ in Eq. (6.41) and involves only a small number of derivatives and summed terms, $a = \mathcal{O}(1)$, vastly reducing numerical efforts when using this unevaluated form. Moreover, for BSF into a specific bound state from any initial angular momentum, $\sum_{\ell'} \mathcal{S}_{p,\ell'} \to \mathcal{B}_{n\ell}$, still only the single hypergeometric function $F_+(0)$ needs to be evaluated according to Eq. (6.50) as it is independent of Δ. In numerical evaluations, only the hypergeometric function demands significant effort, as there are no fast convergence conditions when all parameters are large, $n, \ell \sim n - \ell \gg 1$. Additional numerical stability can be achieved by rewriting the Sommerfeld factor $S_{\ell'}(\zeta_s)$ in terms of a $\sinh(\pi\zeta_s)$, a binomial term, several Gamma functions of $\mathcal{O}(1)$ (half-)integer arguments and Pochhammer symbols of small (half-)integer indices $\sim \Delta$. Lastly, numerical underflow near oscillatory features can be prevented by implementing an evaluation of $\log_2((\sigma\mathrm{v})_{\mathrm{BSF}})$. This implementation is efficient and stable (allowing $n \geq 10^4$ with reasonable effort) and was used for all velocity-dependent analyses below. Maximal angular momentum state BSF, $\ell = n - 1$, remains basically instantaneous even at $n = 10^6$ and higher as no hypergeometric functions need to be evaluated.

6.2.7 Properties of general Coulombic bound state formation

To close this section, some intuition for general Coulombic BSF is derived from a brief numerical study. Despite their compactness, the found analytic expressions for the BSF cross-section are rather opaque to the human eye and it is not apparent

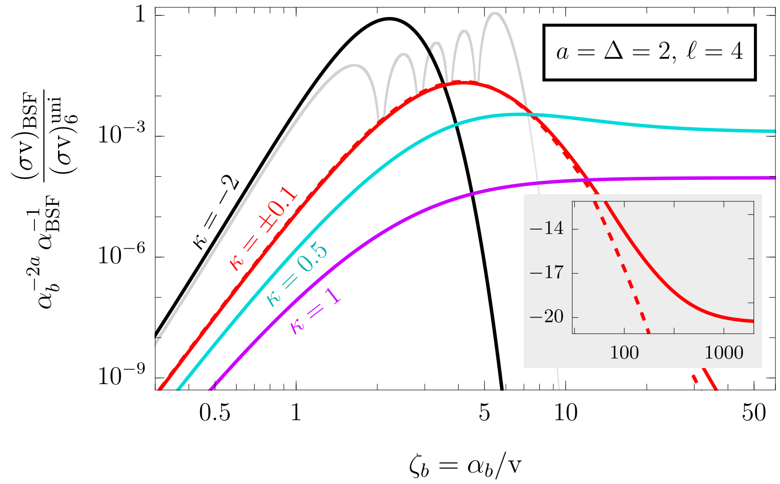

Figure 6.1: Bound state formation cross section normalized to the unitarity bound (6.76), $\alpha_{\mathrm{BSF}} = g_a^{\mathrm{eff}\,2}/4\pi$ and α_b^{2a}, removing all explicit model dependence beyond κ and $\zeta_b = \alpha_b/\mathrm{v}$. Different choices $\kappa = 1,\ 0.5,\ ,\pm 0.1\,, -2$ (purple, blue, red, black) are shown for $n = \ell + 1 = 5$, $\ell = 4$ and $\ell' = 6$ (quadrupole). A thinner gray curve shows $\kappa = -2$ with $n = 9$ (cut off below $\kappa = 0.1$ in the range $1 < \zeta_b < 6$). The inset plot highlights the departure of $\kappa = -0.1$ (dashed red) from $\kappa = 0.1$ (solid) at large ζ_b, the vertical axis here being in logarithms to the base 10.

where various qualitative features arise from. A comprehensive functional analysis of the found BSF cross-section formulas distinctly investigating all free parameters is relegated to App. D in the interest of brevity of this main text. Nevertheless, its insights may prove useful to readers unfamiliar with some of the intricate details of non-Abelian BSF cross-sections. Core aspects which may be understood in terms of classical or basic quantum mechanical physical intuition are listed here to provide a sufficient foundation of understanding to, at least, accept the numerical results presented in the following sections. The phase-space prefactors and angular integral are simple and most aspects of the following discussion relate to I_R.

Different multipoles do not give major qualitative changes aside from $a = 0$ in which case $\kappa = 1$ must vanish due to orthogonality of the wave functions, *cf.* $R_0 \propto (1-\kappa)$ in Eq. (6.51). To distill the special role of $\kappa = 1$ from the analytic expressions more clearly, consider a theoretically simple maximal-ℓ BSF process normalized to the Abelian case,

$$\frac{(\sigma \mathrm{v})^a_{p\ell' \to n\,(n-1)}}{(\sigma \mathrm{v})^a_{p\ell' \to n\,(n-1)}\Big|_{\kappa=1}} = \mathrm{e}^{4n\zeta_n(1-\kappa)\,\mathrm{arccot}(\zeta_n)} \left(1 + \frac{n}{a}(1-\kappa)\right)^2 \frac{S_{\ell'}(\kappa n \zeta_n)}{S_{\ell'}(n\zeta_n)}. \tag{6.57}$$

This equation holds irrespective of the κ in the numerator, a and n, *cf.* Eq. (6.44).

Fig. 6.1 illustrates most of the qualitatively interesting aspects of Coulombic BSF in the exemplary case of $(\sigma \mathrm{v})^{a=2}_{\mathrm{v},6\to 5,4}$ for several κ (denoted) and, additionally, $n = 9$ for $\kappa = -2$ (gray oscillatory curve). The latter has 4 true roots in the range $\zeta_b \in [1, 6]$ which, for clarity of the figure, are not drawn below the red curve. The depicted cross section is normalized to $\alpha_b^{2a}\alpha_{\mathrm{BSF}}$, where $g_2^{\mathrm{eff}} = \sqrt{4\pi\alpha_{\mathrm{BSF}}}$, and for later use also to the applicable partial wave unitarity bound $(\sigma \mathrm{v})_6^{\mathrm{uni}}$, to be defined in Eq. (6.76). The normalization removes all explicit dependence on $\alpha_{s,b,\mathrm{BSF}}$ or v and ζ_b, κ, n and Δ are the only remaining free parameters. Many supplementary figures may be found in App. D.1, separately varying the parameters a, κ, ℓ, n.

- The simplest class of BSF processes is the one of maximal angular momentum, $\ell = n-1$. In general, such processes have a local maximum (peak) in between the low and high velocity regimes. Fig. 6.1 shows $n = \ell + 1 = 5$, $\Delta = 2$, for different values of $\kappa = -2, \pm 0.1, 0.5, 1$ (black, red, cyan and purple) as examples. Note that $\ell \gg 1$ is one necessary condition to make contact to classical physics via the correspondence principle, thus this class of processes is also here of significance.

- The high velocity regime is known to be dictated by ℓ. All depicted choices of κ share the same angular momentum and therefore also the same high-velocity behavior $(\sigma \mathrm{v})_{\mathrm{BSF}}/(\sigma \mathrm{v})_6^{\mathrm{uni}} \sim \zeta_b^{2\ell-2a+5}$ at $\zeta_b \ll 1$.

- At low velocities, BSF cross-sections with $\kappa > 0$ approach a Sommerfeld scaling, $\sigma \mathrm{v} \sim 1/\mathrm{v} \propto (\sigma \mathrm{v})_6^{\mathrm{uni}}$, *cf.* Eq. (6.76), and the respective plotted curves saturate in the chosen normalization. Even tiny initial state potentials eventually reach this Sommerfeld enhanced regime, as can be seen in the inset panel of Fig. 6.1. Any repulsive potentials ($\kappa = -0.1$, dashed red) instead are exponentially suppressed. The black curve, $\kappa < 0$ and $n = \ell + 1$, is an exemplary case with a single global maximum in between the polynomial growth and exponential suppression and may be kept in mind for various later discussions.

- Apart from the change in low-velocity behavior, the free case $\kappa = 0$ is a smooth point in parameter space of no further apparent qualitative significance, hence both red curves largely overlap.

- Another strong simplification is $\kappa = 1$, the Abelian case, which is mostly featureless (see Fig. D.1 in App. C or [138]) beyond the two discussed regimes even for arbitrarily high n. Abelian BSF into high excitations is significantly suppressed in n at $\zeta_n = \mathcal{O}(1)$, compared to non-Abelian cases.

- The peak positions in maximal-ℓ BSF were numerically observed around $\zeta_n \sim 1$, independent of n for fixed κ. That is, for higher $n = \ell + 1$, the peak becomes sharper and shifts to lower v. The peak maximum position will be found to be $\zeta_n = (1-2\kappa)^{-1/2}$, see Eq. (6.85) in section 6.4.

- At lower $\ell < n-1$, the cross section develops a number of $n - \ell - 1$ roots in place of the single peak when $\kappa < 0$ and $\Delta \geq 0$, giving rise to an oscillatory regime in between the high and low velocity limits, originating from the phase factor. This is similar to the Ramsauer-Townsend effect [145–147]. The oscillatory regime expands "outwards", to lower and higher velocities, relative to the maximal-ℓ peak position. Overall, it may be viewed as a distracting nuisance when attempting to understand the physical aspects of non-Abelian BSF. Its quantum mechanical interpretation will become clear in section 6.3. The number of oscillations decreases in the range $\kappa \in [0, 1]$, terminating in the (almost) featureless Abelian case. A low number of additional roots may occur if instead $\Delta < 0$.

6.3 Semi-classical analogy

Albeit intricate in their detailed formulation, the obtained cross sections for BSF into a single bound state n, ℓ lend themselves to a semi-classical interpretation. It provides an intuitive physical picture to the investigated quantum processes. Naturally, the analogy improves for higher n and ℓ in accordance with the correspondence principle. The most "unnatural" aspect to translate to terms of classical physics is the change of potentials, meaning κ. Assuming there to be only the two heavy species $\mathcal{B}$ and $\mathcal{S}$, the emission of multiple quanta of the mediator field by multipole interactions will lead to as many back and forth changes $\alpha_b \leftrightarrow \alpha_s$. For a classical interpretation, emission needs to be treated as a continuous process and a prediction of the effective strength of the potential is not possible. Instead, consider the semi-classical picture of one single multipole mediator emission at a set point in time but treating the heavy two-constituent states still classically prior to and after the interaction. Using the rest frame of one of the constituents, the semi-classical picture, illustrated in Fig. 6.2, is as follows.

An particle incoming from $r = \infty$ with kinetic energy $K > 0$ moves in a central potential $V_s(r)$ on a hyperbolic path (black line). It approaches the second constituent at located at $r = 0$ until the minimal impact distance $r = b$ is reached. Instead of following the elastic scattering path back to $r = \infty$ (dashed), the potential changes exactly at the point $r = b$, $V_s(r) \to V_b(r)$. The BSF mediator field is neglected and, hence, energy conservation is broken here. However, since $r = b$ is an extremum, there is no radial motion at this point in time, therefore momentum and angular momentum remain conserved throughout. For sufficiently small velocities $K < \ell^2/M_\chi b^2$ and attractive $V_b < 0$, thinking of fixed b for the moment, the orbit after changing the potential is now a bound state described by an energy E_n (blue or orange lines).

6.3.1 Classical capture into Keplerian orbits

A classical computation of "BSF" trajectories yields convenient approximations of the oscillatory regime of the BSF cross-section. Restricting $V_{s,b}$ to Coulombic potentials defines the movement before and after the potential change to be Keplerian orbits set by an energy and an eccentricity,

$$e \equiv \sqrt{1 - \frac{\ell^2}{n^2}} \approx \sqrt{1 - \frac{(\ell+1)^2}{n^2}} + \mathcal{O}\left(\frac{1}{n}\right), \tag{6.58}$$

where the approximation $\ell \approx \ell + 1$ allows to naively match onto a circular orbit with maximal angular momentum, $e|_{\ell=n-1} = 0$. This approximation eliminates the otherwise ever-present small uncertainty of quantum states for $\ell = n-1$, rendering movement to a perfect circle. Analogous to Figs. D.1-D.4 which are plotted in v for fix n and ℓ, the final state is set from the beginning and one calculates the required initial velocity in order to match onto the desired orbit. Furthermore, in the introduced picture momentum and angular momentum is conserved at $r = b$ so the initial and final orbits must be tangential at $r = b$. For a circular orbit, the problem is rotational symmetric while for elliptic orbits the matching can take place at the distance of the aphelion or perihelion,

$$r_A = r_n(1-e) \quad \text{or} \quad r_P = r_n(1+e). \tag{6.59}$$

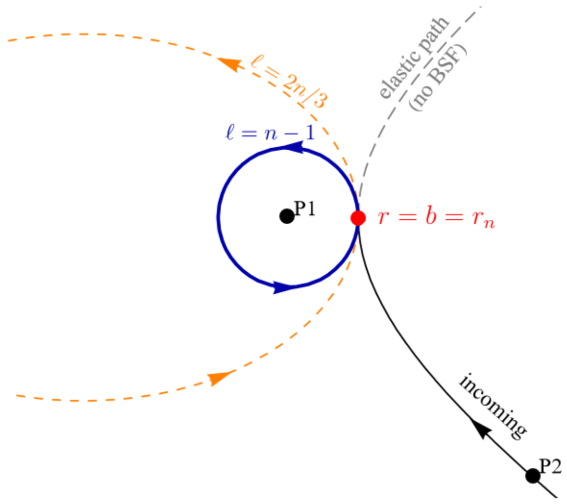

Figure 6.2: Sketch of the semi-classical analogy to obtain approximations for the high and low end of the oscillatory regime of the BSF cross-section. An initial scattering state in a repulsive potential (black) approaches the center P1, reaching the minimal impact distance b where the potential is assumed to abruptly change to be attractive. The velocity is tuned such that the impact parameter matches the Bohr radius, $b = r_n$, of a circular orbit (blue). To match an elliptic orbit (dashed) aphelion distance, $b = r_n(1 - e)$.

The particle initially experiences the effective potential

$$V_{\text{eff}}(r) \approx \frac{(\ell' + 1)^2}{M_\chi r^2} - \frac{\alpha_s}{r} \tag{6.60}$$

and correspondingly for ℓ and α_b after the potential change. Expressing the relative velocity in terms of ζ_n yields $K = \zeta_n^{-2} E_n$ and energy conservation at $r = \infty$ and $r = b = r_{A,P}$ now implies

$$\begin{aligned} K = E_n {\zeta_n}^{-2} = \frac{(\ell' + 1)^2}{M_\chi b^2} - \frac{\alpha_s}{b} &= \frac{(\ell' + 1)^2}{(\ell + 1)^2}\left(-E_n + \frac{\alpha_b}{r_{A,P}}\right) - \kappa \frac{\alpha_b}{r_{A,P}} \\ &= E_n \left[\left(\frac{\ell' + 1}{\ell + 1} \right)^2 \frac{1 \pm e}{1 \mp e} - \frac{2\kappa}{1 \mp e} \right], \end{aligned} \tag{6.61}$$

$$(\zeta_n)_{A,P} = \sqrt{\frac{1 \mp e}{\frac{(\ell'+1)^2}{(\ell+1)^2}(1 \pm e) - 2\kappa}}, \tag{6.62}$$

where the upper sign corresponds to the aphelion. ℓ' and ℓ were kept distinct in the calculation, however, in the reasonable assumption of low multipoles $a \ll n, \ell$ one may use $\ell' = \ell + \mathcal{O}(a/\ell)$. Now, a circular orbit is matched onto when the ratio of momenta and coupling strengths fulfill

$$\zeta_n = \frac{1}{\sqrt{1 - 2\kappa}}. \tag{6.63}$$

The square corresponds to the ratio of energies of the final over the initial state $E_n/K = 1/(1 - 2\kappa)$. Interestingly, this equation only holds for $\kappa < 1/2$, since

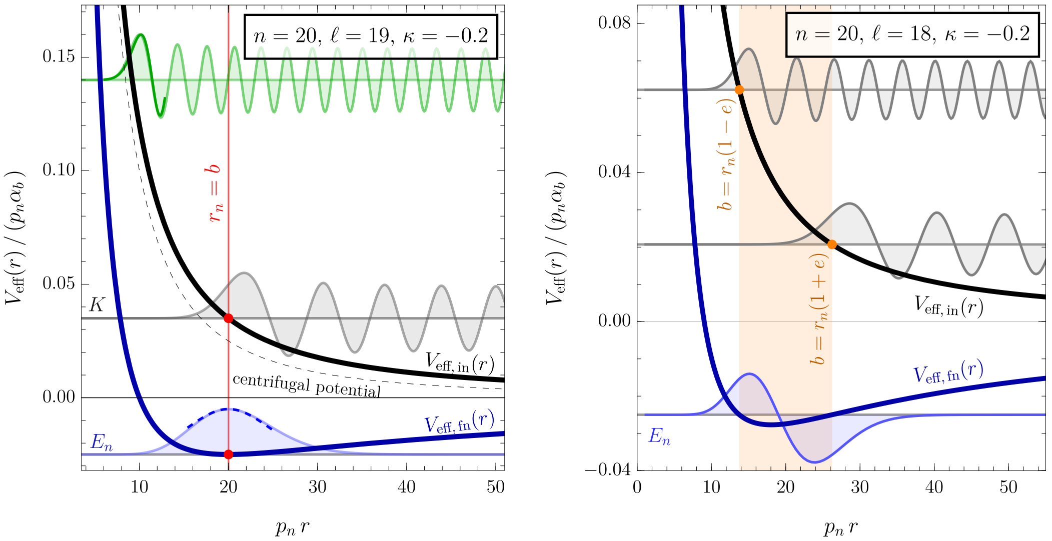

Figure 6.3: Effective potentials V_{eff} for initial state (black) and final state (blue) as, Eq. (6.60), divided by $(p_n\alpha_b)$. Wave-functions for initial scattering states (gray, green) and final bound states (blue) are superimposed at their respective energy with arbitrary normalization. *Left*: The ground state for a given ℓ is shown, $n = \ell + 1 = 20$. The vertical red line indicates its Bohr momentum, coinciding with the impact parameter for the scattering state of energy K. The centrifugal repulsive potential is shown as a dashed curve. *Right*: The first excited bound state $n = \ell + 2 = 20$ is shown with the initial states tuned to match their impact parameter to the semi-classical perihelion and aphelion distances, $b = r_n(1 \pm e)$.

$\zeta_n \in \mathbb{R}$, meaning that no such semi-classical paths exist for Abelian interactions where $\kappa = 1$. The scattering state potential needs to be sufficiently *less* attractive or repulsive to allow the centrifugal term to dominate at ranges where bound states are classically located. Since bound states $n = \ell + 1$ are located at the minimum of the effective potential, the scattering state is simply accelerated inwards, gaining exactly E_n in the Abelian scenario, and thus cannot possibly have coincident (classical) momentum and position with the classical bound state.

Turning to a semi-classical wave function description, for any $\alpha_s > 1/2$ the effective potential is insufficiently repulsive and the scattering state would simply always be rapidly oscillating compared to the bound state wave length at a given radial distance, similar to the green wave in Fig. 6.3, such that the overlap integral remains small and the scattering state cannot sense the presence of the bound states. Fig. 6.3 depicts how the energies, classical radii and Coulomb wave functions relate to each other. The vertical axis shows the scaled effective potential $V_{\text{eff}}/p_n\alpha_b$ in dependence on $p_n r$ for a fixed $n = 20$. The left panel depicts the case $\ell = n - 1 \approx n$ and also includes the centrifugal contribution to V_{eff} as a dashed curve for reference. The classical circular orbit is found at the minimum of the final state effective potential (blue curve) where there is no radial motion (red vertical line). Overlaid (shaded blue) is the reduced bound state wave function for this "ground state" of the effective potential. It is vertically centered around the value of its total energy E_n.

The impact parameter b is given by the intersection of the horizontal gray line at $K = p^2/M_\chi$ and the initial effective potential (black curve), marked by a red dot. For the gray depicted scattering state wave function, $b = r_n$ match and there is clearly a large overlap between the bound state peak and the final maximum of the scattering state. For smaller velocities, b grows, following the black curve outwards and the bound state is found in the suppressed, classically inaccessible tail of the scattering state wave function. Conversely, for too large v the bound state is confined in the rapidly oscillating part of the approximately free wave function of the scattering state, *cf.* green wave with $b = r_n/2$. In the overlap integral, the bound state is not sensed but averaged out over many oscillations suppressing the matrix element at small ζ_n.

The case of capture into elliptic orbits, $\ell < n - 1$, is analogously depicted in the right panel of Fig. 6.3. Instead of a single position r_n, the range $p_n r_A$ to $p_n r_P$ is shown by an orange shaded vertical band. The bound state is now no longer the ground state of the effective potential but the first excitation ($\bar{n} = 1$). The orange band encompasses all bound state oscillations. Reduced scattering state wave functions are shown here for the two cases of tuning either $b = r_A$ or $b = r_P$. The same logic as before applies to the interval $[r_P, r_A]$. Furthermore, this connects the multiple roots of the oscillatory regime in the BSF matrix element the number of nodes of the bound state wave function. Within the classically accessible range of the bound state, the oscillatory wave function features are scanned as $b(\mathrm{v})$ changes. This intuitive explanation will be derived rigorously in the next subsection.

Returning to the Abelian scenario and taking $\ell \approx \ell'$, the initial state potential (black) is here identical to the final state potential (blue). Clearly the best match between the bound state and the scattering state wave functions is reached when $K = 0$ since in all other cases the bulk of the bound state is scanned by a more rapidly oscillating part of the initial state. The overlap is now always dominated by the innermost oscillation of the bound state and the overlap increases gradually as the initial state relative velocity tends to zero. This is a well-known feature of scattering processes where, for $\kappa > 0$, largest cross sections are found in the Sommerfeld enhanced low-velocity limit from the scaling $\propto 1/\mathrm{v}$ as $\mathrm{v} \to 0$.

6.3.2 Wave function approximations

This subsection describes a quantum mechanical treatment of BSF, with the goal of solidifying how the wave function overlap is to be interpreted. To this end, the reduced wave functions $u(r)$ of scattering and bound state are approximated near the Bohr radius r_n and impact b distance, respectively. From the semi-classical picture above, $b = b(\mathrm{v})$ is uniquely defined by the momentum, potential strength and relative velocity as

$$p \times b = \sqrt{\zeta_s^2 + (\ell' + 1)^2} - \zeta_s. \tag{6.64}$$

Starting with the simpler bound state wave function at maximal angular momentum, the single-peak shape is to a good approximation near the maximum given in terms of a Gaussian distribution obtained via standard saddle point expansion,

$$u_n^{\text{Gauß}}(r) = \left(\frac{n}{r_n^2\pi}\right)^{\frac{1}{4}} \exp\left[-\frac{n}{2}\left(\frac{r}{r_n}-1\right)^2\right]. \tag{6.65}$$

In units of r_n, the width of the bound state is thus $n^{-1/2}$. The analytic form of the scattering wave function is more challenging to approximate as the position of the final maximum is not known and, furthermore, it does not easily lend itself to a description in terms of a single peak. Also the commonly employed WKB approximation is not applicable near impact. Instead, a linear approximation of the effective potential in the vicinity of the impact distance becomes useful,

$$V_{\text{eff,in}}(r) \approx V_{\text{eff,in}}(b) + V'_{\text{eff,in}}(b)(r-b) + \mathcal{O}(r-b)^2. \tag{6.66}$$

In terms of the most natural coordinate,

$$z \equiv \left(-M_\chi V'_{\text{eff,in}}(b)\right)^{1/3}(b-r) = z_0(v)\left(1-\frac{r}{b}\right), \tag{6.67}$$

$$z_0 \equiv \left(2\ell'(\ell'+1) - M\alpha_s b(v)\right)^{\frac{1}{3}}, \tag{6.68}$$

the radial Schrödinger equation for this potential takes the simple form

$$\frac{\mathrm{d}^2\,u(z)}{\mathrm{d}z^2} = z\,u(z) \tag{6.69}$$

and its solutions are Airy Ai and Bi functions. With the additional condition of an exponential decay at $r < b$, the reduced wave function is then found to be $u_{\ell'}^{\text{Airy}}(r) = c\,\text{Ai}(z)$. A second boundary condition is needed to define the constant c. One can use the common procedure of WKB approximations to match the solution of the linearized potential at large radii $u_{\ell'}^{\text{Airy}}(r \to \infty)$ onto the WKB approximation near impact $u^{\text{WKB}}(r \approx b)$. The WKB solution is itself matched onto the full solution at $r \to \infty$. The procedure carries the flair of a scale separation in effective theory, in that the long range ($r \gg b$) behavior of the local solution must describe the short range ($r \approx b$) behavior of the solution valid far away from impact. In usual applications, the linearized solution is merely the matching condition by which WKB solutions for $r > b$ and $r < b$ are glued together. Here, instead, $u_{\ell'}^{\text{Airy}}$ is itself the object of interest. Ultimately, the approximate scattering wave function near impact is given by

$$u_{\ell'}^{\text{Airy}}(r) = \sqrt{\frac{2\pi\,b}{Mv\,z_0}}\,\text{Ai}\,(z) \tag{6.70}$$

where the entire dependence on v and ℓ' is hidden in z and b. The correctness of this approximation can be confirmed numerically and improves for large ℓ, being virtually indistinguishable from the full solution within the final oscillation (even giving a reasonably good approximation of the second-to-last oscillations), once $\ell' \gtrsim 20$. Both approximative wave functions, $u_n^{\text{Gauß}}$ and $u_{\ell'}^{\text{Airy}}$, are seen in Fig. 6.3 (left panel), the former as a blue dashed curve near the bound state peak and the latter as a darker green curve drawn near the final oscillation of the upper scattering state wave function. They are shown in ±30% intervals around r_n and $b(\text{v})$, respectively.

Both, the maximal-ℓ bound state peak and the final scattering state oscillation become broad at high n and low v. To compare them more easily, $u_n^{\text{Gauß}}(r)$ is expressed in terms of z, under the condition $b = r_n$, as

$$u_n^{\text{Gauß}}(z) = \frac{\sqrt{M\alpha_b}}{(4n^3\pi)^{1/4}} \exp\left[-\frac{1}{2\sigma_n^2}z^2\right] \tag{6.71}$$

with

$$\sigma_n = \frac{\left(2\ell'(\ell'+1) - M\alpha_b b(v)\right)^{\frac{2}{3}}}{n-1}. \tag{6.72}$$

Represented in terms of z rather than r, the width of the scattering state wave function is trivially constant. σ_n, the width of $u_n^{\text{Gauß}}(z)$, is more easily understood by inserting $b(v) = r_n = n/p_n$,

$$\sigma_n = 2^{\frac{2}{3}}\left[n(1-\kappa) + 2\Delta - 1\right]^{\frac{1}{3}} + \mathcal{O}(n^{-\frac{1}{3}}), \tag{6.73}$$

thus

$$\sigma_n \sim n^{\frac{1}{3}}. \tag{6.74}$$

The width of the bound state wave function in z-coordinates, σ_n, grows with n. Hence, the innermost oscillation of the scattering state wave function should be thought of as a sharp peak scanning through a much broader bound state for high excitations. This picture holds (at least) when tuning the impact distance to the Bohr radius while $n \gg \Delta$. Note that inserting $b = r_n$ and setting $n = \ell + 1 \gg \Delta$, implicitly introduces the condition $\kappa < 1/2$, following from Eq. (6.63).

As the bound state grows infinitely broad in z, also the integral becomes independent of n,

$$\lim_{n\to\infty} \int_{-\infty}^{\infty} dz\, \text{Ai}(z) \mathrm{e}^{-\frac{1}{2\sigma_n}z^2} = \lim_{n\to\infty} \sqrt{2\pi} e^{\frac{\sigma_n^3}{12}} \sqrt{\sigma_n} \text{Ai}\left(\frac{\sigma_n^2}{4}\right) = 1. \tag{6.75}$$

Numerically, one finds that the innermost oscillation dominates the radial overlap integral for maximal ℓ, as expected since farther out oscillations are relatively rapid and cancel against each other. When the integration regime in z is cut off beyond the first root of $\text{Ai}(z)$, the integral approaches a value of around 1.27 for large n. The second oscillation has opposite sign, compensating the overestimate. This validates the qualitative picture of approximating the scattering state by its final oscillation which becomes basically a sharp peak scanning through the bound state probability distribution as v is decreased.

6.3.3 Comparison to the full quantum mechanical result

The semi-classical results based on matching orbits at $r_{A,P}$ do not precisely capture the first and last maxima of the oscillatory regime of the BSF cross-section at finite n but bound the oscillatory regime from above and below in ζ_n. These estimates are useful to preemptively define oscillatory regions, which pose a challenge for example to thermal averaging, and are difficult to prove analytically otherwise.

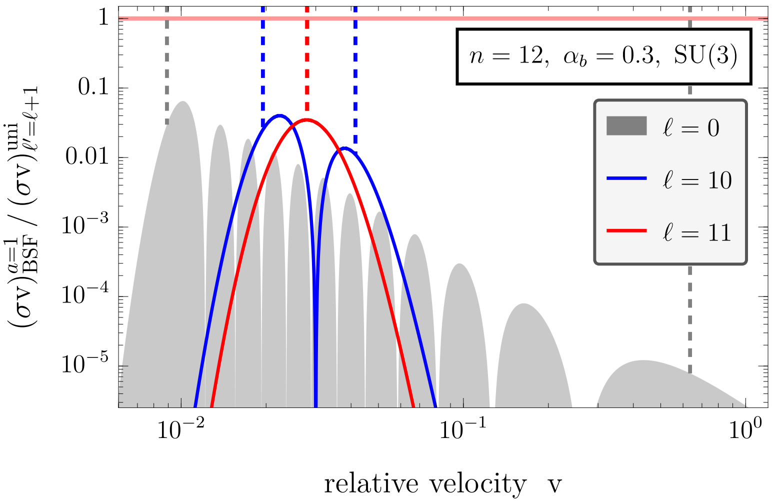

Figure 6.4: Bound state formation cross sections normalized by the appropriate partial wave unitarity bound for $n = 12$ and $\ell = 0, 10, 11$ (gray, blue, red) plotted over relative velocity v. $\ell = 0$ is depicted as the boundary of the gray shaded area for better readability. Vertical lines mark semi-classical approximations of the aphelion and perihelion distance matching in Eq. (6.62). The horizontal red line shows the partial wave unitarity limit (6.76).

Thanks to the perfect circular approximation, $e = 0$, both bounds coincide for $n = \ell + 1$ and the maximal-ℓ peak position is very well approximated.

For illustration, the relative velocities $\alpha_b/n/(\zeta_n)_{A,P}$ according to Eq. (6.62) are shown in Fig. 6.4 as vertical dashed lines in colors corresponding to the three plotted partial waves $\ell = 0$ (gray), $\ell = n - 2$ (blue) and $\ell = n - 1$ (red). The cross section, plotted over relative velocity, is computed specifically for interactions as they are obtained in a SU(3) gauge theory for heavy fundamental particle anti-particle pairs [140, 148], meaning $g^{\mathrm{eff}}_a \to g_s\sqrt{2C_F}/N_c$ as well as $a = 1$ and $\kappa = -1/8$, *cf.* section 6.5. Used numerical inputs are $\alpha_b = 0.3$, $n = 12$ and $\Delta = +1$ (allowing s-wave capture). The vertical axis shows the BSF cross-section for dipole interactions again normalized to the respectively applicable unitarity bound $(\sigma \mathrm{v})^{\mathrm{uni}}_{\ell'}$. Another feature of radiative BSF is understood from the semi-classical approximation. The *reduced* bound state wave function is maximal at its outermost maximum. This means the overall maximal overlap is expected at the low-velocity end of the oscillatory regime. The prediction agrees with Fig. 6.4 where all cross sections increase towards small velocities, even despite being normalized by the unitarity bound, $(\sigma \mathrm{v})^{\mathrm{uni}} \propto 1/\mathrm{v}$. The semi-classical analogy here is that of a time-average probability of finding the bound particle at a certain distance r on an elliptic orbit. This probability is directly proportional to the inverse classical orbit velocity $1/v(r)$ which is maximal at $r = r_P$.

It is apparent from Fig. 6.4 that BSF cross-sections grow rapidly compared to the unitarity bound which of great concern in regards to theoretical self-consistency. This looming issue of unitarity violation is investigated in detail both, analytically and numerically, in the following section.

6.4 Systematic perturbative unitarity violation

Any 2-to-2 particle scattering cross-section obtained in a self-consistent unitary theory must respect the partial wave unitarity bound [89]. Performing a partial wave decomposition on the initial state, the upper bound on a particular partial wave ℓ' inelastic process reads

$$(\sigma \mathrm{v})^{2\to 2,\mathrm{inel}}_{\ell'} \leq (\sigma \mathrm{v})^{\mathrm{uni}}_{\ell'} \equiv \frac{4\pi}{M_\chi^2 \mathrm{v}}\,(2\ell' + 1)\,. \tag{6.76}$$

It holds irrespective of the final state and applies to arbitrarily inclusive inelastic scattering processes. It is of importance to highlight the difference between 2-constituent 2-particle scattering state and 2-constituent single-particle bound states. While both are obtained as solutions to the Schrödinger equation to the same Hamiltonian, the former is indeed part of the multi-particle spectrum of the Fock space while the latter is constructed to correspond to a single particle pole [61]. Bound state formation by emission of a single multipole mediator, unlike bremsstrahlungs processes or bound-to-bound transitions, are therefore inelastic 2-to-2 scatterings of two heavy non-relativistic particles $\mathcal{S}$ into a non-relativistic composite state $\mathcal{B}$ and a light, relativistic mediator particle.

Unitarity bounds have been used in attempts to set upper limits to thermally produced electroweak multiplet dark matter masses M_χ [32, 89, 149–152]. These works typically compute the annihilation rates required in order to achieve the correct DM relic density and set upper bounds whenever either the coupling strength becomes of $\mathcal{O}(1)$, expecting a breakdown of perturbativity at such couplings, or once the computed cross sections overcome the unitarity bound. Interpretations remain identical, demanding to compute higher order, or even all order, results to obtain reliable predictions. A qualitatively different observation was made in a model of charged monopole emission [144]. It showed BSF to violate unitarity even for small couplings and already in capture into the ground state. The findings of this section confirm this known fact and put it into a larger context of systematic UVi for arbitrary (non-vanishing) couplings.

Most works present in the literature on analytic calculation of BSF focus on Abelian-type interactions ($\kappa = 1$) or consider only a small number of bound states, usually $n = 1$ or, in more recent works, $n = 2, 3$. Although of theoretical interest, there are no applications of non-Abelian Coulombic BSF processes in the SM, as the electroweak symmetry is broken, giving rise to Yukawa potentials which demand numerical treatment, and there are no reasonably stable heavy particles far above the confinement scale of the strong interaction, nor are there electromagnetically charged light mediators. This explains why there has not been a systematic treatment of BSF in non-identical Coulombic potentials prior to dark sector model building efforts.

Fig. 6.4 already shows a clear trend to overcome the unitarity bound for lower ℓ. At the same time the gray curve ($n = 9$) of Fig. 6.1 implies an enhancement towards larger n (see also the lower panel in Fig. D.4). To explicitly illustrate perturbative unitarity violation in BSF, Fig. 6.5 is similar to Fig. 6.4 but uses much higher excitations $n = 500$ and, for illustrative purposes only, a slightly stronger effective coupling $\alpha_b = 0.4$. The vertical axis is again normalized to the unitarity bound, showing $(\sigma \mathrm{v})^{1,1}_{p\ell' \to 500\ell}/(\sigma \mathrm{v})^{\mathrm{uni}}_{\ell'}$, and each curve gives the result

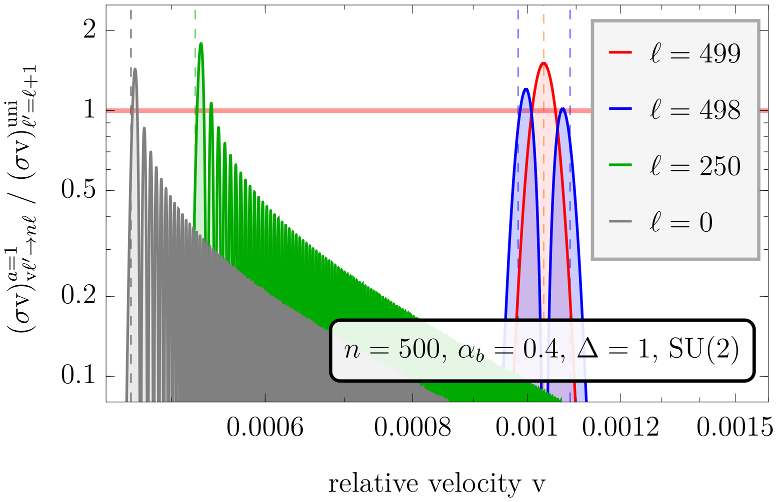

Figure 6.5: Bound state formation cross-sections normalized to the respective partial wave unitarity bound in a SU(2) model ($\kappa = -1/3$, $\alpha_{\mathrm{BSF}} = \alpha_b/2$, dipole, $\ell' = \ell + 1$), plotted over relative velocity using $n = 500$, $\alpha_b = 0.4$ and $\ell = 0, 250, 498, 499$ (gray, green, blue, red). The horizontal red line shows the unitarity limit (6.76) being exceeded at large n. Vertical dashed lines give respective semi-classical aphelion and perihelion matching conditions.

for one partial wave $\ell' = \ell + 1$ for $\ell = 0$, $n/2$, $n - 2$ or $n - 1$. Other inputs are taken to reproduce a model of heavy dark-SU(2) doublet constituents. Vertical dashed lines once more indicate the semi-classical results from Eq. (6.62). The above found results of enhancement at smaller v (higher n) can be recognized again. Every partial wave overcomes the unitarity bound at some velocity, despite regarding only exclusive processes $\mathcal{S}_{p\ell'} \to \mathcal{B}_{n\ell}$. This troublesome feature is studied analytically in detail in subsection 6.4.1 before turning to a numerical analysis of exclusive and, finally, inclusive BSF processes in subsequent subsections.

6.4.1 Analytic proof for capture into high angular momentum

This subsection presents for the first time an analytic proof of perturbative unitarity violation occurring in BSF for non-identical Coulombic potentials. UVi is derived in processes of specified final state bound states $\mathcal{B}_{n\ell}$ assuming $n \gg 1$ and, thus, only conservatively demonstrates theoretical inconsistencies arising in BSF. It does not aim to find the strongest possible bounds on α or v.

As a first estimate, this subsection briefly returns to the approximate wave functions derived in subsection 6.3.2 before investigating the full quantum mechanical result. For the sake of simplicity of the argument, monopole interactions are assumed in this example. From Eq. (6.28), one can see

$$\frac{(\sigma \mathrm{v})^{a}_{p\ell'\to n,(n-1)}}{(\sigma \mathrm{v})^{\mathrm{uni}}_{\ell'}} \sim \frac{\mathrm{v}^3}{2\ell'+1} \times I^{a,\Delta}_A \times I^{a,\Delta}_R . \tag{6.77}$$

The angular integral scales as $I^{a,\Delta}_A \sim n$ for $\ell' \sim \ell \sim n \gg 1$ and $a\Delta \sim 1$. By insertion of the above definitions of $z(r)$ in the integrand and the approximative reduced radial wave functions, one arrives at the power scaling

$$\frac{(\sigma \mathrm{v})^{a}_{p\ell' \to n,(n-1)}}{(\sigma \mathrm{v})^{\mathrm{uni}}_{\ell'}} \sim \frac{M_\chi^2 \mathrm{v}}{n} \times M_\chi \mathrm{v}^2 \times n \times \left| \sqrt{\frac{p_n}{\sqrt{n}}} \times \sqrt{\frac{b}{p z_0}} \times \frac{b}{z_0} \right|^2 \sim \sqrt{n} \gg 1. \quad (6.78)$$

The unitarity bound is eventually exceeded at large n, which is also where the wave function approximations are applicable. Note that constant but small prefactors such as α_{BSF} were dropped. The intermediate step has already inserted Eq. (6.75) but keeps terms originating from the unitarity bound, the phase space, the angular integral and the squared radial integral separate. The latter decomposes into the prefactors of both wave functions and the integral measure. The semi-classical calculation predicts a systematic violation of unitarity from perturbative radiative transitions in bound state formation at high excitations. This shall now be confirmed more carefully in the complete PNREFT result and studied in the following subsections in greater detail for its dependence on a, κ and ζ_b.

Turning to the complete leading order PNREFT result, capture into bound states of maximal angular momentum is once more regarded to simplify the analytic treatment by exploiting the absence of any hypergeometric functions. The relevant result for the radial overlap integral $J^{a,a}_{p,p_n}(n_s, 0, n-1)$ is given in Eq. (6.44) and the cross section normalized to the well known Abelian case in Eq. (6.57). Its velocity dependence is now entirely captured by rational polynomials, the Sommerfeld factor and the typical $\exp\{-4\zeta_s \mathrm{ArcCot}(\zeta_n)\}$ term.

UVi was found at small velocities which directly requires large n for $\kappa < 0$ since exponential suppression sets in when $\zeta_n \gg 1$. Thus, to analyze the impact of high excitations, the limit of large $n \gg \zeta_n, a \sim 1$ is of interest. As shown in Fig. D.4 and indicated by the semi-classical result (6.62), the global maximum of the BSF cross-sections is found at $\zeta_n = \mathcal{O}(1)$ while κ may be considered another $\mathcal{O}(1)$ constant fixed by the EFT Lagrangian. Taking $\mathrm{v} \ll 1$ while g_a^{eff}, $\alpha_{b,s} = \mathrm{const.} = \mathcal{O}(1)$ for this limit of large n, the counting is fixed as

$$\zeta_s = n\kappa\zeta_n = n \times \mathcal{O}(1) \sim n \sim \frac{1}{\mathrm{v}}. \quad (6.79)$$

Neglecting coupling strengths as constant in this limit implies $\mathrm{v} \sim 1/n$. Moreover, since $\zeta_n \sim 1$ remains constant, the condition $p \sim p_n$ is maintained. Crucially, the above requires the validity of PNREFT at arbitrarily small velocities. In PNREFT, only ultrasoft modes are left and no additional particles or interactions are present at that scale other than multipole interactions of the heavy constituents. Because of this, PNREFT is expected to hold also at arbitrarily small velocities despite the condition which indicates the onset of non-perturbativity of potential ladder exchanges being $\alpha \sim \mathrm{v}$. Hence, with all non-perturbative effects appropriately resummed in a controlled way, one concludes that unitarity should be maintained at every perturbative order in the power expansion. Yet, the observed UVi from leading order calculations points towards some misconception of the theory. The observation of UVi for monopole ground state formation [144] corroborates that the here employed large-n limit is not the original source of UVi but merely a useful tool for analytic investigation.

Taking the logarithm on both sides of Eq. (6.76) at $\ell = n-1$ and employing the above described large-n limit together with Stirling's formula,

$$\lim_{|z|\to\infty} \Gamma(z) \approx z^{z-\frac{1}{2}} e^{-z}\sqrt{2\pi}, \tag{6.80}$$

which is also applicable to $S_{\ell'}(\zeta_s)$ according to Eq. (6.25), results in an expansion in n starting from the leading linear order but also including sub-leading terms $\propto \log(n)$,

$$\begin{aligned} 0 &\geq \log\left\{\frac{(\sigma \mathrm{v})^a_{\vec{p},n+a-1\to n,n-1}}{(\sigma\mathrm{v})^{\mathrm{uni}}_{n+a-1}}\right\} && (6.81)\\ &= \log\left\{\frac{g_a^{\mathrm{eff}2} M_\chi^3 (1+\zeta_n{}^2)\mathrm{v}^3}{2^7\pi^2(2n+2a-1)(2a+1)^2} \times I_A^{a,a} \times I_R^{a,a}\right\} && (6.82)\\ &\equiv n\, P(\zeta_n,\kappa) + \mathcal{O}\left(\log(n)\right). && (6.83) \end{aligned}$$

The leading order $P(\zeta_n,\kappa)$ is defined as

$$P(\zeta_n,\kappa) \equiv 2\zeta_n\kappa\left(\frac{\pi}{2} - \mathrm{ArcTan}(\zeta_n\kappa) - 2\mathrm{ArcCot}(\zeta_n)\right) + \log\left(\frac{4\zeta_n^2(1+\zeta_n^2\kappa^2)}{(1+\zeta_n^2)^2}\right). \tag{6.84}$$

Any leading term violating $0 \geq P(\zeta_n,\kappa)$ indicates that BSF is systematically and exponentially enhanced relative to the unitarity bound. This does not occur. After some standard functional analysis, $P(\zeta_n,\kappa)$ can be shown to be a negative semi-definite function with only one root on the real axis,

$$P\left(\frac{1}{\sqrt{1-2\kappa}},\,\kappa\right) = 0. \tag{6.85}$$

In practice, $P(\zeta_n,\kappa)$ is a quite intriguing function and despite its structure rather resilient against analytic simplifications. Remarkably, the root sees the logarithmic and trigonometric terms vanish separately, which can be easily checked by insertion. If the root is real, $\kappa < 1/2$, the curvature at this point is

$$\left.\frac{\mathrm{d}^2 P(\zeta_n,\kappa)}{\mathrm{d}\,\zeta_n^2}\right|_{\zeta_n=1/\sqrt{1-2\kappa}} = -\frac{2(1-2\kappa)^3}{(1-\kappa)^2} < 0. \tag{6.86}$$

With some more effort, $P(\zeta_n,\kappa)$ can also proven to be negative definite when $\kappa > 1$. Equation (6.84) is understood to capture the balancing of the strong enhancement $\sigma\mathrm{v} \sim (\zeta_n)^{2\ell-2a+5}$ before the peak position and the exponential suppression from the repulsive potential small relative velocities. Therefore it is not unexpected to find the leading order expansion of the Stirling formula to vanish at the peak position. Note that the semi-classical result (6.63) exactly agrees with the large-n limit where the quantum process becomes infinitely sharp and coincident with a classical circular orbit. It is the only combination of ζ_n and κ where BSF is not exponentially suppressed in n. For $\kappa > 1/2$, there exists no solution agreeing with the numerical observation of cross sections which show a slight bump but no local maximum in their transition to the low-velocity Sommerfeld enhanced regime, *cf.* Fig. 6.1.

The strength of the peak at its maximum is to be read from the first sub-leading term, $\mathcal{O}(\log(n))$, in Eq. (6.83). It corresponds to polynomial contributions of n to the cross section. Inserting the explicit expressions for monopole, dipole and quadrupole interactions (6.51 - 6.55) yields in every case

$$0 \geq \log\left\{\frac{(\sigma \mathrm{v})^{a}_{\vec{p},n+a-1\to n,n-1}}{(\sigma \mathrm{v})^{\mathrm{uni}}_{n+a-1}}\right\} = P(\zeta_n,\kappa) + \frac{1-4\,\delta_{\kappa 1}}{2}\log(n) + \mathcal{O}(1). \tag{6.87}$$

The partial wave unitarity bound is violated near the peak $\zeta_n = (\zeta_n)_{P,A}$ for $\ell = n-1 = \ell' - a$ because the BSF cross-section on-peak grows with n as

$$\frac{(\sigma \mathrm{v})^{a}_{p\ell'\to n\ell}}{(\sigma \mathrm{v})^{\mathrm{uvi}}_{\ell'}} \sim \sqrt{n} + \mathcal{O}(1) \gg 1. \tag{6.88}$$

At $\kappa = 1$ the previously discussed cancellations occur in R_Δ, *cf.* Eq. (6.57). For $\kappa > 1$ the leading order is known to never vanish (even for non-maximal ℓ) and always dominates over the logarithmic NLO term. This parametric UVi agrees with the introductory result above from integrating the approximate wave functions. The result in Eq. (6.87) is universal for $a = 0, 1, 2$ and $\ell = n-1$ and is assumed to generalize to higher partial waves as well as to higher multipoles as long as $a \ll n$. Functional differences of non-maximal ℓ cross sections are primarily the presence of $|F_+(0)|^2$ which is well behaved in relevant parameter ranges, yet analytic proofs of UVi in other BSF processes than $n = \ell + 1$ were not pursued any further.

The large-n expansion neglects suppression by small numerical constants such as powers in α_b or g^{eff}_a. In practice, these can give rise to prefactors which need to be overcome by the $\sqrt{n}$ enhancement before unitarity can be violated. However, as long as the spectrum supports sufficiently high excitations which are well approximated by Coulomb wave functions, UVi will occur eventually. Conversely, since g^{eff}_a and α_b are in general independent parameters, for sufficiently small g^{eff}_a any given bound state formation process does respect unitarity. In agreement with the single-peak shape of the maximal-ℓ bound state seen in Fig. 6.5 (red curve), the violation from a single bound state can only occur in the vicinity around the peak position before strong suppression sets in. Nevertheless, this does not imply that UVi vanishes to a range of measure zero for large n. Unitarity violating velocity ranges of neighboring energy levels $n, n \pm 1$ eventually overlap such that unitarity is continuously violated at all velocities below a certain critical value when considering inclusive processes into any n.

6.4.2 Unitarity bounds from exclusive processes

In this subsection, UVi in exclusive processes and the dependence on ζ_n an κ will be studied, focusing on maximal angular momenta. To perform a concrete numerical study, still a value for the BSF mediator coupling Wilson coefficient g^{eff}_a must be chosen. Relating to models of theoretical interest, g^{eff}_a is chosen according to the common case of dipole interactions sourced by gauge interactions among fundamental fields. As will be shown later on, see Eqn. (6.101) and (6.102), the

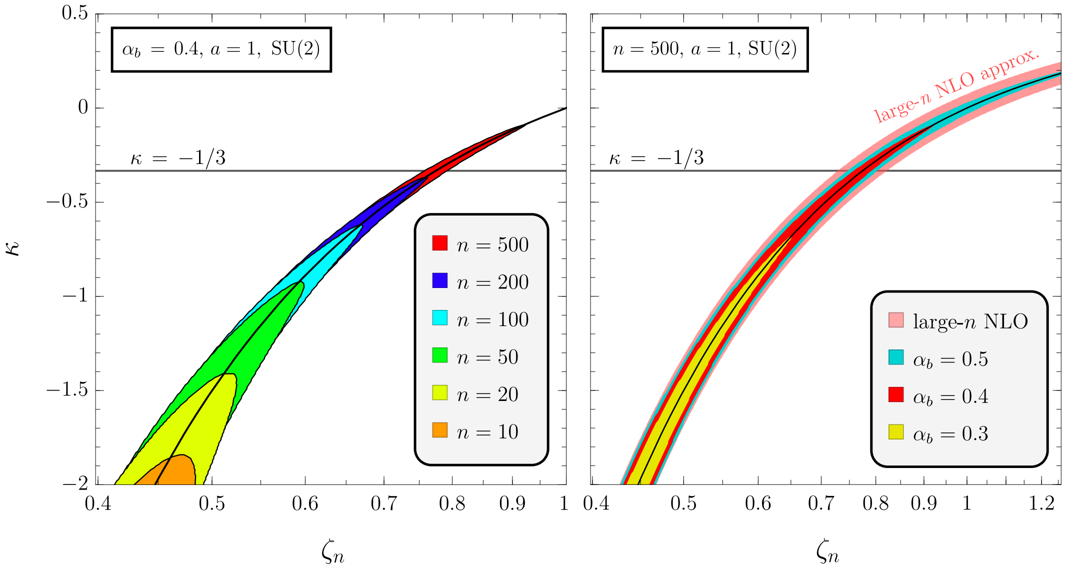

Figure 6.6: Parameter space ζ_n-κ with highlighted areas of unitarity violation in dipole mediated BSF process of SU(2)-like doublet heavy scalars into bound states with $\ell = n - 1$, $\Delta = a = 1$. κ is varied freely with $\kappa = -1/3$ corresponding to true SU(2). The central black line gives the large-n maximum, Eq. (6.85). *Left*: Different n at fixed coupling $\alpha_b = 0.4$. *Right*: Different α_b at fixed $n = 500$ and (light red) the result of the large-n NLO approximation, Eq. (6.87). Vertical axis identical to left panel.

results of scalar interactions derived above can exactly describe this case, provided the multipole mediator gauge boson is treated fully inclusively. The replacement

$$g_1^{\mathrm{eff}} \to \frac{\sqrt{2}}{N_c}\sqrt{4\pi\alpha_b} \tag{6.89}$$

then captures initial state averages for (anti-)fundamental particles and final state polarization sums. The model is still only “SU(N_c)-like” since in genuine gauge theories also $\kappa = \kappa(N_c)$ is fixed by gauge symmetry, whereas here $\alpha_s = \kappa\alpha_b$ is still considered a free parameter. For brevity, simply SU(N_c) is denoted for scans in κ where this difference is obvious. Note that $\kappa(N_c)$ would even pick up a n-dependence if running coupling effects were included in the analysis. In respect to this point, it is important to stress that UVi can indeed be found at scales above the Landau pole of the theory and thus remains a relevant independent theoretical problem. Since all multipole interactions are spin-independent at leading order, treating scalar constituents is actually identical to treating spinful constituents and summing all spin eigenstates analogously to the magnetic quantum number, $\sum_m \to \sum_{s,m}$.

Fig. 6.6 shows in both panels the same parameter space plane in ζ_n-κ with the analytic peak position, Eq. (6.85), as a black line and, in the right panel, also the estimated regime of UVi from the NLO expansion in Eq. (6.87) as a light red shaded area. This estimate neglects all couplings or numerical factors as being of order $\log(\mathcal{O}(1)) = 0$. The horizontal gray line $\kappa = -1/3$ gives the value of genuine SU(2) interactions for fundamental constituents. The different colored areas show where LO perturbative BSF by dipole interaction into maximal angular momentum states, $n = \ell + 1 = \ell'$, violates the partial-wave unitarity bound. The left panel shows different $n \leq 500$ for fixed $\alpha_b = 0.4$. The right panel fixes $n = 500$ and shows different α_b, as listed. Hence, the red area is identical between both panels. Again the rather large value of α_b eases illustration but is not required for UVi. At a given point of α_b and κ, which means a specific theoretical model of interactions in the Lagrangian, higher n yield horizontally thinner areas of UVi simply translating the fact that the peaks in terms of $\log(\zeta_n)$ get ever sharper with higher n.

For a fixed value of κ, the colored part along the corresponding horizontal line shows the regime of UVi, meaning it gives the range of ζ_n where the single peak of the maximal-ℓ BSF cross-section exceeds the partial wave unitarity bound. The red part of the line $\kappa = -1/3$ was thus already seen in Fig. 6.5 by the red curve $\ell = 499$. As also indicated by the vertical dashed line there, the UVi range is centered around the peak position, however now Fig. 6.6 validates the numerical results of previous sections along the entire contour in ζ_n and κ for many n.

For too small $n < 10$, no UVi is found at $\alpha_b = 0.4$ in the exclusive processes considered here which are summed neither in n nor ℓ. More negative $\kappa \ll -1$ enhance the cross-section and formation of already more deeply bound states (lower n) violates unitarity. The reason why the colored areas in the right panel are not coincident with the large-n prediction is the non-negligible smallness of even α_b. The large-n prediction becomes more accurate as $\log(\alpha_b) \to 0$ with UVi regions extending to higher ζ_n as well as shrinking in width to reside within the analytic NLO estimate.

In applications, it is frequently of primary concern to not violate unitarity in a set velocity range, for example at typical velocities of DM in galactic halos for indirect detection searches or $\mathrm{v} \gtrsim 2/\sqrt{20}$ in the usual WIMP freeze-out paradigm. Due to the analytic large-n scaling of the cross section on peak with $\sqrt{n}$ relative to the unitarity bound, one can conveniently estimate at which n, and thus below which velocities, the exclusive maximal-ℓ BSF process will violate unitarity as long as the value of the BSF cross-section is known on-peak for some $n \gtrsim 3$. For instance from Fig. 6.5 the cross section $(\sigma \mathrm{v})^{1,1}_{500,499} = 1.5(\sigma \mathrm{v})^{\mathrm{uni}}_{500}$ from which the reversed logic predicts that $n \lesssim 500/1.5^2 = 222$ should just barely respect the unitarity bound. This is in good agreement with the blue region, $n = 200$, in Fig. 6.6 reaching only below $\kappa = -1/3$.

Additionally, the parameter space analysis of Fig. 6.6 emphasizes that $\kappa = 0$, the free initial state without Sommerfeld enhancement, is not exempted from violating unitarity and, here, behaves unremarkably uniform. The processes computed for Fig. 6.6 take $n = \ell + 1$, where aphelion- and perihelion-matching solution $(\zeta_n)_{A,P} = (1 - 2\kappa)^{-1/2}$ become nonphysical for $\kappa \geq 1/2$, hence the central black lines approach $\kappa = 0.5$ at $\zeta_n \to \infty$. For lower $\ell \to 0$, $(\zeta_n)_P$ becomes nonphysical already at lower $\kappa \to 0$, describing the fact that in absence of Sommerfeld suppression, the final maximum does not form. For $\kappa \geq 1$, also the aphelion solution is always imaginary and no efficient BSF is ever found. Lastly, $\kappa = 0$ may cause numerical complications if treated carelessly, as here many cancellations and simplifications arise to reduce the complexity of an interacting initial state to nothing but a Fourier mode. However, these are mathematical complications with no

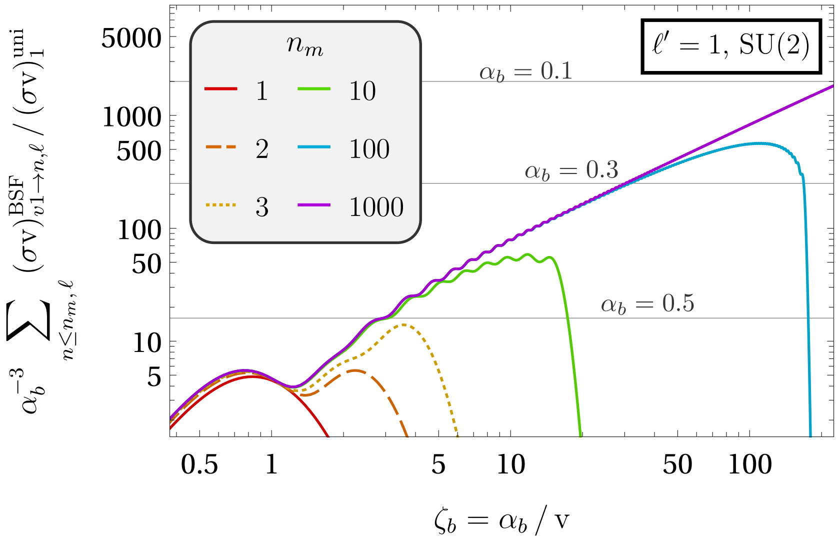

Figure 6.7: Inclusive p-wave ($\ell' = 1$) bound state formation cross-sections normalized by $\alpha_b^3(\sigma\mathrm{v})^{\mathrm{uni}}_1$ and summed in $n \leq n_m$ and $\ell = \ell' \pm 1$, plotted over ζ_b for a SU(2) model ($\kappa = -1/3$). Different values of n_m are shown as tabulated in the legend. Unitarity limits for three values $\alpha_b = 0.1$, 0.3, 0.5 are marked by horizontal lines.

attached physical interpretation.

6.4.3 Unitarity bounds from inclusive processes

The partial wave unitarity bound in Eq. (6.76) constrains inclusive inelastic 2-to-2 scattering processes for specific initial state partial waves. Since radiative BSF is by its very nature inelastic, also the inclusive process for a fixed initial state partial wave, $\ell' \to \sum_{n,\ell,m,a}$, is bounded by it.

The BSF cross-section, Eq. (6.28) with I_R from Eq. (6.50), yields an overall dependence on couplings and velocities outside of $\zeta_{b,s}$ of

$$(\sigma\mathrm{v})^a_{p\ell'\to n\ell} \sim \alpha_{\mathrm{BSF}}\,\mathrm{v}^{2a-1} = \mathrm{v}^{-1}\zeta_b^{-2a} \times N_a, \tag{6.90}$$

$$N_a \equiv \alpha_{\mathrm{BSF}}\,\alpha_b^{2a} = \frac{g_a^{\mathrm{eff}2}}{4\pi}\alpha_b^{2a}. \tag{6.91}$$

Dividing by $(\sigma\mathrm{v})^{\mathrm{uni}}_{\ell'}$ cancels the global dependence on M_χ and one power of v^{-1}. The only overall model dependence is now the multiplicative scaling by N_a. In the double-logarithmic presentation of Fig. 6.7, changes in α_b from 1 translate to simple shifts horizontally by $-\log(\alpha_b)$ and vertically $\log(N_a)$. It is, however, more convenient to simply normalize also by N_a to obtain a plot with one fixed, model-independent curve where instead the partial wave unitarity bound is a unique horizontal line for every choice of $\alpha_{\mathrm{BSF}}\,\alpha_b^{2a}$.

The most prominent modification compared to the exclusive process considered up to this point is that, by summing all n, the low-velocity cutoff of the cross section of repulsive initial states vanishes. Although BSF into any specific n is only relevant near the respective perihelion-matching velocity, there exists always another bound state becoming relevant for every lower velocity. Fig. 6.7 depicts BSF cross-sections summed up to different n_m for each curve, all with a fixed $\ell' = 1$, for the case of SU(2) interactions ($a = 1$, $\kappa = -1/3$, $\alpha_{\mathrm{BSF}} = \alpha_b$). The vertical axis shows, according to the above normalizations and Eq. (6.89),

$$\alpha_b^{-3} \sum_{n=1}^{n_m} \sum_{\ell=0,2} \frac{(\sigma \mathrm{v})^a_{\mathrm{v}1\to n\ell}}{(\sigma \mathrm{v})^{\mathrm{uni}}_1}. \tag{6.92}$$

The momentum suffix on the cross section is replaced by just the relative velocity v since there is no more mass dependence in the shown results. Unitarity bounds for $\alpha_b = 0.5, 0.3, 0.1$ are shown by horizontal lines and even smaller couplings are less constraint and lie higher up in the plot. Each curve cuts off once the respective n_m-th perihelion is matched while larger n_m still extend to smaller velocities. At lower values of ζ_b, more and more n_m still overlap. This convergence allows to use a finite n_m to get reliable results for relatively low values of ζ_b. A comparison of, for example, the solid green curve $n_m = 10$ to the blue or purple results of $n_m = 100, 1000$ shows that notable differences to higher n_m arise already long before the maximum of the highest bound state is reached and the range of reliability is not set by $\zeta_b < (\zeta_{n_m})_P$ but much smaller. Also the enhancement of the inclusive cross-section over the exclusive scenario may be estimated from comparing the last oscillation of $n_m = 10$, *i.e.* the right-most maximum of the green curve at $\alpha/\mathrm{v} = 15$ from $n = 10$ which remains visible even once all other n are exponentially suppressed, to the results with larger n_m. Already at $n = 10$, including higher n increases the cross section by a factor of about 2 and more so at higher n. Nonetheless, the results for $n_m = 100$ and 1000 still coincide at this point, demonstrating a convergence of the inclusive result for high enough n_m.

At low velocities, sufficiently high n_m converge to a power-law like slope which, eventually for very high n_m, will overcome any constant horizontal unitarity bound even for small $\alpha_b \ll 1$.

The oscillatory behavior of the first few bound states is always clearly resolved, yet the summation over many n eventually washes out all features seen in exclusive processes. Most notably, the $n = 1$ peak remains clearly distinguishable for any n_m, dominating the regime around $\alpha_b = \mathrm{v}$. This particularity possibly provides an explanation for why the importance of excited bound states has long been overlooked in studies of non-Abelian DM annihilation. Starting with expectations biased by Abelian interactions where $n = 1$ dominates at all velocities, one does indeed also here observe a dominant contribution of the ground state at largest v and the maximum of the $n = 1$ bump is hardly affected by summing all $n > 1$. The converged behavior emergent at lower velocities from summing n was therefore unforeseen. This power-law like increase of the inclusive cross section at small v suggests that an analytic form may be found by performing a summation in n over the exclusive BSF cross-sections. Yet in light of the found violation of unitarity, the need of additional corrections to the calculated results is apparent and this avenue is not pursued any further in this thesis.

With n and ℓ summed over and all explicit model dependence normalized off by N_a, it is possible to give general results for unitarity constraints as two-dimensional contour plots in the remaining plane of ζ_b-κ. Most intuitively, the contours should indicate the maximally allowed value of the coupling strength. If α_b was identical

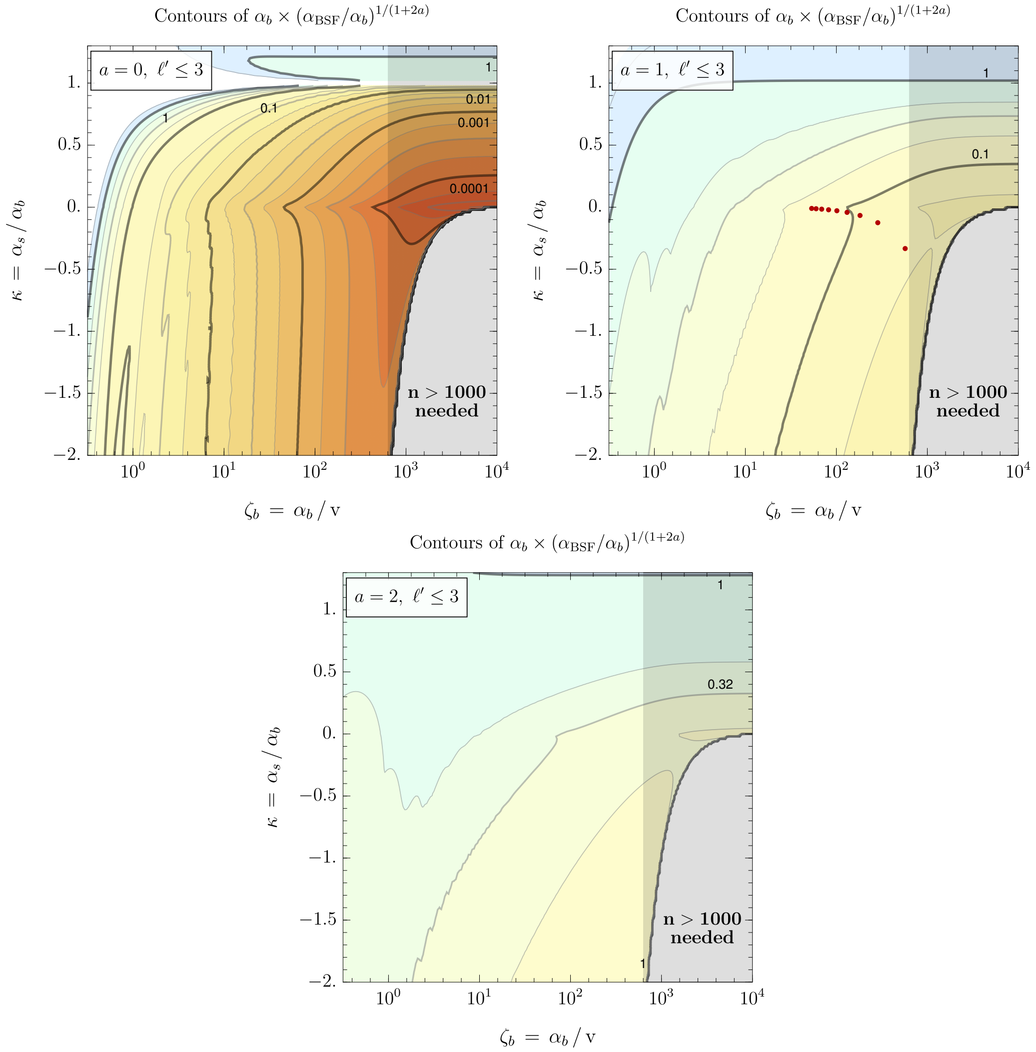

Figure 6.8: Strongest upper bounds on $\alpha_b \times (\alpha_b/\alpha_{\rm BSF})^{1/(2a+1)}$ from any combination of ℓ' partial-wave unitarity bounds, including $\ell' \leq 3$, shown as contours in parameter space ζ_b-κ. *Left panel*: Monopole ($a = 0$). *Right panel*: Dipole ($a = 1$). *Bottom panel*: Quadrupole ($a = 2$). Gray-shaded areas approximate unreliable regions where $n > 1000$ are significant. Contours are in logarithmic steps of $10^{1/4}$ and coloring agrees among all panels. Red points denote velocity bounds for $\alpha = 0.1$ in SU(N_c), $N_c \leq 10$, see Fig. 6.9.

to $\alpha_{\rm BSF}$ this instructs to take the "2a+1"-th root. Although $\alpha_{\rm BSF}$ is independent, it is still convenient to follow this idea, as it renders different multipoles into the same order of magnitude. A single contour plot will thus depict the maximal value of $\alpha_b \times (\alpha_{\rm BSF}/\alpha_b)^{1+2a}$ allowed by the unitarity bound. Phrased in terms of the computed cross sections, this means desired contours for specific a and ℓ' are

$$\left[\sum_{n=1}^{n_m}\sum_{\ell=\ell'\pm a}\frac{1}{N_a}\frac{(\sigma \mathrm{v})_{v\ell'\to n\ell}}{(\sigma \mathrm{v})^{\rm uni}_{\ell'}},\right]^{\frac{-1}{2a+1}}. \tag{6.93}$$

Yet, there is more to be done, since every ℓ' is to obey its unique unitarity bounds but also a sum in ℓ' must obey the summed bounds $\sum_{\ell'}(\sigma \mathrm{v})^{\mathrm{uni}}_{\ell'}$. Mathematically, the strongest constraint is the obtained from the maximum over the power set of the range of some ℓ'_m. Introducing $\mathcal{P}(\ell'_m)$ to be the power set (excluding the empty set) of $\{0, 1, ..., \ell'_m\}$, that is $\mathcal{P}(1) = \{\{0\}, \{1\}, \{0, 1\}\}$, etc., the maximal violation considering all partial waves up to ℓ'_m is given by

$$C_{a,\ell'_m}(\zeta_b, \kappa) \equiv \max_{S\in\mathcal{P}(\ell'_m)} \left\{ \frac{1}{N_a} \frac{\sum_{\ell'\in S} \sum_{n=1}^{n_m} \sum_{\ell=\ell'\pm a} (\sigma \mathrm{v})_{v\ell'\to n\ell}}{\sum_{\ell'\in S} (\sigma \mathrm{v})^{\mathrm{uni}}_{\ell'}}, \right\}. \tag{6.94}$$

Hence, the three panels of Fig. 6.8 each assume a specific multipole interaction $a = 0, 1, 2$ (left, right, bottom) and scan the parameter space for the strongest possible bound where all $\ell' \leq 3$ and $n \leq 1000$ are considered, plotting contours of

$$[C_{a,3}(\zeta_b, \kappa)]^{\frac{-1}{2a+1}} . \tag{6.95}$$

For most parts, especially for all qualitative features, obtained bounds are identical to the simpler s-wave unitarity bounds, $\ell' = 0$ in Eq. (6.93). Slightly stronger bounds arise only at low $\zeta_b \lesssim 10$ (meaning before the converged regime is reached). At large ζ_b, inclusive partial wave BSF cross-sections are almost identical but still obey a sorting in ℓ', see the lower panel in Fig. D.6 in App. D.2. This causes the s-wave bound to be dominant. The color coding in Fig. 6.8 is chosen to transition from blue to orange around the value $N_a/4\pi = 0.5^{2a+1}$, thus marking in darker blue regimes where perturbation theory in α_b becomes increasingly unreliable. Most notable is the systematic enhancement of BSF towards low velocities as long as $\kappa < 1$, converging to the power-law like growth seen in Fig. 6.7. The more densely stacked the contours are along a horizontal line of constant κ, the stronger is the corresponding converged-to power law. The color intensity in Fig. 6.8 along the single horizontal slice $\kappa = -1/3$ is therefore approximately a projection of the vertical values plotted in Fig. 6.7, up to normalizations.

For perturbative coupling strengths, BSF exceed the unitarity bound only at larger α_b/v. The Abelian case $\kappa = 1$ never violates unitarity for perturbative couplings and gives rise to a horizontal cut in the parameter space for $a = 0$ where the orthogonal wave function overlap is identically 0. The region $\kappa > 1$ shows no unexpected UVi, even in the inclusive cross section, in agreement with the analytic finding above that the leading order large-n expansion is strictly exponentially suppressed here. For less attractive initial states, $0 < \kappa < 1$, perturbative UVi is found arbitrarily close to the Abelian case provided sufficiently large α_b/v are considered. Already from Fig. 6.7, it is understood that such small velocities (thinking of constant α_b in a specific model) require extremely highly excited states n. A second horizontal feature in the contours is recognized at the free initial state $\kappa = 0$, showing stronger unitarity constraints on α_b, contrary to typical notions of well-behaved non-interacting states. $\kappa = 0$ is significant due to this additional enhancement but, as pointed out earlier, an otherwise smooth point in the parameter plane and well described in PNREFT. At low $\alpha_b/\mathrm{v} \sim 1$, remnants of the oscillatory features are still noticeable, *cf.* Fig. 6.7. In particular, the ground state peak can be separated clearly in the left panel ($a = 0$) as vertical features present at $\kappa < -1$. For negative κ, low n are exponentially suppressed at large ζ_b, hence there is a white region in the bottom right corner of each panel, where

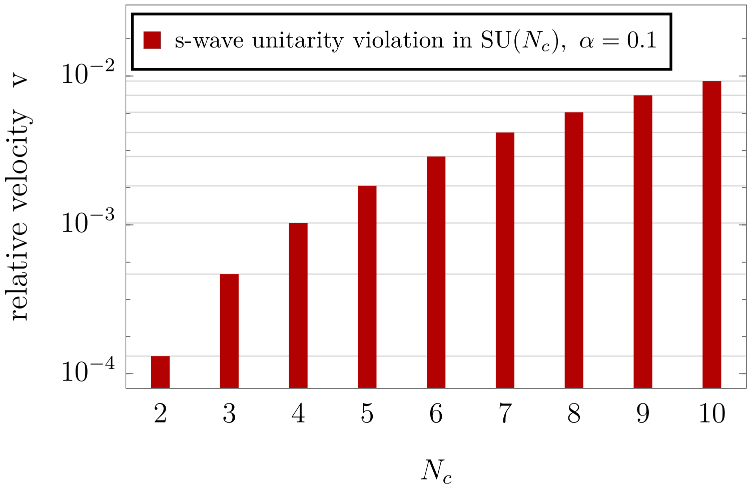

Figure 6.9: S-wave unitarity exclusion bounds on relative velocity v from inclusive bound state formation processes of heavy fundamental SU(N_c) constituents ($\mathbf{F}\bar{\mathbf{F}}$) with a gauge coupling strength $\alpha = 0.1$, *i.e.* $\alpha_b = (N_c^2 - 1)/2N_c\,\alpha$, $\alpha_s = -\alpha/2N_c$.

$n_m = 1000$ becomes insufficient. In the range of large ζ_b but $\kappa > 0$, simple Sommerfeld scaling is instead approached and, due to the normalization by $(\sigma \mathrm{v})^{\mathrm{uni}}$, contours turn horizontal, *cf.* Fig. 6.1. Nevertheless, results at such low velocities for $\kappa > 0$ are equally untrustworthy as for $\kappa < 0$. Higher n will give rise to stronger unitarity bounds such that reliable contours never become horizontal even in a close vicinity of $\kappa = 1$. Analytically, this is evident from Eq. (6.57), where setting $\kappa = 1 + \epsilon$ will still yield UVi once $n\epsilon \gg 1$. Thus, at any finite distance ϵ will very low velocities give rise to unitarity violation for arbitrary couplings and the inclusive cross section must always diverge relative to the unitarity bound as $\zeta_b \to \infty$.

The qualitative behavior of the contours stabilizes for $\kappa < -1$ and no significant new features are expected for strongly repulsive initial states. All features observed in the depicted parameter space are clearly understood as the limits for Abelian or free processes, oscillatory remnants and artifacts of finite n_m. The bounds on higher multipoles are weaker due to the systematically power suppression in v, which here gets rephrased into α_b^{2a}. While the above qualitative analysis still applies, quadrupole BSF respects the unitarity bound for any values of $\alpha_b \leq 0.1$ in the reliable depicted parameter space. The red marking in the right panel for dipole interactions relate to Fig. 6.9.

Returning finally to a representation more directly applicable to phenomenological results, Fig. 6.9 shows which relative velocities are incompatible with s-wave unitarity in leading order BSF formation for different SU(N_c) gauge theories for a gauge couplings strength of $\alpha = 0.1$. The scattering and bound states are formed by a particle anti-particle pair transforming under the fundamental representation which sets $\alpha_{s,b}$ and $\kappa = 1(1 - N_c^2)$ by gauge symmetry, see Eqn. (6.99) and (6.100) in section 6.5 below. Fig. 6.9 is thus discrete on the horizontal N_c-axis and marks the ranges of initial state relative velocities in which partial wave unitarity is violated in BSF at the perturbative leading order. Corresponding red markers in Fig. 6.8 (right panel, $a = 1$) show the minimal allowed relative velocity projected to the κ-ζ_b plane. (Effectively, the parameter space depiction in Fig. 6.8 is rotated 90° clockwise in Fig. 6.9.) The shown results include $n \leq 2000$ and were ensured to not change appreciably by inclusion of $n \leq 10^4$ ($n \leq 6000$) for $N_c = 2$ ($N_c = 10$). Once $N_c \gtrsim 1/\alpha$ the effective coupling α_b becomes non-perturbative. For high $N_c \geq 5$ already typical galactic-center DM velocities of $\mathrm{v} \sim 10^{-3}$ violate unitarity when including very high bound states, $n \geq 500$.

In light of $N_c = 10$ giving rise to rather large $\alpha_b = 0.495$, a different approach by use of the t'Hooft limit of large N_c comes to mind, imposing $\alpha_b = \text{const}$. Opposed to $\alpha = \text{const}$. the cross section now scales as [140]

$$(\sigma \mathrm{v})^{\text{t'Hooft}}_{\text{BSF}} \propto \frac{\alpha_{\text{BSF}}}{N_c^2}\bigg|_{N_c \gg 1} \propto \frac{\alpha_b}{N_c^2}\bigg|_{N_c \gg 1} \to 0. \tag{6.96}$$

Thus, BSF vanishes at large N_c and unitarity remains intact in the t'Hooft limit.

This section investigated theoretical self-consistency from 2-particle scattering unitarity, which requires fixing the initial state partial wave ℓ'. For the following sections of this chapter, radiative capture cross-sections into a specific *final state* $\mathcal{B}_{n\ell}$ is of interest, which no longer bounded directly by Eq. (6.76) as ℓ' is now being averaged over. The analyses in the following still consider highly excited states but were ensured to not be in conflict with unitarity constraints.

6.5 Eternal depletion via BSF in the early universe

This section derives a breakdown of the traditional freeze-out paradigm as introduced in subsection 1.2.1 in dark SU(N_c), $N_c \geq 3$, gauge theories of heavy particles still within the regime of perturbative couplings caused by the inclusion of BSF in depletion processes. To be precise, the freeze-out paradigm is understood to result in a stable late time abundance which has undergone complete chemical decoupling and its applicability to bound-state enhanced depletion breaks down since no such regime is reached in the absence of other physical effects, for example a phase transition.

The first three subsections set up the required formalism for the used particle-abundance Boltzmann equations, the thermally averaging procedure and the effective annihilation cross-section. Finally, subsection 6.5.4 demonstrates scenarios in which the assumption of chemical decoupling implicit in thermal DM production is not fulfilled when including BSF into highly excited states. This introduction describes how above results for BSF cross-sections need to be adapted to gauge boson BSF mediators and gauge-multiplet constituent fields.

Effects of bound state formation at the TeV-scale and above on early Universe dynamics related to dark matter production have drawn increasing attention in the last decade. A wide range of models has been studied, primarily (dark) Abelian [152–155] and non-Abelian [32, 35, 147, 148, 156–162] gauge interactions affecting either the production mechanism of DM directly or that of a BSM partner particles (primarily for colored coannihilation [136, 140, 148, 163–171]). Also scalar interactions have been studied which give rise to quadrupole [61, 138, 172–174] or even monopole transitions [144, 175].

Under the assumption of kinetic equilibrium [20, 21, 176–178] of the relevant dark sector particles, the DM relic abundance (1.1) can be computed from Boltzmann equations governing the abundance evolution of all particle species in the early Universe plasma. The assumption is usually easily justifiable by elastic bath scattering via the same interactions which give rise to Sommerfeld enhancement and bound state formation. To allow a description of the complete plasma by a single temperature parameter, the kinetic equilibrium must also be maintained with the SM bath. Hence, the number of light degrees of freedom of the SM have to be included in the calculation accordingly. Temperature takes the role of a time coordinate by introducing the Hubble rate $H(T) = \dot{a}/a$ as a temperature dependent function. Since for this and the following section only the chemical decoupling of the heavy bound state constituents from a “dark” BMS sector is of interest, it is useful to measure the temperature in terms of the heavy particle mass, introducing

$$x \equiv \frac{M_\chi}{T}. \tag{6.97}$$

For section 6.6, the numerator becomes $M_{\tilde{q}}$.

Both sections regard bound state formation between particle anti-particle pairs in the early universe, which transform under the fundamental representation of some dark non-Abelian SU(N_c) gauge symmetry, see for example [75]. The constituents are here taken to be fermions ($s_\chi = 1/2$) which impacts bound state decay rates to massless gauge bosons. The Lagrangian for the constituents is thus given by $\mathcal{L}_{\mathrm{PNR}}[\chi]$ from Eq. (2.9) where now χ is a gauge N_c-plet transforming under the fundamental representation of the dark gauge symmetry. The two-constituent space of particles $\chi_{a,b}$ with representations $\mathbf{R}_{a,b}$ decomposes into separate irreducible representation $\hat{\mathbf{R}}$ and gives rise to an effective coupling in terms of the quadratic Casimir constants [148, 179]

$$\alpha^{\mathrm{eff}}_{[\hat{\mathbf{R}}]} = \frac{C_2(\mathbf{R}_a) + C_2(\mathbf{R}_b) - C_2(\hat{\mathbf{R}})}{2} \times \alpha \tag{6.98}$$

with α being the dark gauge coupling strength. In particular, for fundamental constituents $\mathbf{F} \otimes \bar{\mathbf{F}} = \mathbf{1} \oplus \mathbf{Ad}$ one gets

$$\alpha_b \equiv \alpha^{\mathrm{eff}}_{[\mathbf{1}]} = \frac{N_c^2 - 1}{2N_c}\alpha = C_F\,\alpha, \tag{6.99}$$

$$\alpha_s \equiv \alpha^{\mathrm{eff}}_{[\mathbf{Ad}]} = \left(C_F - \frac{N_c}{2}\right)\alpha = \frac{-1}{2N_c}\alpha. \tag{6.100}$$

The adjoint representation is always repulsive and, thus, already at this point identified with the initial state species. Since the multipole mediator is now also the SU(N_c) gauge boson, multipole interactions can also affect the representation of the 2-constituent states. While one has $\mathbf{Ad} \subset \mathbf{Ad} \otimes \mathbf{Ad}$, meaning that the adjoint representation can be scattered into itself by bremsstrahlungs processes, $\mathbf{Ad} = \mathbf{1} \otimes \mathbf{Ad}$ defines two important constraints. Firstly, BSF can only take place starting from the adjoint representation which effects $\kappa < 0$. Secondly there are no bound-to-bound transition by single gauge boson emission, nor is there bremsstrahlung between singlet states. Multipole interactions are equally sourced by vector bosons. The leading term is the dipole interactions with an effective coupling

$$g_1^{\text{eff}} = \sqrt{4\pi C_F\,\alpha}. \tag{6.101}$$

Additionally, one must adapt the BSF cross-section (6.28) to include the initial state average of each fundamental constituent, and factors for decoherently summing over the polarizations of the emitted vector boson ($g_A = 2$) and the bound state spin polarization ($g_{\mathcal{B}}$),

$$(6.28) \;\longrightarrow\; (6.28) \times g_A\, g_{\mathcal{B}} \left| \frac{1}{\sqrt{(2s_\chi + 1)N_c}^{2}} \right|^2 \equiv (6.28) \times \frac{2}{N_c^2}\xi\,. \tag{6.102}$$

This relation relates dipole, $a = 1$, BSF processes of scalar BSF mediator to gauge boson BSF mediators. At higher multipoles, instead a factor $(a + 1)/a$ arises in place of the simple factor 2 [180]. ξ takes care of spin degrees of freedom of the bound state, $\xi = 1/4$ for capture into a spin-singlet and $\xi = 3/4$ for capture into a spin-triplet state. When considering the inclusive BSF cross-section irrespective of spins, $\xi = 1$ may be used directly. However, in the effective cross section discussed in the following, spin-singlet and -triplet bound states must be treated as separate particle species as they generally differ in their decay rates, thus making a final state spin summation inapplicable.

This replacement to incorporate the effects of initial state gauge multiplets and vector-boson mediator polarizations was already used in Eq. (6.89), setting $\xi = 1$ as scalar constituents were treated.

6.5.1 Boltzmann equations under steady-state approximation

When considering only the first moment of the phase-space distributions [177], the number density n_X of a particle species X, Boltzmann equations are typically rewritten as a temperature evolution of the abundance Y. Every particle species is technically to be treated separately, however there is no difference between particles and their respective anti-particles for the models of interest in this thesis such that one can write

$$Y_X(x) = \frac{n_X(x) + n_{\bar{X}}(x)}{s(x)} = \frac{g_X + g_{\bar{X}}}{g_X}\frac{n_X(x)}{s(x)} = \frac{2n_X(x)}{s(x)}, \tag{6.103}$$

where $\bar{X}$ denotes the anti-particle of X, g their internal degrees of freedom and $s(x)$ is the entropy density [181]. The respective Boltzmann equation takes the form

$$\frac{\mathrm{d}\,Y_X}{\mathrm{d}x} = \frac{1}{3H}\frac{\mathrm{d}s}{\mathrm{d}x}\left[\frac{1}{2}\langle\sigma_{\text{ann}}\text{v}\rangle\left(Y_X^2 - Y_X^{eq\,2}\right) + \langle\text{“number-changing reactions”}\rangle\right] \tag{6.104}$$

where only the typical annihilation term is given explicitly. The factors of $2^{1-|N|}$ in front of processes where $n_X + n_{\bar{X}}$ particle number is changed by N units are a consequence the definition in Eq. (6.103) [140]. While scattering eigenstates of energy $K = M_\chi \mathrm{v}^2/4$ follow a thermal distribution, each bound state counts as its own unique particle species, since they differ in their various reaction rates. At the same time, different angular momentum eigenstates must also be kept separate, treating $n_{n\ell}(x)$, because their reaction rates depend on ℓ. Note that for particle anti-particle bound states there is no distinct anti-bound state, $\mathcal{B}_{n\ell} = \bar{\mathcal{B}}_{n\ell}$. Magnetic quantum numbers do not affect any processes under consideration and can therefore be included as a simple internal degree of freedom in $n_{n\ell}$. No 2-bound-state (4-constituent particle) processes are of significance, so there is no additional subtlety as above from an inclusion of the magnetic multiplicity.

As long as all light degrees of freedom are efficiently kept in equilibrium at temperatures far above their mass scale, it is viable to simply approximate their abundances by the equilibrium attractor solution of the Boltzmann equations [20],

$$n_X(x)|_{\text{light}} \approx n_X^{eq} \equiv g_X \frac{M_\chi \, m_{\text{light}}^2}{2\pi^2 x} K_2\left(\frac{m_{\text{light}}}{M_\chi} x\right), \tag{6.105}$$

K_2 being the modified Bessel function of second kind.

Imposing a quasi steady state assumption, which approximates there to be efficient equilibration process between the various bound states such that $\mathrm{d}Y_{n\ell}/\mathrm{d}x \approx 0$, one can solve for their abundances in Eq. (6.104) algebraically. The assumption is in fact rather weak as it only requires one of the processes to be efficient at any given point in time as long as one of the thus efficiently-coupled states is also maintaining equilibrium with the (SM) plasma. The network of Boltzmann equations for bound states can now be included as only a single effective cross section $\langle \sigma_{\text{BSF}} \mathrm{v} \rangle$. This ansatz of including excited states was separately formalized to include the three bound state processes, bound-to-bound transitions, bound state decay and ionization, in the two works [140] and [182]. The notation for the present thesis follows the former. The Boltzmann equation describing the abundance evolution in the dark sector then takes the simple form

$$\frac{\mathrm{d}\, Y_X}{\mathrm{d}x} = \frac{1}{3H} \frac{\mathrm{d}s}{\mathrm{d}x} \frac{1}{2} \langle \sigma \mathrm{v} \rangle_{\text{eff}} \left(Y_X^2 - Y_X^{eq\,2} \right), \tag{6.106}$$

where

$$\langle \sigma \mathrm{v} \rangle_{\text{eff}} \equiv \langle \sigma_{\text{ann}} \mathrm{v} \rangle + \langle \sigma \mathrm{v} \rangle_{\text{BSF,eff}} \tag{6.107}$$

and the angle brackets indicate the thermal average. The detailed definition of $\langle \sigma \mathrm{v} \rangle_{\text{BSF,eff}}$ is given in subsection 6.5.3. Beforehand, some intricacies of the thermal averaging procedure are discussed.

6.5.2 Thermal averaging procedure for highly excited bound states

The thermally averaged cross section of radiative capture by emission of a single dark gauge boson into a particular bound state $\mathcal{B}_{n\ell}$ yields

$$\begin{aligned} \langle \sigma_{n\ell} \mathrm{v} \rangle &= \left(\frac{M_\chi}{4\pi T} \right)^{\frac{3}{2}} \int \mathrm{d}^3 \vec{\mathrm{v}}\, \mathrm{e}^{-\frac{x v^2}{4}} \left[1 + f(\omega) \right] \, (\sigma \mathrm{v})^{\text{BSF}}_{p\ell\pm1\to n\ell} \\ &= \left(\frac{x}{4\pi} \right)^{\frac{3}{2}} \int_{\mathrm{v}_{\min}}^{\mathrm{v}_{\max}} \mathrm{d}^3 \vec{\mathrm{v}} \, \frac{1}{\mathrm{e}^{\frac{x}{4}\mathrm{v}^2} - \mathrm{e}^{-\frac{E_n}{T}}} \, (\sigma \mathrm{v})^{\text{BSF}}_{p\ell\pm1\to n\ell} \, . \end{aligned} \tag{6.108}$$

where the distribution functions of the initial and final states are combined into a single term, using $f(\omega) = 1/(\mathrm{e}^{\omega/T} - 1)$ and $\omega/T = x\mathrm{v}^2(1 + \zeta_n^2)/4$. While the thermal distribution functions of the non-relativistic particles have been approximated by Maxwell-Boltzmann distributions, this is not applicable to the emitted massless BSF mediator as the region $T \sim E_n \sim K$ is of significance. The physical lower boundary of the integration is naturally 0. The upper limit of the integral is physically bounded by $\mathrm{v}_{\max} \leq 1$, yet in the non-relativistic approximation there is no sensitivity to relativistic corrections and, to remain consistent with this picture, v would have to be integrated to ∞. Since BSF is suppressed at large velocities, this modification has little impact on the final results given large enough $\mathrm{v}_{\max}$. To make numerical evaluation more efficient, the distribution function is also cut off for temperatures $T < E_n/100$ at which point the exponential Boltzmann suppression is strong. Moreover, the highly oscillatory behavior of BSF cross-sections poses a challenge to numerical integration methods. This problem has been dealt with by splitting the considered velocity range $10^{-5} \leq \mathrm{v} \leq 10^{0.3}$ into a number of logarithmic equidistant steps. These steps help numerical routines by reducing the number of oscillations per step but also allow more manual control than fully automated samplings of the integration range. Knowing the total number of roots to be $n - \ell - 1$, a convenient step size has been found to be $4\log(\mathrm{v}_{\max}/\mathrm{v}_{min})/(n - \ell + 9)$. The offset by $+9$ ensures efficiency when only few oscillations are present and the prefactor 4 sets the expected mean number of roots in each integration step to be 4. Such an estimate assumes all roots to be homogeneously distributed across the complete integration regime. This is evidently not satisfied, as seen in Fig. D.4 but serves sufficiently well for practical purposes. To additionally avoid useless evaluation of lower n all the way until $\mathrm{v} = 10^{-5}$, the following automatic stop-condition was introduced making use of the systematic behavior of the BSF cross-section. Neglecting oscillations, the enveloping behavior of non-Abelian BSF cross-section increases monotonically until the global maximum is reached. Therefore, avoiding all reliance on the semi-classical aphelion or perihelion estimates, all smaller velocity integration steps $m > l$ are neglected once the integral I_l of the presently computed step l fulfills

$$\frac{n - \ell + 9}{4} I_l \; < \; 10^{-3} \sum_{k \leq l} I_k. \tag{6.109}$$

This condition estimates that even if all steps contribute the present amount to I_l, the total effect on the already summed integral is less than 0.1%, effectively targeting a sub-percent precision. More efficient choices may be built exploiting the aphelion and perihelion positions $(\zeta_n)_{A,P}$ found in section 6.3. High n are most expensive to compute and thus most important to properly constrain in their integration range. To this end, the steep exponential suppression beyond the perihelion helps with the above condition. Additionally, the lower boundary to the integration range, $\mathrm{v} \geq 10^{-5}$, was adjusted specifically to the maximal $n = 1000$ ($\ell = 0$) states included in the analyses. Typical coupling strengths are $\alpha \sim 0.3 - 0.01$, such that $\mathrm{v}_{\min} = 10^{-5} \leq \alpha/n$. Note that for all $N_c > 2$ on additionally has $\alpha_b > \alpha$.

The fact that the roots are not logarithmic equally spaced means there are significantly more than only 4 roots included in the smallest-velocity steps and a larger step size generates problems with numerical convergence. Performing the integration in reciprocal or logarithmic space of v did not yield significant improvement in stability or efficiency. The numerical integration was performed using "Global Adaptive" routines available by default in MATHEMATICA with adjusted minimal and maximal recursion parameters (2 and 30) as well as precision and accuracy goals (8 and $20 + 2\log(M_\chi)$) to mitigate this. The accuracy goal was scaled with M_χ since the cross section was not normalized to a dimensionless quantity.

6.5.3 Effective cross section

The computation of the effective cross section follows directly [140] (with minor adjustments to the notation) and the central equations are repeated here for completeness. The effective cross section encodes the complete network of Boltzmann equations for all bound states by weighing the thermally averaged BSF cross-section for all bound states $\mathcal{B}_i = \mathcal{B}_{n\ell}$ with an depletion efficiency factor R_i,

$$\langle \sigma \mathrm{v} \rangle_{\mathrm{BSF,eff}} = \sum_{n,\ell} R_{n\ell} \, \langle \sigma_{n\ell} \mathrm{v} \rangle \, . \tag{6.110}$$

R_i captures the interplay of the decay rate Γ_i^{dec}, ionization rate Γ_i^{ion} and also all bound-to-bound transition rates

$$\Gamma_{ij}^{\mathrm{trans}} = \Gamma_{j \to i}^{\mathrm{trans}} . \tag{6.111}$$

The ordering of the indices is relevant since $\Gamma_{ij}^{\mathrm{trans}} \neq \Gamma_{ji}^{\mathrm{trans}}$, for example all excitation processes vanish in vacuum while de-excitations remain possible. More precisely, detailed balance dictates

$$\Gamma_{ji}^{\mathrm{trans}} = \Gamma_{ij}^{\mathrm{trans}} \frac{Y_j^{eq}}{Y_i^{eq}} . \tag{6.112}$$

The chosen subscript ordering allows to think about processes in a vector-matrix notation going right to left from initial to final states. Being an efficiency factor, $R_i \in [0, 1]$ for any i. In practice one finds R_i to increase monotonically, roughly resembling a step function as temperature drops below its the respective binding energy E_n. This is natural since a formed bound state i which can no longer be ionized or excited will only de-excite to even more deeply bound states. Yet, for the effective cross section it is insignificant through which channel a formed bound state decays, thus $R_i \approx 1$. This simple argument is less transparent in the full definition of the depletion efficiency factors

$$R_i \equiv 1 - \sum_j (M^{-1})_{ij} \frac{\Gamma_j^{\mathrm{ion}}}{\Gamma_j^{\mathrm{full}}} \tag{6.113}$$

where

$$\Gamma_i^{\mathrm{full}} \equiv \Gamma_i^{\mathrm{ion}} + \Gamma_i^{\mathrm{dec}} + \sum_j \Gamma_{ji}^{\mathrm{trans}} , \tag{6.114}$$

$$M_{ij} \equiv \delta_{ij} - \frac{\Gamma_{ji}^{\mathrm{trans}}}{\Gamma_i^{\mathrm{full}}} \, . \tag{6.115}$$

As mentioned above, there are no bound-to-bound transitions in the dark $\mathrm{SU}(N_c)$ setup at leading order approximation and $\Gamma_{ij}^{\text{trans}} = 0$. This "no-transitions" limit trivializes M_{ij}. Now,

$$R_i^{\text{no-trans}} = 1 - \frac{\Gamma_i^{\text{ion}}}{\Gamma_i^{\text{full}}} = \frac{\Gamma_i^{\text{dec}}}{\Gamma_i^{\text{dec}} + \Gamma_i^{\text{ion}}} \tag{6.116}$$

is clearly the branching ratio of the decay process for the bound state i. In this limit, the "network" of coupled Boltzmann equations sees all bound states to only be in connection via the free two-particle state species. Using once more the detailed balance condition in thermal equilibrium in form of the Milne relation,

$$\Gamma_i^{\text{ion}} = \frac{s}{4} \frac{\left(Y_\chi^{eq}\right)^2}{Y_{\mathcal{B}_i}^{eq}} \langle \sigma_i \mathrm{v} \rangle \ , \tag{6.117}$$

the ionization rate is easily computed from the thermally averaged BSF cross-section, summed over all initial states and also all possible interactions if there are multiple. This summation removes any dependence on the spin, meaning ξ cancels out in the ionization rate. The decay rate for spin-singlet s-wave bound states $\mathcal{B}_{n0}^{S=1}$ into a pair of gauge bosons AA is [140, 148]

$$\Gamma_{n0}^{\text{dec}} = \Gamma^{\mathcal{B}_{n0}^{S=1} \to AA} \frac{K_1(x)}{K_2(x)} = \Gamma^{\mathcal{B}_{n0}^{S=1} \to AA} + \mathcal{O}(x^{-1}), \tag{6.118}$$

$$\Gamma^{\mathcal{B}_{n0}^{S=1} \to AA} = \frac{M_\chi C_F}{8n^3} \hat{\alpha}(M_\chi)^2 \, \alpha_b^3. \tag{6.119}$$

The ratio of Bessel-K functions encodes the thermal average which, however, tends to 1 for large x effectively negating any influence of the thermal average at $T \ll M_{\tilde{q}}$. In anticipation of the later inclusion of renormalization group running, α_b is kept separate from the gauge coupling strength evaluated at the hard scale $\hat{\alpha}(M)$ in the vacuum decay rate. Spin-triplet bound states will be neglected for the analysis of dark $\mathrm{SU}(N_c)$ interactions in this section since their decay rate is suppressed by one additional power in α [183].

Lastly, annihilation of scattering states into two gauge bosons is possible from singlet as well as adjoint states and given by the short-distance annihilation term and the Sommerfeld factor [135]

$$(\sigma \mathrm{v})_{\text{ann}}^{\ell'=0} = \frac{\pi \hat{\alpha}(2M_\chi)^2}{M_\chi^2} \frac{C_F}{4} \frac{N_C^2 - 2}{N_c^2} \left(\frac{2}{N_c^2 - 2} S_0^{[\mathbf{1}]} + \frac{N_c^2 - 4}{N_c^2 - 2} S_0^{[\mathbf{Ad}]} \right) + \mathcal{O}(\mathrm{v}) \tag{6.120}$$

where the gauge couplings are now evaluated at the center-of-mass energy of the process and the Sommerfeld factors are explicitly

$$S_0^{[\mathbf{1}]} = \frac{\hat{\alpha}(p)}{\mathrm{v}} \frac{2\pi C_F}{1 - \mathrm{e}^{-2\pi C_F \hat{\alpha}(p)/\mathrm{v}}} \,, \tag{6.121}$$

$$S_0^{[\mathbf{Ad}]} = \frac{\hat{\alpha}(p)}{\mathrm{v}} \frac{2\pi (C_F - C_A/2)}{1 - \mathrm{e}^{-2\pi (C_F - C_A/2) \hat{\alpha}(p)/\mathrm{v}}} \,. \tag{6.122}$$

The running gauge couplings are evaluated at the potential scale of the scattering state $p = M_\chi \mathrm{v}/2$. Hence, the effective singlet coupling $C_F \, \hat{\alpha}(p)$ here, in general, differs from α_b, which is defined at its own respective potential scale,

$$\alpha_b = C_F\,\hat{\alpha}(p_n), \tag{6.123}$$

$$\alpha_s = \frac{-1}{2N_c}\,\hat{\alpha}(p), \tag{6.124}$$

whereas the multipole mediator coupling (6.101) is evaluated at the ultrasoft energy scale

$$\frac{(g_a^{\text{eff}})^2}{4\pi} = C_F\hat{\alpha}(\omega). \tag{6.125}$$

Since $p_n \propto \alpha_b$, the the effective bound state couplings are implicitly defined by a recursive equation which must be solved numerically for each n. The running couplings are computed to one loop accuracy. Subsections 6.5.3 and 6.5.4 treat a minimalistic dark SU(N_c) model with no additional light degrees of freedom such that the pure Yang-Mills RGE holds,

$$\hat{\alpha}(\hat{\mu}) = \frac{\hat{\alpha}(M_\chi)}{1 + \frac{22}{3}\frac{\hat{\alpha}(M_\chi)}{4\pi}\,N_c \log\left(\frac{\hat{\mu}}{M_\chi}\right)}. \tag{6.126}$$

Constraints on perturbativity arise first in g_a^{eff} as it is evaluated at the lowest scale. If RG running was neglected, even the results for the thermally averaged cross-sections would be universal in x, and α_b meaning that as long as N_c, or equivalently κ, is kept fixed, simple rescalings of x and $\langle\sigma \mathrm{v}\rangle_{\text{eff}}$ suffice to obtain results for any α_b and M_χ, analogous to the discussion after Eq. (6.91). This conceptual independence of α_b, up to rescaling, is broken by the inclusion of running couplings. Upon choosing a value for $\hat{\alpha}(M_\chi)$, the Landau pole Λ_{N_c} is fixed in terms of the only available mass scale M_χ,

$$\log\left(\frac{\Lambda_{N_c}}{M_\chi}\right) = -\frac{6\pi}{11}\left(\frac{1}{N_c\,\hat{\alpha}(M_\chi)} - \frac{1}{N_c}\right). \tag{6.127}$$

This distance between the hard scale and the Landau pole generally defines also the maximal number of bound states which can be reasonably included before a perturbative approach in $\alpha \ll 1$ breaks down. For $N_c = 10$, barely the ground state can be resolved before reaching $\hat{\alpha}(\omega) = 1$. In the following section 6.6, the non-Abelian interaction is given by the strong interaction of the SM where the running is significantly weakened by the presence of quarks and quantitative results from this section do not apply. Furthermore, the solutions to the Boltzmann equations depend on more mass scales through the number of relativistic degrees of freedom $h_{\text{eff}}(T)$ contributing in $s(x)$ [20], if equilibrium with the SM bath is assumed.

Before turning to numerical results, the employed simplifications must be emphasized. Firstly, as mentioned, bound-to-bound transitions are only mediated by higher order multipole interactions (the non-Abelian two-gluon term $\vec{A}\cdot\vec{A}$ does not contribute here). Secondly, only bound state decay of s-wave states is considered, since all higher partial waves are parametrically suppressed in α, which renders $R_{n\ell} \propto \delta_{0\ell}$. In combination, one may view this simplification as the assumption that ionization rates dominate parametrically over transition and decay rates for non-s-wave bound states. Such an argument, however, ignores that any $\Gamma_{n\ell}^{\text{ion}}$ becomes Boltzmann suppressed once $T \ll E_n$. Results presented in the remainder of

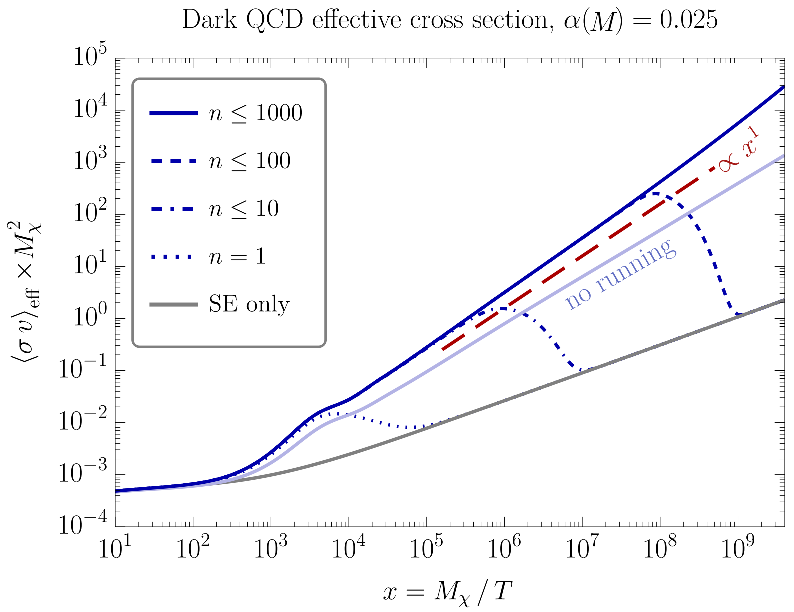

Figure 6.10: Effective cross section (6.107) over inverse temperature $x = M_\chi/T$, including bound state formation up to different n_m (different blue curves) and one-loop running couplings in a dark SU(3) model. Additionally, a curve of only $\langle\sigma_{\rm ann}{\rm v}\rangle$ including Sommerfeld enhancement but no bound states (gray) and of $\langle\sigma{\rm v}\rangle_{\rm eff}$ including $n \leq 1000$ but neglecting RG running (light blue) are shown. A dashed red line $\propto x$ indicates critical power scaling.

this section are thus obtained as a conservative lower bound to the true effective annihilation cross-section.

Fig. 6.10 shows $M_\chi^2 \langle\sigma{\rm v}\rangle_{\rm eff}$ for $N_c = 3$ and $\hat{\alpha}(M_\chi) = 0.025$, including different numbers of bound states up to $n \leq 1000$ (blue curves). The gray curve "SE only" includes no bound states in the calculation but does include SE in the annihilation cross-section, Eq. (6.120). The thermal averaging smears out every single cross section, removing the precise roots present in velocity dependent exclusive cross sections and resulting in an overall peak-shaped contribution similar to what is observed for $n = 1$ (dotted). Thus, analogous to effects observed in Fig. 6.7, each bound $\mathcal{B}_{n\ell}$ predominantly contributes in roughly the regime $T \sim E_n$, albeit now initial ℓ' are summed and n, ℓ are weighed by $R_{n\ell}$. Despite the complicated summation, the resulting effective cross section converges once more to a smooth, power-law like slope when summing sufficiently high n. Because of this, the different blue curves coincide before reaching the exponential cutoff of the respectively highest included n. The light blue curve depicts the result for $n \leq 1000$ when neglecting the running of the gauge coupling and is distinctly smaller and yields a weaker power law. Estimating $M_\chi/E_1 = 4/0.025^2 = 6400$ gives a reasonably good prediction for the position of the maximal contribution of the ground state, keeping in mind that actually $\alpha_b|_{n=1} > 0.025$. From this simple estimate it is clear that the on-set of the bound-state enhancement is directly given by the choice of $\hat{\alpha}(M_\chi)$. However, qualitatively the picture remains unchanged since also the on-set of the Sommerfeld enhancement to the annihilation cross-section "SE-only" must shift correspondingly to larger x. The significance of the dashed red line indicating a power-law $\langle\sigma \mathrm{v}\rangle_{\text{eff}} \sim 1/T$ will be discussed next.

6.5.4 Temperature dependence of annihilation via bound states

This subsection studies the temperature dependence of the effective cross-section. It derives and demonstrates a systematic lack of late-time chemical decoupling due to large enhancements at low temperature. This effect is titled "eternal depletion" and is incompatible with the traditional freeze-out paradigm.

After detaching from chemical equilibrium, $x > x_{cd}$, the abundance Y_χ stops following the equilibrium abundance and the contribution of Y_χ^{eq} in Eq. (6.106) becomes exponentially suppressed and negligible. As long as x_{cd} is known, the present day ($x \approx \infty$) relic abundance can then be solved for by separation of variables and integrating in x [184],

$$Y_\chi(\infty) = \left[Y_\chi(x_{cd}) - \int_{x_{cd}}^{\infty} \mathrm{d}x \frac{1}{3H}\frac{\mathrm{d}s}{\mathrm{d}x}\frac{1}{2}\langle\sigma \mathrm{v}\rangle_{\text{eff}}\right]^{-1}. \tag{6.128}$$

The detaching usually happens around $x = 25$ whereas the BSF contributions set in much later for $\alpha < 0.2$. Assuming that no significant changes in the entropy density of the heat bath occur, one can estimate the parametric temperature dependences as $s(x) \sim T^3$ and $H(T) \sim T^2$, *i.e.* radiation domination. Suppressing the constant contribution $Y_\chi(x_{cd})$ one finds

$$\Omega_{\text{DM}}h^2 \propto \frac{1}{\text{const.} - \int_{x_0}^{\infty}\mathrm{d}x\, x^{-2}\langle\sigma \mathrm{v}\rangle_{\text{eff}}}. \tag{6.129}$$

Independent of the finite positive constant one can see that the integral only converges as long as the effective cross section yield at late times a parametric power scaling exponent γ of

$$\langle\sigma \mathrm{v}\rangle_{\text{eff}} \sim x^\gamma\,, \quad \text{with } \gamma < 1. \tag{6.130}$$

This implies that, for an effective cross section growing more strongly than $\gamma = 1$, the annihilation rate will exceed the Hubble rate at late times and, hence, there is no freeze-out. This behavior is referred to as "super-critical" in the following, while "sub-critical" refers to $\gamma < 1$ allowing for a frozen-out relic abundance. Disregarding the smearing of the thermal average, one may also think of this critical temperature dependence as $x^\gamma \sim \mathrm{v}^{-2\gamma}$. The critical value $\gamma = 1$ requires a power-law twice as strong as the Sommerfeld effect.

Fig. 6.10 shows that a generic dark SU(3) slightly exceeds the critical power scaling once RG running is included. Nevertheless, the super-critical scaling is not to be read as a pure running coupling effect. Rather, the sub-critical scaling in the absence of running being close to critical is a numerical coincidence for SU(3). The effect for different N_c, or correspondingly κ, is demonstrated in fig 6.11. It depicts the BSF contribution to the effective cross section (6.110), excluding the direct annihilation contribution, for $N_c = 2, 3, 4, 5, 10$ plotted over x. Accordingly colored vertical lines denote temperatures of the respective Landau pole. Again, the the critical power scaling is indicated by a dashed red line. Clearly all $N_c > 2$ are super-critical. Apart from $N_c = 2$, summing all contributions of $n \leq 1000$ suffices to compute reliably converged effective cross-sections for all $T > \Lambda_{N_c}$.

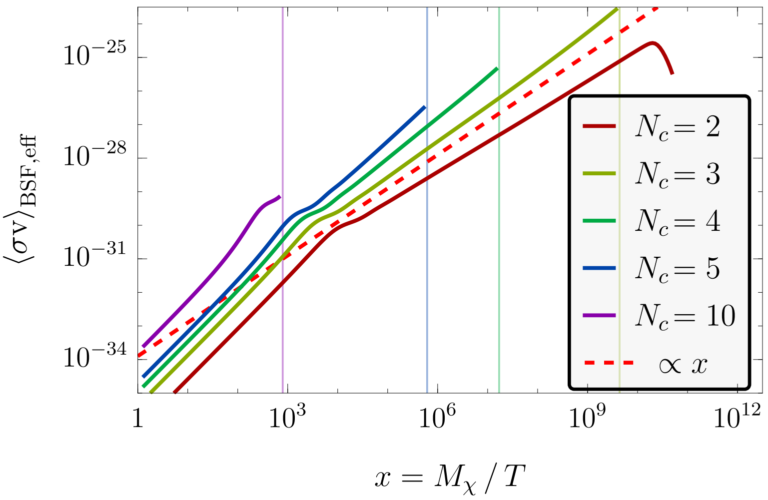

Figure 6.11: Inverse temperature dependence of the effective BSF annihilation cross-section (6.110) in SU(N_c) models $(\mathbf{F}\bar{\mathbf{F}})$ for different N_c including $n \leq 1000$ $(\ell \leq n-1, \ell' = \ell \pm 1)$ bound states and one-loop RG evolution from $\hat{\alpha}(M_\chi) = 0.025$. Vertical lines indicate respective positions of the Landau pole, $x = M_\chi/\Lambda_{N_c}$, color-coded to the shown N_c and the plotted curves end for $\hat{\alpha}(\hat{\mu}) = 1$.

A fit to the power scaling of $\langle\sigma v\rangle_{\mathrm{BSF,eff}}$ can reliably be performed sufficiently long after the ground state peak and the subsequent first few $n \lesssim 5$ excitations and stopping sufficiently long before the end point of each of the lines where $\hat{\alpha}(\hat{\mu}) = 1$. Excluding both these ranges removes influences from oscillatory features of single n and strong running effects near the Landau pole. The fitted slopes are depicted as black dots in Fig. 6.12 for $N_c \leq 5$. The gray dashed line indicates the degraded fitting behavior when including also the strong running regime up to $\hat{\alpha}(\hat{\mu}) = 1$. For $N_c = 2$, even $n = 1000$ does not reach up to the Landau pole and both values coincide. It is important to emphasize that the super-criticality is not sourced by RG running but truly a consequence of the different potentials $\kappa \neq 1$. This will become evident in the next section where bound-to-bound transitions give another strong enhancement resulting in $\gamma > 1.5$. A linear function $0.6 + 0.15 N_c$ is depicted in Fig. 6.12, highlighting the fact that there appears to be a simple linear relationship between N_c and γ. This numerical observation is not investigated any further but, possibly, could be understood from an analysis of the peak heights and densities for a given $\kappa(N_c)$.

These results demonstrate that the inclusion of bound states in the abundance evolution of heavy particles transforming in the fundamental representation of non-Abelian SU(N_c) gauge interactions do not freeze-out in the perturbative regime for $N_c > 2$. Apart from clearly stating the significance of long range interactions and particularly bound states to dark matter relic density computations, the practical influence in this specific numerical example is somewhat limited. For $N_c = 3$, the additional depletion relative to the SE-only result is approximately a factor of $1/8$ until the non-perturbative scale is reached. It is known that there are large additional corrections occurring once the non-Abelian interaction undergoes the transition to the confined phase and hadronization occurs [157, 159, 185, 186].

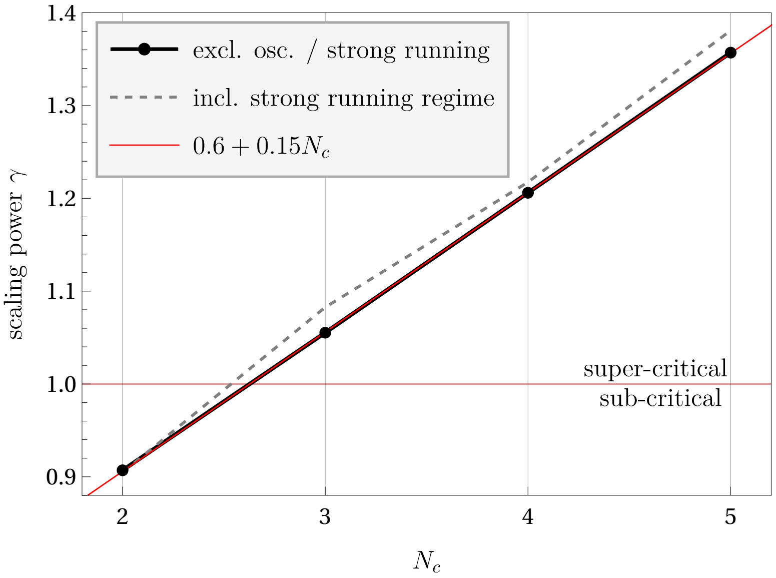

Figure 6.12: Power scaling exponent γ plotted shown for $N_c \leq 5$ (connected black dots). $\gamma(N_c)$ was extracted from Fig. 6.11 by fitting the double-logarithmic slope in the linear regime between the first few $n \lesssim 5$ and the strong running regime near $\hat{\alpha}(\mu) = 1$ (fitting windows manually adjusted to each N_c). The linear model $\gamma(N_c) \approx 0.6 + 0.15N_c$ (red diagonal) agrees well. A worse matching including all results up to $\hat{\alpha}(\hat{\mu}) = 1$ is shown (dashed).

Nevertheless, the corrections due to the phase transition are usually a multiplicative modification to the relic abundance at the onset of the transition, which was *ab initio* assumed to exist in these works. From the results here it is clear that one cannot simply assume a freeze-out production at temperatures around $x \sim 25$ but has to consider the "eternal" depletion effect due to bound states all throughout. Also other corrections might modify the effect of bound states on the effective cross section. Most importantly, the calculations here rely on the existence of highly excited bound states $n \gg 1$ which is valid provided the potential is Coulombic but can break down when extending the framework carelessly to include additional interactions or too heavy potential mediators. Thermal or higher order corrections are impressively un-impactful on the dipole approximation of PNREFT [78, 152, 154, 158], which is due to contributions from any given bound state being significant only once the temperature is of or below its binding energy. Thus, no sizable melting effects are expected since they only set in for temperatures at or above the respective Bohr-momentum scale.

In light of the systematic unitarity violation found in section 6.4, also unitarization effects may play a role eventually. For the results presented here it was ensured for $N_c = 3$ that unitarity remains respected for all depicted values. Additionally, the range $T \approx \Lambda$ was ensured to respect unitarity for $N_c = 2, 3, 10$ in velocity ranges corresponding to temperatures near the Landau pole. It is important to understand that the perturbativity constraints originate from $\Lambda < T \sim E_n, K$ whereas the couplings are evaluated at the *momentum* scales $\hat{\mu} = p, p_n \sim \sqrt{MT}$ and are thus still quite far from $\hat{\alpha}(\hat{\mu}) = 1$, except for the single insertion of $g_a^{\text{eff}^2} \propto \hat{\alpha}(\omega)$.

Since no $\hat{\alpha}(\hat{\mu}) > 1$ is ever evaluated, there is no divergent enhancement caused by vicinity to the Landau pole. From Fig. 6.6 it is clear that $\kappa \to 0$ requires increasingly higher n (smaller v) while the suppression by $\langle \sigma \mathrm{v} \rangle_{\mathrm{eff}} \propto N_c^{-2}$ further helps avoiding the unitarity bound. In the following section concerning BSF by colored interactions the SM, the unitarity bound is avoided by two orders of magnitude, hence, no sizable corrections from unitarization are expected [133].

6.6 Phenomenological impact in a realistic Dark Matter model

As a final piece to the present chapter on bound state formation, a phenomenological study in a t-channel mediator DM model is presented which is crucially affected by the non-Abelian formation of bound states in the early universe. The model includes bound-to-bound level transitions which source another strong enhancement of the effective BSF cross-section.

In the previous section, the abundance evolution was only regarded in the temperature regime of small, perturbative coupling strength. To still avoid an investigation of the evolution of heavy constituent abundances over the course of a phase transition in the SU(N_c) gauge interaction [159, 185, 187] in a more realistic model, the bound state constituents are assumed to have a finite life-time leading to efficient decay within the perturbative regime. This, obviously, makes it impossible to construct a reasonable DM candidate from the bound states or their constituents. Hence, one of the decay products is assumed to be a massive SM gauge singlet fermion χ, coupling exclusively feebly to the heavy constituents thus providing a stable DM candidate. To remain minimal and simultaneously allow for detectability or falsification of the theory, the long-range Coulomb potential and multipole interactions are embedded within the gauge symmetries already existing in the SM. The second decay product may now be a SM quark thus giving rise to a portal between χ and the SM via the (colored) t-channel mediator $\tilde{q}$ [188]. Introducing a dependence on the strong and electromagnetic force allows to combine the above non-Abelian BSF from repulsive initial states with radiative level-transitions between bound states. Furthermore, this embedding also lifts concerns of dark-glueball contributions, which otherwise add to the dark matter energy budget and may conflict with warm DM constraints form structure formation and Lyman-α bounds [159]. In turn, it introduces constraints from collider searches or Big Bang nucleosynthesis. The setup is closely related to coannihilation [24, 176, 189] and conversion-driven freeze-out [25, 26, 190], differing technically only in the size of the t-channel interaction.

Notably, the bound state constituents $\tilde{q}$ now differ from the DM χ which is taken to be much lighter. The mass $m_\chi \ll M_{\tilde{q}}$ will merely be chosen to saturate the relic density abundance and is insignificant to all considered dynamics. This setup induces a slight shift in notation from previous sections, writing the DM mass as m_χ while the hard scale is set by $M_{\tilde{q}}$.

The first three subsections introduce the considered model and the ingredients necessary for the later numerical solutions of the Boltzmann equations by use of quasi-steady state approximation, including a study of the importance of bound-to-bound transitions to the effective cross section. A detailed discussion of the validity of the adopted framework is delayed until subsection 6.6.4 where it will be covered together with formally higher order corrections.

6.6.1 Colored and charged t-channel mediator model

The considered t-channel mediator model extends the SM by two new fields, one colored and hypercharged scalar $\tilde{q}$, which is heavy but still assumed to be thermally produced in the very early universe, and one gauge singlet Majorana fermion χ coupling to the t-channel mediator $\tilde{q}$ and a right-handed SM quark through

$$\mathcal{L}_{\text{int}} = \lambda_\chi \, \bar{q}_R \chi \tilde{q} + \text{h.c.}\,. \tag{6.131}$$

For such an operator to maintain gauge symmetry, the representations of $\tilde{q}$ must coincide with those of the quark. Conceptually, also couplings to left-handed fermion are conceivable but disregarded here due to the attached complications of EWSB, massive gauge bosons and multiple interacting SM fermions. The coupling is taken to be exclusively to the bottom quark, $q = b$, hence the electromagnetic charge of $\tilde{q}$ is $Q_{\tilde{q}} = 1/3$. The regime of the superWIMP production mechanism [23, 191] is found in $M_{\tilde{q}} \gg m_\chi$ and $\lambda_\chi \lesssim 10^{-6}$. Here, λ_χ is so small that χ plays essentially no role in the dynamics in the early universe. Production of χ via typical freeze-in exists yet remains a sub-dominant contribution to the DM relic density. Instead $\tilde{q}$ undergoes mostly the usual thermal production until it efficiently decays via $\tilde{q} \to q + \chi$. This is found once the t-channel mediator width $\Gamma_{\tilde{q}}$ becomes large compared to the Hubble rate at which point the abundance of the abundance of $\tilde{q}$ shifts almost at a 1-to-1 ratio into χ. In usual superWIMP production, $\tilde{q}$ freezes-out prior to its decay and the model becomes insensitive to its exact lifetime. Due to the negligible abundance of χ prior to this decay and the smallness of λ_χ no other processes, such as the inverse decay or annihilation into χ, are relevant here. Too low values of λ_χ need to be avoided in order to ensure $\tilde{q}$ decays before reaching the QCD phase transition, where perturbative calculations break down and, eventually, strong constraints from nucleosynthesis arise.

According to Eq. (6.98), the roles of $\mathcal{S}$ and $\mathcal{B}$ in Eq. (6.11) are taken by the color singlet and octet representations. Since the electromagnetic interaction is much weaker than QCD even at high energies, further corroborated by $Q_{\tilde{q}}^2 < 1$, its contribution to the long range Coulomb potentials is neglected and the effective potential strengths are just given in Eqn. (6.123) and (6.124) with $\hat{\alpha}(\hat{\mu}) = \hat{\alpha}_3(\hat{\mu})$. The renormalization group running of the electromagnetic coupling strength will be neglected in the following, using simply $\alpha_{\text{em}} = 1/128.9$. Numerical values for the strong coupling are obtained using RunDec 3.1 [121].

Differences from the analysis of dark SU(N_c) interactions in section 6.5, set aside the finite constituent lifetime, arise from the presence of the additional U(1) interactions of electromagnetism allowing singlet-to-singlet BSF and, more importantly, bound-to-bound level transitions. Since the constituents are now scalar particles (thus $\xi = 1$) there is no additional complication from forbidden spin-triplet bound states. Considered BSF processes include the leading order, single gauge boson dipole emission for gluons as well as photons, however the latter turn out numerically sub-dominant in the effective cross section and are ultimately neglected when solving the Boltzmann equations. According to Eq. (6.125), the multipole mediator interaction is evaluated at the energy of the emitted gauge boson

$$\left(\tilde{q}^{\dagger}\tilde{q}\right)_{[\mathbf{8}]} \to \mathcal{B}_{n\ell} + g: \quad \frac{(g_1^{\text{eff}})^2}{4\pi} = \frac{4}{3} \times \hat{\alpha}_3 \left(\frac{M_{\tilde{q}}\mathrm{v}^2}{4}(1+\zeta_n^2)\right) \tag{6.132}$$

and for the color neutral BSF process by photon emission

$$\left(\tilde{q}^{\dagger}\tilde{q}\right)_{[\mathbf{1}]} \to \mathcal{B}_{n\ell} + \gamma: \quad \frac{(g_1^{\text{eff}})^2}{4\pi} = \frac{1}{9} \times \alpha_{\text{em}} \tag{6.133}$$

where in both cases the cross section in Eq. (6.28) still gains the factor $2/N_c^2$ accounting for color average and spin sums. Pair annihilation and decay of bound states depend on the center-of-mass energies $2M_{\tilde{q}}$ and $M_{\tilde{q}}$, as before.

The treatment of QCD as a perturbative theory is only valid above the confinement scale, which is taken as $\Lambda_{\text{QCD}} = 1\,\text{GeV}$. The multipole mediator coupling in Eq. (6.132) limits when the non-perturbative regime is reached. This means that when the binding energies of a given bound state contribution reach $E_n \sim 1\,\text{GeV}$ the Coulomb potential is still described by a parametrically perturbative scale $\hat{\alpha}_3(p_n) \ll 1$.

Imposing again the quasi steady state approximation to employ the effective cross section formalism, there are only the two particle species $x = \tilde{q}, \chi$ left in the network of Boltzmann equations. Due to the large mass splitting $M_{\tilde{q}} \gg m_\chi$ and the feeble nature of λ_χ, the inverse decay process $q + \chi \to \tilde{q}$ can be neglected, as well as 2-to-2 conversions or annihilation which are suppressed by four powers of λ_χ, *e.g.* qq, $\tilde{q}\tilde{q} \leftrightarrow \chi\chi$. The coupled Boltzmann equations are therefore

$$\frac{\mathrm{d}Y_{\tilde{q}}}{\mathrm{d}x} = \frac{1}{3H}\frac{\mathrm{d}s}{\mathrm{d}x}\left[\frac{1}{2}\langle\sigma\mathrm{v}\rangle_{\text{eff}}\left(Y_{\tilde{q}}^2 - Y_{\tilde{q}}^{eq\,2}\right) + \frac{\Gamma^{\text{conv}}_{\tilde{q}\to\chi}}{s}\left(Y_{\tilde{q}} - Y_\chi\frac{Y_{\tilde{q}}^{eq}}{Y_\chi^{eq}}\right)\right], \tag{6.134}$$

$$\frac{\mathrm{d}Y_\chi}{\mathrm{d}x} = \frac{1}{3H}\frac{\mathrm{d}s}{\mathrm{d}x}\left[-\frac{\Gamma^{\text{conv}}_{\tilde{q}\to\chi}}{s}\left(Y_{\tilde{q}} - Y_\chi\frac{Y_{\tilde{q}}^{eq}}{Y_\chi^{eq}}\right)\right], \tag{6.135}$$

with the equilibrium yields defined by

$$Y_x^{eq} = \frac{g_x}{s}\int\frac{\mathrm{d}^3p}{(2\pi)^3}\mathrm{e}^{-\sqrt{m_x^2+p^2}/T} \tag{6.136}$$

where g_x are the degrees of freedom of the respective particles, $g_{\tilde{q}} = 2N_c = 6$ (particle and anti-particle color triplets) and $g_\chi = 2$ (for two spin polarizations) states. The degrees of freedom of the bound states included in the effective cross section take care of the otherwise averaged or summed magnetic quantum number, $g_{\mathcal{B}_{n\ell}} = 2\ell + 1$.

6.6.2 Relevant rates and cross sections

To clarify some notational subtleties, note that thermally averaged cross sections are denoted explicitly by angle brackets while for reaction rates, such notation is rather unconventional. Instead, vacuum rates are superscripted by their respective reaction while thermally averaged rates appearing in the Boltzmann equations are written as $\Gamma^{\text{dec, trans, ion}}$ with disambiguation by suffixes as needed.

The bound state formation and ionization rates have been discussed already. Their definitions are found in Eqn. (6.28), (6.108) and (6.117), see also section 6.5.2. The direct annihilation cross-section for a pair of color-triplet scalars including Sommerfeld enhancement is

$$(\sigma \mathrm{v})_{\text{ann}} = \frac{14}{27} \frac{\pi \hat{\alpha}_3 (2M_{\tilde{q}})^2}{M_{\tilde{q}}^2} \left(\frac{2}{7} S_0^{[\mathbf{1}]} + \frac{5}{7} S_0^{[\mathbf{8}]} \right), \tag{6.137}$$

using Eqn. (6.121) and (6.122) with $\mathbf{Ad} = \mathbf{8}$, $C_A = N_c = 3$ and $C_F = 4/3$. Bound state decay is only included for s-wave states, where [140, 148]

$$\Gamma^{n\ell \to gg} = \delta_{0\ell} \frac{M_{\tilde{q}} C_F}{8n^3} \hat{\alpha}(M_{\tilde{q}})^2 \, \alpha_b^3, \tag{6.138}$$

which differs from the fermionic bound-state decay rate, Eq. (6.118), by a factor of 1/2. Formally, the decay of the constituents $\tilde{q} \to \chi q$ after thermal averaging is [140]

$$\Gamma_{\tilde{q}}^{\text{dec}} = \Gamma^{\tilde{q} \to \chi q} \frac{K_1(x)}{K_2(x)} \approx \Gamma^{\tilde{q} \to \chi q}, \tag{6.139}$$

$$\Gamma^{\tilde{q} \to \chi q} = \frac{\lambda_\chi^2 \left(M_{\tilde{q}} - m_b^2 - m_\chi^2 \right)}{16 \pi M_{\tilde{q}}^3} \sqrt{\lambda \left(M_{\tilde{q}}^2, m_\chi^2, m_q^2 \right)}, \tag{6.140}$$

λ denoting the Källen function $\lambda(a, b, c) = a^2 + b^2 + c^2 - 2(ab + bc + ac)$. In practice $\Gamma^{\tilde{q} \to \chi q}$ may be directly used as an input parameter of the theory, implicitly defining λ_χ, since no other processes depend on it. Direct annihilation $\chi\chi \to qq$ or t-channel mediator production $\chi\chi \to \tilde{q}\tilde{q}$ are proportional to λ_χ^4 and completely negligible here. Bath-scattering conversions $\tilde{q}X \to \chi Y$ are proportional to λ_χ^2 and dominate the conversion at high temperatures. However, $\tilde{q}$ remains in chemical decoupling until around typical values $x_{cd} \sim 25$ and conversions only are significant at low temperatures where the decay term $\tilde{q} \to \chi q$ dominates. These are significant simplification for the superWIMP production compared to conversion-driven freeze-out where all processes need to be considered [140].

Transitions between bound states levels $i = (n'\ell') \to (n\ell) = j$ mediated by electromagnetic dipole interactions require $n - n' \neq 0$ and $|\ell - \ell'| = 1$. The former condition avoids zero-energy photon modes interacting with the bound state and the latter is the dipole angular momentum selection rule. Transitions between discrete bound state energy levels are in many aspects related to the transition of positive-energy scattering states to bound states that is BSF [141]. This includes the detailed balance relation between de-excitations, $i \to j$ for $E_n < E_{n'}$, and the reverse excitation process $j \to i$ following Eq. (6.112). The de-excitation rates can be computed by analogous steps as for BSF where, as a simplification, now a second real integer parameters n' occurs instead of iζ_s. They relate to the matrix element by

$$\begin{aligned}\Gamma^{n'\ell'\to n\ell} &= \frac{4Q_{\tilde{q}}^2\alpha_{\text{em}}}{3}(2\ell+1)\omega_{n'n}\left|\langle\mathcal{B}_{n'\ell'}|\,\omega_{n'n}\vec{r}\,|\mathcal{B}_{n\ell}\rangle\right|^2 \\ &= M_{\tilde{q}}\,\frac{Q_{\tilde{q}}^2\alpha_{\text{em}}(\alpha_b)^2}{3}\,\frac{n'^2-n^2}{n'^2n^2(2\ell'+1)}\left(\ell'\delta_{\ell'-1,\ell}\,I_{R,\text{t}}^{1,+1}+\ell\delta_{\ell'+1,\ell}\,I_{R,\text{t}}^{1,-1}\right) \qquad (6.141)\end{aligned}$$

A more detailed analysis for different multipole transitions is omitted here. It is expected to follow similar lines as for BSF. By exploiting the same hypergeometric relations used in section 6.2.5, see also App. C.1, additional simplification of the expressions provided in [3] is possible,

$$\begin{aligned}I_{R,\text{trans}}^{1,+1} &= 4(\alpha_b)^2\frac{z^{2\ell}|1-z|^{1+n-n'}}{\Gamma(2\ell+2)^2}\,\frac{\Gamma(n+\ell+1)}{\Gamma(n-\ell)}\,\frac{\Gamma(n'+\ell+2)}{\Gamma(n'-\ell-1)} \\ &\quad\times\left(\frac{F_{+,\text{t}}(0)}{(n'-n)^2}-\frac{F_{+,\text{t}}(2)}{(n'+n)^2}\right)^2, \qquad (6.142) \\ I_{R,\text{trans}}^{1,-1} &= 4(\alpha_b)^2\frac{z^{2\ell'}|1-z|^{1+n'-n}}{\Gamma(2\ell'+2)^2}\,\frac{\Gamma(n+\ell+1)}{\Gamma(n-\ell)}\,\frac{\Gamma(n'+\ell)}{\Gamma(n'-\ell+1)} \\ &\quad\times\left(\frac{F_{-,\text{t}}(0)}{(n'+n)^2}-\frac{F_{-,\text{t}}(2)}{(n'-n)^2}\right)^2, \qquad (6.143)\end{aligned}$$

with $z = 4n'n/(n'+n)^2$ and

$$\begin{aligned}F_{+,\text{t}}(X) &\equiv {}_2F_1\left(-n+\ell+1, X+n'+\ell;\ 2+2\ell;\ z\right). \qquad (6.144) \\ F_{-,\text{t}}(X) &\equiv {}_2F_1\left(X-n+\ell+1,\ n'+\ell;\ 2\ell;\ z\right). \qquad (6.145)\end{aligned}$$

These functions are related to the hypergeometric function for BSF by replacing $\mathrm{i}\zeta_s \to n'$, $\zeta_n \to p_n/(\mathrm{i}p_{n'})$, *cf.* Eqn. (6.41), (6.42) and (6.46). This simple prescription cannot directly relate the BSF and bremsstrahlungs radial integrals as different imaginary parts are picked up [141]. Further, the reduction to a result in terms of only $F_+(0)$ as performed for BSF is now not possible since $n' \in \mathbb{R}$. Hence, complex conjugation does no longer reproduce the sign change $\mathrm{i}\zeta_s \to -\mathrm{i}\zeta_s$ necessary in deriving Eq. (6.49) from hypergeometric relations. Note that the above bound-to-bound transition rates already implement $\kappa = 1$ which is of course required in $\mathrm{U}(1)_{\text{em}}$ interactions. Furthermore, $a = 1$ is already inserted giving rise to compact results. In more complicated models, $\kappa \neq 1$ is conceivable even in bound-to-bound transitions. Simply regarding larger gauge representations than the fundamental already yields multiple differently attractive 2-constituent representations [32]. In such a scenario, more general formulas are required to describe "not-Abelian" bound-to-bound transitions. At the same time, radiative transitions become possible by emission of a non-Abelian gauge boson without the need to have an additional U(1) charge for $\tilde{q}$.

The thermal average for bound-to-bound transitions must be carefully included, since the energy splittings between two highly excited energy levels are suppressed relative to the ground state by n^{-3},

$$\Delta E_{n'n} = E_{n'} - E_n = \frac{M_{\tilde{q}}\alpha_b^2}{4}\,\frac{n^2-n'^2}{n'^2n^2}. \qquad (6.146)$$

Numerically, though not parametrically in PNREFT, level energy gaps become even much smaller than the ultrasoft scale E_1, which is not of concern in regards to unitarity nor perturbativity, since the coupling evaluated at this ultrasoft scale is only α_{em}. Detailed thermal distributions of the photons need to be considered as long as $T \gtrsim \Delta E_{n'n}$. The thermally averaged rates are

$$\text{de-excitation } (n > n') : \Gamma^{\mathrm{trans}}_{n'\ell' \to n\ell} = \Gamma^{n'\ell' \to n\ell} \times \left(\frac{1}{\mathrm{e}^{|\Delta E_{n'n}|/T} - 1} + 1 \right) , \tag{6.147}$$

$$\text{excitation } (n' > n) : \Gamma^{\mathrm{trans}}_{n'\ell' \to n\ell} = \Gamma^{n'\ell' \to n\ell} \times \left(\frac{1}{\mathrm{e}^{|\Delta E_{n'n}|/T} - 1} \right) . \tag{6.148}$$

The explicit $+1$ defines the vacuum contribution to de-excitations whereas excitations are exclusively possible in a thermal environment.

6.6.3 Effective cross section for charged and colored particles

This subsection analyses the numerical results found for the effective cross section for the colored and charged t-channel mediators $\tilde{q}$ including effects from highly excited bound states and transitions among them. In pushing for high excitations $n \gg 10$, practicability of the numerical implementation of the transition rates needs to be kept in mind as the number of possible transitions grows rapidly. There are $n_m(n_m - 1)/2$ distinctly treated bound states $\mathcal{B}_{n\ell}$ where the magnetic quantum number degeneracy is already absorbed into the degrees of freedom $g_{\mathcal{B}}$. Bound-state dipole transitions by photon emission occur between any pair of bound states where $n > \ell \wedge n' > \ell' \wedge \ell = \ell' \pm 1$. Already s-wave, $\ell' = 0$, alone thus allows for n_m^2 unique processes and the total number of transitions nears n_m^3. Since the transition matrix needs to be evaluated on a dense grid in x, brute-force attempts quickly reach runtimes of $\mathcal{O}(\text{days})$ even for millisecond speeds of each individual rate. A more efficient method is to compute the temperature dependence from the thermal distributions in Eq. (6.147) separately and multiply the vacuum transition rates after only computing all of them once. This approach also allows to treat $\Delta E_{n'n}$ and hence the thermal distributions as degenerate in $\ell^{(\prime)}$ which improves efficiency by one order of n_m. Another practical advantage of this approach is that there is no need to store large $n_m^2 \times n_m^2$ matrices in each temperature step, significantly reducing memory requirements during the computation. Altogether, this method allows to use one unique matrix of pre-evaluated vacuum transition rates in order to compute the temperature dependent $\Gamma_{\mathrm{trans}}(x)$ as needed on-the-fly.

With the results of the previous section, all ingredients to compose the effective cross section, Eq. (6.107), are known. The obtained numerical results are given in Fig. 6.13 including all bound states $\mathcal{B}_{n\ell}$, up to three different maximal $n_m = 1, 10, 100$ (blue curves), and all electric dipole transitions among them. The discrete level transitions, sourced by the addition of Abelian gauge interactions, constitute the main conceptual difference to the pure $\mathrm{SU}(N_c)$ results shown in Fig. 6.10. To ease comparison, Fig. 6.13 shows also the no-transitions limit, including all $n \leq 1000$ (green curve), and the Sommerfeld enhanced direct annihilation including no effects from bound states (gray curve). The t-channel mediator is taken to have a mass of $M_{\tilde{q}} = 4 \times 10^6\,\mathrm{GeV}$ and the non-perturbative

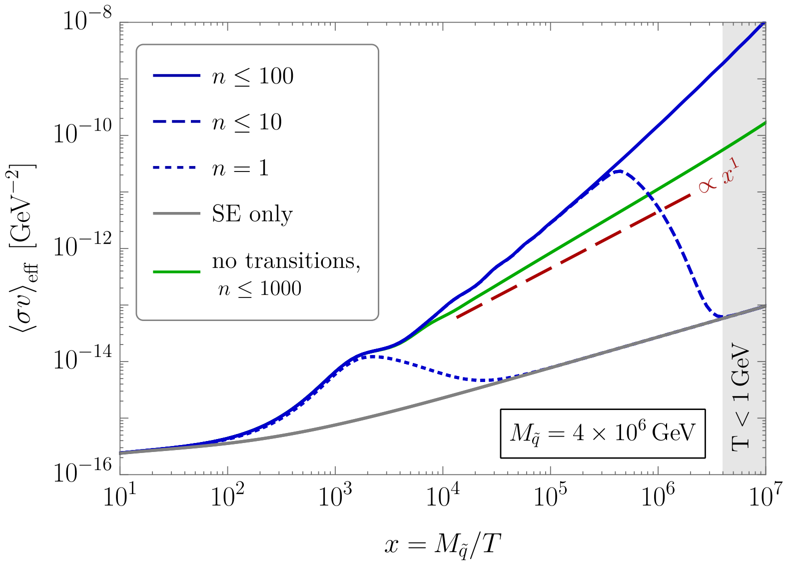

Figure 6.13: Effective cross sections of the colored and electrically charged t-channel mediator $\tilde q$ plotted in inverse temperature for $M_{\tilde q} = 4 \times 10^6$ GeV. Contributions from all bound state levels n and ℓ, accounting for all dipole transitions among them, are included up to different $n \leq 1, 10, 100$ (dotted, dashed and solid blue). The no-transitions limit is shown including $n \leq 1000$, $\ell = 0$ (green). All grow more strongly than $\propto x$ (dashed red line) once sufficiently high n are included.

regime of QCD is correspondingly reached at $x = 4 \times 10^6$ (gray shaded area, $T < 1\,\text{GeV}$). Perturbative EFT results are no longer trustworthy at such low temperatures as $\hat\alpha_3(1\text{GeV}) = 0.48$ becomes of $\mathcal{O}(1)$. Any concerns of the influence of non-perturbative QCD running couplings are refuted by evaluating $\langle\sigma \text{v}\rangle_{\text{eff}}$ for three different conventions for $\hat\alpha_3$. The first convention simply sets $\hat\alpha_3 = 0$ whenever $\hat\mu < 1\,\text{GeV}$. The second convention disables the running and freezes $\hat\alpha_3(\hat\mu \leq 1\,\text{GeV}) = \hat\alpha_3(1\,\text{GeV})$ in this regime. The third convention continues the running until $\hat\alpha_3(\hat\mu_1) = 1$ and freezes it only there. Results of all three prescriptions are drawn in Fig. 6.13 yet fully coincident.

The effective cross section in Fig. 6.13 shares the Sommerfeld enhanced direct annihilation cross-section and the ground state contribution ($n = 1$, dotted) with the no-transitions limit. Differences between the solid blue and green curves arise only once capture into $n = 2$ becomes notable in the no-transitions limit around $x = 10^4$. Hence, excitations of the ground state into higher excited states does not significantly affect the effective cross section at high temperatures. As also differences between the different blue curves occur analogously, one may conclude this to hold for all excitations.

Ground state capture becomes relevant around $x \gtrsim 10^3$. A simplistic estimate assumes this to coincide with the point where temperature drops below it binding energy and ionization becomes inefficient. Defining $x_n \equiv M_{\tilde q}/E_n$, one finds $x_1 = 7 \times 10^2$, $x_{10} = 5 \times 10^4$ and $x_{100} = 3 \times 10^6$ as naive estimates for significance of the respective bound state levels, expecting the exponential cutoff due to the repulsive nature of the initial octet state shortly thereafter. By comparing these values to the locations of the low-temperature cutoff of the respective curves one observes that $\mathcal{B}_{n\ell}$, in practice, impact significantly lower temperatures than just $T = E_n$ by over one order of magnitude. This is presumably caused by thermal distributions of particles in the plasma and the summation of many $\ell < n$, *cf.* Fig. D.4.

The inclusion of bound states $n \leq 100$ is found to give good convergence for any $T > 1\,\mathrm{GeV}$. While $n_m = 10$ (dashed blue) is clearly still insufficient at $x > 2 \times 10^5$, relative differences between $n_m = 50$ and $n_m = 100$ are less than 0.2% in the entire perturbative regime. Fitting the converged power law yields a power scaling exponent according to Eq. (6.130) of $\gamma = 1.6$, being significantly super-critical. Again, a dashed red line $\propto 1/T$ serves as guidance. Compared to the no-transitions limit, where $\gamma = 1.1$, the contribution of bound-to-bound transitions now allow de-excitation and decay of any-ℓ bound states opposed to just s-wave. The contribution of bound-to-bound transitions to the temperature dependence of $\langle\sigma \mathrm{v}\rangle_{\mathrm{eff}}(x)$ is found to be of roughly the same strength as the SE, $1/\mathrm{v} \sim 1/\sqrt{T} \propto x^{0.5}$.

SE is commonly taken to be the dominant source of correction while any other effects at low temperatures are insignificant for the obtained relic abundance, since the annihilation rate is already negligible compared to $H(x)$ after chemical decoupling. This line of argument is now seen to no longer apply to $\gamma > 1$. There may well be an intermediate temperature range where $\Gamma_{\mathrm{BSF}} < H$ and the number density appears to be frozen out, yet at sufficiently low temperatures, Γ_{BSF} must eventually exceed the Hubble rate and the bound state constituents recouple to a second phase of (eternal) depletion. In a model where α_{BSF} or α_b can be chosen freely, this recoupling may be shifted to arbitrarily late times (ignoring for the moment the QCD phase transition) by decreasing the coupling strengths and thereby the recoupling temperature. Slight intermediary decoupling will be visible in Fig. 6.16 around $x = 10^2$, however, in that model already the ground state contribution suffices to recouple the system around $x = 10^3$.

6.6.4 Validity of the effective cross section formalism

Before turning to numerical solutions of the Boltzmann equations (6.134) and (6.135), this section discusses in detail the different approximations entering the various rates as well as the applicability of the quasi-steady state approximation in the considered theory.

The validity of the multipole expansion is limited by $r_n\omega \sim \alpha_b T/E_n \ll 1$, hence one does not expect a good description for $x \lesssim n^2/\alpha_b$. However, as long as $T > E_n$, meaning $x \lesssim n^2/\alpha_b^2$, bound state ionization dominates the reaction rate of $\mathcal{B}_{n\ell}$, suppressing the depletion efficiency factors $R_{n\ell} \to 0$. Therefore, the regime where the multipole expansion breaks down parametrically never contributes to the effective cross section. This suppression also explains the absence of strong thermal corrections to the calculated reaction rates. Such finite temperature corrections can affect the BSF or transition rates by orders of magnitude and even melt the discrete bound state spectrum into a continuum contribution continuously connected to the traditional scattering states [78], such melting also only occurs when the temperature exceeds the respective Bohr momentum, $T \gtrsim p_n \gg E_n$ [192, 193]. At lower temperatures corrections are small and, eventually, even Boltzmann suppressed. Finite temperature effects most strongly impact bound-to-bound transition since the level splitting $\Delta E_{n'n} \sim E_n/n$ for neighboring $n' \approx n$. To numerically investigate possible higher-order effects, the effective cross section was also computed including finite temperature NLO corrections to bound-to-bound transition rates for several parameter points. To a good approximation, the corrections take the form of a simple multiplication of the vacuum transition rates by a temperature dependent factor in addition to the phase space densities [158],

$$\Gamma^{\text{trans}}_{n\ell \to n'\ell'} \to \Gamma^{\text{trans}}_{n\ell \to n'\ell'} \times \left[1 + 12 \times \alpha_{\text{em}} \times f_{\text{NLO}}\left(\frac{\Delta_{n'n}}{T}\right)\right], \tag{6.149}$$

where 12 is the number of light fermionic degrees of freedom in the SM plasma, neglecting the top quark, and the approximate fit function is defined as

$$f_{\text{NLO}}(x) = \begin{cases} \frac{7.3823 - 8\log(x)}{x^2\pi} & \text{for} \quad x \leq 1, \\ 7.3823\, x^{-5/2}/\pi & \text{for} \quad 1 \leq x \leq 2.626, \\ 10\, x^{-4} & \text{else.} \end{cases} \tag{6.150}$$

Corrections to the effective cross-section from these finite temperature effects remained negligible, mostly at a sub-percent level, and thus far below the expected accuracy of the calculation. As mentioned earlier, the effective cross section can only increase if finite temperature effects give rise to enhanced bound-to-bound transition rates [182] and obtained results are thus understood as a conservative lower bound.

To demonstrate the dominance of ionization rates at low temperatures and justify the use of the steady state approximation at the heart of the effective cross section formalism, Fig. 6.14 shows the different reaction rates of the first ten $\tilde{q}$ bound states ($n \leq 4$, $\ell < n$). Gluon and photon ionization (green dashed and dotted curves), bound state decay (red dashed) and bound-to-bound transitions (blue) are drawn as functions of the inverse temperature parameter x. Vertical gray lines indicate $T = E_n$ for the respective bound state $\mathcal{B}_{n\ell}$.

The ground state (upper left panel, $(1,0)$) cannot undergo any further de-excitations and the transition rate is Boltzmann suppressed once $T \ll E_1 - E_2$. Dipole selection rules limit accessible transitions to $\ell' - \ell = \pm 1$ and the same argument also applies to the first excited s-wave state $(2,0)$. Numerically, gluonic ionization rates dominate over photonic ones by more than three orders of magnitude and, by the detailed balance relation to the inverse process, the same holds for BSF cross-sections. Both ionization rates are suppressed at high x whereas decay and de-excitation rates approach their non-vanishing in-vacuum values where available. The enhancement of ionization and BSF due to being mediated by the strong interaction also demands $T \ll E_n$ by roughly an order of magnitude before the electromagnetic de-excitation rates can become dominant. Decay of bound states is only included for s-wave states. In every bound state, there is at least one reaction rate (either de-excitation or decay) which becomes constant at low temperatures and therefore large compared to $xH \sim x^{-1}$, keeping the full network of bound states in chemical equilibrium [24, 182]. Hence, it is justified to assume a quasi-steady state approximation and employ the effective cross section formalism in the first place, which was assumed thus far.

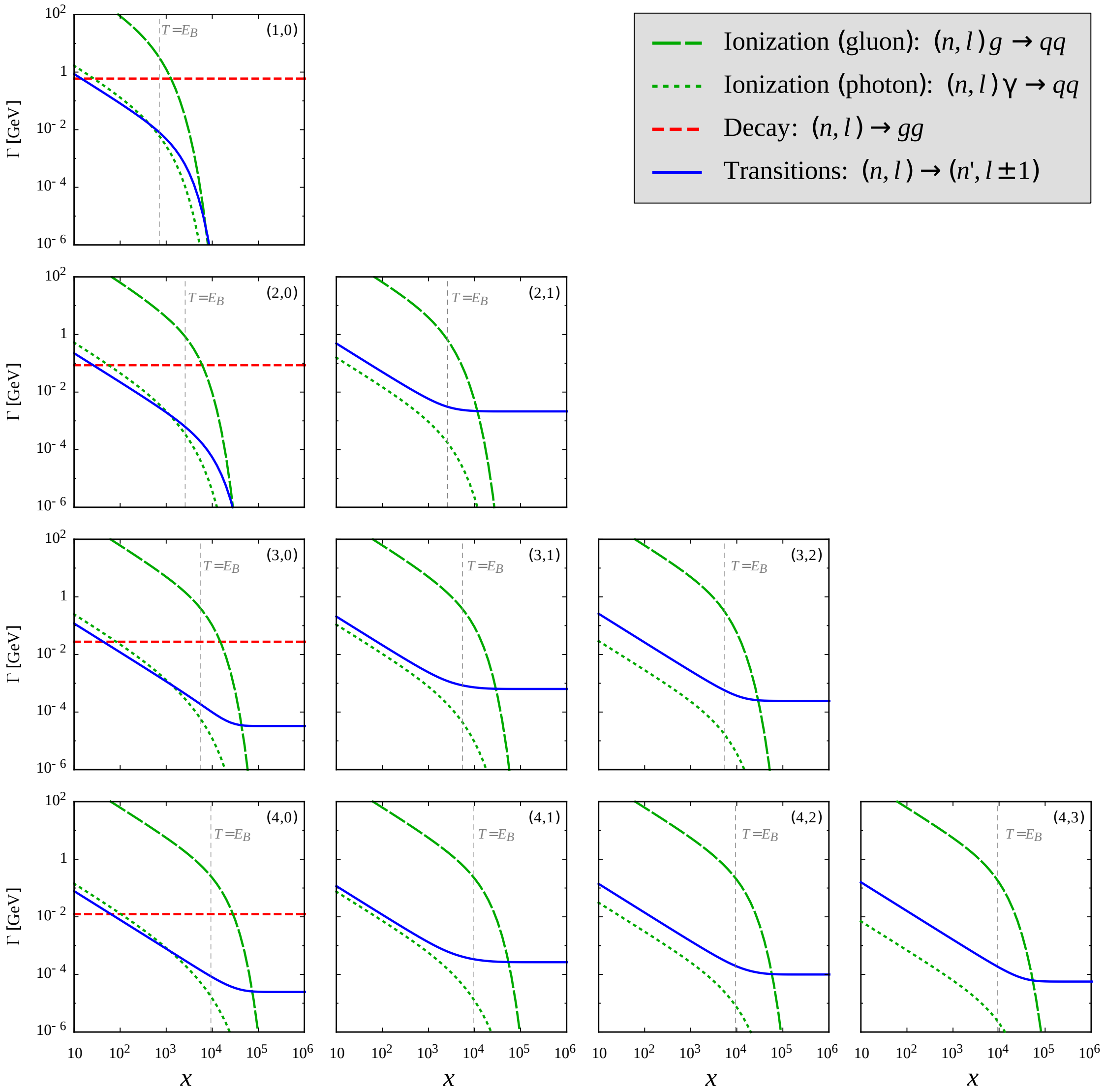

Figure 6.14: Plots of temperature dependences, $x = M_{\tilde{q}}/T$, of the different reaction rates listed in the legend are tabulated for the lowest 10 bound states $n \leq 4$. Each panel depicts horizontally $10 < x < 10^6$ and vertically the different rates in ranges 10^{-6} - 10^2 GeV. Panels for the respective states (n, ℓ) are sorted from *top left:* (1,0) to *bottom right:* (4,3).

Apart from the validity of the quasi-steady approximation it still remains to justify why the inclusion of only s-wave bound state decay suffices. Before presenting the argumentation, it should be emphasized that any inclusion of additional decay rates only ever increases the depletion efficiency and therefore strengthen the result of eternal annihilation found in section 6.5. To begin with, pair annihilation of bound state constituents involves the ℓ-th derivative of the wave function at the origin, $\partial_r^\ell \mathcal{B}_{n\ell}(0)$, and is therefore systematically suppressed in higher partial waves by $(\alpha_b)^{1+\ell}$ relative to s-wave annihilation. The s-wave decay rate into two gluons is itself already of $\mathcal{O}(\alpha_3^5)$. On the other hand, dipole transition rates among bound states $\mathcal{B}_{n'\ell'}$ and $\mathcal{B}_{n\ell}$ are proportional to $\alpha_{\text{em}}\alpha_b^4$. For p-wave bound states this naive analysis predicts the decay rate into two gluons to compare to the transition rate $np \to n's$ by powers $\alpha_3^3/\alpha_{\text{em}}$. However, there is a special cancellation for the tree-level p-wave decay rate into two gluons happening among the color-antisymmetric Abelian and the non-Abelian parts of the wave functions [194]. Note that this only holds only at tree level as the Landau-Yang theorem does not apply to all orders in QCD [195]. Hence, the dominant term in p-wave decay is the NLO contribution and therefore

$$\frac{\Gamma^{np\to gg}}{\Gamma^{np\to n's}} \sim \frac{\alpha_3^{5+2+2}}{Q_{\tilde{q}}^2\alpha_{\text{em}} \times \alpha_3^4} \sim Q_{\tilde{q}}^{-2}\alpha_3^3 \tag{6.151}$$

where the second $+2$ in the exponent denotes the suppression from vanishing LO amplitudes. The second step in Eq. (6.151) assumes the widespread counting $\alpha_{\text{em}} \sim \alpha_3^2$ to allow for a systematic comparison of α_{em} and α_3. The p-wave decay into two gluons is suppressed equally as much as the genuine NLO process of decay into three gluons and both are therefore identically negligible.

Also a comment on the negligence of two-gluon transitions is in order. Since the two-gluon operator $\propto \vec{A}\cdot\vec{A}$ in the Lagrangian cannot mediate between continuum and bound states as it does not carry away energy, two-gluon processes are obtained from double insertions of single gluon multipole operators. Again in the counting $\alpha_{\text{em}} \sim \alpha_3^2$, such matrix elements would not be suppressed relative to single photon emissions, however some qualitative arguments can be made in favor of neglecting two-gluon transitions. The price of emitting two gluons has to be paid in phase space. From a simplistic comparison of electromagnetic hydrogen life times dominated by 1-photon and 2-photon emissions, $\tau_{2p\to1s} = 1.6\,\text{ns}$ and $\tau_{2s\to1s} = 0.12\,\text{s}$ [196], one may estimate a suppression of $\mathcal{O}(\alpha^3)$. Secondly, by inserting two gluon dipole operators, there must be an intermediate color-octet state with a repulsive potential. From classical arguments one expects this overlap to yield additional suppression. However, in light of the here developed semi-classical picture of repulsive-to-attractive BSF and the observed enhancement of such processes, this naive expectation should be doubted and warrants further investigation. For this thesis, two gluon operators shall be neglected solely based on the strict limitation to single-boson emissions. Yet again, the neglected bound-to-bound transition channels can give an enhancement over the computed effective cross-section.

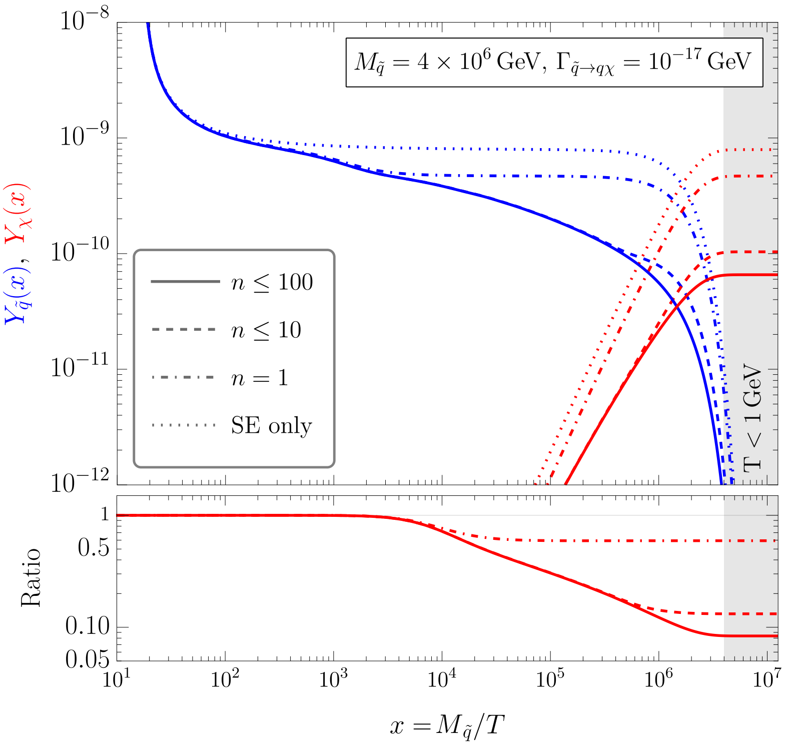

Figure 6.15: Abundance evolutions of $\tilde{q}$ and χ for $M_{\tilde{q}} = 4 \times 10^6\,\mathrm{GeV}$ and $\Gamma_{\tilde{q}} = 1 \times 10^{-17}\,\mathrm{GeV}$ in inverse temperature $x = M_{\tilde{q}}/T$. *Upper panel*: Abundances $Y_{\tilde{q}}$ (blue) and Y_{χ} (red) are shown, including bound states $n \leq 1, 10, 100$ (dot-dashed, dashed, bold), and "SE only" (dotted) including none. All electric dipole transitions among bound state levels are included. *Lower panel*: The ratio of $Y_{\chi}(x)$ over the "SE only" solution is shown.

6.6.5 Abundance evolution in presence of bound states

The system of Boltzmann equations for the particle abundances of χ and $\tilde{q}$, Eqn. (6.134) and (6.135), decouples in the approximation of negligible inverse decay $\chi + q \to \tilde{q}$. This allows to first solve for $Y_{\tilde{q}}$ and then integrate the remaining term to find the abundance of Y_{χ} as

$$Y_{\chi}(x_1) - Y_{\chi}(x_0) = \int_{x_0}^{x_1} \frac{\mathrm{d}Y_{\chi}}{\mathrm{d}x}\mathrm{d}x \approx \int_{x_0}^{x_1} \mathrm{d}x\, \frac{-1}{3H}\frac{\mathrm{d}\,s}{\mathrm{d}x}\frac{\Gamma_{\mathrm{conv}}^{\tilde{q}\to\chi}}{s}\, Y_{\tilde{q}}(x). \tag{6.152}$$

Stability is ensured by iteratively solving for each decade in x separately and using available implicit backward differentiation methods. Starting conditions are $Y_{\tilde{q}}(x_0) = Y_{\tilde{q}}^{eq}(x_0)$, $Y_{\chi}(x_0) = 0$ and $x_0 = 4$. Any initial abundance of χ may be neglected as there is a small freeze-in contribution to Y_{χ} produced at early times when $\tilde{q}$ is still in thermal equilibrium with the SM bath which is almost instantly approached by the numerical solution. Even when starting from $x = 4$, this freeze-in contribution can be reproduced but is desired to remain negligible to contributions from late time mediator decay.

To begin the analysis of the obtained numerical solutions, Fig. 6.15 shows the mediator and DM abundance (blue and red curves) upon including differently many bound state excitations $n \leq n_m$. At small $x < 20$, $Y_{\tilde{q}}$ follows the exponentially suppressed equilibrium abundance but falls out of equilibrium around $x = 20$. When omitting all bound states (dotted curves), $Y_{\tilde{q}}$ almost instantly freezes-out with only mild noticeable depletion until $x = 10^3$, as is usual for Sommerfeld-enhanced annihilation. The mediator abundance remains constant until the age of the Universe reaches its life time $\tau_{\tilde{q}} = 1/\Gamma_{\tilde{q}}$ at which point $\tilde{q}$ rapidly decays to χ, converting the abundance in a 1-to-1 ratio. The corresponding decay-time inverse-temperature parameter is

$$x_{\mathrm{dec}} = \left(\Gamma_{\tilde{q}\to q\chi}/H(m_{\tilde{q}})\right)^{-1/2} . \tag{6.153}$$

For the given example, $M_{\tilde{q}} = 4 \times 10^6\,\mathrm{GeV}$, $\Gamma_{\tilde{q}} \approx \Gamma_{\tilde{q}\to q\chi} = 10^{-17}\,\mathrm{GeV}$ is chosen such that $\tau_{\tilde{q}}$ reaches almost to the QCD phase transition around $T = 1\,\mathrm{GeV}$. The relic abundance when neglecting bound states is thus insensitive to $\Gamma_{\tilde{q}}$ in a wide range of parameters. Including only the ground state (dot-dashed lines) would lead to a similar conclusion, although with a lowered relic abundance due to the additional depletion via ground state formation around $x = 2 \times 10^3$. The inclusion of higher excitations ($n_m = 10, 100$ in dashed and bold lines) gives rise to eternal depletion up until x_{dec} and, consequently, result in a direct dependence of $Y_\chi^0 = Y_\chi|_{\mathrm{today}}$ on $\Gamma_{\tilde{q}}$, in contrast to usual superWIMP production.

The abundances $Y_\chi(x)$ including bound states normalized by $Y_{\chi,\text{“SE only”}}(x)$ are shown in the subtended panel. The relic abundance reduces by a factor of 11 (1.7) for $n_m = 100$ ($n_m = 1$) due to annihilation via unstable BSF. Hence, the contribution of excited states $n \geq 2$ is a factor of 7 and sizably more important than the contribution of the ground state alone, unlike what is known from widely studied Abelian scenarios. Since the effective cross-section for $n \leq 100$ in Fig. 6.13 is well converged, the corresponding obtained abundance is expected to remain stable under inclusion of even higher bound states in the entire perturbative temperature range.

The emerging dependence on $\Gamma_{\tilde{q}}$ caused by the eternal depletion of the t-channel mediator is explicitly exemplified in Fig. 6.16. The given dotted and bold curves in blue and red are analogous to Fig. 6.15 but now shown simultaneously for three choices of $\Gamma_{\tilde{q}\to q\chi}$ as denoted in the figure. Neglecting BSF, Y_χ always reaches the same relic abundance at late times, apparent from the three red dotted curves overlapping at large x. Smaller decay rates lead to longer lifetimes $\tau_{\tilde{q}}$ and thus to lower relic abundances once BSF is accounted for. Hence, eternal depletion from non-Abelian BSF also changes the picture of usual superWIMP production, where Y_χ^0 is understood to be produced from a frozen-out abundance of $\tilde{q}$. The light-blue dashed curve extends the result for absolutely stable $\tilde{q}$ into the non-perturbative regime of QCD without respecting any further corrections. It serves to emphasize the effect of finite lifetimes in all three models. The freeze-in contribution to χ gives rise to the plateau of Y_χ at early times but remains small compared to the superWIMP production in all shown parameter choices.

For larger $\Gamma_{\tilde{q}\to q\chi}$, first the initial freeze-in contribution becomes significant to the relic abundance and, eventually, the decay takes place when $\tilde{q}$ is (almost) in equilibrium, changing the picture of the production mechanism and more processes need to be considered.

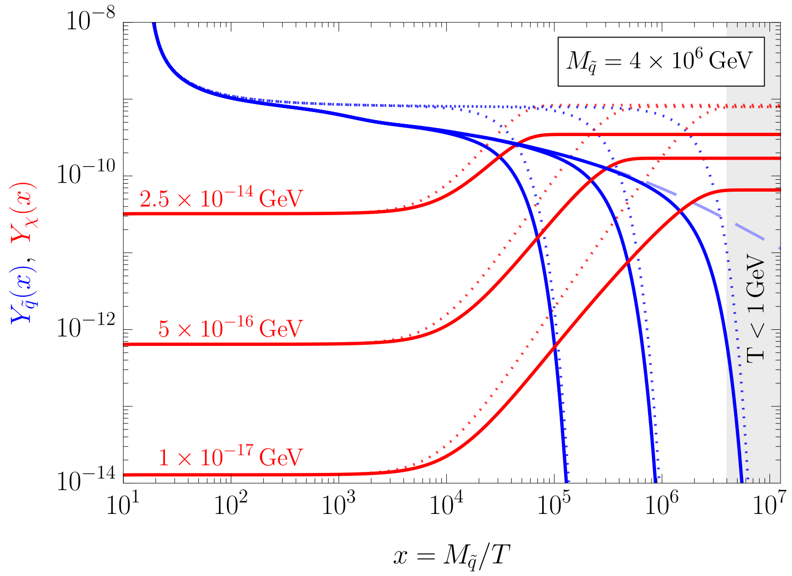

Figure 6.16: Abundance evolutions of $\tilde{q}$ and χ for $M_{\tilde{q}} = 4 \times 10^6\,\mathrm{GeV}$ in inverse temperature $x = M_{\tilde{q}}/T$. Dotted curves neglect bound state formation while bold curves include all $n \leq 100$ and all electric dipole transitions among them. Abundances $Y_{\tilde{q}}$ (blue) and Y_χ (red) for three values of the t-channel mediator decay rate, $\Gamma_{\tilde{q}} = 2.5 \times 10^{-14}, 5 \times 10^{-16}, 1 \times 10^{-17}\,\mathrm{GeV}$ are shown. A light-blue dashed curve shows $\Gamma_{\tilde{q}} = 0\,\mathrm{GeV}$.

6.6.6 Dark Matter relic density constraints

So far only the DM relic abundance Y_χ^0 has been calculated and without any need of m_χ. Hence, m_χ may be chosen freely so long as it remains negligible compared to $M_{\tilde{q}}$ to leave decay kinematics unaffected. The parameter space in m_χ and $\Gamma_{\tilde{q}\to q\chi}$ is shown in Fig. 6.17 for the already above investigated mediator mass $M_{\tilde{q}} = 4\times10^6\,\mathrm{GeV}$. The top horizontal axis gives x_{dec} as computed from Eq. (6.153). The four different curves, corresponding to the same values of $n_m = 0, 1, 10, 100$ as in Fig. 6.15, show the obtained DM relic density Y_χ^0 (right vertical axis) for every given value of $\Gamma_{\tilde{q}\to q\chi}$ (bottom horizontal axis). Y_χ^0 linearly relates to a specific value of m_χ upon imposing the condition that χ should saturate the DM relic density bound, *cf.* Eq. (1.1),

$$\Omega_{\mathrm{DM}}h^2 \equiv \frac{s_0 h^2}{\rho_c} Y_\chi^0 m_\chi = 2.744 \times 10^8 \frac{Y_\chi^0 m_\chi}{\mathrm{GeV}} = 0.120. \tag{6.154}$$

The used present-day values are the Hubble constant $h = 0.678$, the entropy density $s_0 = 2.8912 \times 10^9\,\mathrm{m}^{-3}$ and the critical density $\rho_c = 10.537h^2\,\mathrm{GeV\,m}^{-3}$ [197]. Larger m_χ at each value of Y_χ^0 overclose the Universe and are incompatible with experimental observations for cold DM. Furthermore, DM produced by decay from a much heavier mediator is subject to constraints from small scale structure formation as its momentum distribution after is peaked at much higher energies than typical cold DM. For too energetic DM, this eventually suppresses structure formation as the increased free-streaming length of χ washes out structures on smaller scales which are experimentally probed by measurements of the Lyman-α

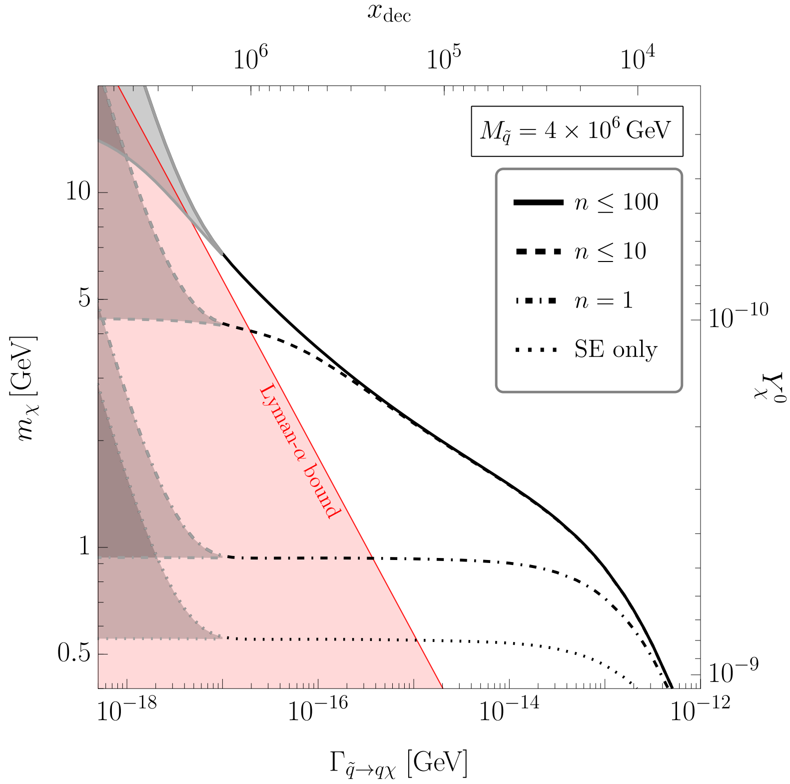

Figure 6.17: Combinations of Dark Matter mass m_χ and t-channel mediator decay rate $\Gamma_{\tilde{q}}$ for which the relic density bound is saturated for a mediator mass $M_{\tilde{q}} = 4 \times 10^6\,$GeV. Different curves include bound states $n \leq 0, 1, 10, 100$ (dotted, dot-dashed, dashed, bold) and all ℓ. All electric dipole transitions among bound state levels are included. Exclusion-regions at 95% confidence level by Lyman-α forest observations [52] are indicated by red shading. Gray bands bracket uncertainties due to non-perturbative effects near the QCD confinement scale, $T < 1\,$GeV. The upper horizontal and right-hand vertical axes are obtained using Eqn. (6.153) and (6.154).

forest spectral lines. The lower bound on m_χ is then given by [52]

$$\frac{m_\chi}{\rm keV} > 3.8 \times x_{\rm dec} \times \left(\frac{106.75}{g_{*S}(x_{\rm dec})}\right)^{1/3} \tag{6.155}$$

where g_{*S} is the number of relativistic degrees of freedom in the thermal bath which contribute to the entropy density [181].

The Lyman-α -exclusion bounds are shown as a red shaded region in Fig. 6.17. Each black curve fans out into a gray band at low decay rates where the mediator evolution becomes subject to non-perturbative QCD effects from $T < 1\,$GeV. The upper bound is obtained by assuming all $\tilde{q}$ vanish instantly by efficient annihilation once $T = 1\,$GeV is reached. The lower bound instead assumed that the entire mediator abundance is converted into χ, $Y_\chi(\infty) = Y_\chi(1{\rm GeV}) + Y_{\tilde{q}}(1{\rm GeV})$.

As discussed above, the Sommerfeld enhanced direct annihilation result barring any bound state contributions becomes independent of $\Gamma_{\tilde{q}\to q\chi}$ once the $x_{\rm dec} \gg x_{cd}$. Complete chemical decoupling is typically only a good approximation in presence of SE at $x > 10^3$. Decay rates below $2 \times 10^{-15}\,\text{GeV}$ would thus be excluded if no bound state effects were present. However, experimental bounds are entirely evaded when effects of excited bound states are properly included. The model remains in agreement with current Lyman-α forest measurements by virtue of the additional t-channel mediator depletion being compensated for by larger m_χ in order to satisfy the relic density constraint.

Lyman-α bounds become more severe at larger $M_{\tilde{q}}$ and, in particular, set upper bounds on x_{dec} more stringent than the theoretical limitations due to the QCD phase transition once $M_{\tilde{q}} > 4 \times 10^6\,\text{GeV}$. In the representation of Fig. 6.17, this means that also the solid black line extends into the excluded region before fanning out into its uncertain, gray area. Lower lifetimes of the t-channel mediator are needed to evade such strong constraints but in turn give rise to lower m_χ. The entire superWIMP production regime of the considered sbottom-like model is excluded for $M_\chi > 4 \times 10^8\,\text{GeV}$. On the other hand, effects of BSF become less prominent at lower $M_{\tilde{q}}$ since the chemical decoupling takes place already closer to the QCD phase transition. There is thus less time for the eternal depletion to affect on the t-channel mediator abundance before the temperature cools down to the confinement scale. In Fig. 6.17, this implies a shrinking of the parameter range between the gray uncertainty bands to the left and the steep cutoff to the right, where the decay takes place around or before x_{cd}. From the top horizontal axis, one can estimate the lowest accessible mass for the superWIMP production mechanism where the t-channel mediator chemical decoupling still occurs in the unconfined phase to be $M_{\tilde{q}}/\Lambda_{\text{QCD}} = 10^3\,\text{-}\,10^4$.

7 Conclusion

Effective field theories were shown to be a useful and often times needed tool in the realm of WIMP DM or extended dark sectors. With the interest of theoretical physics shifting to increasingly larger Dark Matter masses of the TeV scale and beyond, a plethora of non-perturbative effects arise from the large scale separation to the Standard Model. The paradigm of GeV-scale WIMPs, where interactions are readily estimated at tree level, becomes insufficient and a much richer landscape of physical phenomena opens up. The capabilities of EFT to rephrase problems in appropriate degrees of freedom and resum to all orders emerging non-perturbative interactions enable simple and physically intuitive descriptions even of such complex systems. Although, for the most parts, each of the chapters 3 - 6 focused predominantly on a single non-perturbative effect in order to highlight their individual relevance, all may as well be treated simultaneously within a single theoretical framework.

7.1 Summary

Four non-perturbative effects were discussed (each associated with a systematic power counting), namely:

1. s-channel resonances (small mass splittings relative to the mass),
2. long-range potentials (small or similar velocities relative to a small coupling),
3. jet formation (small final state masses relative to their energy) and
4. excited bound state formation (small or similar momenta relative to a Bohr momentum).

Particular attention was spent on the last point. All considered processes involve non-relativistic BSM initial state particles, making Sommerfeld enhancement from long-range potentials a recurring theme.

At first, s-channel resonance enhancements were proven to simply factorize, at leading order, from non-relativistic initial state physics, without sourcing any additional soft gauge boson interactions in the process. Consequently, Sommerfeld and resonance enhancements could be studied as parallel effects, unless unitarity becomes of concern. Depending on the exact value of the mass splitting, resonance enhancement can significantly alter late time indirect detection signals or the thermal production history of DM (or both), and were demonstrated to change the obtained thermal mass in a Higgsino inspired toy model setup by a factor of a few.

An updated analysis of Sommerfeld ehanced mixed neutralino DM models was presented making use of derived state-of-the-art SM input values and improving upon previous results by including one-loop running gauge and Yukawa couplings with automated treatment of a light or heavy BSM Higgs sector. Reproducing all known features in the a two-dimensional plane of wino-Higgsino mixed models, especially the location of the first Sommerfeld resonance, thermal mass predictions are affected only at the percent level. Notable effects were found in late-time annihilation cross-sections of models hosting large primary $t\bar{t}$ branching fractions.

Another improvement to the same numerical code used to compute SE in arbitrarily mixed neutralino models was the addition of accurate semi-inclusive cross sections for annihilation processes into highly energetic photons near the kinematic endpoint of the spectrum. This was possible in consequence of the completion of a framework which includes LO Sommerfeld and NLL Sudakov resummation while reliably ensuring to only neglect systematically power suppressed terms in PNRDM. As the original EFT construction assumes fully degenerate electroweakinos, virtual contributions of heavy states needed to be decoupled by use of a manually implemented matching function. A set of benchmark points distributed throughout the most relevant areas in parameter space found effects from Sudakov resummation to yield a reduction of the cross section by about one third in most models. This pushes several mixed bino-wino or fully-mixed models out of the projected reach of the upcoming Cherenkov Telescope Array.

At the core of this thesis stands an in-depths analysis of radiative bound state formation effects in Coulombic potentials under general multipole interactions where initial and final state potential strengths are separately kept general. Analytic results of radial overlap integrals keeping multipole order and all quantum numbers general were found in a compact form readily evaluated to closed-form expressions for specific processes. An algorithmic approach was outlined to arrive at simplified closed-form expressions allowing both, convenient analytic and efficient numerical treatments. This recipe finds the entirety of leading order BSF for Coulombic potentials in terms of only a single hypergeometric function, independent of the multipole order, in combination with long-known factors and simple rational polynomials. Explicit results for monopole, dipole and quadrupole were presented and used in subsequent numeric studies. Significant cancellations occur when initial and final state potentials are identical. More general results, thus, do not align with naive intuition from QED but lend themselves to a semi-classical interpretation. Whenever the initial state is repulsive or even just less attractive than the final state, BSF is enhanced over the case of identical couplings in a limited velocity range specific to each bound state. The enhancement increases for capture into higher excitations. Therefore, BSF of such non-identical couplings can systematically violate partial wave unitarity at the perturbative leading order in the EFT power counting for arbitrarily small couplings, provided sufficiently high excitations are considered. Carefully avoiding regions in parameter space where unitarity is violated, the phenomenological impact of highly excited bound states on DM thermal production was studied in toy models involving SU(N_c) gauge symmetries. Annihilation via bound state decay remains efficient at all times and the bound state constituents never undergo complete chemical decoupling, instead seeing an “eternal” depletion. The depletion may, however, be interrupted by other effects such as finite constituent lifetimes, unitarization or, eventually, phase transitions in the gauge theory close to the Landau pole. An exemplary application to a colored and charged t-channel mediator DM model in a superWIMP-production scenario showed that in addition to BSF, transitions between bound-state levels significantly further enhance the depletion and eternal depletion sources a depenence of the relic density on the mediator lifetime. The effects from excited bound states were shown to help evade experimental constraints from Lyman-α observations and increase DM mass predictions by up to an order of magnitude.

7.2 Outlook

One clear-cut extension of the presented work is to exceed the set of manually constructed benchmarks for the analysis of indirect detection constraints from gamma-rays line searches. All necessary tool-chains to perform a detailed scan of parameter spaces of interest exist and first attempts at more systematic investigations have already been started. Such analyses become especially interesting in relation to future data releases from the Cherenkov Telescope Array which should provide world leading sensitivity to cosmic rays originating from the galactic center.

A full-force investigation might still await yet further improvements to the numerical Sommerfeld calculation since, with the decoupling theorem of soft modes from s-channel resonance enhancement and SE at hand, also the treatment of resonant models was understood. Some work may be required to include resonances on a technical level within the limitations of the existing numerical code basis. Such a modification will open up one of the few remaining MSSM parameter space regions currently inaccessible to thermal neutralino DM mass predictions.

Several open theoretical questions regarding BSF remain, first and foremost, to understand the cause of the observed perturbative unitarity violation. Typically, such a breakdown of an EFT power counting is indicative of a novel scale emerging in the considered process which had not been respected in the construction of the EFT. So far, no candidate for such a scale has been identified and in the common picture of PNREFT no such hypothesized energy scale exists. Alternatively, the unique role of identical Coulomb potentials, where systematic UVi was shown to be absent, possibly hints towards a different explanation in terms of overlapping mathematically unrelated wave functions. Apart from this conceptual question, demonstrating unitarization of BSF in all its technical glory from a realistic PNREFT Lagrangian poses a daunting unresolved task, even though it was recently shown on a conceptual level. Secondly, the converged smooth, power-law-like behavior of inclusive BSF cross-sections and effective cross sections remains mathematically mysterious. An analytic understanding of this power-law may prove useful for understanding unitarity violating parameter spaces and aid phenomenological estimates.

Since the topic of Sommerfeld enhancement, especially Sommerfeld resonances, is intimately linked to bound states, both must be considered simultaneously during thermal production to reach accurate predictions of relic densities. Modern day studies of minimal WIMP models for quintuplet and higher representations only include few excited states, naively expecting higher excitations to be suppressed while bound states are currently completely disregarded in the computation of neutralino relic densities. Possible improvements are thus apparent.

This corroborates how all here separately discussed non-perturbative effects can coexist in a single theory. Altogether, they give rise to a wide field of emergent phenomena, which can aid either side in the ever-prominent fight of falsifiability and viability of theoretical models once one steps into the TeV-realm in the hunt for clear hints of Dark Matter.

Acknowledgments

This thesis is devoted to χ, for I see clarity and brightness within.

Above all, I thank first Professor Martin Beneke who offered me this project under his supervision, supplied the resources for my employment over more than three years and, above all, has been in continuously close contact throughout this time. Secondly, I thank Mathias Garny, my PhD mentor who set my cosmological education in motion with his in-depths explanations of any question or Journal Club paper we could come up with. I acknowledge the funding and training provided by the *ORIGINS* cluster of excellence and the Deutsche Forschungsgemeinschaft, *Sonderforschungsbereich 1258*.

I am also deeply indebted to both of my officemates, Kai Urban and Tobias Binder (whom I am doing wrong by naming him in historical order here): Kai primarily, once more, for his support during my Master thesis, the shadow of which still loomed over two chapters of this work, and his BSF code; Tobias for uncountable discussions, advice and immediate feedback. Specifically, I owe him much of my understanding of the scientific community as well as my first extrabavarial position. We had a great adventure organizing and running QMDM2024 together with Gramos (thanks also to Nora and Antonio for having me on the project). Further, I thank Lorenzo for doublechecking many results from chapter 6 and all members of T31, among others Lea, Domenico, Julian (with best wishes and thanks for setting up PhD game nights) and Andrea and, not the least, Stefan® as well as our secretary Elke for managing all my holidays.

None of this scientific work would have ever been possible without the immeasurable support from my family for nigh three decades: MJL, JML, MML, SML, ML & mL. I thank my parents, my sister (for early career upbringing and setting perspective) and the ML-triple in hopes that the little M will eventually find this work as fascinating as his stars. They all deserve my greatest gratitude for patience and providing comfort, despite times when I was in some way absent for science.

Lastly, I would like to commemorate here the CANARY ISLAND WINTER SCHOOL XXXIII 2022 on Tenerife, especially *los Chicos*. Those were two of the most memorable weeks I spent in the last five years and I remain indebted to each person and all choices involved in getting me there. Shall they be defining as well.

A Notation Index

This appendix provides an index of the most important notations and conventions used throughout this thesis.
Shared between all chapters is, most importantly, the notion of

v : Relative velocity of non-relativistic two-particle states, $\mathrm{v} = |\vec{\mathrm{v}}_1 - \vec{\mathrm{v}}_2|$.

All chapters treat processes in the centre-of-mass frame. Heavy, non-relativistic particles with masses of the hard scale in (P)NREFT use generally capital M, subscripted accordingly and M_χ denotes heavy DM masses. Soft-scale masses use the letter m instead. Despite the omnipresent theme of two-constituent states, the total mass of the system is never abbreviated by a designated symbol while reduced masses (μ) are only rarely used and clearly denoted in these cases.

A.1 Resonant particle decay

Most notation is only briefly required for the technical proof of soft decoupling of the unstable resonance field. The resonance field R is later identified with A. Physically relevant quantities are:

M_R : Mass of the s-channel resonant field.

Γ_R : Total decay width of the s-channel resonant field. The pole mass value is $M_R^2 - \mathrm{i} M_R \Gamma_R$.

δM_R : Resonance detuning, $\delta M_R = M_R - M_1 - M_2$.

$\hat{\Gamma}_R$: Partial decay width of R for an unspecified channel.

A.2 Sommerfeld-effect for neutralino Dark Matter

SM input parameters may be read from Tab. 1. Core definitions are:

$\hat{\mu}$: Dimensional regularization renormalization scale.

μ : Higgsino mass parameter.

$M_{1,2,\tilde{H}}$: Masses of the bino (1), wino (2) or Higgsino ($\tilde{H}$).

$\chi_i^\pm$: Chargino (anti-) particles, $i = 1, 2$.

χ_i^0 : Neutralino particles, $i = 1, 2, 3, 4$.

M_{LSP} : The LSP mass which is identical with the DM mass $M_\chi = M_{\chi_1^0}$.

δM_x : Mass splitting relative to LSP, $\delta M_x \equiv M_x - M_{\mathrm{LSP}}$, typically of the (ultra-)soft scale.

Fields in the various Higgs bases and Higgs parameters are:

$H_{1,2}$: SUSY basis (MSSM Higgs superfield scalar components).

h, H : Mass eigenbasis in the EW symmetric phase.

h^0, H^0 : Neutral scalars in the EW broken mass eigenbasis.

A^0 : Pseudoscalar in the EW broken mass eigenbasis. It is the lightest "BSM" Higgs boson.

$H^\pm$: Charged scalars in the EW broken mass eigenbasis.

m_{h,H,A^0} : Masses of the respective bosons, denoted by small letters independent of their actual scale.

α_H : Mixing angle in the EW unbroken phase.

$v_{1,2}$: VEVs of the neutral components $H_1^0 = (H_1)^1$ and $H_2^0 = (H_2)^2$, respectively.

v_{sm} : SM Higgs VEV value, 246.22 GeV.

β : Ratio of vacuum expectation values, $t_\beta = \tan(\beta) = v_2/v_1$.

A.3 Sudakov-resummation in neutralino annihilation

The majority of used conventions is introduced in chapter 4 already. Here, most importantly, Γ_{IJ} denotes the (not further specified) short distance annihilation matrix into primary photons in semi-inclusive processes for "external" two-particle states I and J. Superscripts Tree, LL and NLL indicate which orders in the logarithmic expansion have been resummed. More intricate differences are:

Γ_{IJ} : Unspecified annihilation matrix. Either formal or identical to $\Gamma_{IJ}^{\mathrm{NLL}}$.

$\Gamma_{IJ}^{\mathrm{NLL,EFT}}$: NLL Sudakov resummed annihilation matrix obtained in PNRDM.

$\Gamma_{IJ}^{\mathrm{Tree,exact}}$: LO perturbative annihilation matrix in the relativistic theory.

$\mathcal{G}_{IJ}$: improvement factor correcting LO mass dependences in $\Gamma_{IJ}^{\mathrm{EFT}}$.

$\Gamma_{IJ}^{\mathrm{NLL},imp}$: NLL resummed, leading order corrected annihilation matrix.

$\Gamma_{IJ}^{\mathrm{NLL}}$: NLL Sudakov resummed, leading order corrected annihilation matrix including smooth decoupling of heavy internal states.

A.4 Bound state formation

The considered processes see an initial scattering state $\mathcal{S}_{p\ell'}$ transition to a final bound state $\mathcal{B}_{n\ell}$ (both already partial wave decomposed) under emission of a BSF mediator field ϕ, which is largely assumed to be massless. Bound state formation in general Coulombic potentials $V = -\alpha^{\mathrm{eff}}/r$ by radiative multipole emission of ultrasoft modes are characterized by the following model parameters:

M_χ : Mass of initial and final state constituents (differences are negligible).
For section 6.6, $\tilde{q}$ forms the bounds state, hence $M_{\tilde{q}}$ is used.

a : The multipole order of the specified transition.

g_a^{eff} : Coupling of the a-th multipole.

α_s : Effective initial (scattering) state potential strength.

α_b : Effective final (bound) state potential strength.

For ultrasoft emitted BSF mediators, the total mass of the initial scattering and final bound two-constituent states must agree up to ultrasoft differences and mass splittings are thus negligible to leading order. Nevertheless, corrections would only arise as modifications to p and p_n and therefore only multiplicatively modify ζ_n without sourcing any new terms in the calculation.
A particular BSF transition is further defined by various process variables:

p : Initial state relative momentum, $\vec{p} = p\,\hat{p}$.

ℓ' : Initial (scattering) state angular momentum quantum number.

n : Final (bound) state major quantum number.

ℓ : Final (bound) state angular momentum quantum number.

From the above model parameters and input variables, the following convenient definitions are derived (which values are to be considered as derived is an arbitrary, intuitive choice):

$\alpha_{\mathrm{BSF}}:$ $\alpha_{\mathrm{BSF}} = g_a^{\mathrm{eff}^2}/4\pi$.

$E_n:$ Bound state energy absolute value, $E_n = M_\chi \alpha_b^2/4n^2$.

$p_n:$ Bound state Bohr momentum $p_n \equiv M_\chi \alpha_b/2n$.

$\zeta_n:$ Ratio of momenta, $\zeta_n \equiv p_n/p = \alpha_b/\mathrm{v}n$.

$\kappa:$ Ratio of effective potential strengths, $\kappa \equiv \alpha_s/\alpha_b$.

$\zeta_{b,s}:$ Coupling strength-velocity ratio, $\zeta_{b,s} \equiv \alpha_{b,s}\,/\,\mathrm{v}$, also $\zeta_s = n\kappa\zeta_n$.

$\Delta:$ Change in angular momentum, $\Delta \equiv \ell' - \ell$.

$K:$ Initial state kinetic energy, $K \equiv p^2/M_\chi = M_\chi \mathrm{v}^2/4 = E_n \zeta_n^{-2}$.

$b:$ Impact parameter, $b = b(\mathrm{v}) = (\sqrt{\ell'(\ell'+1) + \zeta_s^2} - \zeta_s)/p$.

$r_n:$ Bound state Bohr radius, $r_n = n/p_n$.

$\omega:$ BSF mediator energy, $\omega = K + E_n = (1+\zeta_n^2) M_\chi \mathrm{v}^2/4$.

$\vec{p}_\omega:$ Emitted BSF mediator momentum.

Further abbreviations are

$$\begin{aligned}
\bar{n} &\equiv n - \ell - 1,\\
\bar{n}_s &\equiv \mathrm{i}\zeta_s - \ell' - 1,\\
F_+(x) &\equiv {}_2F_1\left(-\bar{n}, x + \ell + \mathrm{i}\zeta_s; 2\ell + 2; \tfrac{-4\mathrm{i}\zeta_n}{(\mathrm{i}-\zeta_n)^2}\right),\\
\gamma_n &\equiv \mathrm{ArcCot}(\zeta_n),\\
\gamma_a &\equiv \arg(R_a),\\
\gamma_F &\equiv \arg(F_+(0)),
\end{aligned}$$

Since $\gamma_{n,a}$ is never written for concrete values of n and a, there is no ambiguity here. For the treatment of thermally averaged quantities in freeze-out computations in this chapter's final subsection, a fine separation between thermally averaged rates, *e.g.* $\Gamma_{\tilde{q}}^{\mathrm{dec}}$, and vacuum process rates, *e.g.* $\Gamma^{\tilde{q}\to\chi q}$, is used. Corresponding definitions of the physical process type (decay, ionization or transition) is denoted as a superscript on thermally averaged rates while the a superscript denoting a specific reaction such as $\tilde{q} \to \chi q$ is given to vacuum processes.

B Neutralino Dark Matter benchmarks

model	μ	M_1	M_2	$\tan\beta$	m_{A^0}	M_{sf}
pure models						
`*B`	7	2.145	8	15	2.9	12
`H`	-1.112	7.5	7	15	2.9	12
`W`	9	8	2.85	15	2.9	13
2-component						
`BH`	-1.069	1.116	10	2.24	2.9	29
`BW`	2.91	2.145	2.148	15	2.9	12
`HW`	-2.977	30	2.839	3	2.9	20
fully mixed						
`BHW-mix`	-2.041	1.92	1.929	2.5	1.96	20
`BHW-mix2`	-2.094	1.97	1.978	2.5	2.045	20
`BHW-mass`	-1.701	1.625	1.642	2.2	1.725	25
`BHW-nh2`	-1.94	1.802	1.819	3.6	0.67	25
additional						
`*BW-coan`	7	2.145	2.148	15	2.9	12
`*H+`	1.112	7.5	7	15	2.9	12
`H2`	-1.24	8	1.419	2.4	1.25	29
`BW-2520`	-3.3	2.525	2.52	20	2.5	7.25
`BW-e`	-2.27	1.829	1.836	15	2.446	5.45
`BW-e-nh2`	3.6	2.055	2.058	15	0.55	10
`HW-nh2`	-3.065	20	2.92	3	0.78	25
`BH-undet`	-1.363	1.3	1.33	2.19	1.305	25
`BW-nfw`	3.38	2.075	2.078	15	2.9	12
`BW-ce`	-3.2	2.287	2.288	13	2.8	13.8
`BW-2670`	-3.1	2.677	2.67	20	2.7	12
`BW-nh2`	-3.15	2.4417	2.44	15	0.62	9
`BW-ce-nh2`	3.42	2.165	2.1665	15	0.57	9.5

Table 4: Benchmark MSSM inputs used for the analyses in chapters 4 and 5. Masses are given in TeV. An asterisk ($*$) marks models which are not constructed to produce the observed DM relic density. The split into 4 categories serves ease of reference. Further SM inputs are taken from Tab. 1.

Originally [2], all benchmarks without an asterisk marking (*i.e.* all except for `B`, `BW-coan` and `H+`) were constructed to yield experimentally indistinguishable values $\Omega_{\mathrm{DM}}h^2 = 0.1186 \pm 0.0005$. For the present thesis, an updated numerical analysis was performed using improved SM inputs, *cf.* Tab. 1, and one-loop running Yukawa couplings. The listed benchmarks are therefore spread within a 3% band around $\Omega_{\mathrm{DM}}h^2 = 0.128$ and hence slightly overclose the Universe.

C Supplementary material to bound state formation

This appendix collects various smaller addenda to chapter 6. Mathematical identities of hypergeometric functions are found in section C.1 and a summarized outline of the algorithmic simplification procedure to arrive at the compact expressions for I_R of Eqn. (6.50-6.55) is given in section C.2.

The well known discrete bound state and continuous scattering state solutions to the Schrödinger problem in presence of a Coulomb potential $V_{b,s}(r) = -\alpha_{b,s}/r$ are given in the main text, Eqn. (6.21-6.24). Their dependence on (confluent) hypergeometric functions and the corresponding overlap integral demand several useful simplification transformation of hypergeometric functions.

The radial wave functions lend themselves to a mathematically more efficient notation, identifying the respective first arguments of $\mathcal{B}_{n,\ell}(r)$ and $\mathcal{S}_{p\ell'}(r)$ as $-\bar{n}$ and $-\bar{n}_s$. This notation suggests the close relation between radiative processes into positive-energy final states (*i.e.* bremsstrahlung) and negative-energy final states (*i.e.* BSF). However this comes at the cost of needing to perform a careful case separation in order to use correct contours in overlap elements [141]. Note also that the integral in (6.33) cannot be used for the case of bremsstrahlung since the integration regime demands at least one confluent hypergeometric function to have a real-valued argument $t \in \mathbb{R}$.

C.1 Hypergeometric Functions

The first part of this appendix, C.1.1, collects some of the many known mathematical identities for hypergeometric functions which make up the basis of the more directly applicable relations of $F_+(X)$ provided in section C.1.2, therein also already using the notation of chapter 6.

C.1.1 Properties of confluent and Gauss hypergeometric functions

Some rather well-known general properties of the general hypergeometric functions ${}_pF_q(a_1, ..., a_p; b_1, ..., b_q; z)$ are their symmetry between interchange among a_i and interchange among b_i. Moreover, if any single one a_i becomes zero, one finds ${}_pF_q(0, ...) = 1$. For this thesis, confluent and Gauss-hypergeometric functions, ${}_1F_1$ and ${}_2F_1$, suffice. For the sake of rudimentary completeness, formulas stated in the main text are repeated here.

By iteration of known identities between confluent hypergeometric functions with neighboring first parameters, on can obtain the distant-neighbor relation for $\Delta \in \mathbb{Z}$:

$$ {}_1F_1(a; c + 2|\Delta|; x) = \frac{\Gamma(c + 2|\Delta|)}{x^{2|\Delta|}\Gamma(c)} \sum_{j=0}^{2|\Delta|} (-1)^j \binom{2|\Delta|}{j} {}_1F_1(a - j; c; x). \tag{C.1} $$

The notation Δ is already suggestive of how it is employed.

The relevant integral of two confluent hypergeometric functions with additional monomial and exponential terms, see also Eq. (6.33) [142], is

$$\int_0^\infty \mathrm{d}t\, \mathrm{e}^{-st}\, t^{(c-1)}\, {}_1F_1(a;c;t)\, {}_1F_1(\alpha;c;\lambda t) \;= \\ = \Gamma(c)(s-1)^{-a}(s-\lambda)^{-\alpha} s^{a+\alpha-c}\, {}_2F_1\left(a,\alpha;c;\frac{\lambda}{(s-1)(s-\lambda)}\right), \tag{C.2}$$

With $a = 0$, the integral solution reduces to

$$\int_0^\infty \mathrm{d}t\, \mathrm{e}^{-st}\, t^{(c-1)}\, {}_1F_1(\alpha;c;\lambda t) \;=\; \Gamma(c)(s-\lambda)^{-\alpha} s^{\alpha-c}. \tag{C.3}$$

For Gauss hypergeometric functions, some simpler relations between neighboring parameters are

$${}_2F_1(a,b;c;z) = \frac{(c-1)}{(a-1)z}\left[{}_2F_1(a-1,b;c-1;z)) - {}_2F_1(a-1,b-1;c-1;z)\right], \tag{C.4}$$

$${}_2F_1(a,b;c;z) = \frac{(b-c-1)(bz-cz+c)}{c(c+1)(z-1)}\, {}_2F_1(a,b;c+2;z) \\ - \frac{b(z(a+b-1)-2cz+c)}{c(c+1)(z-1)}\, {}_2F_1(a,b+1;c+2;z), \tag{C.5}$$

$${}_2F_1(a,b;c;z) = \frac{(c-2)(c-1)(z(a+b+3-2c)+c-2)}{z^2(a-c+1)(c-b-2)(c-b-1)}\, {}_2F_1(a-1,b;c-2;z) \\ + \frac{(c-2)(c-1)(z-1)(z(a+1-c)+c-2)}{z^2(a-c+1)(c-b-2)(c-b-1)}\, {}_2F_1(a,b;c-2;z), \tag{C.6}$$

$${}_2F_1(a,b;c;z) = \frac{(c-1-a-b)}{c-a-1}\, {}_2F_1(a+1,b;c;z) \\ - \frac{b(z-1)}{c-a-1}\, {}_2F_1(a+1,b+1;c;z). \tag{C.7}$$

Involving changes in the argument, $z \notin [1,\infty[$, it obeys

$${}_2F_1(a,b;c;z) = (1-z)^{-a}\, {}_2F_1\left(a,c-b;c;1-\frac{1}{1-z}\right). \tag{C.8}$$

The derivative with respect to the argument is known to be

$$\partial_z\, {}_2F_1(a,b;c;z) = \frac{a\,b}{c}\, {}_2F_1(a+1,b+1;c+1;z) \\ = \frac{b}{z}\left[{}_2F_1(a,b+1;c;z) - {}_2F_1(a,b;c;z)\right]. \tag{C.9}$$

C.1.2 Properties of the hypergeometric function $F_+(x)$

For a compact notation of the hypergeometric functions, the abbreviations $\bar{n}$ and $\bar{n}_s$ are introduced in Eqn. (6.34) and (6.35), *cf.* App. A.4. These definitions also see usage in section 6.2, yet in most other places they are instead expressed through n and ζ_s (as well as ℓ and Δ or ℓ') for a better physical intuition. As a convenient function in radial overlap integrals, one finds

$$F_+(X) \;=\; {}_2F_1\left(-\bar{n},\, X+\ell+\mathrm{i}\zeta_s;\, 2\ell+2;\, \frac{-4\mathrm{i}\zeta_n}{(\mathrm{i}-\zeta_n)^2}\right), \tag{C.10}$$

The function has two main additional symmetries compared to a fully general hypergeometric function ${}_2F_1(a,b;c;z)$ for independent parameters or arguments, firstly $b^* = c-b-2+2X$ and secondly $(1-z)^* = 1/(1-z)$. Three neighboring values of X are related by hypergeometric identities, hence any $F_+(X)$ can always be expressed through $X = 0, 2$.
To increase X (if $X < 0$):

$$\begin{aligned} F_+(X) = {} & \frac{(\zeta_n+\mathrm{i})^2(1+\ell+X+\mathrm{i}\zeta_s)}{(\zeta_n-\mathrm{i})^2(1+\ell-X-\mathrm{i}\zeta_s)} F_+(X+2) \\ & + 2\frac{(1-\zeta_n^2)\,(X+\mathrm{i}\zeta_s) - 2in\zeta_n}{(\zeta_n-\mathrm{i})^2(1+\ell-X-\mathrm{i}\zeta_s)} F_+(X+1), \end{aligned} \tag{C.11}$$

To decrease X (if $X > 2$):

$$\begin{aligned} F_+(X) = {} & \frac{(\zeta_n-\mathrm{i})^2(\mathrm{i}\zeta_s-\ell+X-3)}{(\zeta_n+\mathrm{i})^2(1-\ell-X-\mathrm{i}\zeta_s)} F_+(X-2) \\ & + 2\frac{(1-\zeta_n^2)\,(X-2+\mathrm{i}\zeta_s) - 2\mathrm{i}n\zeta_n}{(\zeta_n+\mathrm{i})^2(1-\ell-X-\mathrm{i}\zeta_s)} F_+(X-1). \end{aligned} \tag{C.12}$$

Inserting $X = 0$ in (C.11) yields, explicitly for $F_+(1)$,

$$F_+(1) = \frac{1+\zeta_n^2}{2\mathrm{i}\zeta_s} \frac{(1+\ell+\mathrm{i}\zeta_s)\,\mathrm{e}^{2\mathrm{i}\gamma_n} F_+(2) - (1+\ell-\mathrm{i}\zeta_s)\,\mathrm{e}^{-2\mathrm{i}\gamma_n} F_+(0)}{\zeta_n^2 - \left(1-\frac{2}{\kappa}\right)}, \tag{C.13}$$

Lastly, $F_+(X)$ obeys a symmetry around $X = 1$ which relates $X = 0, 2$ as complex conjugates with an additional factor phase

$$F_+(X) = \mathrm{e}^{4\mathrm{i}\gamma_n(n-\ell-1)} F_+^*(2-X). \tag{C.14}$$

C.2 Algorithmic radial overlap evaluation

Before defining the algorithm to obtain simple forms of the radial overlap integral, it should be noted that there exist also distant-neighbor relations for parameters of Gauss hypergeometric functions with coefficients in terms of recursive objects. Their insertion into the sum and derivative of *cf.* Eqn. (6.41) and (6.42) does thus still not result in general closed-form expressions. On the contrary, after evaluation of the derivatives, solutions are then found to be intractable high order recursive functions which permit any reasonable physical interpretation and promises no gains beyond automating the procedure below.

The following steps allow to systematically extract the squared radial overlap integral in the form of Eq. (6.50) by virtue of simplifying the more minimal integral $J^{a,\Delta}_{p,p_n}$ appearing in Eq. (6.45). It is advised to gather up all identical ${}_2F_1$ functions in between steps.

1. Starting from the general definition of $J^{a,\Delta}_{p,p_n}$, Eq. (6.36), the second parameters of the confluent hypergeometric functions must be made to coincide by applying (C.1) on the respectively higher one, *i.e.* the scattering state if $\Delta > 0$ and the bound state if $\Delta < 0$.
2. Introduce an ancillary variable s in the exponential function, according to Eq. (6.40).
3. With the integral (C.2) ($c = 2\ell_m + 2$) and some simplifications, the expressions for $J^{a,\pm|\Delta|}_{p,p_n}$ in Eqn. (6.41) and (6.41) are obtained.
4. Insert, latest now, the desired transition a and Δ.
5. Perform the derivatives in s and set $s = 0$, with further basic simplifications applied as needed. According to (C.9), this can only affect the second argument.
6. Explicitly write out the finite summation in j.
7. If $\Delta < 0$, apply Eq. (C.5) repeatedly, to shift the third parameter to $2\ell + 2$.
8. If $\Delta < 0$, apply Eq. (C.7) repeatedly until all hypergeometric functions have as their first parameter exactly $-\bar{n}$. All hypergeometric functions are now of the form $F_+(X)$.
9. Iterate $F_+(X)$ by Eqn. (C.11) and (C.12) such that only $X = 0, 1, 2$ are present in the expression.
10. Eliminate $F_+(1)$ using Eq. (C.13)
11. Lastly, identify $F_+(2)$ in terms of $F_+(0)^*$ by (C.14) for the case $X = 2$.
12. Upon taking the absolute square in (6.45), the sum of $F_+(0)$ and $F_+(0)^*$ can be decomposed into its overall amplitude square, the phase factor and polynomial terms to be identified with R_Δ in (6.50).

The use of computer algebra systems is recommended as intermediate expressions become lengthy in this outlined procedure, especially for $\Delta < 0$ due to the additional shifts between the first two parameters of the hypergeometric function in step 3. Nevertheless, the final expressions for $\Delta = \pm a$ are very similar in many aspects, *cf.* Eqn. (6.52-6.55). The fact that $R_{\pm a}$ differ in their power in n in the large-n limit suggests that there should be some form of $I^{a,\Delta}_R$, possibly in terms of a different hypergeometric function than $F_+(0)$, which balances both cases. However the large-n case is primarily of analytic interest and, moreover, the cases $\Delta = \pm a$ are qualitatively very similar at maximal $\ell \gg 1$. Thus, the here derived expression (6.50) is satisfactory and also numerically efficiently evaluated.

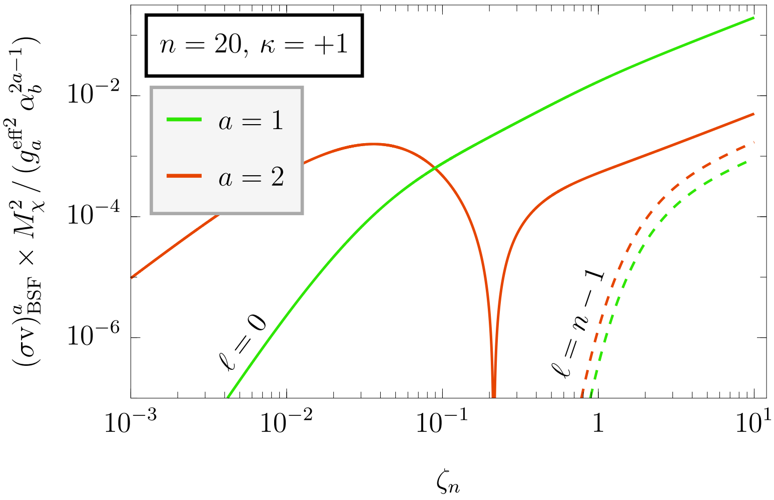

Figure D.1: Various bound state formation cross-sections, normalized by $g_a^{\mathrm{eff}^2}\alpha_b^{2a-1}/M_\chi^2$, plotted over ζ_n. Different multipoles $a = 1, 2$ (green, orange) are shown for $\kappa = 1$, $n = 20$ and $\ell = 0, 19$ (solid, dashed).

D Analyses of Coulombic bound state formation

The first section of this appendix includes a thorough functional analysis of the BSF cross-section in all independent parameters and should allow readers unfamiliar in the subject to understand in detail the functional behavior of $(\sigma \mathrm{v})^a_{p\,\ell' \to n\ell}$ from Eq. (6.28). Since the phase space factor and angular integral are straightforward, especially in their velocity dependence as one expects from an unpolarized spherically symmetric process, the discussion is primarily defined by I_R, Eq. (6.50). Section D.2 illustrates additionally inclusive bound state formation processes in dark U(1) and dark SU(3) models.

D.1 Parametric dependence of exclusive cross sections

BSF cross-sections depend in a complicated way on the parameters κ (the initial to final state potential ratio), n and ℓ (the bound state quantum numbers) and the initial state scattering angular momentum ℓ'. Up to quadrupole interactions, $a = |\ell' - \ell|$ is ensured by angular momentum selection rules. The focus of this thesis resides on the regime $\kappa \leq 1$, especially so on $\kappa < 0$ which is of interest for BSF in non-Abelian gauge theories. Qualitatively, there is little difference between $\Delta = \pm a$ once $\ell \gg a$ and, for simplicity, this appendix shall consider only $\Delta \geq 0$ as it allows capture into $\ell = 0$. Cross sections are plotted in $\zeta_n = \alpha_b / n\mathrm{v}$ and all explicit dependence on M_χ, α_b and g_a^{eff} is absorbed in the normalization of the vertical axis by plotting $(\sigma \mathrm{v})^a_{p\ell' \to n\ell} \times M_\chi^2 / g_a^{\mathrm{eff}^2} \alpha_b^{2a-1}$. This allows to conveniently depict different multipoles in a single plot which otherwise are far separated in their absolute values.

To begin the discussion with a simple case, consider $\kappa = 1$. Fig. D.1 shows the BSF cross-sections for $n = 20$ and $\kappa = 1$ for the first three multipoles. Dashed curves give the maximal angular momentum $\ell = n - 1 = 19$ while bold ones give the s-wave $\ell = 0$. The Abelian dipole setup $a = \kappa = 1$ has been widely studied in non-relativistic quantum electrodynamics will be discussed in greater detail in section D.2. Note that the monopole term is known to vanish due to orthonormality of the wave functions. The orthogonality is explicitly unique to $\alpha_b = \alpha_s$. This observation suggests an interesting hypothesis that by computing overlap between orthogonal full wave functions for general κ, that is when multipole interactions are resummed to to all orders in the two-constituent Green function, any monopole interactions of properly projected eigenstates must vanish and, correspondingly, general κ may yield a behavior more similar to $\kappa = 1$ than what is found here. While it must be that a complete all-order treatment of a hermitian Hamiltonian maintains unitarity, this line of argument sheds a new interpretation on the observations of UVi in this thesis, namely that the overlap of wave functions of technically unrelated (free) Hamiltonians is simply by construction not expected to maintain unitarity. In this reasoning, there is no need for a new physical scale breaking the perturbative expansions.

Once the velocity drops far below all other scales, $\zeta_n \gg 1$, all cross sections are essentially featureless and yield the well known Sommerfeld enhancement $\sim 1/\mathrm{v}$. According to (6.50), the cross section must vanish whenever

$$\frac{2\gamma_n(n-\ell) - \gamma_a - \gamma_F}{\pi} \in \mathbb{Z}, \tag{D.1}$$

apart from the lifted pole in the denominator $\zeta_n^2 = 1 - 2/\kappa$. As γ_n changes with ζ_n, see Eq. (6.47), large $n - \ell$ allows for many solution of this condition unless $\gamma_{a,F}$ balance it. Each solution gives rise to a sign flip in the radial overlap integral which results in a root of the squared matrix element and the cross section yields (strongly) oscillatory behavior. Between two consecutive roots, I_R necessarily forms a local maximum. Since the oscillations become very rapid, their numerical resolution is tedious yet not insightful.

In light of Fig. D.1, the rather vague statement of the Abelian case being “mostly featureless” stated in section 6.2.7 can be discussed concretely. Even the Abelian-case cross section develops a minor peak and (at sufficiently high n) also one additional root for quadrupole interactions. The additional root is not yet present at very low $n \sim \mathcal{O}(1)$ [138]. Mathematically, this is understood from $R_{\pm 2}|_{\kappa=1}$ maintaining a non-trivial complex part, which is not yet the case in $R_{0,\pm 1}$. No further roots were observed to develop up to $n = 1300$. Such additional roots also occur in general κ, yet they never grow in number as for the rapid oscillatory regime found in non-Abelian cases at large $n \gg \ell$ from the phase term $(n-\ell)\gamma_n$. With the semi-classical analogies of section 6.3 these roots are physically understood as a consequence of a non-negligible change in the centrifugal potential $\ell' \neq \ell$. For $\Delta = \ell' - \ell > 0$, the classical impact distance gets shifted outwards, thus eventually enabling to probe the oscillatory part of the bound state wave function even with $\kappa = 1$.

The mentioned oscillatory behavior is for example visible in the repulsive case $\kappa = -1$ depicted for s-wave capture in Fig. D.2. Unlike the Abelian case, the monopole interaction is now non-vanishing as there is no orthonormality condition. Note that the depicted parameter ranges differ from Fig. D.1 but agree with

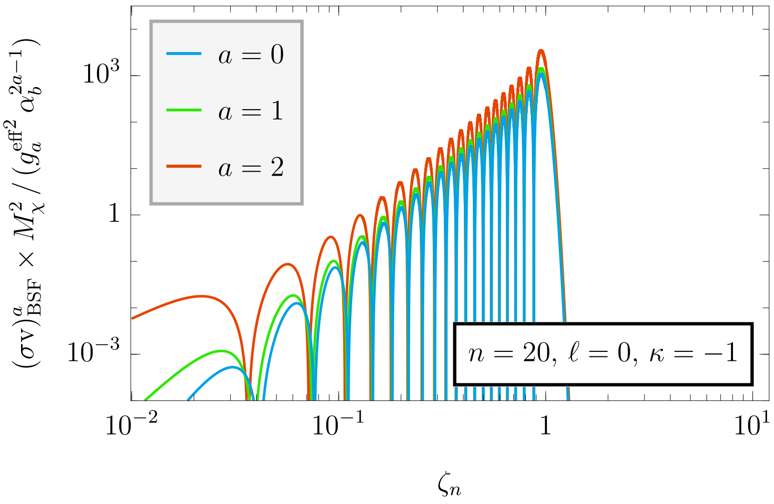

Figure D.2: Various bound state formation cross-sections, normalized by $g_a^{\mathrm{eff}^2} \alpha_b^{2a-1}/M_\chi^2$, plotted over ζ_n. Different multipoles $a = 0, 1, 2$ (blue, green, orange) are shown for $\kappa = -1$, $n = 20$, $\ell = 0$.

Figs. D.3 and D.4. The number of oscillations (counting local maxima) is now in all cases $n - \ell$. The last maximum is constructed differently where the high ζ_n edge is not due to another root but due to an exponential suppression term at small velocities $\zeta_n \gg 1$ found in the Sommerfeld factor $S_{\ell'}(\zeta_s)$, *cf.* (6.25). Physically, this is understood as a consequence of the repulsive nature of the initial potential $\alpha_s < 0$. In a classical line of thought, once the total initial energy becomes too small the constituent pair simply bounces off each other without ever coming close enough to see significant overlap with a bound state wave function. Note that the Bohr radius grows for higher excitations, however, due to the definition of $\zeta_n = \alpha_b / n\mathrm{v}$, higher n already imply smaller v for constant $\zeta_n = 1$ and the cutoff onset is largely unaffected by n, only becoming steeper.

Nonetheless, the position of the cutoff is shifted to lower ζ_n by more negative κ, as seen by comparing the curves $\kappa = -1, 0$ (red, green) in Fig. D.3 which illustrates the exponential suppression sourced by repulsion. The plot is similar to Fig. 6.1 in the main text, albeit with $a = 1$, $\ell = 0$ and a different normalization. The case of dipole interactions $a = 1$ is of special interest due to its connection to gauge interactions of the UV complete theory, hence it is shown here and below. $n = 5, \ell = 0$ is depicted in Fig. D.3. For $\kappa = 0$ (green), no low-velocity Sommerfeld scaling is obtained and once $\kappa < 0$, exponential suppression sets in. A detailed comparison of $\kappa = \pm 0.01$ may be found in the inset panel of Fig. 6.1.

As mentioned, there are no oscillations at $\kappa = 1 = a$ (purple), however, they successively develop as κ decreases and once $\kappa = 0.5$ (blue), one root can be seen at $\zeta_n = 0.45$. Hence, there are fine tuned ratios between the initial and final state potential for which specific excitations become essentially invisible at low velocities, despite $\kappa.0$, as the cross section decreases forever and never reaches the regime of Sommerfeld enhancement. In the depicted case of $a = 1, n = 5, \ell = 0$ this was found at $\kappa = 0.4767464447$ where the onset of Sommerfeld enhancement in found only at $\zeta_n \sim 3 \times 10^5$ and suppressed by 10^{-15} relative to the case $\kappa = 1$.

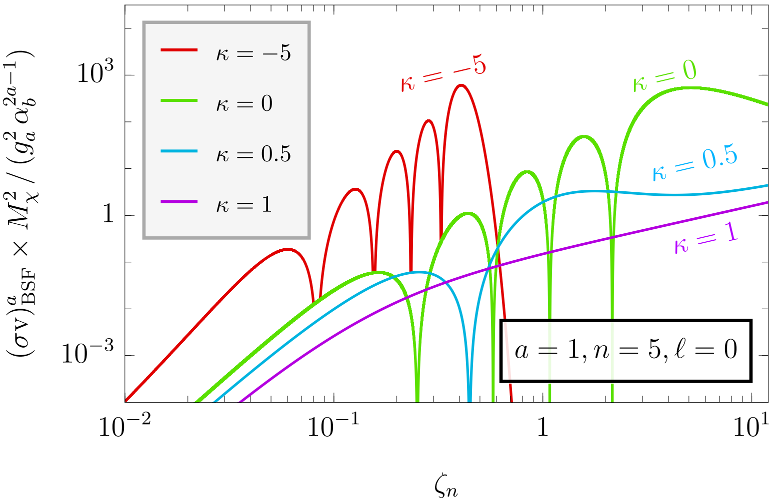

Figure D.3: Various bound state formation cross-sections, normalized by $g_a^{\text{eff}^2}\alpha_b^{2a-1}/M_\chi^2$, plotted over ζ_n. Different multipoles $\kappa = -5$, 0, 0.5, 1 (red, green, blue, purple) are shown for $a = 1$ (dipole), $n = 5$, $\ell = 0$.

The behavior is analogous to the Ramsauer-Townsend effect [145–147]. In it's simplest form, it occurs in a finite potential well tuned to host a zero energy bound state which leads to a vanishing reflection index and the potential becomes fully transparent in tuned points.

An understanding of the qualitative behavior, especially at small velocities is relevant for model building as new, interesting or required effects can be identified with a specific parametric range in a and κ to then construct a model satisfying these requirements. On the flip side, in phenomenology the specific model is fixed which usually means a and κ are not to be changed. The most interesting parameters are now n and ℓ to define the dominantly contributing energy levels and whether or to what degree observables are affected. As a small caveat, complicated systems of even more than two species can have more than only one ratio of potentials κ and thus yield effects from different parametric ranges simultaneously. Fig. D.4 depicts the scaled BSF cross-sections as above in the case of $a = 1$ and $\kappa = -1$ for different bound state angular momentum $\ell = \ell' - 1 = 0, 10, 19$ at $n = 20$ (upper panel) and different $n = 1, 5, 20$ at $\ell = 0$ (lower panel). The red curves on both plots thus shows the same BSF process, $n = 20, \ell = 0$. The upper panel clearly demonstrates how the number of oscillations is given by $n - \ell$. The particularly simple radial integral for $\Delta = 1$, $\ell = n - 1$, *cf.* Eq. (6.44), results in one simple peak peak here. The oscillatory regime for $\ell < n - 1$ extends on both sides, a feature which is nicely understood from the bound state wave functions and by the semi-classical analogy in section 6.3, since $r_{A,P} = r_n(1 \mp e)$.

Finally turning to variations of n, a striking feature is found. Higher n are no longer suppressed relative to capture into lower lying bound states, as it is the case in Abelian BSF. The horizontal axis $\zeta_n = p_n/p$ scales differently for each n such that, overall, each bound state contributes maximally when the initial energy is of the order of the respective bound state energy $\zeta_n \sim 1 \Leftrightarrow p \sim p_n$. Note that while higher n systematically overcome lower n at a fixed ℓ, this does not translate

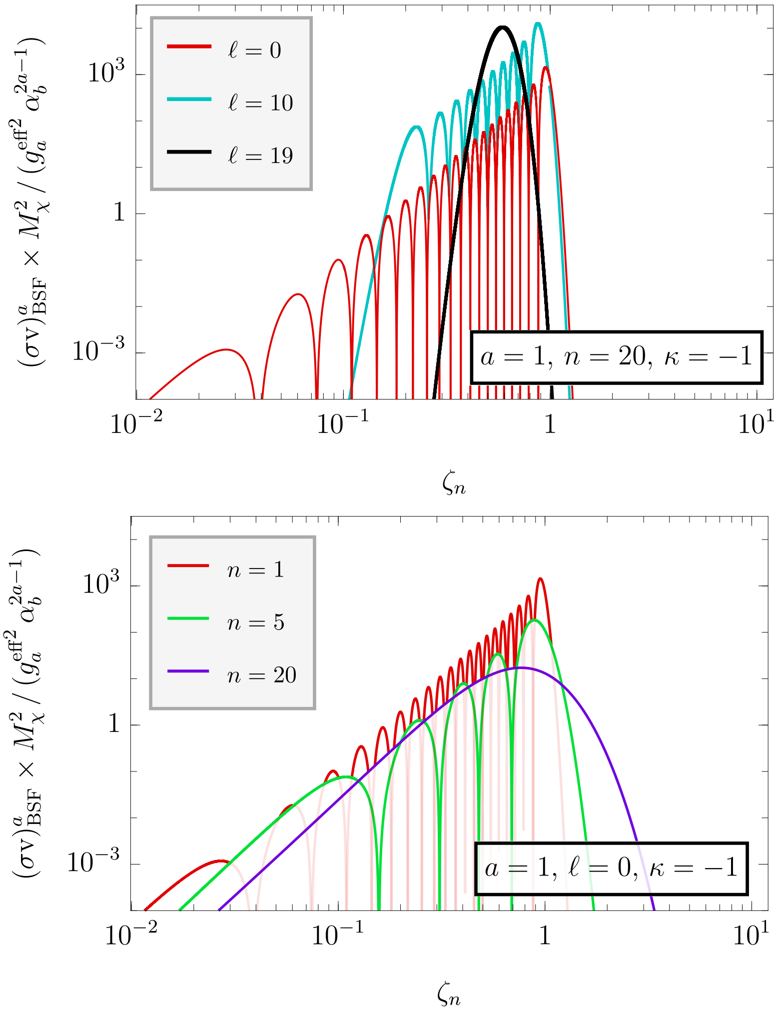

Figure D.4: Various bound state formation cross-sections, normalized by $g_a^{\mathrm{eff}^2} \alpha_b^{2a-1}/M_\chi^2$, plotted over ζ_n. *Upper panel*: Different angular momenta $\ell = 0$, $n/2$, $n-1$ (red, blue, black) are shown for $n = 20$, $\kappa = -1$ and $a = 1$ (dipole). *Lower panel*: Different bound state levels $n = 1$, 5, 20 (red, green, purple) are shown for $\ell = 0$, $\kappa = -1$ and $a = 1$ (dipole). The cross section for $n = 20$, $\ell = 0$ is thus depicted in both panels.

to the angular momentum. The maximal angular momentum $\ell = n - 1$ reaches its maximum, where it also exceeds all other partial waves, at largest velocity as seen in the upper panel, yet the exclusive BSF cross-section across the full velocity range is maximized for an intermediate $\ell \neq 0, n-1$ (here exemplary satisfied by $\ell = 10$, the blue curve). As the overall scaling by interpolating successive maxima grows still faster than $1/\mathrm{v}$, *cf.* Fig. D.3, this makes a prediction of which partial wave gives strongest constraints from unitarity bounds impossible and, in fact, this turns out to be a velocity dependent statement for the intricate comparison of exclusive processes. Nevertheless, for inclusive processes the s-wave bound $\ell' = 0$ generically is strongest, though by very small numerical factors, see Fig. D.6.

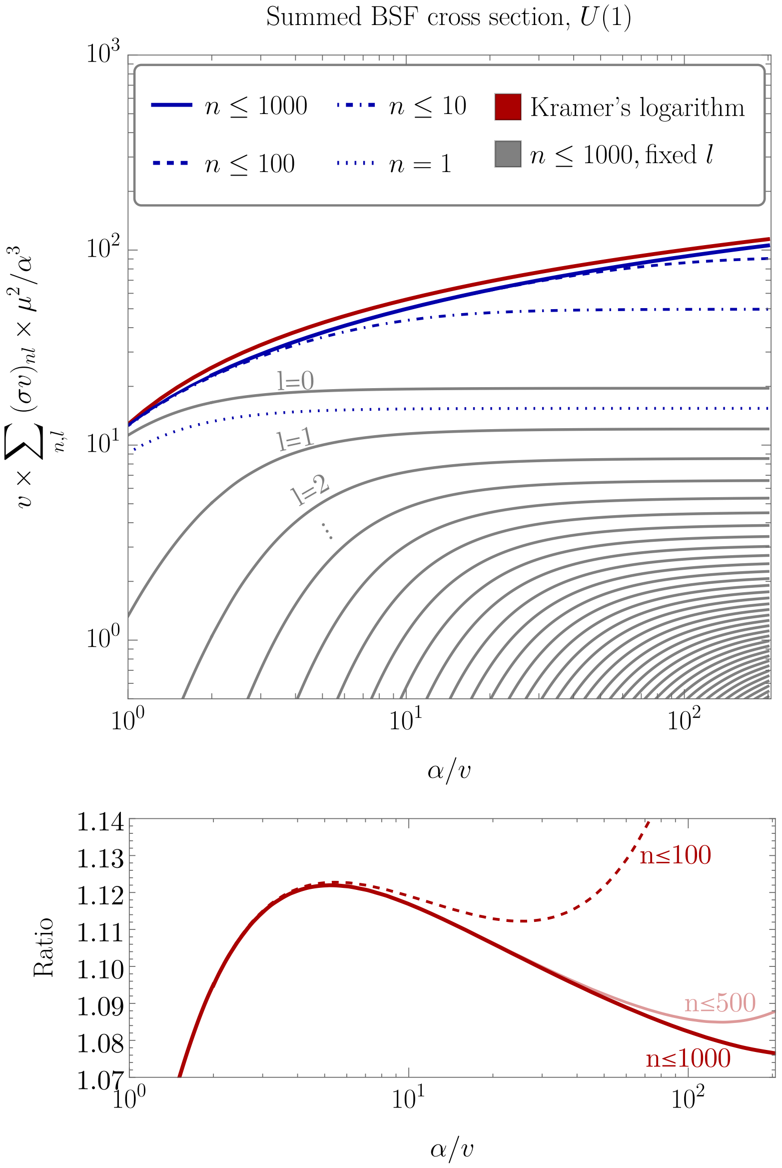

Figure D.5: *Upper panel*: Bound state formation cross-sections summed in $n \leq 1000$ for different $\ell = 0, ..., 17$ (various gray curves) and summed in all $\ell < n \leq 1$, 10, 100, 1000 (blue curves as indicated) plotted over α/v for a U(1) model ($a = 1$, $\kappa = 1$). Cross sections are normalized by $4\alpha^3/M_\chi^2\mathrm{v}$. Kramer's estimate, Eq. (D.2), is shown for comparison (red). *Lower panel*: Ratio of Kramer's estimate divided by the various fully-summed results $n \leq 1$, 10, 500, 1000 (dashed red, solid orange, solid red) on the same horizontal axis.

D.2 Inclusive cross sections under U(1) or SU(3)

The Figs. D.5 and D.6 show BSF cross-sections of fermions charged under gauge symmetries (with gauge coupling strength α) summed in n (gray) or n and ℓ (blue) plotted over the inverse velocity α/v ($v = \mathrm{v}$, $\mu = M_\chi/2$, using notation from [3]).

Abelian U(1) gauge interactions are shown in Fig. D.5. The upper panel includes summed cross sections normalized by $M^2\mathrm{v}/4\alpha^3$, thus rendering the low

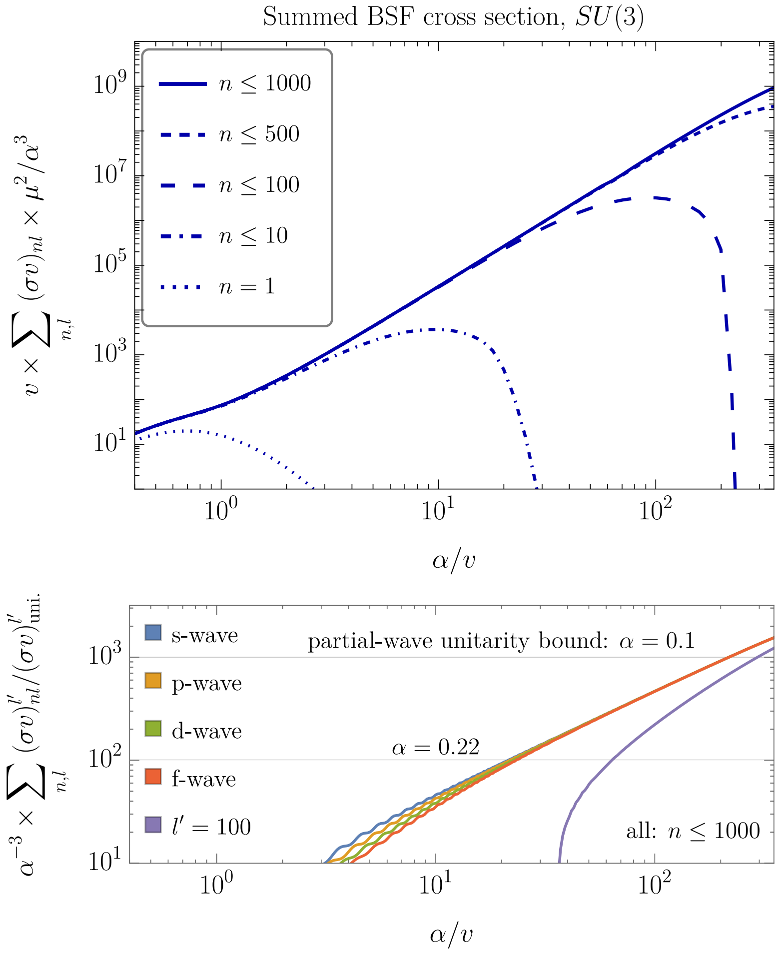

Figure D.6: *Upper panel*: Bound state formation cross-sections summed in $\ell < n$ and $n \leq$1, 10, 100, 500, 1000 plotted over α/v for a SU(3) model ($a = 1$, $\kappa = -1/8$). Cross sections are normalized by $4\alpha^3/M_\chi^2$v. *Lower panel*: Cross sections now summed in ℓ and $n \leq 1000$ for fixed initial state partial waves $\ell' = 0, 1, 2, 3, 100$ normalized by $\alpha^3(\sigma\text{v})^{\text{uni}}_{\ell'}$. Constant horizontal lines are thereby upper bounds from partial wave unitarity for one specific value of α, exemplified by $\alpha = 0.1$, 0.22.

velocity limit of simply Sommerfeld enhanced quantities horizontal. Various gray lines show results for summing $n \leq 1000$ each with one fixed $\ell = 0$, 1, 2, ... Blue dotted, dot-dashed, dashed and bold curves include summation in of all $\ell \leq n - 1$ and $n \leq$ 1, 10, 100 and 1000. From comparing the uppermost gray curve $\ell = 0$ to the dotted curve $n = 1$, one can see how in Abelian models the ground state dominates and all higher states give only a small enhancement by a factor of 1.268. Summing in ℓ and n overcomes the low-velocity Sommerfeld scaling. For comparison, the approximate summed, low-velocity result known as Kramer's logarithm [198, 199],

$$\sum_{n,\ell} (\sigma\text{v})_{n\ell} \approx \frac{128\pi}{3\sqrt{3}} \frac{\alpha^3}{M_\chi^2 \text{v}} \left[\log(\alpha/\text{v}) + \gamma_E\right] \tag{D.2}$$

is shown by a red curve. In the bottom panel, the ratio of Kramer's logarithm over the numeric results ($n \leq$100, 500, 1000) is depicted. It agrees well with the numerically observed converged result as long as sufficiently many n are summed and for $\alpha/\mathrm{v} \to \infty$ the ratio is expected to tend to unity. The shown ratios remains limited around the 7% level due to the numerical limitation $n \leq 1000$.

Fig. D.6 is similar to the previous one, but now showing results for a fermion transforming under the fundamental representation of a (dark) SU(3) gauge symmetry, thus $\kappa = 1/(1-N_c^2) = -1/8$. The enhancement of higher n is obvious and the low-velocity behavior converges to seemingly a power-law. Note that the here given results are summed in n and ℓ, which differs from all other representations throughout this thesis and are not subject to partial wave unitarity anymore. However, even the applicable summed unitarity bound $\sum_{\ell' \leq 1001} (\sigma\mathrm{v})^{\mathrm{uni}}_{\ell'}$ would be exceeded for perturbative couplings $\alpha > 0.15$ in the upper panel.

Decomposed into separate initial state angular momenta ℓ' and normalized to α^3 and the respective unitarity bound, Eq. (6.76), the obtained curves remain model independent but upper bounds from self-consistency with unitarity are now indicated by horizontal lines for each choice of α. The form of representation is analogous to Fig. 6.7 in the main text, however indicating α rather than $\alpha_b = C_F\alpha$. Partial waves up to $\ell' = 3$ (f-wave) and specifically $\ell' = 100$ are shown in different colors. One can observe some remaining oscillations at higher velocities before the summation in n hides such features. Furthermore, the previous statement regarding s-wave giving the strongest constraints from unitarity is now observed. It holds at low velocities once all curves are well converged and featureless. While the depicted lines largely overlap, there is a detailed ordering of the cross sections according to their partial waves which is more easily observed around $\alpha/\mathrm{v} = 40$. It is because of this sorting of the partial wave unitarity bounds, that also the optimization in Eq. (6.4.3) does not yield appreciable improvements at $\zeta_n \gg 1$ with respect to s-wave unitarity bounds. Correspondingly, the mentioned summed upper bound $\alpha = 0.15$ found in the upper panel is weaker than what is observed in the lower panel for each separated partial wave constraint, which overcome even the $\alpha = 0.1$ line.

Bibliography

[1] Martin Beneke, Stefan Lederer, and Kai Urban. "Sommerfeld enhancement of resonant dark matter annihilation". In: *Phys. Lett. B* 839 (2023), p. 137773. DOI: `10.1016/j.physletb.2023.137773`. arXiv: `2209.14343 [hep-ph]`.

[2] Martin Beneke, Stefan Lederer, and Clara Peset. "Electroweak resummation of neutralino dark-matter annihilation into high-energy photons". In: *JHEP* 01 (2023), p. 171. DOI: `10.1007/JHEP01(2023)171`. arXiv: `2211.14341 [hep-ph]`.

[3] Tobias Binder et al. "Excited bound states and their role in dark matter production". In: *Phys. Rev. D* 108.9 (2023), p. 095030. DOI: `10.1103/PhysRevD.108.095030`. arXiv: `2308.01336 [hep-ph]`.

[4] Martin Beneke et al. "Perturbative Unitarity Violation in Radiative Capture Transitions to Dark Matter Bound States". In: *To be published* (Nov. 2024). arXiv: `2411.08737 [hep-ph]`.

[5] Martin Beneke et al. "TBD". In: *To be published* (2025).

[6] F. Zwicky. "Die Rotverschiebung von extragalaktischen Nebeln". In: *Helv. Phys. Acta* 6 (1933), pp. 110–127. DOI: `10.1007/s10714-008-0707-4`.

[7] Simon D. M. White, C. S. Frenk, and M. Davis. "Is the Universe made of massive neutrinos?" In: *3rd Moriond Astrophysics Meeting: Galaxies and the Early Universe*. 1983, pp. 117–123.

[8] Benjamin W. Lee and Steven Weinberg. "Cosmological Lower Bound on Heavy Neutrino Masses". In: *Phys. Rev. Lett.* 39 (1977). Ed. by M. A. Srednicki, pp. 165–168. DOI: `10.1103/PhysRevLett.39.165`.

[9] Douglas Clowe et al. "A direct empirical proof of the existence of dark matter". In: *Astrophys. J. Lett.* 648 (2006), pp. L109–L113. DOI: `10.1086/508162`. arXiv: `astro-ph/0608407`.

[10] James S. Bullock and Michael Boylan-Kolchin. "Small-Scale Challenges to the ΛCDM Paradigm". In: *Ann. Rev. Astron. Astrophys.* 55 (2017), pp. 343–387. DOI: `10.1146/annurev-astro-091916-055313`. arXiv: `1707.04256 [astro-ph.CO]`.

[11] Wolfgang Enzi et al. "Joint constraints on thermal relic dark matter from strong gravitational lensing, the Ly α forest, and Milky Way satellites". In: *Mon. Not. Roy. Astron. Soc.* 506.4 (2021), pp. 5848–5862. DOI: `10.1093/mnras/stab1960`. arXiv: `2010.13802 [astro-ph.CO]`.

[12] N. Aghanim et al. "Planck 2018 results. VI. Cosmological parameters". In: *Astron. Astrophys.* 641 (2020). [Erratum: Astron.Astrophys. 652, C4 (2021)], A6. DOI: `10.1051/0004-6361/201833910`. arXiv: `1807.06209 [astro-ph.CO]`.

[13] T. M. C. Abbott et al. "Dark Energy Survey Year 3 results: Cosmological constraints from galaxy clustering and weak lensing". In: *Phys. Rev. D* 105.2 (2022), p. 023520. DOI: `10.1103/PhysRevD.105.023520`. arXiv: `2105.13549 [astro-ph.CO]`.

[14] Raul E. Angulo and Oliver Hahn. “Large-scale dark matter simulations”. In: (Dec. 2021). DOI: 10.1007/s41115-021-00013-z. arXiv: 2112.05165 [astro-ph.CO].

[15] Benjamin Audren et al. “Strongest model-independent bound on the lifetime of Dark Matter”. In: *JCAP* 12 (2014), p. 028. DOI: 10.1088/1475-7516/2014/12/028. arXiv: 1407.2418 [astro-ph.CO].

[16] Y. Fukuda et al. “Evidence for oscillation of atmospheric neutrinos”. In: *Phys. Rev. Lett.* 81 (1998), pp. 1562–1567. DOI: 10.1103/PhysRevLett.81.1562. arXiv: hep-ex/9807003.

[17] Eldad Gildener. “Gauge Symmetry Hierarchies”. In: *Phys. Rev. D* 14 (1976), p. 1667. DOI: 10.1103/PhysRevD.14.1667.

[18] Marc Schumann. “Direct Detection of WIMP Dark Matter: Concepts and Status”. In: *J. Phys. G* 46.10 (2019), p. 103003. DOI: 10.1088/1361-6471/ab2ea5. arXiv: 1903.03026 [astro-ph.CO].

[19] Georges Aad et al. “Observation of a new particle in the search for the Standard Model Higgs boson with the ATLAS detector at the LHC”. In: *Phys. Lett. B* 716 (2012), pp. 1–29. DOI: 10.1016/j.physletb.2012.08.020. arXiv: 1207.7214 [hep-ex].

[20] Paolo Gondolo and Graciela Gelmini. “Cosmic abundances of stable particles: Improved analysis”. In: *Nucl. Phys. B* 360 (1991), pp. 145–179. DOI: 10.1016/0550-3213(91)90438-4.

[21] Tobias Binder et al. “Dark matter relic abundance beyond kinetic equilibrium”. In: *Eur. Phys. J. C* 81 (2021), p. 577. DOI: 10.1140/epjc/s10052-021-09357-5. arXiv: 2103.01944 [hep-ph].

[22] Lawrence J. Hall et al. “Freeze-In Production of FIMP Dark Matter”. In: *JHEP* 03 (2010), p. 080. DOI: 10.1007/JHEP03(2010)080. arXiv: 0911.1120 [hep-ph].

[23] Jonathan L. Feng, Arvind Rajaraman, and Fumihiro Takayama. “SuperWIMP dark matter signals from the early universe”. In: *Phys. Rev.* D68 (2003), p. 063504. DOI: 10.1103/PhysRevD.68.063504. arXiv: hep-ph/0306024 [hep-ph].

[24] Kim Griest and David Seckel. “Three exceptions in the calculation of relic abundances”. In: *Phys. Rev.* D43 (1991), pp. 3191–3203. DOI: 10.1103/PhysRevD.43.3191.

[25] Mathias Garny et al. “Coannihilation without chemical equilibrium”. In: *Phys. Rev.* D96.10 (2017), p. 103521. DOI: 10.1103/PhysRevD.96.103521. arXiv: 1705.09292 [hep-ph].

[26] Raffaele Tito D’Agnolo, Duccio Pappadopulo, and Joshua T. Ruderman. “Fourth Exception in the Calculation of Relic Abundances”. In: *Phys. Rev. Lett.* 119.6 (2017), p. 061102. DOI: 10.1103/PhysRevLett.119.061102. arXiv: 1705.08450 [hep-ph].

[27] Eric D. Carlson, Marie E. Machacek, and Lawrence J. Hall. “Self-interacting dark matter”. In: *Astrophys. J.* 398 (1992), pp. 43–52. DOI: 10.1086/171833.

[28] Manuel A. Buen-Abad, Razieh Emami, and Martin Schmaltz. “Cannibal Dark Matter and Large Scale Structure”. In: *Phys. Rev. D* 98.8 (2018), p. 083517. DOI: `10.1103/PhysRevD.98.083517`. arXiv: `1803.08062 [hep-ph]`.

[29] Andrzej Hryczuk and Maxim Laletin. “Dark matter freeze-in from semi-production”. In: *JHEP* 06 (2021), p. 026. DOI: `10.1007/JHEP06(2021)026`. arXiv: `2104.05684 [hep-ph]`.

[30] Torsten Bringmann et al. “Dark Matter from Exponential Growth”. In: *Phys. Rev. Lett.* 127.19 (2021), p. 191802. DOI: `10.1103/PhysRevLett.127.191802`. arXiv: `2103.16572 [hep-ph]`.

[31] Lucas Puetter et al. “Bouncing dark matter”. In: *Phys. Rev. D* 109.2 (2024), p. 023032. DOI: `10.1103/PhysRevD.109.023032`. arXiv: `2208.08453 [hep-ph]`.

[32] Salvatore Bottaro et al. “Closing the window on WIMP Dark Matter”. In: *Eur. Phys. J. C* 82.1 (2022), p. 31. DOI: `10.1140/epjc/s10052-021-09917-9`. arXiv: `2107.09688 [hep-ph]`.

[33] Gerard Jungman, Marc Kamionkowski, and Kim Griest. “Supersymmetric dark matter”. In: *Phys. Rept.* 267 (1996), pp. 195–373. DOI: `10.1016/0370-1573(95)00058-5`. arXiv: `hep-ph/9506380 [hep-ph]`.

[34] A. Abada et al. “FCC-hh: The Hadron Collider: Future Circular Collider Conceptual Design Report Volume 3”. In: *Eur. Phys. J. ST* 228.4 (2019), pp. 755–1107. DOI: `10.1140/epjst/e2019-900087-0`.

[35] Salvatore Bottaro et al. “The last complex WIMPs standing”. In: *Eur. Phys. J. C* 82.11 (2022), p. 992. DOI: `10.1140/epjc/s10052-022-10918-5`. arXiv: `2205.04486 [hep-ph]`.

[36] Stephen P. Martin. “A Supersymmetry primer”. In: *Adv. Ser. Direct. High Energy Phys.* 18 (1998). Ed. by Gordon L. Kane, pp. 1–98. DOI: `10.1142/9789812839657_0001`. arXiv: `hep-ph/9709356`.

[37] Glennys R. Farrar and Pierre Fayet. “Phenomenology of the Production, Decay, and Detection of New Hadronic States Associated with Supersymmetry”. In: *Phys. Lett.* B76 (1978), pp. 575–579. DOI: `10.1016/0370-2693(78)90858-4`.

[38] Nicholas L. Rodd, Benjamin R. Safdi, and Weishuang Linda Xu. “CTA and SWGO can Discover Higgsino Dark Matter Annihilation”. In: (May 2024). arXiv: `2405.13104 [hep-ph]`.

[39] Julien Billard et al. “Direct detection of dark matter—APPEC committee report*”. In: *Rept. Prog. Phys.* 85.5 (2022), p. 056201. DOI: `10.1088/1361-6633/ac5754`. arXiv: `2104.07634 [hep-ex]`.

[40] Georges Aad et al. “Search for chargino–neutralino pair production in final states with three leptons and missing transverse momentum in $\sqrt{s} = 13$ TeV pp collisions with the ATLAS detector”. In: *Eur. Phys. J. C* 81.12 (2021), p. 1118. DOI: `10.1140/epjc/s10052-021-09749-7`. arXiv: `2106.01676 [hep-ex]`.

[41] Armen Tumasyan et al. “Search for electroweak production of charginos and neutralinos in proton-proton collisions at $\sqrt{s} = 13$ TeV”. In: *JHEP* 04 (2022), p. 147. DOI: 10.1007/JHEP04(2022)147. arXiv: 2106.14246 [hep-ex].

[42] Saikat Karmakar. “Searches for RPV SUSY in ATLAS, CMS and LHCb”. In: *PoS* LHCP2022 (2023), p. 073. DOI: 10.22323/1.422.0073.

[43] Georges Aad et al. “ATLAS searches for additional scalars and exotic Higgs boson decays with the LHC Run 2 dataset”. In: (May 2024). arXiv: 2405.04914 [hep-ex].

[44] S. Abe et al. “Dark matter line searches with the Cherenkov Telescope Array”. In: *JCAP* 07 (2024), p. 047. DOI: 10.1088/1475-7516/2024/07/047. arXiv: 2403.04857 [hep-ph].

[45] A. Acharyya et al. “Sensitivity of the Cherenkov Telescope Array to a dark matter signal from the Galactic centre”. In: *JCAP* 01 (2021), p. 057. DOI: 10.1088/1475-7516/2021/01/057. arXiv: 2007.16129 [astro-ph.HE].

[46] M. Ackermann et al. “Searching for Dark Matter Annihilation from Milky Way Dwarf Spheroidal Galaxies with Six Years of Fermi Large Area Telescope Data”. In: *Phys. Rev. Lett.* 115.23 (2015), p. 231301. DOI: 10.1103/PhysRevLett.115.231301. arXiv: 1503.02641 [astro-ph.HE].

[47] J. Einasto. “On the Construction of a Composite Model for the Galaxy and on the Determination of the System of Galactic Parameters”. In: *Trudy Astrofizicheskogo Instituta Alma-Ata* 5 (Jan. 1965), pp. 87–100.

[48] Julio F. Navarro, Carlos S. Frenk, and Simon D. M. White. “The Structure of cold dark matter halos”. In: *Astrophys. J.* 462 (1996), pp. 563–575. DOI: 10.1086/177173. arXiv: astro-ph/9508025 [astro-ph].

[49] Andrzej Hryczuk et al. “Testing dark matter with Cherenkov light - prospects of H.E.S.S. and CTA for exploring minimal supersymmetry”. In: *JHEP* 10 (2019), p. 043. DOI: 10.1007/JHEP10(2019)043. arXiv: 1905.00315 [hep-ph].

[50] Solène Chabanier et al. “The Completed Sloan Digital Sky Survey IV Extended Baryon Oscillation Spectroscopic Survey: The Damped Lyα Systems Catalog”. In: *Astrophys. J. Supp.* 258.1 (2022), p. 18. DOI: 10.3847/1538-4365/ac366e. arXiv: 2107.09612 [astro-ph.CO].

[51] Martin. J. Rees. “Lyman absorption lines in quasar spectra: evidence for gravitationally-confined gas in dark minihaloes”. In: *Monthly Notices of the Royal Astronomical Society* 218.1 (Jan. 1986), 25P–30P. DOI: 10.1093/mnras/218.1.25P. eprint: https://academic.oup.com/mnras/article-pdf/218/1/25P/3010626/mnras218-025P.pdf. URL: https://doi.org/10.1093/mnras/218.1.25P.

[52] Quentin Decant et al. “Lyman-α constraints on freeze-in and superWIMPs”. In: *JCAP* 03.03 (2022), p. 041. DOI: 10.1088/1475-7516/2022/03/041. arXiv: 2111.09321 [astro-ph.CO].

[53] Céline Boehm, Matthew J. Dolan, and Christopher McCabe. "A Lower Bound on the Mass of Cold Thermal Dark Matter from Planck". In: *JCAP* 08 (2013), p. 041. DOI: `10.1088/1475-7516/2013/08/041`. arXiv: `1303.6270 [hep-ph]`.

[54] B. P. Abbott et al. "Observation of Gravitational Waves from a Binary Black Hole Merger". In: *Phys. Rev. Lett.* 116.6 (2016), p. 061102. DOI: `10.1103/PhysRevLett.116.061102`. arXiv: `1602.03837 [gr-qc]`.

[55] Gabriella Agazie et al. "The NANOGrav 15 yr Data Set: Evidence for a Gravitational-wave Background". In: *Astrophys. J. Lett.* 951.1 (2023), p. L8. DOI: `10.3847/2041-8213/acdac6`. arXiv: `2306.16213 [astro-ph.HE]`.

[56] Torsten Bringmann et al. "Hunting WIMPs with LISA: correlating dark matter and gravitational wave signals". In: *JCAP* 05 (2024), p. 065. DOI: `10.1088/1475-7516/2024/05/065`. arXiv: `2311.06346 [astro-ph.CO]`.

[57] Tomohiro Abe, K. S. Babu, and Ajay Kaladharan. "Gravitational wave signatures of a chiral fermion dark matter model". In: *JCAP* 07 (2024), p. 048. DOI: `10.1088/1475-7516/2024/07/048`. arXiv: `2312.17203 [hep-ph]`.

[58] B. P. Abbott et al. "Multi-messenger Observations of a Binary Neutron Star Merger". In: *Astrophys. J. Lett.* 848.2 (2017), p. L12. DOI: `10.3847/2041-8213/aa91c9`. arXiv: `1710.05833 [astro-ph.HE]`.

[59] Isaac Newton. *Philosophiæ Naturalis Principia Mathematica*. England, 1687.

[60] M. Beneke and Vladimir A. Smirnov. "Asymptotic expansion of Feynman integrals near threshold". In: *Nucl. Phys. B* 522 (1998), pp. 321–344. DOI: `10.1016/S0550-3213(98)00138-2`. arXiv: `hep-ph/9711391`.

[61] Kalliopi Petraki, Marieke Postma, and Michael Wiechers. "Dark-matter bound states from Feynman diagrams". In: *JHEP* 06 (2015), p. 128. DOI: `10.1007/JHEP06(2015)128`. arXiv: `1505.00109 [hep-ph]`.

[62] S. Lederer. "Resumming Large Logarithms in Dark Matter Annihilation into Photons". MA thesis. TU Munich, 2020.

[63] Geoffrey T. Bodwin, Eric Braaten, and G. Peter Lepage. "Rigorous QCD analysis of inclusive annihilation and production of heavy quarkonium". In: *Phys. Rev. D* 51 (1995). [Erratum: Phys.Rev.D 55, 5853 (1997)], pp. 1125–1171. DOI: `10.1103/PhysRevD.55.5853`. arXiv: `hep-ph/9407339`.

[64] M. Beneke, C. Hellmann, and P. Ruiz-Femenia. "Non-relativistic pair annihilation of nearly mass degenerate neutralinos and charginos I. General framework and S-wave annihilation". In: *JHEP* 03 (2013). [Erratum: JHEP 10, 224 (2013)], p. 148. DOI: `10.1007/JHEP03(2013)148`. arXiv: `1210.7928 [hep-ph]`.

[65] R. E. Cutkosky. "Singularities and discontinuities of Feynman amplitudes". In: *J. Math. Phys.* 1 (1960), pp. 429–433. DOI: `10.1063/1.1703676`.

[66] M. Beneke et al. "Effective theory approach to unstable particle production". In: *Phys. Rev. Lett.* 93 (2004), p. 011602. DOI: `10.1103/PhysRevLett.93.011602`. arXiv: `hep-ph/0312331`.

[67] M. Beneke et al. "Effective theory calculation of resonant high-energy scattering". In: *Nucl. Phys. B* 686 (2004), pp. 205–247. DOI: `10.1016/j.nuclphysb.2004.03.016`. arXiv: `hep-ph/0401002`.

[68] Estia Eichten and Brian Russell Hill. "An Effective Field Theory for the Calculation of Matrix Elements Involving Heavy Quarks". In: *Phys. Lett. B* 234 (1990), pp. 511–516. DOI: `10.1016/0370-2693(90)92049-O`.

[69] A. Pineda and J. Soto. "Effective field theory for ultrasoft momenta in NRQCD and NRQED". In: *Nucl. Phys. Proc. Suppl.* 64 (1998). [,428(1997)], pp. 428–432. DOI: `10.1016/S0920-5632(97)01102-X`. arXiv: `hep-ph/9707481 [hep-ph]`.

[70] W. E. Caswell and G. P. Lepage. "Effective Lagrangians for Bound State Problems in QED, QCD, and Other Field Theories". In: *Phys. Lett. B* 167 (1986), pp. 437–442. DOI: `10.1016/0370-2693(86)91297-9`.

[71] Patrick Labelle. "Effective field theories for QED bound states: Extending nonrelativistic QED to study retardation effects". In: *Phys. Rev. D* 58 (1998), p. 093013. DOI: `10.1103/PhysRevD.58.093013`. arXiv: `hep-ph/9608491`.

[72] A. Pineda and J. Soto. "Potential NRQED: The Positronium case". In: *Phys. Rev. D* 59 (1999), p. 016005. DOI: `10.1103/PhysRevD.59.016005`. arXiv: `hep-ph/9805424`.

[73] M. Beneke and T. Feldmann. "Multipole expanded soft collinear effective theory with nonAbelian gauge symmetry". In: *Phys. Lett. B* 553 (2003), pp. 267–276. DOI: `10.1016/S0370-2693(02)03204-5`. arXiv: `hep-ph/0211358`.

[74] Martin Beneke and Matthias Steinhauser. "Non-relativistic high-energy physics: top production and dark matter annihilation". In: *Nucl. Part. Phys. Proc.* 261-262 (2015). Ed. by Johannes Blümlein et al., pp. 378–413. DOI: `10.1016/j.nuclphysbps.2015.03.024`. arXiv: `1506.07962 [hep-ph]`.

[75] Simone Biondini et al. "Effective field theories for dark matter pairs in the early universe: cross sections and widths". In: *JHEP* 07 (2023), p. 006. DOI: `10.1007/JHEP07(2023)006`. arXiv: `2304.00113 [hep-ph]`.

[76] Junji Hisano et al. "Non-perturbative effect on dark matter annihilation and gamma ray signature from galactic center". In: *Phys. Rev.* D71 (2005), p. 063528. DOI: `10.1103/PhysRevD.71.063528`. arXiv: `hep-ph/0412403 [hep-ph]`.

[77] M. Beneke, C. Hellmann, and P. Ruiz-Femenia. "Non-relativistic pair annihilation of nearly mass degenerate neutralinos and charginos III. Computation of the Sommerfeld enhancements". In: *JHEP* 05 (2015), p. 115. DOI: `10.1007/JHEP05(2015)115`. arXiv: `1411.6924 [hep-ph]`.

[78] Tobias Binder, Laura Covi, and Kyohei Mukaida. "Dark Matter Sommerfeld-enhanced annihilation and Bound-state decay at finite temperature". In: *Phys. Rev. D* 98.11 (2018), p. 115023. DOI: `10.1103/PhysRevD.98.115023`. arXiv: `1808.06472 [hep-ph]`.

[79] Christian W. Bauer, Sean Fleming, and Michael E. Luke. "Summing Sudakov logarithms in $B \to X_s\gamma$in effective field theory." In: *Phys. Rev. D* 63 (2000), p. 014006. DOI: 10.1103/PhysRevD.63.014006. arXiv: hep-ph/0005275.

[80] Christian W. Bauer, Dan Pirjol, and Iain W. Stewart. "Soft collinear factorization in effective field theory". In: *Phys. Rev. D* 65 (2002), p. 054022. DOI: 10.1103/PhysRevD.65.054022. arXiv: hep-ph/0109045.

[81] V. V. Sudakov. "Vertex parts at very high-energies in quantum electrodynamics". In: *Sov. Phys. JETP* 3 (1956), pp. 65–71.

[82] M. Beneke et al. "Resummed photon spectrum from dark matter annihilation for intermediate and narrow energy resolution". In: *JHEP* 08 (2019). [Erratum: JHEP 07, 145 (2020)], p. 103. DOI: 10.1007/JHEP08(2019)103. arXiv: 1903.08702 [hep-ph].

[83] Philipp Böer et al. "Renormalization-group improved resummation of superleading logarithms". In: *JHEP* 08 (2024), p. 035. DOI: 10.1007/JHEP08(2024)035. arXiv: 2405.05305 [hep-ph].

[84] M. Beneke et al. "Energetic γ-rays from TeV scale dark matter annihilation resummed". In: *Phys. Lett. B* 786 (2018). [Erratum: Phys.Lett.B 810, 135831 (2020)], pp. 347–354. DOI: 10.1016/j.physletb.2018.10.008. arXiv: 1805.07367 [hep-ph].

[85] Matthew Baumgart et al. "Resummed Photon Spectra for WIMP Annihilation". In: *JHEP* 03 (2018), p. 117. DOI: 10.1007/JHEP03(2018)117. arXiv: 1712.07656 [hep-ph].

[86] Andrzej Hryczuk, Roberto Iengo, and Piero Ullio. "Relic densities including Sommerfeld enhancements in the MSSM". In: *JHEP* 03 (2011), p. 069. DOI: 10.1007/JHEP03(2011)069. arXiv: 1010.2172 [hep-ph].

[87] Martin Beneke et al. "Precise yield of high-energy photons from Higgsino dark matter annihilation". In: *JHEP* 03 (2020), p. 030. DOI: 10.1007/JHEP03(2020)030. arXiv: 1912.02034 [hep-ph].

[88] G. Breit and E. Wigner. "Capture of Slow Neutrons". In: *Phys. Rev.* 49 (1936), pp. 519–531. DOI: 10.1103/PhysRev.49.519.

[89] Kim Griest and Marc Kamionkowski. "Unitarity Limits on the Mass and Radius of Dark Matter Particles". In: *Phys. Rev. Lett.* 64 (1990), p. 615. DOI: 10.1103/PhysRevLett.64.615.

[90] Kfir Blum, Ryosuke Sato, and Tracy R. Slatyer. "Self-consistent Calculation of the Sommerfeld Enhancement". In: *JCAP* 06 (2016), p. 021. DOI: 10.1088/1475-7516/2016/06/021. arXiv: 1603.01383 [hep-ph].

[91] Martin Beneke et al. "The last refuge of mixed wino-Higgsino dark matter". In: *JHEP* 01 (2017), p. 002. DOI: 10.1007/JHEP01(2017)002. arXiv: 1611.00804 [hep-ph].

[92] Arnold Sommerfeld. "Zur Quantentheorie der Spektrallinien". In: *Annalen der Physik* 356 (), pp. 1–94. URL: https://api.semanticscholar.org/CorpusID:121179188.

[93] Junji Hisano, Shigeki Matsumoto, and Mihoko M. Nojiri. “Explosive dark matter annihilation”. In: *Phys. Rev. Lett.* 92 (2004), p. 031303. DOI: `10.1103/PhysRevLett.92.031303`. arXiv: `hep-ph/0307216 [hep-ph]`.

[94] Steven Weinberg. “Implications of Dynamical Symmetry Breaking”. In: *Phys. Rev. D* 13 (1976). [Addendum: Phys.Rev.D 19, 1277–1280 (1979)], pp. 974–996. DOI: `10.1103/PhysRevD.19.1277`.

[95] Leonard Susskind. “Dynamics of Spontaneous Symmetry Breaking in the Weinberg-Salam Theory”. In: *Phys. Rev. D* 20 (1979), pp. 2619–2625. DOI: `10.1103/PhysRevD.20.2619`.

[96] Sezen Sekmen. “Highlights on Supersymmetry and Exotic Searches at the LHC”. In: *32nd Rencontres de Blois on Particle Physics and Cosmology*. Apr. 2022. arXiv: `2204.03053 [hep-ex]`.

[97] Timothy Cohen et al. “Wino Dark Matter Under Siege”. In: *JCAP* 10 (2013), p. 061. DOI: `10.1088/1475-7516/2013/10/061`. arXiv: `1307.4082 [hep-ph]`.

[98] Martin Beneke, Robert Szafron, and Kai Urban. “Wino potential and Sommerfeld effect at NLO”. In: *Phys. Lett. B* 800 (2020), p. 135112. DOI: `10.1016/j.physletb.2019.135112`. arXiv: `1909.04584 [hep-ph]`.

[99] Martin Beneke, Robert Szafron, and Kai Urban. “Sommerfeld-corrected relic abundance of wino dark matter with NLO electroweak potentials”. In: *JHEP* 02 (2021), p. 020. DOI: `10.1007/JHEP02(2021)020`. arXiv: `2009.00640 [hep-ph]`.

[100] Martin Beneke, Kai Urban, and Martin Vollmann. “Matching resummed endpoint and continuum γ-ray spectra from dark-matter annihilation”. In: *Phys. Lett. B* 834 (2022), p. 137248. DOI: `10.1016/j.physletb.2022.137248`. arXiv: `2203.01692 [hep-ph]`.

[101] Varun Vaidya, Matthew Baumgart, and Ira Rothstein. “The Story of WINO Dark Matter”. In: *PoS* DIS2015 (2015), p. 125. DOI: `10.22323/1.247.0125`.

[102] Matthew Baumgart and Varun Vaidya. “Semi-inclusive wino and higgsino annihilation to LL’”. In: *JHEP* 03 (2016), p. 213. DOI: `10.1007/JHEP03(2016)213`. arXiv: `1510.02470 [hep-ph]`.

[103] Matthew Baumgart et al. “Precision Photon Spectra for Wino Annihilation”. In: *JHEP* 01 (2019), p. 036. DOI: `10.1007/JHEP01(2019)036`. arXiv: `1808.08956 [hep-ph]`.

[104] Salvatore Bottaro and Diego Redigolo. “The dark matter unitarity bound at NLO”. In: (May 2023). arXiv: `2305.01680 [hep-ph]`.

[105] Janusz Rosiek. “Complete set of Feynman rules for the MSSM: Erratum”. In: (Nov. 1995). arXiv: `hep-ph/9511250`.

[106] Piotr H. Chankowski, Stefan Pokorski, and Janusz Rosiek. “Complete on-shell renormalization scheme for the minimal supersymmetric Higgs sector”. In: *Nucl. Phys. B* 423 (1994), pp. 437–496. DOI: `10.1016/0550-3213(94)90141-4`. arXiv: `hep-ph/9303309`.

[107] M. Beneke et al. "Relic density of wino-like dark matter in the MSSM". In: *JHEP* 03 (2016), p. 119. DOI: `10.1007/JHEP03(2016)119`. arXiv: `1601.04718 [hep-ph]`.

[108] Bjorn Herrmann and Michael Klasen. "SUSY-QCD Corrections to Dark Matter Annihilation in the Higgs Funnel". In: *Phys. Rev. D* 76 (2007), p. 117704. DOI: `10.1103/PhysRevD.76.117704`. arXiv: `0709.0043 [hep-ph]`.

[109] J. Harz et al. "Neutralino-stop coannihilation into electroweak gauge and Higgs bosons at one loop". In: *Phys. Rev. D* 87.5 (2013), p. 054031. DOI: `10.1103/PhysRevD.87.054031`. arXiv: `1212.5241 [hep-ph]`.

[110] Julia Harz et al. "Precision predictions for dark matter with DM@NLO in the MSSM". In: *Eur. Phys. J. C* 84.4 (2024), p. 342. DOI: `10.1140/epjc/s10052-024-12660-6`. arXiv: `2312.17206 [hep-ph]`.

[111] C. Hellmann and P. Ruiz-Femenía. "Non-relativistic pair annihilation of nearly mass degenerate neutralinos and charginos II. P-wave and next-to-next-to-leading order S-wave coefficients". In: *JHEP* 08 (2013), p. 084. DOI: `10.1007/JHEP08(2013)084`. arXiv: `1303.0200 [hep-ph]`.

[112] Aoife Bharucha et al. "Consistent on shell renormalisation of electroweakinos in the complex MSSM: LHC and LC predictions". In: *JHEP* 05 (2013), p. 053. DOI: `10.1007/JHEP05(2013)053`. arXiv: `1211.3134 [hep-ph]`.

[113] Tracy R. Slatyer. "The Sommerfeld enhancement for dark matter with an excited state". In: *JCAP* 02 (2010), p. 028. DOI: `10.1088/1475-7516/2010/02/028`. arXiv: `0910.5713 [hep-ph]`.

[114] P. S. Bhupal Dev and Apostolos Pilaftsis. "Maximally Symmetric Two Higgs Doublet Model with Natural Standard Model Alignment". In: *JHEP* 12 (2014). [Erratum: JHEP 11, 147 (2015)], p. 024. DOI: `10.1007/JHEP12(2014)024`. arXiv: `1408.3405 [hep-ph]`.

[115] Serguei Chatrchyan et al. "Observation of a New Boson at a Mass of 125 GeV with the CMS Experiment at the LHC". In: *Phys. Lett. B* 716 (2012), pp. 30–61. DOI: `10.1016/j.physletb.2012.08.021`. arXiv: `1207.7235 [hep-ex]`.

[116] S. Navas et al. "Review of particle physics". In: *Phys. Rev. D* 110.3 (2024), p. 030001. DOI: `10.1103/PhysRevD.110.030001`.

[117] Luminita N. Mihaila, Jens Salomon, and Matthias Steinhauser. "Renormalization constants and beta functions for the gauge couplings of the Standard Model to three-loop order". In: *Phys. Rev. D* 86 (2012), p. 096008. DOI: `10.1103/PhysRevD.86.096008`. arXiv: `1208.3357 [hep-ph]`.

[118] Luminita N. Mihaila, Jens Salomon, and Matthias Steinhauser. "Gauge Coupling Beta Functions in the Standard Model to Three Loops". In: *Phys. Rev. Lett.* 108 (2012), p. 151602. DOI: `10.1103/PhysRevLett.108.151602`. arXiv: `1201.5868 [hep-ph]`.

[119] A. V. Bednyakov, A. F. Pikelner, and V. N. Velizhanin. "Yukawa coupling beta-functions in the Standard Model at three loops". In: *Phys. Lett. B* 722 (2013), pp. 336–340. DOI: `10.1016/j.physletb.2013.04.038`. arXiv: `1212.6829 [hep-ph]`.

[120] H. Bahl et al. “Precision calculations in the MSSM Higgs-boson sector with FeynHiggs 2.14”. In: *Comput. Phys. Commun.* 249 (2020), p. 107099. DOI: `10.1016/j.cpc.2019.107099`. arXiv: `1811.09073 [hep-ph]`.

[121] Florian Herren and Matthias Steinhauser. “Version 3 of RunDec and CRunDec”. In: *Comput. Phys. Commun.* 224 (2018), pp. 333–345. DOI: `10.1016/j.cpc.2017.11.014`. arXiv: `1703.03751 [hep-ph]`.

[122] Stephen P. Martin. “Three-loop QCD corrections to the electroweak boson masses”. In: *Phys. Rev. D* 106.1 (2022), p. 013007. DOI: `10.1103/PhysRevD.106.013007`. arXiv: `2203.05042 [hep-ph]`.

[123] Peter Athron et al. “Combined collider constraints on neutralinos and charginos”. In: *Eur. Phys. J. C* 79.5 (2019), p. 395. DOI: `10.1140/epjc/s10052-019-6837-x`. arXiv: `1809.02097 [hep-ph]`.

[124] G. L. Bayatian et al. “CMS technical design report, volume II: Physics performance”. In: *J. Phys. G* 34.6 (2007), pp. 995–1579. DOI: `10.1088/0954-3899/34/6/S01`.

[125] Maria Eugenia Cabrera-Catalan et al. “Indirect and direct detection prospect for TeV dark matter in the nine parameter MSSM”. In: *Phys. Rev. D* 92.3 (2015), p. 035018. DOI: `10.1103/PhysRevD.92.035018`. arXiv: `1503.00599 [hep-ph]`.

[126] D. S. Akerib et al. “Projected WIMP sensitivity of the LUX-ZEPLIN dark matter experiment”. In: *Phys. Rev. D* 101.5 (2020), p. 052002. DOI: `10.1103/PhysRevD.101.052002`. arXiv: `1802.06039 [astro-ph.IM]`.

[127] E. Aprile et al. “Dark Matter Search Results from a One Ton-Year Exposure of XENON1T”. In: *Phys. Rev. Lett.* 121.11 (2018), p. 111302. DOI: `10.1103/PhysRevLett.121.111302`. arXiv: `1805.12562 [astro-ph.CO]`.

[128] B. C. Allanach et al. “SUSY Les Houches Accord 2”. In: *Comput. Phys. Commun.* 180 (2009), pp. 8–25. DOI: `10.1016/j.cpc.2008.08.004`. arXiv: `0801.0045 [hep-ph]`.

[129] Genevieve Belanger, Ali Mjallal, and Alexander Pukhov. “Recasting direct detection limits within micrOMEGAs and implication for non-standard Dark Matter scenarios”. In: *Eur. Phys. J. C* 81.3 (2021), p. 239. DOI: `10.1140/epjc/s10052-021-09012-z`. arXiv: `2003.08621 [hep-ph]`.

[130] H. Abdallah et al. “Search for γ-Ray Line Signals from Dark Matter Annihilations in the Inner Galactic Halo from 10 Years of Observations with H.E.S.S.” In: *Phys. Rev. Lett.* 120.20 (2018), p. 201101. DOI: `10.1103/PhysRevLett.120.201101`. arXiv: `1805.05741 [astro-ph.HE]`.

[131] Valentin Lefranc et al. “Dark Matter in γ lines: Galactic Center vs dwarf galaxies”. In: *JCAP* 09 (2016), p. 043. DOI: `10.1088/1475-7516/2016/09/043`. arXiv: `1608.00786 [astro-ph.HE]`.

[132] Christopher Dessert et al. “Higgsino Dark Matter Confronts 14 Years of Fermi γ-Ray Data”. In: *Phys. Rev. Lett.* 130.20 (2023), p. 201001. DOI: `10.1103/PhysRevLett.130.201001`. arXiv: `2207.10090 [hep-ph]`.

[133] Marcos M. Flores and Kalliopi Petraki. "Unitarity in the non-relativistic regime and implications for dark matter". In: (May 2024). arXiv: 2405.02222 [hep-ph].

[134] Andrea De Simone, Gian Francesco Giudice, and Alessandro Strumia. "Benchmarks for Dark Matter Searches at the LHC". In: *JHEP* 06 (2014), p. 081. DOI: 10.1007/JHEP06(2014)081. arXiv: 1402.6287 [hep-ph].

[135] Sonia El Hedri, Anna Kaminska, and Maikel de Vries. "A Sommerfeld Toolbox for Colored Dark Sectors". In: (2016). arXiv: 1612.02825 [hep-ph].

[136] Mathias Becker et al. "Impact of Sommerfeld effect and bound state formation in simplified t-channel dark matter models". In: *JHEP* 08 (2022), p. 145. DOI: 10.1007/JHEP08(2022)145. arXiv: 2203.04326 [hep-ph].

[137] Steven H. Weintraub. "Reverse Legendre polynomials". In: *Arch. Math.* 118 (2022), pp. 593–604. DOI: 10.1007/s00013-022-01740-2.

[138] Simone Biondini and Vladyslav Shtabovenko. "Bound-state formation, dissociation and decays of darkonium with potential non-relativistic Yukawa theory for scalar and pseudoscalar mediators". In: *JHEP* 03 (2022), p. 172. DOI: 10.1007/JHEP03(2022)172. arXiv: 2112.10145 [hep-ph].

[139] H. M. Pilkuhn. *Relativistic Particle Physics*. 1979. ISBN: 978-3-540-09348-0.

[140] Mathias Garny and Jan Heisig. "Bound-state effects on dark matter coannihilation: Pushing the boundaries of conversion-driven freeze-out". In: *Phys. Rev. D* 105.5 (2022), p. 055004. DOI: 10.1103/PhysRevD.105.055004. arXiv: 2112.01499 [hep-ph].

[141] Walter Gordon. "Zur Berechnung der Matrizen beim Wasserstoffatom". In: *Annalen der Physik* 394 (1929), pp. 1031–1056.

[142] I. S. Gradshteyn and I. M. Ryzhik. *Table of Integrals, Series, and Products*. 1943. ISBN: 978-0-12-294757-5, 978-0-12-294757-5.

[143] M. Stobbe. "Zur Quantenmechanik photoelektrischer Prozesse". In: *Annalen der Physik* 399 (Mar. 2006), pp. 661 –715. DOI: 10.1002/andp.19303990604.

[144] Ruben Oncala and Kalliopi Petraki. "Dark matter bound state formation via emission of a charged scalar". In: *JHEP* 02 (2020), p. 036. DOI: 10.1007/JHEP02(2020)036. arXiv: 1911.02605 [hep-ph].

[145] Carl Ramsauer. "Über den Wirkungsquerschnitt der Gasmoleküle gegenüber langsamen Elektronen". In: *Annalen der Physik* 369.6 (1921), pp. 513–540. DOI: https://doi.org/10.1002/andp.19213690603.

[146] Eung Jin Chun, Jong-Chul Park, and Stefano Scopel. "Non-perturbative Effect and PAMELA Limit on Electro-Weak Dark Matter". In: *JCAP* 12 (2012), p. 022. DOI: 10.1088/1475-7516/2012/12/022. arXiv: 1210.6104 [astro-ph.CO].

[147] Andrea Mitridate et al. "Cosmological Implications of Dark Matter Bound States". In: *JCAP* 1705.05 (2017), p. 006. DOI: 10.1088/1475-7516/2017/05/006. arXiv: 1702.01141 [hep-ph].

[148] Julia Harz and Kalliopi Petraki. "Radiative bound-state formation in unbroken perturbative non-Abelian theories and implications for dark matter". In: *JHEP* 07 (2018), p. 096. DOI: `10.1007/JHEP07(2018)096`. arXiv: `1805.01200 [hep-ph]`.

[149] Felix Kahlhoefer et al. "Implications of unitarity and gauge invariance for simplified dark matter models". In: *JHEP* 02 (2016), p. 016. DOI: `10.1007/JHEP02(2016)016`. arXiv: `1510.02110 [hep-ph]`.

[150] Juri Smirnov and John F. Beacom. "TeV-Scale Thermal WIMPs: Unitarity and its Consequences". In: *Phys. Rev. D* 100.4 (2019), p. 043029. DOI: `10.1103/PhysRevD.100.043029`. arXiv: `1904.11503 [hep-ph]`.

[151] Iason Baldes et al. "Supercool composite Dark Matter beyond 100 TeV". In: *JHEP* 07 (2022), p. 084. DOI: `10.1007/JHEP07(2022)084`. arXiv: `2110.13926 [hep-ph]`.

[152] Christiana Vasilaki and Kalliopi Petraki. "Radiation back-reaction during dark-matter freeze-out via metastable bound states". In: *JCAP* 06 (2024), p. 027. DOI: `10.1088/1475-7516/2024/06/027`. arXiv: `2402.13069 [hep-ph]`.

[153] Benedict von Harling and Kalliopi Petraki. "Bound-state formation for thermal relic dark matter and unitarity". In: *JCAP* 12 (2014), p. 033. DOI: `10.1088/1475-7516/2014/12/033`. arXiv: `1407.7874 [hep-ph]`.

[154] S. Biondini et al. "Effective field theories for dark matter pairs in the early universe: center-of-mass recoil effects". In: (Feb. 2024). arXiv: `2402.12787 [hep-ph]`.

[155] Tobias Binder et al. "Dark matter bound-state formation at higher order: a non-equilibrium quantum field theory approach". In: *JHEP* 09 (2020), p. 086. DOI: `10.1007/JHEP09(2020)086`. arXiv: `2002.07145 [hep-ph]`.

[156] Valerio De Luca et al. "Colored Dark Matter". In: *Phys. Rev. D* 97.11 (2018), p. 115024. DOI: `10.1103/PhysRevD.97.115024`. arXiv: `1801.01135 [hep-ph]`.

[157] Pouya Asadi et al. "Thermal squeezeout of dark matter". In: *Phys. Rev. D* 104.9 (2021), p. 095013. DOI: `10.1103/PhysRevD.104.095013`. arXiv: `2103.09827 [hep-ph]`.

[158] Tobias Binder et al. "Non-Abelian electric field correlator at NLO for dark matter relic abundance and quarkonium transport". In: *JHEP* 01 (2022), p. 137. DOI: `10.1007/JHEP01(2022)137`. arXiv: `2107.03945 [hep-ph]`.

[159] Pouya Asadi et al. "Glueballs in a thermal squeezeout model". In: *JHEP* 07 (2022), p. 006. DOI: `10.1007/JHEP07(2022)006`. arXiv: `2203.15813 [hep-ph]`.

[160] Mathias Becker et al. "Implications of Nonperturbative Effects for Colored Dark Sectors". In: *LHEP* 2023 (2023), p. 363. DOI: `10.31526/lhep.2023.363`.

[161] Benoit Assi and Michael L. Wagman. "Baryons, multi-hadron systems, and composite dark matter in non-relativistic QCD". In: (May 2023). arXiv: `2305.01685 [hep-ph]`.

[162] Ayuki Kamada, Masaki Yamada, and Tsutomu T. Yanagida. “Unification for darkly charged dark matter”. In: *Phys. Rev. D* 102.1 (2020), p. 015012. DOI: 10.1103/PhysRevD.102.015012. arXiv: 1908.00207 [hep-ph].

[163] John Ellis, Feng Luo, and Keith A. Olive. “Gluino Coannihilation Revisited”. In: *JHEP* 09 (2015), p. 127. DOI: 10.1007/JHEP09(2015)127. arXiv: 1503.07142 [hep-ph].

[164] John Ellis et al. “Scenarios for Gluino Coannihilation”. In: *JHEP* 02 (2016), p. 071. DOI: 10.1007/JHEP02(2016)071. arXiv: 1510.03498 [hep-ph].

[165] Seng Pei Liew and Feng Luo. “Effects of QCD bound states on dark matter relic abundance”. In: *JHEP* 02 (2017), p. 091. DOI: 10.1007/JHEP02(2017)091. arXiv: 1611.08133 [hep-ph].

[166] Seyong Kim and M. Laine. “Rapid thermal co-annihilation through bound states in QCD”. In: *JHEP* 07 (2016), p. 143. DOI: 10.1007/JHEP07(2016)143. arXiv: 1602.08105 [hep-ph].

[167] Julia Harz and Kalliopi Petraki. “Higgs Enhancement for the Dark Matter Relic Density”. In: *Phys. Rev. D* 97.7 (2018), p. 075041. DOI: 10.1103/PhysRevD.97.075041. arXiv: 1711.03552 [hep-ph].

[168] S. Biondini and M. Laine. “Thermal dark matter co-annihilating with a strongly interacting scalar”. In: *JHEP* 04 (2018), p. 072. DOI: 10.1007/JHEP04(2018)072. arXiv: 1801.05821 [hep-ph].

[169] S. Biondini and Stefan Vogl. “Coloured coannihilations: Dark matter phenomenology meets non-relativistic EFTs”. In: *JHEP* 02 (2019), p. 016. DOI: 10.1007/JHEP02(2019)016. arXiv: 1811.02581 [hep-ph].

[170] Hajime Fukuda, Feng Luo, and Satoshi Shirai. “How Heavy can Neutralino Dark Matter be?” In: *JHEP* 04 (2019), p. 107. DOI: 10.1007/JHEP04(2019)107. arXiv: 1812.02066 [hep-ph].

[171] Simone Biondini and Stefan Vogl. “Scalar dark matter coannihilating with a coloured fermion”. In: *JHEP* 11 (2019), p. 147. DOI: 10.1007/JHEP11(2019)147. arXiv: 1907.05766 [hep-ph].

[172] Mark B. Wise and Yue Zhang. “Stable Bound States of Asymmetric Dark Matter”. In: *Phys. Rev. D* 90.5 (2014). [Erratum: Phys.Rev.D 91, 039907 (2015)], p. 055030. DOI: 10.1103/PhysRevD.90.055030. arXiv: 1407.4121 [hep-ph].

[173] Haipeng An, Mark B. Wise, and Yue Zhang. “Strong CMB Constraint On P-Wave Annihilating Dark Matter”. In: *Phys. Lett. B* 773 (2017), pp. 121–124. DOI: 10.1016/j.physletb.2017.08.010. arXiv: 1606.02305 [hep-ph].

[174] Simone Biondini and Vladyslav Shtabovenko. “Non-relativistic and potential non-relativistic effective field theories for scalar mediators”. In: *JHEP* 08 (2021), p. 114. DOI: 10.1007/JHEP08(2021)114. arXiv: 2106.06472 [hep-ph].

[175] Ruben Oncala and Kalliopi Petraki. “Bound states of WIMP dark matter in Higgs-portal models. Part II. Thermal decoupling”. In: *JHEP* 08 (2021), p. 069. DOI: 10.1007/JHEP08(2021)069. arXiv: 2101.08667 [hep-ph].

[176] Joakim Edsjö and Paolo Gondolo. “Neutralino relic density including coannihilations”. In: *Phys. Rev.* D56 (1997), pp. 1879–1894. DOI: `10.1103/PhysRevD.56.1879`. arXiv: `hep-ph/9704361 [hep-ph]`.

[177] Laura G. van den Aarssen, Torsten Bringmann, and Yasar C Goedecke. “Thermal decoupling and the smallest subhalo mass in dark matter models with Sommerfeld-enhanced annihilation rates”. In: *Phys. Rev. D* 85 (2012), p. 123512. DOI: `10.1103/PhysRevD.85.123512`. arXiv: `1202.5456 [hep-ph]`.

[178] Tomohiro Abe. “Effect of the early kinetic decoupling in a fermionic dark matter model”. In: *Phys. Rev. D* 102.3 (2020), p. 035018. DOI: `10.1103/PhysRevD.102.035018`. arXiv: `2004.10041 [hep-ph]`.

[179] Yevgeny Kats and Matthew D. Schwartz. “Annihilation decays of bound states at the LHC”. In: *JHEP* 04 (2010), p. 016. DOI: `10.1007/JHEP04(2010)016`. arXiv: `0912.0526 [hep-ph]`.

[180] John Markus Blatt and Victor Frederick Weisskopf. *Theoretical nuclear physics*. New York: Springer, 1952. ISBN: 978-0-471-08019-0. DOI: `10.1007/978-1-4612-9959-2`.

[181] Sz. Borsanyi et al. “Calculation of the axion mass based on high-temperature lattice quantum chromodynamics”. In: *Nature* 539.7627 (2016), pp. 69–71. DOI: `10.1038/nature20115`. arXiv: `1606.07494 [hep-lat]`.

[182] Tobias Binder et al. “Saha equilibrium for metastable bound states and dark matter freeze-out”. In: *Phys. Lett. B* 833 (2022), p. 137323. DOI: `10.1016/j.physletb.2022.137323`. arXiv: `2112.00042 [hep-ph]`.

[183] A. Ore and J. L. Powell. “Three photon annihilation of an electron - positron pair”. In: *Phys. Rev.* 75 (1949), pp. 1696–1699. DOI: `10.1103/PhysRev.75.1696`.

[184] Robert J. Scherrer and Michael S. Turner. “On the Relic, Cosmic Abundance of Stable Weakly Interacting Massive Particles”. In: *Phys. Rev. D* 33 (1986). [Erratum: Phys.Rev.D 34, 3263 (1986)], p. 1585. DOI: `10.1103/PhysRevD.33.1585`.

[185] Luca Di Luzio, Federico Mescia, and Enrico Nardi. “Window for preferred axion models”. In: *Phys. Rev. D* 96.7 (2017), p. 075003. DOI: `10.1103/PhysRevD.96.075003`. arXiv: `1705.05370 [hep-ph]`.

[186] Gonzalo Alonso-Álvarez, James M. Cline, and Tianzhuo Xiao. “The flavor of QCD axion dark matter”. In: *JHEP* 07 (2023), p. 187. DOI: `10.1007/JHEP07(2023)187`. arXiv: `2305.00018 [hep-ph]`.

[187] Edward Witten. “Cosmic Separation of Phases”. In: *Phys. Rev. D* 30 (1984), pp. 272–285. DOI: `10.1103/PhysRevD.30.272`.

[188] Mathias Garny, Alejandro Ibarra, and Stefan Vogl. “Signatures of Majorana dark matter with t-channel mediators”. In: *Int. J. Mod. Phys.* D24.07 (2015), p. 1530019. DOI: `10.1142/S0218271815300190`. arXiv: `1503.01500 [hep-ph]`.

[189] Satoshi Mizuta and Masahiro Yamaguchi. "Coannihilation effects and relic abundance of Higgsino dominant LSP(s)". In: *Phys. Lett. B* 298 (1993), pp. 120–126. DOI: 10.1016/0370-2693(93)91717-2. arXiv: hep-ph/9208251.

[190] Harun Acaroğlu et al. "Flavoured Majorana Dark Matter then and now: from freeze-out scenarios to LHC signatures". In: *JHEP* 06 (2024), p. 179. DOI: 10.1007/JHEP06(2024)179. arXiv: 2312.09274 [hep-ph].

[191] Laura Covi, Jihn E. Kim, and Leszek Roszkowski. "Axinos as cold dark matter". In: *Phys. Rev. Lett.* 82 (1999), pp. 4180–4183. DOI: 10.1103/PhysRevLett.82.4180. arXiv: hep-ph/9905212 [hep-ph].

[192] Nora Brambilla et al. "Static quark-antiquark pairs at finite temperature". In: *Phys. Rev. D* 78 (2008), p. 014017. DOI: 10.1103/PhysRevD.78.014017. arXiv: 0804.0993 [hep-ph].

[193] Y. Burnier, M. Laine, and M. Vepsalainen. "Heavy quarkonium in any channel in resummed hot QCD". In: *JHEP* 01 (2008), p. 043. DOI: 10.1088/1126-6708/2008/01/043. arXiv: 0711.1743 [hep-ph].

[194] Matteo Cacciari et al. "A note on the fate of the Landau–Yang theorem in non-Abelian gauge theories". In: *Phys. Lett. B* 753 (2016), pp. 476–481. DOI: 10.1016/j.physletb.2015.12.053. arXiv: 1509.07853 [hep-ph].

[195] W. Beenakker, R. Kleiss, and G. Lustermans. "No Landau-Yang in QCD". In: (Aug. 2015). arXiv: 1508.07115 [hep-ph].

[196] Oliverio Jitrik and Carlos F. Bunge. "Transition Probabilities for Hydrogen-Like Atoms". In: *Journal of Physical and Chemical Reference Data* 33.4 (Jan. 2005), pp. 1059–1070. ISSN: 0047-2689. DOI: 10.1063/1.1796671. URL: https://doi.org/10.1063/1.1796671.

[197] Genevieve Bélanger et al. "micrOMEGAs5.0 : Freeze-in". In: *Comput. Phys. Commun.* 231 (2018), pp. 173–186. DOI: 10.1016/j.cpc.2018.04.027. arXiv: 1801.03509 [hep-ph].

[198] H. A. Kramers. "XCIII. On the theory of X-ray absorption and of the continuous X-ray spectrum". In: *Philosophical Magazine Series 1* 46 (1923), pp. 836–871.

[199] V. M. Katkov and V. M. Strakhovenko. "Radiative recombination and its application in experiments on electron cooling". In: *Soviet Journal of Experimental and Theoretical Physics* 48 (Oct. 1978), p. 639.